*Author:*
**Sugic, Danica**

*Title:*
**Unravelling the dark focus of light**

*a study of knotted optical singularities*

# Unravelling the dark focus of light: a study of knotted optical singularities

Danica Sugic

School of Physics

January 2019

A dissertation submitted to the University of Bristol in accordance with the requirements of the degree of Ph.D. in the Faculty of Science

Word count: 53623

# Abstract

The discovery of nontrivial topological objects is a challenging task for physicists and mathematicians. This thesis investigates and extends the theory of knotted and linked optical vortex lines to additional singular topological conformations. The study demonstrates that singular optics is deeply connected with the polarisation texture of focused fields characterised by a dark focus. Optical vortices are defined as nodal lines of the intensity in monochromatic scalar fields, *e.g.* laser light, and correspond to lines of darkness that are usually embedded in a low-intensity volume. Theoretical and numerical topological methods are applied to paraxial and nonparaxial optical fields to analyse their phase and polarisation singularities. New types of knots and links are constructed explicitly in the focal volume of optical wavefunctions propagating in free space. For knot structures approaching the scale of wavelength, a bundle of intertwined knotted nodal structures in the transverse and longitudinal polarisation components of the electric and magnetic fields is described. Additionally, a whole family of Hopfions, which are mathematically described by Hopf fibrations, is shown to emerge in the 3D polarisation texture of focused light. Experiments to measure these phenomena are proposed, some of which have been confirmed in the laboratory. Singular knot bundles and optical Hopfions reveal potential applications of light-matter interaction in nanophotonic systems. Their practical implementation could be used to store topological states into soft-materials or quantum physical systems.

# Acknowledgements

This research was funded by the Leverhulme Trust Research Programme Grant No. RP2013-K-009, *SPOCK: Scientific Properties of Complex Knots*. This work was carried out using the computation environments offered by *Mathematica* and *MATLAB*, the vector graphics editor *Inkscape* and the computational facilities of the Advanced Computing Research Centre of the University of Bristol.

I would like to express my gratitude to Prof. Mark Dennis for his extremely valuable and constructive supervision on the development of this study. I have always admired his passion for physics and his approach to problem solving, which make his scientific style unique.

I would also like to thank Prof. Mervyn Miles for taking the role of my supervisor in Mark's absence, Henkjan Gersen, who welcomed me in his group of students for several months during my second year, and Martin Gradhand, who has given important support and motivation over the years. I am grateful to Robert King, Kevin O'Holleran and James Ring, whose doctoral theses had inspired my work. I would like to thank my collaborators Eileen Otte, Ramon Runde, Alessandro Zannotti, Prof. Cornelia Denz, Hugo Larocque, Dominic Mortimer, Robert Fickler, Prof. Robert Boyd, Prof. Ebrahim Karimi and Asier Marzo. I also had the great pleasure of discussing my results with Prof. Miguel Alonso, Peter Banzer, Etienne Brasselet, Ruiqing He, Martin Neugebauer, Prof. Miles Padgett and David Phillips. I would like to offer my special thanks to Prof. Sir Michael Berry, for being such an inspirational physicist and kind colleague.

This adventure would not have been the same without my precious student companions: Keith Alexander, Ben Bode, Elena Boniolo, Alex Houston, Lauren Scanlon and Teuntje Tijssen. We shared happiness and pain and I feel so blessed to have had them in my team. I also had the pleasure of working with David Foster and Alexander

Taylor: our SPOCK big brothers. I would like to the thank the academic administrators Emma Creasey, Martisse Foster, Caroline Jarrett and Briony Spraggon for their great efficiency. Furthermore, friends in the School of Physics: Thomas Chillimamp, Abi Coveney, Chiara Giroletti, David Hughes, Xi Peng and Renato Quagliani.

Profound gratitude goes to the people who believed in me from day one, these are my life-time friends in Monsano: Andrea Avaltroni, Alessandro Baldini, Giulia Bianchi, Serena Bronzini, Francesca Crinò, Laura D'Ascanio, Matteo Filipponi, Eva Gelosi, Giacomo Gigli, Giacomo Mazzarini and Carmen Riggio. The completion of my dissertation would not have been possible without Davide Cieri and Giacomo Ferranti, who filled me up with the best carbonara on Earth (multiple times). Thanks to Gaetano Arena, Michele Carrabba, Alessia Di Cuia, Leonardo Feliciani, Elpida Katsiveli, Teresa Reis and Cyril Torre: my second family in Bristol. We shared magic moments which I will always bring in my heart. A special thanks goes to Gae, who has been my guide, my example and my shoulder; there are no words to describe what a supportive friend he has been to me in achieving this goal. I would like to acknowledge that Michael Fielding is the 'unraveller' of the thesis title and has inspired me with many ingenious phrases. I also want to express my infinite gratitude to Virginia Andreani and Witek Smereta, who kindly proof read parts of this work. The important people who pushed me into the achievement of this goal are Sharon Baker, Sofia Dall'orso, Paolo Enrico de Falco, Matteo Giangolini, Joost Iwema, Lucia Giordano, Camille Locatelli, Alizée Navarro, Marta Rossetti and Ilda Rrapaj. I would not have been here without their constant encouragement. Along the same lines, I must say that Cecilia Vona has given me the most invaluably constructive criticism that a friend can hope for. She was my 'buddy'. A big thanks goes to my wonderful family: mum Ana, Ivka and Ivo Šugić. Their presence in my life is a sweet background noise, which never abandons me.

Nobody has been more important to me in the pursuit of this project than Dicken Richards. He brought love and happiness in my life. For this and for being my rock, I am extremely grateful to him. His patience cannot be underestimated.

*This work is wholeheartedly*

*dedicated to my father.*

# Author's declaration

I declare that the work in this dissertation was carried out in accordance with the requirements of the University's Regulations and Code of Practice for Research Degree Programmes and that it has not been submitted for any other academic award. Except where indicated by specific reference in the text, the work is the candidate's own work. Work done in collaboration with, or with the assistance of, others, is indicated as such. Any views expressed in the dissertation are those of the author.

SIGNED:  DATE: 7th May 2019

# Contents

# List of Figures

# List of Tables

# 1 Introduction

**There are horrible people who, instead of solving a problem, tangle it up and make it harder to solve for anyone who wants to deal with it.**

*Friedrich Nietzsche*

## 1.1 General introduction

Light is intuitively bright. When we are asked to think about light, we might visualise luminous regions, without realising that darkness is not necessarily characterised by the absence of light. In fact, low intensity regions are characterised by the phase, or the polarisation state of an optical field, as well as bright regions. With the same misconception, some people believe that optical structures smaller than a wavelength do not exist, because they are counter-intuitive to many and go against common experience. However, it has been shown that optical beams propagating in free space and characterised by low intensity regions manifest interesting properties which have not been equally observed into 'bright beams'. The main focus of this study is to describe the fine structure of the *topology of darkness*. These terms indicate 'dark beams', which, when interpreted by tools from topology and geometry, reveal nontrivial light patterns of subwavelength size, or larger.

Topology is a branch of mathematics that formally defines qualitative properties of objects, which do not change under continuous transformations. Topology can be

applied to physical systems to characterise certain behaviours. Specifically, we investigate the topological properties of *optical vortices*, which are perfect loci of darkness identified by zeros of intensity. Optical vortices are points on a plane and lines in a three-dimensional volume. Due to their 3D geometrical nature, they can form nontrivial conformations, such as tangled loops, which can be understood as mathematical *knots* or *links*. These nontrivial 3D conformations are the main focus of this study.

Optical vortices occur in beams in which the polarisation state of light can be ignored. This is because the polarisation is uniform in every point in space. When the polarisation properties of light are considered, zeros of intensity can occur only when every single component of the electromagnetic vector is null. We do not investigate absolute zeros of the total intensity in this thesis, but we study other points associated to the electric and magnetic vectors, called *polarisation singularities*. These points show interesting topologies in dark regions of light. We show that, although they are 'bright' points, they have similar properties to optical vortices. The analogy arises because polarisation singularities are also lines in three-dimensions and they can be knotted and linked. Furthermore, we find that polarisation states can form volume filling configurations made of a continuous bundle of knotted filaments, corresponding to topological objects called *Hopf fibrations*. These structures are more complicated than a single knotted line, because the entire volume manifests a nontrivial knotted texture.

The phenomena described theoretically in this study are predicted to appear in *dark foci*, generated by focused light distributions. The optical topological objects we describe are of subwavelength size, or larger, and they either occur 'naturally' in light beams or result from the precise control of interference phenomena. Throughout this study we present the design of several experiments, some of which have been implemented in the laboratory to successfully prove our theoretical results.

The rest of this chapter is structured as follows. In § 1.2, the overall structure of this thesis is presented. § 1.3 gives an overview of knots and links formation in

physical systems. In § 1.4, singularities arising in scalar and vector fields are described in detail. In § 1.5, different experimental devices by which optical vortices can be generated are listed. In § 1.6, the historical steps in which optical vortex knots and links were generated theoretically and experimentally are presented. Finally, Hopf fibrations arising in several different physical systems are described in § 1.7.

## 1.2 Thesis outline

This thesis may require the reader, who is not an expert in optics and topology, to go back and forth between the different chapters[1]. We anticipate that the later chapters (4, 5 and 6), where the original results of this study are presented, were developed from the simple ideas reported in the background chapters, concerning optics (chapter 2) and topology (chapter 3). These include technical details and methods from the literature. The contents are arranged as follows.

The rest of this introductory chapter gives a historical overview of the fundamental optical quantities and the main topological concepts *propaedeutic* to this thesis. It is not necessary for experts in either singular optics, or topology, to follow the details.

Chapter 2 presents some basic concepts in physical optics, such as Maxwell's equations, Laguerre-Gaussian modes and the Stokes parameters. It also summarises the wave propagation methods used throughout this study: some standard routines, such as Richards-Wolf vector diffraction theory, and less standard routines, such as polynomial beam propagation.

In chapter 3, optical vortices and polarisation singularities are mathematically defined, but also knots, links and Hopf fibrations. Furthermore, the mathematical theory to explicitly construct knotted scalar functions is reported, and also the numerical methods to perform the topological analysis of optical fields.

In the first original chapter, 4, the theory of optical vortex knots and links is extended to a new class of curves. Further, the procedures to design holograms for ex-

[1]The pdf version of this this thesis has hyperlinks associated to the crossreferences.

perimental implementation are presented. The chapter continues by showing a new method to analyse the properties of polarised fields around knotted polarisation singularities.

In chapter 5, the theory of optical vortex knots is also extended to the nonparaxial vector regime by showing a subwavelength singular structure made of a bundle of knotted filaments. These appear as the nodal lines of each component of the electric and magnetic vectors and form a singular knot bundle.

In chapter 6, a knotted topological object occurring naturally in tightly focused fields is presented. This has the topology of a Hopf fibration. This significant result describes the importance of topological quantities, namely the Hopf index and the Skyrmion number, in the field of singular optics. In the first part of the chapter, the Richards-Wolf vector diffraction integral is solved by using spin weighted spherical harmonics. In the second part, the results are extended to the paraxial regime, by engineering Hopf fibrations in polarised Laguerre-Gaussian beams.

In the final chapter, 7, the findings of this study are summarised and the possibilities for further investigation are covered. Particular interest is taken in the analogy between optical waves and waves describing sound or matter. The extension of our results to other physical systems, where knots, links, Hopf fibrations and other knotted configurations could manifest, is discussed.

Some parts of this study were published in scientific journals:

• § 4.4 was published in H. Larocque, D. Sugic, D. Mortimer, A. J. Taylor, R. Fickler, R. W. Boyd, M. R. Dennis, and E. Karimi, "Reconstructing the topology of optical polarization knots," *Nat. Phys.* **14**, 1079–1082 ( 2018);

• chapter 5 was published in D. Sugic and M. R. Dennis, "Singular knot bundle in light," *J. Opt. Soc. Am. A* **35**, 1987–1999 (2018).

Three articles are in preparation:

• one article relative to the lemniscate optical knots, treated in § 4.2;

• two articles describing theoretical and experimental optical Hopf fibrations, treated

in chapter 6.

## 1.3 Knots in physics

The concept of *knottedness* is somehow intuitive: any closed curve in three-dimensional space is a knot. Therefore there are 'no ends to tie or untie' in such a curve. Links are the combination of two or more knots, which can be of the same type or of different

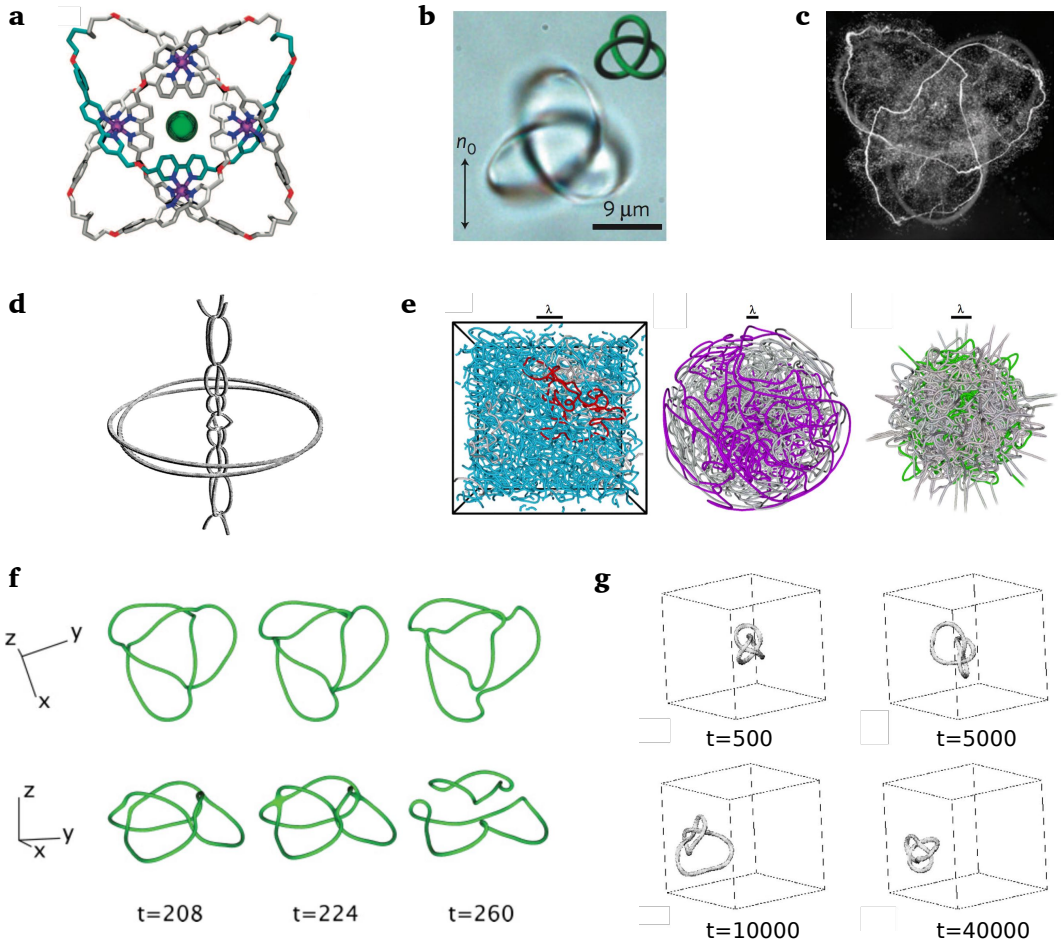


Figure 1.1: **Knots and links occurring in physical systems**. (a) Knotted molecule (knot type $8_{19}$) [5]. (b) Trefoil-knotted liquid crystals [7]. (c) Trefoil-knotted vortex lines in water [8] . (d) Zero lines of hydrogen wavefunctions [9]. (e) Zero lines of quantum wavefunctions [11]. Time-evolving vortex lines in (f) Bose-Einstein Condensates [12] and (g) excitable media [13].

types; the curves can entwine about each other in infinitely many ways. In fact, there exist infinitely many types of knots and links. Two knots are distinguished if it is not possible to smoothly deform one into the other without passing the curve through itself; if this deformation is possible the two curves are topologically identical and they correspond to the same knot type. This property extends to links as well. A curve in the shape of a ring is often called the *unknot* and any curve that can be continuously deformed into the ring without cutting the line is said to be unknotted [1].

Knots and links are found in a large variety of disciplines such as statistical mechanics, quantum field theory and quantum computing. Knots came into prominence in physics in the late $19^{\text{th}}$ century, when Lord Kelvin proposed to explain elementary particles as vortices in an ether that pervades space; his ideas were considered by Tait, Maxwell and Poynting. Eventually the ether was discredited. This and the discovery of the electron by Thompson (1897) and Rutherford's model (1911) discredited Kelvin's conjecture on knotted atoms. Even though these ideas are nowadays considered a 'failure', Kelvin's work pioneered the use of mathematical knot theory to investigate the nature of intricately tangled closed lines occurring in a variety of physical systems, and their interaction with the environment.

Knots and links occur in several different physical systems, shown in Figure 1.1. In nature, they form spontaneously in molecules and exist in three major classes of biopolymers: DNA, RNA and proteins knots [2–4]. Knotting at the molecular level has progressed extensively in recent years; this is demonstrated in Figure 1.1 (a) showing the tightest knot ever made, which is the $8_{19}$ knot featuring eight non-alternating crossings in a 192-atom closed loop $\sim 20$ nanometers in length [5].

Other tangles do not spontaneously form in nature, but are deliberately constructed in physical systems. For example, knots and links were engineered as defects around colloidal structures in liquid crystals [6, 7], illustrated in Figure 1.1 (b), or fluid vortex lines in water [8], shown in Figure 1.1 (c). At the atom level, the Hopf link and the trefoil knot have been predicted theoretically in the zero lines of com-

plex superpositions of degenerate hydrogen wavefunctions [9] represented in Figure 1.1 (d). This work inspired the proof of the existence of knotted complex-valued eigenfunctions of the harmonic oscillator in $\mathbb{R}^3$ [10] and their explicit construction in other types of quantum wavefunctions, shown in Figure 1.1 (e) [11]. Vortex knot states have been theoretically predicted in Bose-Einstein Condensates (BECs) superfluid wave functions [12], shown in Figure 1.1 (f); these structures evolve in time by breaking into simpler curves. Other types of time-evolving knots were generated in the vortices of naturally occurring excitable media [13], shown in Figure 1.1 (g).

Knotted lines were constructed in light beams in two different forms. This study is concerned with optical vortex knots and links [14–19], which will be treated in more detail in § 1.4. The other type of knotted light is encoded in time-dependent electromagnetic field lines [20–22]. In some cases the infinitely large amount of field lines present in the beam constitute a highly complicated knotted structure topologically equivalent to the Hopf fibration. We will describe this topological object in more detail in § 1.7 and we will present the same structure embedded in the polarisation texture of optical beams in chapter 6.

## 1.4 Historical review of optical vortices and polarisation singularities

This section gives a brief introduction to the field of singular optics [23]. The first analytical treatment of an optical vortex was reported by Wolter in 1950 [24]. He analysed the spatial interference pattern arising in the optical phenomenon of the Goos-Hänchen effect [25] in detail. This optical phenomenon describes the small lateral shift experienced by a finite width linearly polarised beam under total internal reflection at a dielectric interface. Wolter derived a theoretical explanation, his original plot showing an optical vortex surrounded by the phase contours of the total wave is reported in Figure 1.2. His astonishing results were the first observation of

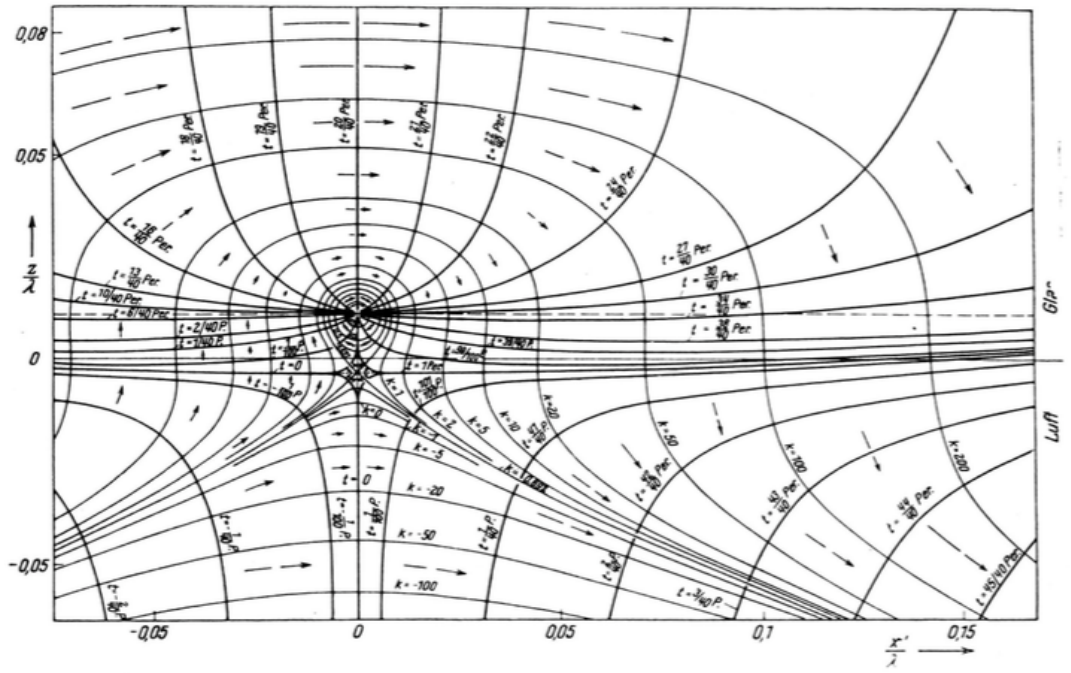


Figure 1.2: **First plot of an optical vortex by Wolter**. Total internal reflection at a dielectric interface in the Goos-Hänchen effect. The thick curves represent phase contours meeting at the vortex point. The thin lines and the vectors represent the time-averaged energy current, which circulates around the vortex. Image from [24].

'circulating waves', by which he meant that there are areas in which the time-averaged energy flow circulates in closed streamlines. This circulation property is a general feature of optical vortex points. In 1967 Boivin, Dow and Wolf [26] derived similar features while analysing the field near a focus. Their results showed that the flow lines of the time averaged Poynting vector have, again, circulating features. Later, optical vortices were created in superpositions of plane waves by Braunbek [27], Braunbek and Laukien [28], Sommerfeld [29] and Born and Wolf [30].

The work mentioned so far did not give a detailed investigation of the phase structure around a singularity. The breakthrough paper, in which such topic was treated, was the work of Nye and Berry, published in 1974 [31]. The theoretical paper followed unpublished experiments by Nye and Walford (University of Bristol) on ultrasound scattered from crumpled aluminium foil [23], which showed the presence of phase

singularities. These were described as general features of wave interference and they were called *wave dislocations*, in analogy to the dislocations in crystal lattices. The similarity between optics and crystals is shown in Figure 1.3, where the edge dislocation and the screw dislocation in optical fields are compared to crystal lattices. Screw dislocations are also called optical vortices. This is because the scalar field around such points has a similar behaviour to the vortices of fluid dynamics.

Optical vortices are represented in singular optics as simple optical elements determined by the phase singularities of the light field. However, this is not their unique representation, as they can also be defined by *superoscillations*. Regions of low in-

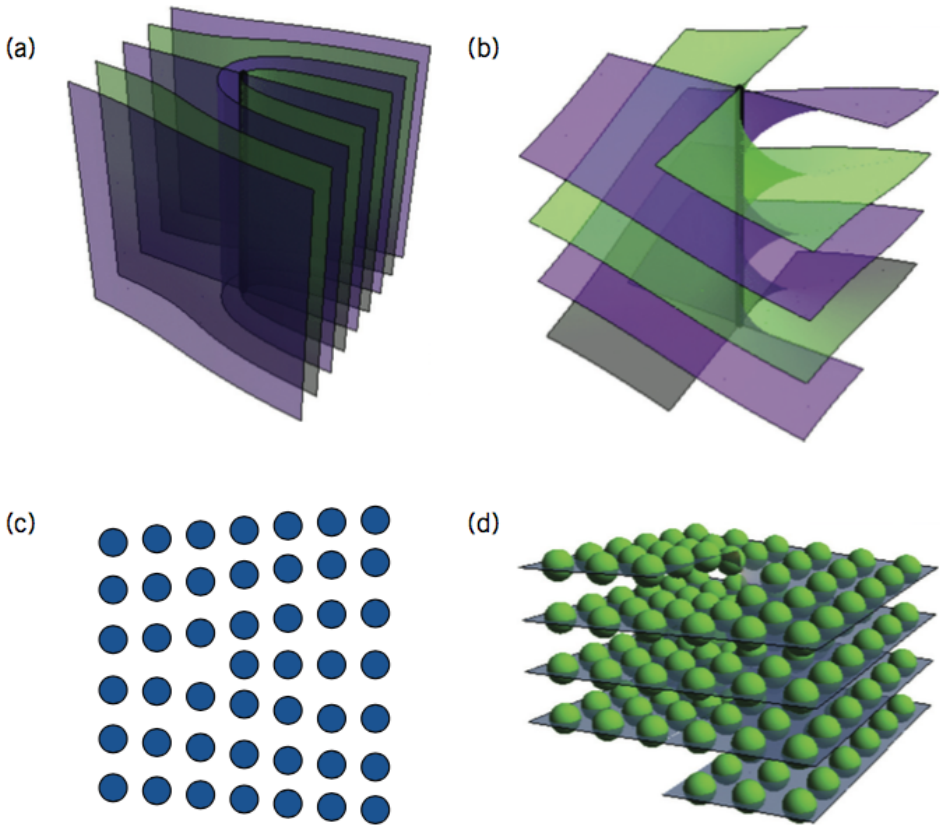


Figure 1.3: **Dislocations in optical waves and crystal lattices**. The real and imaginary parts of a complex scalar optical field intersect at an edge dislocation in (a) and at a screw dislocation in (b). These are similar to the atoms' arrangement in a crystal forming an edge dislocation (2D view) in (c) and a screw dislocation in (d). Image from [23].

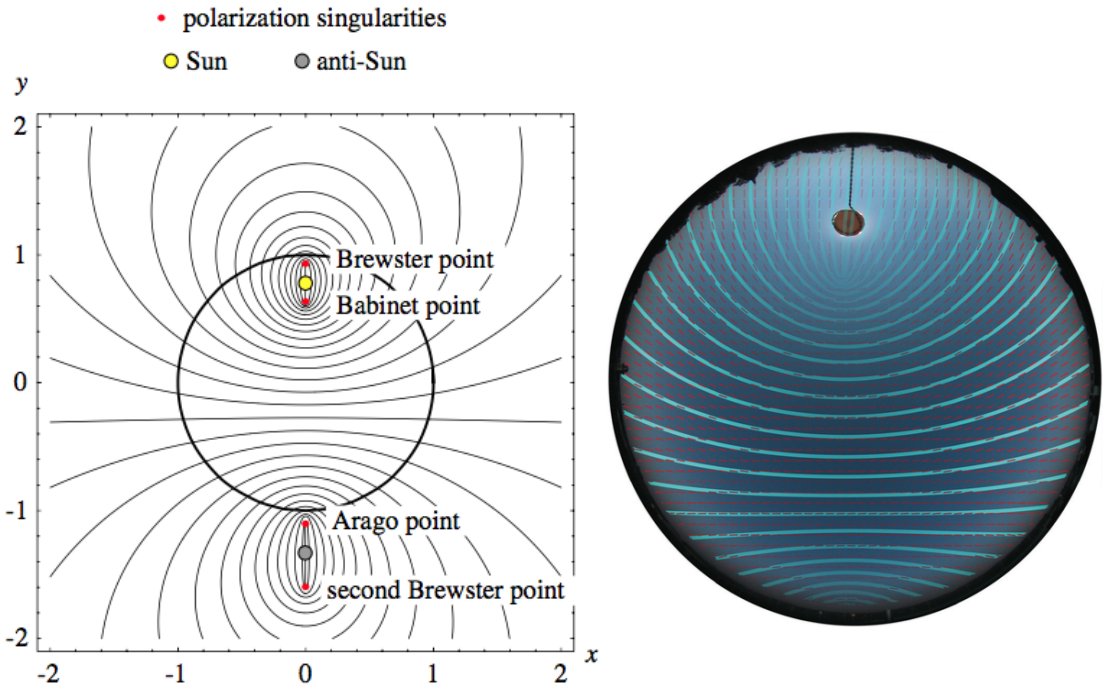


Figure 1.4: **Polarisation singularities in the blue sky**. (a) The theoretical model of [32] predicts the polarisation pattern (lines) in the stereographic plane of the sky and its neutral points (the Arago point, the Babinet point, the Brewster points). Image from [32]. (b) Disk representing the full visible sky hemisphere. The cyan lines are the theoretical predictions of [32] and the segments are the experimentally detected directions of partial polarisation. The position of the sun is covered; the Babinet point and the Arago point can be observed. Image from [23].

tensity are very often found in optical fields characterised by a superoscillatory behaviour [33]. This means that the optical system can be described in terms of band-limited functions oscillating arbitrarily faster than their highest Fourier components. Practically, this formalism is used to describe delicate interference patterns created at the expense of an exponential intensity grow in other regions. This phenomenon is general and holds for a wide variety of optical fields, including paraxial light, or tightly focused light (such as monochromatic laser beams). The application of super-oscillations to physical systems, traditionally probed with evanescent waves, was used to beat the diffraction limit [34]. In fact, a precisely tailored interference of multiple

waves can form a focus in free space of arbitrarily small size.

Phase singularities were discovered long after polarisation singularities [35]. The discovery of polarisation is usually attributed to Bartholinus [36, 37], who published the first scientific observation of a polarisation effect in 1669. More than a century later (1808), Malus discovered the polarisation of natural light [38]. The first discovery of a polarisation singularity is attributed to Arago, who observed a *neutral* point in the blue sky. The term neutral stands for a node in the degree of polarisation, but it also identifies a singularity of the azimuthal angle $\alpha$ in the Poincaré sphere (§ 2.1.7). The Arago point can be observed in the bottom of Figure 1.4 [23, 32]. More scientists became interested in the neutral points of the sky, and more were discovered; namely the Babinet point (1840) and the Brewster points [39, 40], also shown in Figure 1.4.

The type of singularities that are important for this study belong to completely polarised monochromatic fields. These are not neutral points because, unlike the sky, where the polarisation is an incoherent mixture over different frequencies, the fields we investigate are characterised by well defined states of polarisation varying with position. The singular objects manifesting in such fields are C lines, $C^T$ lines, L surfaces and $L^T$ lines (§ 3.1.2). These singularities were identified by Nye in 1983 in his celebrated work [41, 42], they were further discussed in detail by Berry and Dennis [35, 43, 44].

Nowadays phase singularities and polarisation singularities are topological objects of fundamental importance. Their relationship with the optical angular momentum created a boost of interest in modern optics which has been growing exponentially.

Figure 1.5: **Spatial light modulator (SLM)**. SLMs are computer-controlled devices used in experimental optics to generate arbitrary intensity, phase and polarisation patterns. Image from [54].

## 1.5 Devices for the experimental generation of optical vortices

Optical vortices of topological charge $\ell$ appear on the axis of Laguerre-Gaussian (LG) modes (§ 2.1.4). The first of such beams containing an optical vortex of charge $|\ell| = 1$, whose positive or negative sign could be arbitrarily switched, was engineered by Tamm and Weiss [45]. Several others [46, 47] have built similar optical systems that emit LG-beams directly. However, starting from the 1990s, diffractive optical elements for the generation of dislocations in optical beams [48, 49] became much more popular than direct generation of LG modes. Other methods to generate optical vortices experimentally involve cylindrical lenses [45, 50–52] and spiral phase plates [53].

Even though there exist several different methods to generate optical vortices into light beams (some listed above), none of them is as easy to use and flexible as computer-generated holograms [23]. The popularity of such diffractive optical ele-

ments is due to the commercial availability and high quality of *spatial light modulators* (SLMs). These devices are made of computer-controlled pixels which are capable of defining the phase spatial distribution of reflected light. Figure 1.5 shows a modern SLM from the company *Meadowlark Optics*. Nowadays SLMs are used to fully structure the intensity, phase and polarisation of light beams [54] at very high resolution. SLMs are our proposed experimental prototype for the holograms designed in this study.

## 1.6 The construction of knotted optical fields

The explicit construction of complex scalar fields that satisfy the wave equation and whose nodal lines form knots and links is a challenging problem. This section reviews the methods to embed knotted vortex lines into optical beams.

The first optical beam solutions of the scalar Helmholtz equation, whose dislocation lines were intentionally shaped in the form of knots and links, was given by Berry and Dennis in 2001 [14]. These knotted optical fields were built as sums of Bessel

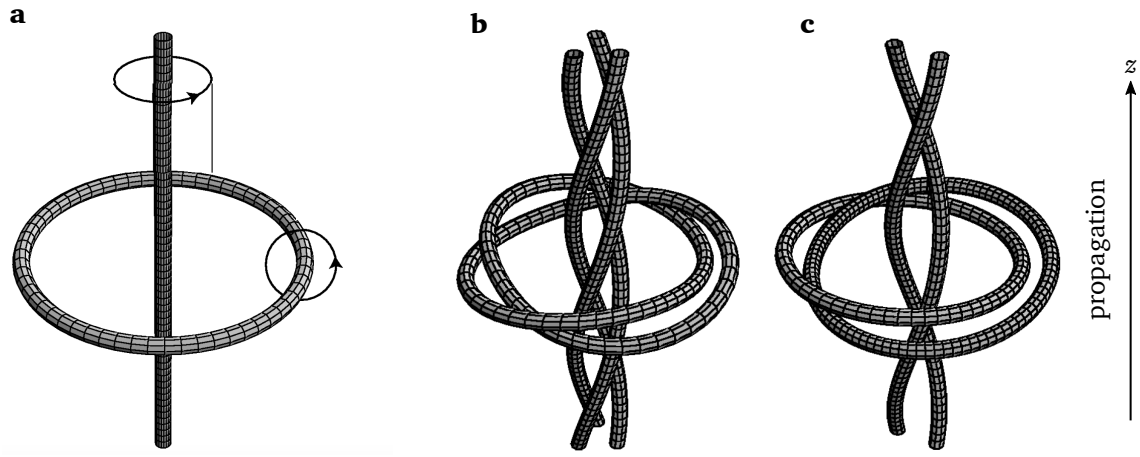


Figure 1.6: **The first construction of knots and links in beams of light**, adapted from [14]. (a) A structurally unstable vortex ring of topological strength $m$, threaded by an axial vortex line of topological strength $n$, unfolds into knotted lines under perturbation. (b) When $m = 2$ and $n = 3$ the unfolding gives the trefoil knot threaded by a triple-stranded helix; (c) when $m = 2$ and $n = 2$ the unfolding gives the Hopf link threaded by a double-stranded helix.

beam solutions [55, 56]. The construction strategy involves a structurally unstable high-order vortex ring, threaded by an axial high-order vortex line, shown in Figure 1.6 (a); the dislocation loop is located at the plane $z = 0$ and the dislocation line is positioned along the $z$-axis, which also indicates the propagation direction. The argument is that such vortex lines form a structurally unstable configuration which, under the perturbation of a weak wave that does not itself possess any nodal line, unfolds into a knotted conformation and additional curves closely twisted around the optical axis. The Hopf link and the trefoil knot are illustrated, respectively, in Figure 1.6 (b) and (c).

Initially, it was thought that the knotted solutions could not be implemented in paraxial fields[2]. However, the same authors adapted the strategy described above to the paraxial regime [15], contributing to the theoretical and experimental realisation of optical vortex knots in monochromatic light beams. In this regime the formation of knots and links is not given by small perturbations, but the Hopf link and the trefoil knot were constructed explicitly by choosing a sufficiently large perturbation parameter, which causes reconnections of the vortex lines in the correct topological conformation. The analytic expressions for the knotted beams were sums of polynomial wavefunctions inspired by the work of Nye [57] and defined in both the paraxial and the nonparaxial regime; the simplicity of such polynomial functions allowed fast manipulation of the field's nodal lines.

Based on the knotted paraxial polynomials, the trefoil knot and the Hopf link were embedded in a finite sum of Laguerre-Gaussian beams theoretically [15] and then, also experimentally by Leach *et al.* in 2004 [16, 17]. Their generation scheme is illustrated in Figure 1.7, in which the beam is structured directly through a computer-controlled spatial light modulator. Since optical vortex knots are threads of darkness, their detection is extraordinarily difficult because the position of phase singularities is determined via interferometry, which rely on intensity measurements. For this reason, the

[2]Appendix D of [14] proves that the paraxial approximation prohibits non-axial dislocations with strength greater than unity, required by the construction of [14].

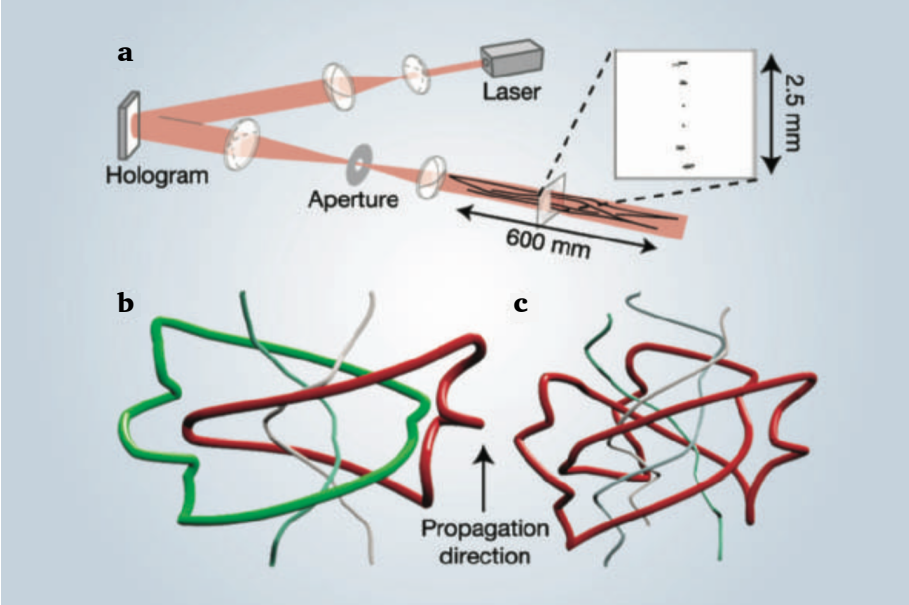


Figure 1.7: **The first experimental configuration to generate optical vortex knots and links**, adapted from [16]. (a) The He–Ne laser light is expanded and collimated before being reflected by the computer-controlled hologram (SLM). The beam is spatially filtered through a lens to separate the diffraction orders; only the first diffracted order is selected by passing the light through an aperture. The last lens recollimates the beam and images the desired focal plane (coincident with the function on the hologram). The intensity of the beam at different planes is measured by a CCD camera. Refer to [17] for more details.

experimental superposition of Laguerre-Gaussian modes were slightly modified from the theoretical calculations in order to enhance the intensity around the vortex lines; in particular, the beam waist was not coincident for the different modes (contrarily to theory). As a consequence, the knotted beams experimentally generated could not be represented by simple analytical forms such as polynomials, which made it difficult to further investigate the properties of knotted optical fields.

A new procedure to generate several different types of optical vortex knots and links was reported in 2010 [18]; algebraic topology was discovered to be a powerful tool for transferring the knot type embedded in mathematical abstract functions into propagating light fields. Only the Hopf link and the trefoil knot were constructed previously in optical beams and they were threaded by infinite vortex lines along the

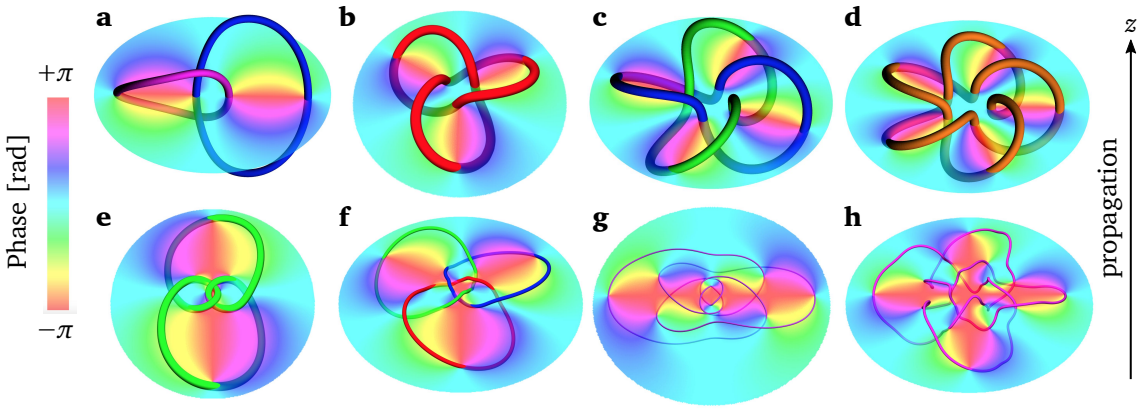


Figure 1.8: **Theoretical optical vortex knots and links** generated from the paraxial propagation of Milnor polynomials. Images (b) and (e)–(h) taken from [18, 58]. The hue coloured slices represent the phase of the fields at the plane $z = 0$. (a) Hopf link, (b) trefoil knot, (c) link $4_1^2$, (d) cinquefoil knot, (e) figure-eight knot, (f) Borromean rings, (g) knot $7_7$, (h) knot $8_{18}$.

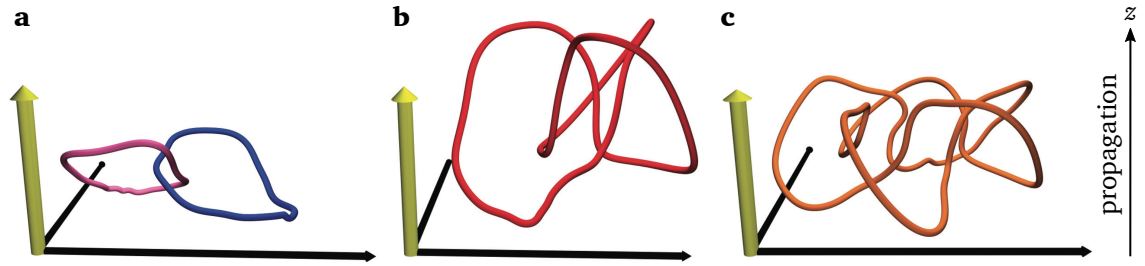


Figure 1.9: **Experimentally generated optical vortex knots and links** from [18]. The size of the knots along the propagation direction is of the order of the Rayleigh distance, indicated by the yellow axes; their size on the transverse plane is of the order of the Gaussian width, indicated by the black axes. Reconstructed 3D topology of the detected vortex lines in the form of (a) the Hopf link, (b) the trefoil knot and (c) the cinquefoil knot.

axis. On the other hand, the complex scalar fields of the new scheme of [18] embedded a larger variety of knots and links, which were isolated from additional vortex lines (there was no presence of the axial threads).

A set of mathematical functions called *Milnor polynomials* were used to generate polynomial solutions to the paraxial wave equation in the form of complex scalar fields with the same nodal lines topology of their mathematical counterpart [18]. Such knot-

ted polynomials were the unique solution to the paraxial wave equation that coincided with the Milnor polynomial at the focal plane. This procedure was used to successfully build the polynomial optical fields embedding the Hopf link, the trefoil knot and several more torus knots, but also the figure-eight knot, the Borromean rings, the knot $8_{18}$ and others, illustrated in Figure 1.8, together with their 'Milnor like' phase profile at the focal plane [18, 58].

The Hopf link, the trefoil knot and the cinquefoil knot were generated and detected experimentally thanks to an automated optimisation algorithm which increased the contrast in the field's intensity without changing the topology of its vortex lines [18, 19, 59]. The 3D reconstruction of the experimental vortex knots and links are reproposed in Figure 1.9.

## 1.7 Hopfions in physics

This section describes another topological object with knotted features, which is extremely important in mathematics and physics. We will see in § 3.3 that the term *Hopfion* usually refers to soliton field configurations with integer-value Hopf index, which can be represented by a Hopf fibration. The Hopf fibration has a wide variety of physical applications.

Urbantke [60] investigated this structure in detail for several different physical system in his famous article "The Hopf fibration–seven times in physics". Applications include magnetic monopoles [61], rigid body mechanics [62] and the geometry of entangled states in quantum information theory [63]. Hopfions also manifest as solutions of the equations of magnetohydrodynamics of an ideal incompressible fluid with infinite conductivity [64], but also as lines of force of gravitational fields [65].

Solutions to Maxwell's equations, constructed by Rañada [66], give all electromagnetic field lines in the form of closed loops generating the Hopf fibration; field lines are not static and their time evolution dissolves the topology. Figure 1.10 (h) shows the trefoil-knotted Hopfion in its initial configuration of the electric and mag-

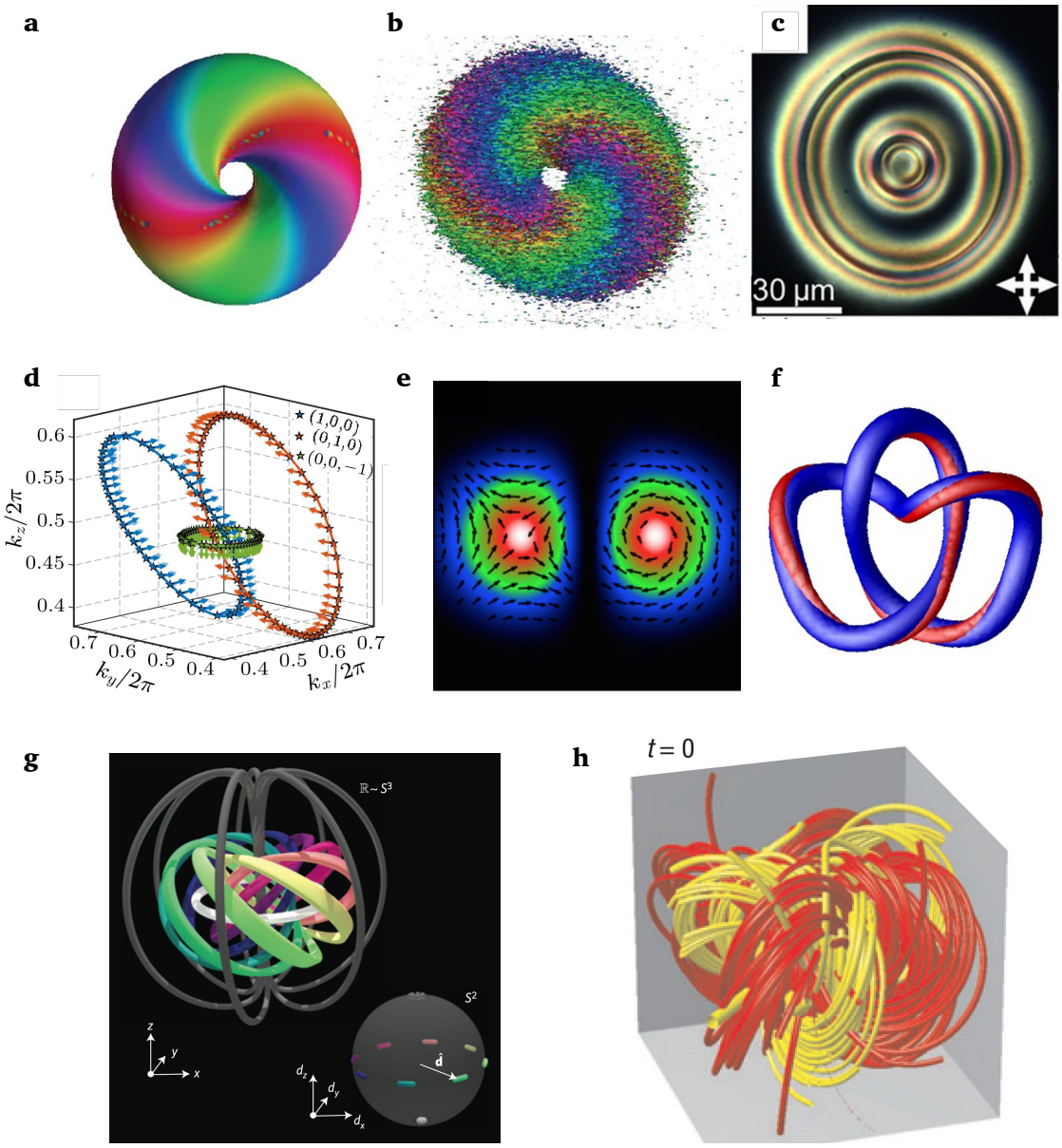


Figure 1.10: **Hopfions occurring in physical systems**. The Hopf fibration manifests in a large variety of physical applications. (a) Theoretical and (b) experimental texture in nematic liquid crystals [71] and (c) optical micrograph of a similar configuration [72]. (d) Solid-state quantum simulators [76]. (e) Frustrated magnets [70]. (f) Solution to the Skyrme-Faddeev model represing a nuclear particle [69]. (g) Texture given by the order parameter of a spinor Bose–Einstein condensate [74]. (h) The magnetic (red) and electric (yellow) field lines at time zero in the conformation of a trefoil-knotted Hopfion [20].

netic field lines [20].

Hopfions in physics are very often associated to *Skyrmions* that are topological solitons originated from the Skyrme model [67]. The Skyrme-Faddeev model representing nuclear particles has minimum-energy soliton solutions in the form of Hopfions (looped, knotted or linked) [68]. A trefoil-knotted solution [69] is shown in Figure 1.10 (f). The results have been extended recently to magnetic Skyrmions. These are 2D topological solitons arising in thin slices of magnetic materials in which the direction of the local magnetisation winds exactly once around the sphere of all possible directions. Computational results on frustrated magnets demonstrated that they are ideal hosts for Hopfions [70], shown in Figure 1.10 (e).

The controlled sculpting of the Hopf fibration has been implemented experimentally in nematic liquid crystals through the control of point defects in [71]; this was a demonstration of a topologically stable, smooth texture in the global configuration of a field. The theoretical predictions and the experimental data are shown, respectively, in Figure 1.10 (a) and (b). A polarising optical micrograph of a Hopfion in a confined chiral nematic liquid crystal by [72] is shown in Figure 1.10 (c).

At the quantum level, Hopf fibrations have been constructed in the order parameter of a spinor Bose–Einstein condensate (a texture) [73–75], shown in Figure 1.10 (g). They were also found recently in intricate 3D topological models of solid-state quantum simulators [76], illustrated in Figure 1.10 (d).

Chapter 6 will present Hopfion textures in the 3D polarisation distribution of monochromatic light fields. Similarly to optical vortex knots, these are static solutions to Maxwell's equations which do not evolve in time and are the result of superoscillatory interference phenomena; hence they are found in dark beams.

# 2 | Background and methods in optics

**In order to arrive at knowledge of the motions of birds in the air, it is first necessary to acquire knowledge of the winds...**

*Leonardo da Vinci*

Topological structures in light arise as 3D patterns from interference and diffraction phenomena, which are studied in the field of physical optics. The first part of this chapter presents a brief background in optics, the second part introduces standard and less-standard optical propagation methods in the paraxial and nonparaxial regimes.

The electric and magnetic field vectors are often expressed in circular components defined as follows[1]

$$\begin{cases} \widehat{\boldsymbol{e}}_+ = (\widehat{\boldsymbol{e}}_x + \mathrm{i}\,\widehat{\boldsymbol{e}}_y)/\sqrt{2}, \\ \widehat{\boldsymbol{e}}_- = (\widehat{\boldsymbol{e}}_x - \mathrm{i}\,\widehat{\boldsymbol{e}}_y)/\sqrt{2}. \end{cases} \tag{2.1}$$

## 2.1 Background in optics

This section introduces basic concepts in optics. § 2.1.1 gives a reminder of Maxwell's equations in free space and § 2.1.2 considers their form for time-periodic fields.

[1] This convention is sometimes called optics convention, which differs from the engineering convention.

§ 2.1.3 shows how the electric and magnetic fields are related to the Helmholtz wave equation. § 2.1.4 presents the mathematical properties of Laguerre-Gaussian modes, and § 2.1.5 presents the Zernike aperture modes in a similar fashion. In § 2.1.6, the mathematical formalism of the angular spectrum is given, showing its relationship with Fourier transforms. In § 2.1.7, Stokes parameters and the Poincaré sphere are used to characterise the polarisation states of light.

### 2.1.1 Maxwell's equations and the wave equation

The electromagnetic fields considered in this study do not contain charges or currents; nor the effects of nonlinear, dispersive, inhomogeneous or anisotropic media are included. The time-dependent electric vector $\mathcal{E}(x,y,z,t)$ and the time-dependent magnetic vector $\mathcal{B}(x,y,z,t)$ propagate in free space. Under these assumptions Maxwell's equations [77] simplify to[2]

$$\nabla \cdot \mathcal{E} = 0, \tag{2.2a}$$

$$\nabla \cdot \mathcal{B} = 0, \tag{2.2b}$$

$$\nabla \times \mathcal{E} = -\dot{\mathcal{B}}, \tag{2.2c}$$

$$\nabla \times \mathcal{B} = \frac{1}{c^2}\dot{\mathcal{E}}, \tag{2.2d}$$

where $c$ is the speed of light in vacuum and the dot notation indicates differentiation with respect to time. It is not hard to introduce the influence of a homogeneous medium by using Maxwell's equations in terms of *electric displacement* and *magnetic induction* [30]; this is beyond the scope of this thesis and it will not be done explicitly here. Nevertheless, it is a required step for the experimental implementation of the results presented in this thesis, that preferably occurs in laser light propagated through air.

Each Cartesian component of the electric and magnetic vectors satisfy the time-

[2]The SI unit system is used here.

dependent scalar wave equation

$$\nabla^2 u - \frac{1}{c^2}\ddot{u} = 0, \tag{2.3}$$

where $\nabla^2 = \partial_x^2 + \partial_y^2 + \partial_z^2$ is the Laplacian operator. Expression (2.3) is a partial differential equation in both space and time. In § 2.1.2, the problem will be simplified by considering solutions to equation (2.3) which can be found by the separation of variables. This implies that $u$ can be expressed as a product of two functions: one depending on the spatial variables and the other depending on time.

### 2.1.2 Time harmonic wave functions

From here until the end of this thesis, only time-periodic optical waves will be considered. These are monochromatic with wavenumber $k$ and can be expressed as $u = \psi e^{-i\omega t}$, where $\omega = kc$ is the angular frequency. Wavefunctions of this type are called time harmonic and are characterised by the fact that the time dependence can be factored out. We consider $\mathcal{E}(x,y,z,t) = \boldsymbol{E}(x,y,z)e^{-ikct}$ and $\mathcal{B}(x,y,z,t) = \boldsymbol{B}(x,y,z)e^{-ikct}$ for which the time harmonic Maxwell's equations (2.2) reduce to

$$\nabla \cdot \boldsymbol{E} = 0, \tag{2.4a}$$

$$\nabla \cdot \boldsymbol{B} = 0, \tag{2.4b}$$

$$\nabla \times \boldsymbol{E} = ikc\boldsymbol{B}, \tag{2.4c}$$

$$\nabla \times \boldsymbol{B} = -\frac{ik}{c}\boldsymbol{E}. \tag{2.4d}$$

The scalar wave equation (2.3) can be rearranged into the Helmholtz equation for the spatial-dependent wavefunction $\psi$, as follows

$$\nabla^2 \psi + k^2 \psi = 0. \tag{2.5}$$

The scalar Helmholtz equation not only describes wave phenomena related to optics but also represents other physical systems, such as acoustic waves. It is straightforward to show that each Cartesian component of the electric and magnetic vectors $\boldsymbol{E}$ and

$\boldsymbol{B}$ individually satisfy the Helmholtz wave equation. This condition, together with the divergenceless condition, is necessary and sufficient to satisfy all of Maxwell's equations (2.4).

### 2.1.3 The reduced Helmholtz equation and the paraxial approximation

This section considers waves propagating along a preferential direction, *e.g.* the positive $z$-axis. In the case of waves describing laser light, which are of the form $u = \psi e^{i(kz-\omega t)}$, $\psi$ is the *complex amplitude* of the field and satisfies the reduced scalar Helmholtz equation

$$\nabla^2\psi + 2ik\partial_z\psi = 0. \tag{2.6}$$

If we consider the electric and magnetic vectors to be $\mathcal{E} = \boldsymbol{E}e^{ik(z-ct)}$ and $\mathcal{B} = \boldsymbol{B}e^{ik(z-ct)}$, each of the components of $\boldsymbol{E}$ and $\boldsymbol{B}$ satisfy (2.6) separately. Note that in this case the vectors satisfying Maxwell's equations (2.4) are $\boldsymbol{E}e^{ikz}$ and $\boldsymbol{B}e^{ikz}$.

The paraxial approximation is given by $|\partial_z^2\psi| \ll |\partial_x^2\psi|, |\partial_y^2\psi|$, whose physical meaning is that the complex amplitude $\psi$ varies along the optical axis slower than along the transverse axis, and $|\partial_z^2\psi| \ll |k\partial_z\psi|$, implying that the variation of $\psi$ along the direction of propagation is small over a distance of the order of the wavelength. Under this regime, the reduced Helmholtz equation (2.6) simplifies to the paraxial wave equation

$$\nabla_\perp^2\psi + 2ik\partial_z\psi = 0, \tag{2.7}$$

where $\nabla_\perp^2 = \partial_x^2 + \partial_y^2$ is the transverse Laplacian.

Equation (2.7) describes beams of light that are largely collimated, meaning that they have a well-defined propagation direction whilst their complex amplitude varies transversely. This is the case, for example, of light emitted by a laser cavity. The paraxial regime implies that the electric and magnetic fields are perpendicular to the direction of propagation because their longitudinal components are negligible compared to their transverse components. The paraxial regime does not describe laser

light which is tightly focused by a lens; this case is represented by the more general Helmholtz equation (2.5) in its vector version.

There is no rigorous mathematical boundary between the reduced Helmholtz equation and its paraxial approximation. We will explore the transition between these two regimes for optical vortex knots in chapter 5. We will adopt different representations of light beams (*i.e.* scalar and vectorial, paraxial and nonparaxial) to be the framework in which knotted beams of light can be generated.

### 2.1.4 Laguerre-Gaussian paraxial beams

Solutions to the paraxial wave equation (2.7) can be found by solving the beforementioned differential equation with the method of separation of variables in several different coordinate systems. In cylindrical coordinates $(R, \phi, z)$ the solutions are the widely used *Laguerre-Gaussian* (LG) modes given by

$$\mathrm{LG}^{\mathrm{3D}}_{p\ell}(R,\phi,z;w) = \sqrt{\frac{p!}{\pi(|\ell|+p)!}}\frac{(R/w)^{|\ell|}\mathrm{e}^{\mathrm{i}\ell\phi}}{w}\frac{(1-\mathrm{i}z/z_R)^p}{(1+\mathrm{i}z/z_R)^{p+|\ell|+1}} \times \mathrm{L}^{|\ell|}_p\left(\frac{(R/w)^2}{1+(z/z_R)^2}\right)\exp\left(-\frac{(R/w)^2}{2(1+\mathrm{i}z/z_R)}\right), \tag{2.8}$$

where $p \geq 0$ and $\ell$ are integers associated, respectively, to the number of radial nodes and to the optical angular momentum (OAM). $\mathrm{L}^{\ell}_p$ are the associated Laguerre polynomials, $w$ characterises the amplitude profile and is called the *beam waist radius* and $z_R = kw^2$ is the Rayleigh range of the propagating mode. Expression (2.8) shows that $R$ scales linearly with $w$ and $z$ scales quadratically with $w$. When $R = w$, the fundamental Gaussian mode $\mathrm{LG}^{\mathrm{3D}}_{00}$ is characterised by the fact that the amplitude drops to $1/\mathrm{e}$ times its axial value $R = 0$ at the plane $z = 0$. This means that $w$ is the effective radius of the circularly symmetric distribution in the focal plane[3]. This is the reason why $w$ is often called the *minimum spot size* [78].

The fraction of power of $\mathrm{LG}^{\mathrm{3D}}_{00}$ included within a circle of a certain radius $R$ in-

[3]The term focal plane refers to the plane $z = 0$ because the beam's intensity profile is focused into the most concentrated spot there.

creases smoothly with increasing $R$. On the other hand, higher order modes are characterised by power concentrated away from the optical axis. As a consequence, the waist of the beam $w$ does not indicate accurately the transverse extent of higher order LG-beams. In chapter 5, we will see that the size of Laguerre-Gaussian beams is of fundamental importance in the context of optical vortex knots.

In this thesis, the Laguerre-Gaussian basis will be rarely used in their propagating form, but the main interest is in their properties on the $z = 0$ plane. At this plane, expression (2.8) takes the form

$$\mathrm{LG}_{p\ell}(R,\phi;w) = \frac{1}{w}\sqrt{\frac{p!}{\pi(|\ell|+p)!}} \times \frac{R^{|\ell|}}{w^{|\ell|}} \mathrm{e}^{\mathrm{i}\ell\phi} \mathrm{L}_p^{|\ell|}\left(\frac{R^2}{w^2}\right) \mathrm{e}^{-\frac{R^2}{2w^2}}. \tag{2.9}$$

The functions (2.9) form a complete and orthonormal basis in the infinite transverse $R\phi$-plane. Therefore, they satisfy the following equation[4]

$$\int_0^\infty \int_0^{2\pi} \mathrm{LG}^*_{p\ell}(R,\phi;w)\mathrm{LG}_{p'\ell'}(R,\phi;w) R\, d\phi\, dR = \delta_{pp'}\delta_{\ell\ell'}. \tag{2.10}$$

A function $\psi$ defined on the $R\phi$-plane can be decomposed into the LG-basis as follows

$$\psi(R,\phi) = \sum_{p\ell} c_{p\ell}(w)\mathrm{LG}_{p\ell}(R,\phi;w), \tag{2.11}$$

where

$$c_{p\ell}(w) = \int_0^\infty \int_0^{2\pi} \mathrm{LG}^*_{p\ell}(R,\phi;w)\psi(R,\phi;w) R\, d\phi\, dR. \tag{2.12}$$

These properties of the LG-modes are very useful to engineer light patterns; indeed, each mode can be used as a building block to create a superposition in which intensity and phase distributions are decided *a priori*.

Another important property of each LG-beam (2.9) is that its Fourier transform, with coordinates $(\rho,\varphi)$, coincides with the beam itself apart from a multiplication factor, as follows

$$\mathcal{F}\left(\mathrm{LG}_{p\ell}(R,\phi;w)\right) = \frac{1}{2\pi}\int_0^\infty \int_0^{2\pi} \mathrm{LG}_{p\ell}(R,\phi;w)\mathrm{e}^{-\mathrm{i}R\rho\cos(\phi-\varphi)} R\, d\phi\, dR$$

[4]The superscript symbol '$*$' indicates complex conjugation.

$$= \mathrm{i}^{2p-|\ell|}\mathrm{LG}_{p\ell}(\rho,\varphi;1/w). \tag{2.13}$$

Fourier space is important in the context of lenses, since the propagation through paraxial lenses can be mathematically expressed in terms of Fourier optics [79].

In chapters 4–6, we will see how the elementary properties of LG-beams defined here are used to shape knots in laser beams.

### 2.1.5 The Zernike aperture modes

This section introduces another set of functions of fundamental importance in optics, namely the *Zernike aperture modes*. We will use this family of functions as an alternative to Laguerre-Gaussian functions in two-dimensions. Even though LG-modes are defined on the infinite plane, they work well in practice because their amplitude at large $R$ is much smaller than around the optical axes. However, for practical experiments involving focused light incident on lens apertures, making use of LG-modes can become difficult.

Zernike aperture modes, on the other hand, are naturally defined on the disk. They are a complete set of functions that are orthogonal over the interior of the unit circle with coordinates $(\rho,\varphi)$. The explicit form of the circle polynomials of Zernike is given with the convention of [30], as follows

$$\mathrm{Z}_{n\ell}(\rho,\varphi) = \mathrm{R}_n^{|\ell|}(\rho)\mathrm{e}^{\mathrm{i}\ell\varphi}, \tag{2.14}$$

where $n$, $\ell$ are integers, $n \geq |\ell| \geq 0$, $n-|\ell|$ is even and

$$\mathrm{R}_n^m(\rho) = \begin{cases} \sum_{l=0}^{(n-m)/2} \dfrac{(-1)^l (n-l)!}{l!\left[\frac{1}{2}(n+m)-l\right]!\left[\frac{1}{2}(n-m)-l\right]!}\rho^{n-2l} & \text{for } n-m \text{ even} \\ 0 & \text{for } n-m \text{ odd,} \end{cases} \tag{2.15}$$

are the radial Zernike polynomials, defined for integer $m \geq 0$. The index $\ell$ is related to the orbital angular momentum (OAM) and the index $n$ is the mode order $n = |\ell| + 2p$ associated with the energy eigenvalue. With the normalisation factor, the

modes satisfy

$$\frac{n+1}{\pi}\int_0^1\int_0^{2\pi} \mathrm{Z}^*_{n\ell}(\rho,\varphi)\mathrm{Z}_{n'\ell'}(\rho,\varphi)\rho\, d\varphi\, d\rho = \delta_{nn'}\delta_{\ell\ell'}. \tag{2.16}$$

A function defined on the disk can be expanded into Zernike polynomials, as follows

$$\psi(\rho,\varphi) = \sum_{n\ell} c_{n\ell}\mathrm{Z}_{n\ell}(\rho,\varphi), \tag{2.17}$$

where

$$c_{n\ell} = \frac{n+1}{\pi}\int_0^1\int_0^{2\pi} \psi(\rho,\varphi)\mathrm{R}_n^{|\ell|}(\rho)\mathrm{e}^{-\mathrm{i}\ell\varphi}\rho\, d\varphi\, d\rho. \tag{2.18}$$

These properties of the Zernike aperture modes demonstrate that they form a basis set analogous to the LG-modes. A difference between these two sets of modes is that the LG-basis has the term $R^{|\ell|}$ factored out, whereas the Zernike basis has this term incorporated into its radial polynomials $\mathrm{R}_n^m$. Historically, Zernike polynomials were not employed as beam solutions in their own right, but superposition of these modes accounted of aberrations in an optical system. Nijboer proved the important relationship between the radial Zernike polynomials and the Bessel functions of the first kind $\mathrm{J}_n(R)$ [80], given by the following integral

$$\int_0^1 \mathrm{R}_n^{|\ell|}(\rho)\mathrm{J}_\ell(R\rho)\rho\, d\rho = (-1)^{(n-\ell)/2}\frac{\mathrm{J}_{n+1}(R)}{R}, \tag{2.19}$$

this integral holds for any integer value of $n \geq 0$ and $\ell$.

We will show how to use Zernike aperture modes as building blocks to shape complex light patterns, analogously to what is currently done in theory and experiments with the LG-modes. Our approach to beam shaping will be presented in § 4.3 and chapter 6. Our methods are closely related to the Extended Nijboer-Zernike (ENZ) theory (§ 2.2.2).

### 2.1.6 The angular spectrum of plane waves

This section is a brief demonstration of the physical interpretation of the angular spectrum of an optical field; the mathematical formalism is taken from [79]. The an-

gular spectrum is a mathematical technique to propagate a wave field, where the field amplitude is expressed as a sum of plane waves and evanescent waves. The angular spectrum representation describes accurately paraxial and tightly focused laser beams. Furthermore, in the paraxial regime, the angular spectrum representation coincides with the framework of Fourier optics [81].

A wave propagating in the positive $z$ direction is incident on the $xy$-plane for which $z = 0$; let the complex amplitude on this plane be $\psi(x, y, 0)$. We will now show that when the complex field distribution across the plane is Fourier transformed, the spatial Fourier components can be identified as plane waves travelling in different directions [79]. Across the plane $z = 0$, the function $\psi(x, y, 0)$ has a two-dimensional Fourier transform $\widetilde{\psi} = \mathcal{F}(\psi)$ given by

$$\widetilde{\psi}(k_x, k_y; 0) = \frac{1}{4\pi^2} \iint_{-\infty}^{\infty} \psi(x, y, 0) \mathrm{e}^{-\mathrm{i}(k_x x + k_y y)} \, dx \, dy, \tag{2.20}$$

where $(x, y)$ are the Cartesian transverse coordinates and $(k_x, k_y)$ the corresponding spatial frequencies. A Fourier transform may be considered as the operation by which a complicated function is decomposed into simpler exponential functions. This becomes evident by calculating the inverse Fourier transform of (2.20), as follows

$$\psi(x, y, 0) = \iint_{-\infty}^{\infty} \widetilde{\psi}(k_x, k_y; 0) \mathrm{e}^{\mathrm{i}(k_x x + k_y y)} \, dk_x \, dk_y. \tag{2.21}$$

It is recalled that the equation for a unit-amplitude plane wave propagating with direction cosines $(\alpha, \beta, \gamma)$ with $\gamma = \sqrt{1 - \alpha^2 - \beta^2}$ is $\mathrm{e}^{\mathrm{i}k(\alpha x + \beta y + \gamma z)}$. Thus, across $z = 0$ the function $\mathrm{e}^{\mathrm{i}(k_x x + k_y y)}$ may be considered as a plane wave propagating with direction cosines $\alpha = k_x/k, \beta = k_y/k, \gamma = \sqrt{1 - (k_x/k)^2 - (k_y/k)^2}$. For this reason, the following expression

$$\widetilde{\psi}(k\alpha, k\beta; 0) = \frac{1}{4\pi^2} \iint_{-\infty}^{\infty} \psi(x, y, 0) \mathrm{e}^{-\mathrm{i}k(\alpha x + \beta y)} \, dx \, dy \tag{2.22}$$

is called the *angular spectrum* of the wavefunction $\psi(x, y, 0)$.

We now want to evaluate the effect of the propagation of $\psi$ along $z$ on the angular spectrum. The angular spectrum of $\psi$ on a transverse plane positioned at $z$ is

represented by the function $\widetilde{\psi}(k\alpha, k\beta; z)$, that is

$$\widetilde{\psi}(k\alpha, k\beta; z) = \frac{1}{4\pi^2} \iint_{-\infty}^{\infty} \psi(x, y, z) \mathrm{e}^{-\mathrm{i}k(\alpha x + \beta y)} \, dx \, dy. \tag{2.23}$$

For our purpose, it is required to find the relationship between $\widetilde{\psi}(k\alpha, k\beta; z)$ and $\widetilde{\psi}(k\alpha, k\beta; 0)$. Note that

$$\psi(x, y, z) = \iint_{-\infty}^{\infty} \widetilde{\psi}(k\alpha, k\beta; z) \, \mathrm{e}^{\mathrm{i}k(\alpha x + \beta y)} \, d(k\alpha) \, d(k\beta) \tag{2.24}$$

and that $\psi$ must satisfy the scalar Helmholtz equation (2.5). Direct application of the latter requirement to (2.24) gives the following differential equation

$$\partial_z^2 \widetilde{\psi}(k\alpha, k\beta; z) + k^2 \left(1 - \alpha^2 - \beta^2\right) \widetilde{\psi}(k\alpha, k\beta; z) = 0. \tag{2.25}$$

An elementary solution to equation (2.25) is

$$\widetilde{\psi}(k\alpha, k\beta; z) = \widetilde{\psi}(k\alpha, k\beta; 0) \, \mathrm{e}^{\mathrm{i}k\sqrt{1-\alpha^2-\beta^2}\, z}. \tag{2.26}$$

This result demonstrates that when $\alpha^2 + \beta^2 < 1$, the effect of the propagation over $z$ is simply a phase change in the components of the angular spectrum. This is due to the fact that each plane-wave component travels a different distance to reach a given $(x, y, z)$ point, meaning that a relative phase delay is introduced. On the other hand, when $\alpha^2 + \beta^2 > 1$ the square root in (2.26) is imaginary and that solution is rearranged as

$$\widetilde{\psi}(k\alpha, k\beta; z) = \widetilde{\psi}(k\alpha, k\beta; 0) \, \mathrm{e}^{-k\sqrt{\alpha^2+\beta^2-1}\, z}. \tag{2.27}$$

These are *evanescent waves* and are strongly attenuated under propagation. Finally, we calculate the inverse Fourier transform of (2.26), which is

$$\psi(x, y, z) = \iint_{-\infty}^{\infty} \widetilde{\psi}(k\alpha, k\beta; 0) \, \mathrm{e}^{\mathrm{i}k(\alpha x + \beta y)} \mathrm{e}^{\mathrm{i}k\sqrt{1-\alpha^2-\beta^2}\, z} \, d(k\alpha) \, d(k\beta). \tag{2.28}$$

This integral is often written in the form

$$\psi(x, y, z) = \iint_{-\infty}^{\infty} \widetilde{\psi}(k_x, k_y; 0) \mathrm{e}^{\mathrm{i}(k_x x + k_y y)} \mathrm{e}^{\mathrm{i}k_z z} \, dk_x \, dk_y, \tag{2.29}$$

which is the angular spectrum of the three-dimensional field $\psi(x,y,z)$.

The result (2.29) can be simplified when the paraxial approximation holds. Indeed, since $k_x^2+k_y^2+k_z^2=k^2$, the Taylor expansion of $k_z=k\sqrt{1-(k_x/k)^2-\left(k_y/k\right)^2}$ about $(k_x/k)^2+\left(k_y/k\right)^2=0$ is

$$k_z \approx k-\left(\frac{k_x^2+k_y^2}{2k}\right). \tag{2.30}$$

The angular spectrum (2.29) in the paraxial regime becomes

$$\psi(x,y,z)=\mathrm{e}^{\mathrm{i}kz}\iint_{-\infty}^{\infty}\widetilde{\psi}(k_x,k_y;0)\mathrm{e}^{\mathrm{i}(k_x x+k_y y)}\mathrm{e}^{-\mathrm{i}(k_x^2+k_y^2)/(2k)z}\,dk_x\,dk_y. \tag{2.31}$$

The angular spectrum is applicable to each component of the electric and magnetic field vectors [81] and constitutes the foundation of the propagation methods in this thesis.

### 2.1.7 The Poincaré sphere and the polarisation states of light

This section presents a parametrisation of the polarisation states of light. When time harmonic two-dimensional vectors are used to represent the electric and magnetic fields at a specific point in space (*e.g.* transverse fields), the curve which the end points of these vectors describe on the plane is the *polarisation ellipse* [30]. When this ellipse degenerates into a straight line or a circle, the polarisation state of light is, respectively, linear or circular; otherwise the polarisation is said to be elliptical.

The characterisation of the polarisation ellipse is given by three independent quantities. For instance, the *Stokes parameters* proposed by G. G. Stokes in 1852 give the state of polarisation in all its particulars. These parameters for monochromatic coherent radiation are defined[5] in [77] as

$$s_0=|E_x|^2+|E_y|^2=|E_+|^2+|E_-|^2, \tag{2.32a}$$

[5]The definition of Stokes parameters varies between different conventions.

$$s_1 = |E_x|^2 - |E_y|^2 = 2\mathrm{Re}\left(E_+^* E_-\right), \tag{2.32b}$$

$$s_2 = 2\mathrm{Re}\left(E_x^* E_y\right) = 2\mathrm{Im}\left(E_+^* E_-\right), \tag{2.32c}$$

$$s_3 = 2\mathrm{Im}\left(E_x^* E_y\right) = |E_+|^2 - |E_-|^2. \tag{2.32d}$$

Only three of them are independent, given that they are related by the identity

$$s_1^2 + s_2^2 + s_3^2 = s_0^2. \tag{2.33}$$

When (2.32) are normalised, they define a sphere of unit radius called the *Poincaré sphere*. The *normalised Stokes parameters* are defined as

$$S_i = \frac{s_i}{s_0}, \qquad i = 1, 2, 3. \tag{2.34}$$

The Poincaré sphere gives a simple geometrical representation of all the different possible states of polarisation of 2D fields[6] (*e.g.* paraxial optical fields). The surface of the sphere can be parametrised by two angular coordinates, as follows

$$S_1 = \cos\alpha \cos\beta \tag{2.35a}$$

$$S_2 = \sin\alpha \cos\beta \tag{2.35b}$$

$$S_3 = \sin\beta, \tag{2.35c}$$

where $\alpha$ ($-\pi \leq \alpha < \pi$) is the azimuthal angle and $\beta$ ($-\pi/2 \leq \beta \leq \pi/2$) is the elevation angle. The spherical angular coordinates $\alpha$ and $\beta$ are related to the polarisation ellipse as follows. The angle $\alpha/2$ ($-\pi/2 \leq \alpha/2 < -\pi/2$) is the orientation of the ellipse and $\beta/2$ ($-\pi/4 \leq \beta/2 \leq \pi/4$) characterises the eccentricity of the ellipse. It is easy to show that the equatorial circle $S_3 = 0$ represents all the possible linearly-polarised states. When $S_2 = 0$, the horizontal states are given by $S_1 = 1$ and the vertical states are given by $S_1 = -1$. The right-handed polarisation is found at the north pole of the sphere ($S_3 = 1$) and the left-handed polarisation is found at the south pole ($S_3 = -1$).

[6]The analogue of the Poincaré sphere for 3D beams, where the longitudinal component is non-negligible, is not uniquely defined [82].

The Poincaré sphere and the Stokes parameters will be used in chapter 6 to analyse the topology of the polarisation states in light beams.

## 2.2 Methods for optics

This section presents the methods to calculate explicit analytical representations of optical fields. The methods are all based on the angular spectrum representation of § 2.1.6. The topics presented here are taken from the existing literature and rearranged in our notation. § 2.2.1 presents a polynomial representation of light beams around the optical axes. § 2.2.2 presents the Extended Nijboer-Zernike (ENZ) theory of propagation. Richards and Wolfs vector theory of diffraction is summarised in § 2.2.3. The methods presented in § 2.2.2 and § 2.2.3 are concerned with the propagation of light beams through a circular aperture and will be brought together in § 6.2.2, where ENZ-theory will be used to solve the Richards and Wolf vector diffraction integral.

### 2.2.1 Polynomial beam propagation

Polynomial beams are sets of solutions to the paraxial wave equation or the reduced Helmholtz equation, which are polynomials in their spatial variables. They were originally introduced to investigate the behaviour of optical vortices by Berry [83] and Nye [57], and have subsequently been studied by several groups [15,84–86]. Paraxial polynomials are analogous to the heat polynomials which solve the heat equation [87] when time is imaginary [84]. Here, we adopt the definition of Dennis *et al.* [84], who identified the relationship between polynomial waves in Cartesian and cylindrical coordinates and the generating function of the Hermite and Laguerre polynomials.

Polynomial beams are monomials in $R$ in the plane $z = 0$. Their 1D-angular spectrum (§ 2.1.6) is a derivative $\delta$-function (ignoring the phase factor $e^{ikz}$). Since the angular spectrum in the paraxial regime is given by (2.31), the paraxial polynomials

are defined in 1D by the following integral [84]

$$\mathrm{P}_p^{\ell}(x,z;k) = \int_{-\infty}^{\infty} \mathrm{i}^{2p+|\ell|}\delta^{(2p+|\ell|)}(k_x)\mathrm{e}^{\mathrm{i}\left(k_x x - k_x^2/(2k)z\right)}\,dk_x. \tag{2.36}$$

The evaluation of (2.36) gives the explicit expression of the paraxially propagating polynomials along $z$, which are defined in cylindrical coordinates $(R,\phi,z)$ as [84]

$$\mathrm{P}_p^{\ell}(R,z;k) = p!(2\mathrm{i}zk^{-1})^p \mathrm{L}_p^{|\ell|}\left(\mathrm{i}R^2kz^{-1}/2\right), \tag{2.37}$$

where $k$ is the transverse wavenumber, and $\mathrm{L}_p^{\ell}$ is a homogeneous associated Laguerre polynomial of indices $p \geq 0$, $\ell$. The expressions $R^{|\ell|}\mathrm{e}^{\mathrm{i}\ell\phi}\mathrm{P}_p^{|\ell|}(R,z;k)$ are solutions to the paraxial wave equation and represent light beams with vortices of order $\ell$ on axis. Polynomial beams do not represent physical beams globally because their intensity increases in direction transverse to the $z$-axis, and diverges at infinity. For practical purposes, they are suited to describe the behaviour of some physical beams about the optical axis. This is the case, for instance, of LG-beams with large width $w$.

Nonparaxial polynomials solving the reduced Helmholtz equation are constructed by considering the angular spectrum without the paraxial approximation, (2.29). The nonparaxial propagator can be rearranged using the following exponential generating function

$$\mathrm{e}^{Z(1-\sqrt{1-2t})} = \sum_{j=0}^{\infty} \frac{t^j}{j!}\theta_j^-(Z), \tag{2.38}$$

where $\theta_j^-(Z)$ are the reverse Bessel polynomials defined [88] (noting a typo in [84])

$$\theta_j^-(Z) = \begin{cases} 1 & \text{for } j = 0 \\ \displaystyle\sum_{t=1}^{j} \frac{(2j-t-1)!}{(j-t)!(t-1)!}\cdot\frac{Z^t}{2^{j-t}} & \text{for } j > 0. \end{cases} \tag{2.39}$$

Nonparaxial polynomials are derived from the corresponding paraxial polynomial by adding the appropriate nonparaxial corrections—by substituting each power $(-\mathrm{i}z)^j(2k)^{-j}$, appearing in each paraxial polynomial, by $\theta_j^-(-\mathrm{i}kz)(2k^2)^{-j}$—which are negligible in the paraxial approximation. As a result [84], the nonparaxial propagating

polynomials are defined as

$$\mathrm{H}_p^{\ell}(R,z;k)=\sum\nolimits_{j=0}^{p}(-1)^{j+p}\frac{p!(\ell+p)!}{j!(j+\ell)!(p-j)!}\left(k^2/2\right)^{j-p}R^{2j}\theta_{p-j}^{-}(-\mathrm{i}kz)\,. \tag{2.40}$$

These functions recover the paraxial polynomials in the asymptotic limit $k\to\infty$. Formal solutions to the reduced Helmholtz equation are given by $R^{|\ell|}\mathrm{e}^{\mathrm{i}\ell\phi}\mathrm{H}_p^{|\ell|}(R,z;k)$.

Since the wave equation is linear, any field distribution at $z=0$ expressed as a power series in $R$ and $\mathrm{e}^{\mathrm{i}\ell\phi}$, can be propagated paraxially (nonparaxially) by constructing its corresponding sum of paraxial (nonparaxial) polynomials. Such sum is found by substituting each monomial $R^n\mathrm{e}^{\mathrm{i}\ell\phi}$ in the initial field by $R^{|\ell|}\mathrm{e}^{\mathrm{i}\ell\phi}\mathrm{P}_{(n-|\ell|)/2}^{|\ell|}(R,z;k)$ ($R^{|\ell|}\mathrm{e}^{\mathrm{i}\ell\phi}\mathrm{H}_{(n-|\ell|)/2}^{|\ell|}(R,z;k)$).

In § 4.2 we will describe how to use this approach to systematically create optical vortex knots and links; in chapter 5 we will use polynomial beams to study how nonparaxial effects modify the topology of knotted curves.

### 2.2.2 Extended Nijboer-Zernike theory

This section presents the Extended Nijboer-Zernike (ENZ) theory, which was originally concerned with the study of the effects of aberrations on the basis of diffraction theory. When a monochromatic spherical wave emerges from a circular aperture and converges towards the focal point, the field in the neighbourhood of the focus can be calculated with the *diffraction integral*. Aberrations are deviations of the actual wavefront from a perfectly spherical convergent wave issued from the circular aperture [30]. They were traditionally represented in the field distribution at the aperture plane by the exponential factor $\mathrm{e}^{\mathrm{i}\Phi}$, where $\Phi$ is known as the aberration function [30]. A detailed treatment of the diffraction pattern forming in the presence of aberrations is due to Nijboer [80]. He expanded the aberration function in a series of radial polynomials of Zernike (2.15). However, Nijboer-Zernike (NZ) theory considered only small aberrations, where the departures from a spherical wavefront was smaller than a wavelength. In recent years, ENZ-theory [89] dropped this assumption and considered arbitrarily large aberration functions. This was achieved by expanding the

whole exponential $e^{i\Phi}$ in a Zernike series, rather than the exponent $\Phi$ [30]. The results of Janssen [89] expressed optical fields as series expansions in the Zernike basis.

Our approach differs from the original treatment of NZ and ENZ-theory based on aberrations. We will treat each Zernike aperture mode $Z_{n\ell}$ like a 'true' light mode defined on the aperture and use ENZ-theory to evaluate explicitly the diffraction integral for a single Zernike aperture mode incident on a circular aperture.

### The scalar diffraction integral

Several theoretical methods are available to define the diffraction integral, for example techniques based on the Huygens-Fresnel principle [30] or the Debye integral representation [90]. The predictions of the different theories differ from each other under extreme conditions [91]. We adopt the Debye approximation to calculate the three-dimensional distribution near the focus of a converging wave, which assumes that the angular spectrum (§ 2.1.6) of the incident field on the aperture is nonzero only for directions inside the cone that is formed by joining the edges of the aperture to the focal point [90, 92]. In the paraxial regime, it is possible to express the diffraction integral by using the angular spectrum of the field propagating in the positive $z$-direction, which is given by (2.31) and imposing the Debye condition, as follows. We represent the aperture by the dimensionless coordinates $\rho = k^{-1}\sqrt{k_x^2 + k_y^2}$ and $\varphi = \mathrm{Arg}(k_x, k_y)$. Thus, given the cylindrical coordinates $(R, \phi, z)$ representing the focal volume, the diffraction integral in the presence of a circular aperture is

$$E(R,\phi,z) = e^{ikz} \int_0^1 \int_0^{2\pi} \widetilde{\psi}(\rho,\varphi)\, e^{ikR\rho\cos(\varphi-\phi)} e^{-i\rho^2 kz/2} \rho\, d\varphi\, d\rho. \tag{2.41}$$

The integral representation of the field in the form employed by Debye gives accurate results when the diffracting aperture is large compared to the wavelength and the observed diffracted field is not close to the aperture [30]. This expression is valid under the validity of Fourier optics [79], which is sufficient if the focusing is not too tight. For a more accurate treatment involving the focusing parameters see [30] in the

paraxial regime and § 2.2.3 for the tightly focused regime.

The rest of this section presents mathematical solutions to the integral (2.41) given by ENZ-theory. The analytical form of fields whose Fourier transforms are the Zernike aperture modes ($\widetilde{\psi}(\rho,\varphi) = \mathrm{Z}_{n\ell}(\rho,\varphi)$) is calculated.

### NZ-theory on the focal plane

At the focal plane $z = 0$ the diffraction integral (2.41) for a single Zernike aperture mode is the following

$$\int_0^1 \int_0^{2\pi} \mathrm{Z}_{n\ell}(\rho,\varphi)\, \mathrm{e}^{\mathrm{i}kR\rho\cos(\varphi-\phi)} \rho\, d\varphi\, d\rho = 2\pi i^n \frac{\mathrm{J}_{n+1}(kR)}{kR} \mathrm{e}^{\mathrm{i}\ell\phi}, \tag{2.42}$$

where $\mathrm{J}_n(kR)$ is a Bessel function of the first kind. This result can be derived using the main result of Nijboer [80] given by (2.19) and the following elementary property of the Bessel functions

$$\int_0^{2\pi} \mathrm{e}^{\mathrm{i}\ell\varphi}\, \mathrm{e}^{\mathrm{i}R\cos(\varphi-\phi)}\, d\varphi = 2\pi \mathrm{i}^{\ell} \mathrm{J}_{\ell}(R) \mathrm{e}^{\mathrm{i}\ell\phi}, \tag{2.43}$$

which holds for any integer $\ell \gtreqless 0$. Thus,

$$\int_0^1 \int_0^{2\pi} \mathrm{Z}_{n\ell}(\rho,\varphi)\, \mathrm{e}^{\mathrm{i}kR\rho\cos(\varphi-\phi)} \rho\, d\varphi\, d\rho = \int_0^1 \mathrm{R}_n^{|\ell|}(\rho)\rho \left( \int_0^{2\pi} \mathrm{e}^{\mathrm{i}\ell\varphi}\, \mathrm{e}^{\mathrm{i}kR\rho\cos(\varphi-\phi)}\, d\varphi \right) d\rho$$

$$= 2\pi \mathrm{i}^{\ell} \mathrm{e}^{\mathrm{i}\ell\phi} \int_0^1 \mathrm{R}_n^{|\ell|}(\rho) \mathrm{J}_{\ell}(kR\rho)\rho d\rho = 2\pi \mathrm{i}^n \frac{\mathrm{J}_{n+1}(kR)}{kR} \mathrm{e}^{\mathrm{i}\ell\phi}. \tag{2.44}$$

Note that expression (2.43) shows how a single Zernike aperture mode propagates on the focal plane in either the paraxial or the nonparaxial regime.

### Paraxial ENZ-theory in the focal volume

The main contribution of ENZ-theory is to extend NZ-theory to any aberration function but also to evaluate the diffraction integral for $z \neq 0$ near the focus [89]

and far away from the focus [93]. The first contribution was to expand the following integral[7]

$$\int_0^1 \mathrm{R}_n^{|\ell|}(\rho)\mathrm{J}_\ell(kR\rho)\mathrm{e}^{-\mathrm{i}kz\rho^2}\rho\, d\rho = \mathrm{i}^{n-\ell}\mathrm{e}^{-\mathrm{i}kz}\sum_{l=1}^{\infty}(2\mathrm{i}kz)^{l-1}\sum_{j=0}^{(n-|\ell|)/2}\nu_{lj}\frac{\mathrm{J}_{|\ell|+l+2j}(kR)}{l(kR)^l}, \quad (2.45)$$

where

$$\nu_{lj} = (|\ell|+l+2j)\binom{|\ell|+j+l-1}{l-1}\binom{j+l-1}{l-1}\binom{l-1}{(n-|\ell|)/2-j}\binom{(n+|\ell|)/2+l+j}{l}^{-1}. \quad (2.46)$$

Expression (2.45) is used to solve the diffraction integral (2.30) when the paraxial approximation holds, as follows

$$\begin{aligned}
&\mathrm{e}^{\mathrm{i}kz}\int_0^1\int_0^{2\pi}\mathrm{Z}_{n\ell}(\rho,\varphi)\,e^{\mathrm{i}kR\rho\cos(\varphi-\phi)}\mathrm{e}^{-\mathrm{i}\rho^2kz/2}\rho\, d\varphi\, d\rho\\
&= \mathrm{e}^{\mathrm{i}kz}\int_0^1 \mathrm{R}_n^{|\ell|}(\rho)\mathrm{e}^{-\mathrm{i}\rho^2kz/2}\rho\left(\int_0^{2\pi}\mathrm{e}^{\mathrm{i}\ell\varphi}\,\mathrm{e}^{\mathrm{i}kR\rho\cos(\varphi-\phi)}\,d\varphi\right)d\rho\\
&= \mathrm{e}^{\mathrm{i}kz}2\pi\mathrm{i}^\ell\mathrm{e}^{\mathrm{i}\ell\phi}\int_0^1 \mathrm{R}_n^{|\ell|}(\rho)\mathrm{J}_\ell(kR\rho)\mathrm{e}^{-\mathrm{i}\rho^2kz/2}\rho d\rho\\
&= \mathrm{e}^{\mathrm{i}kz/2}2\pi\mathrm{i}^n\mathrm{e}^{\mathrm{i}\ell\phi}\sum_{l=1}^{\infty}(\mathrm{i}kz)^{l-1}\sum_{j=0}^{(n-|\ell|)/2}\nu_{lj}\frac{\mathrm{J}_{|\ell|+l+2j}(kR)}{l(kR)^l}. \quad (2.47)
\end{aligned}$$

In the particular case $z = 0$ only the term with $l = 1$ is present on the right-hand side sum, therefore the sum over $j$ reduces only to the term with $j = (n-|\ell|)/2$, and corresponds to (2.42).

We will use the result (2.47) in § 4.3 to design holograms for optical vortex knots. The nonparaxial version of this diffraction integral is proposed in § 6.2.2 and applied in § 6.3.3.

### 2.2.3 The Richards-Wolf vector diffraction theory

The scalar diffraction theory presented in § 2.2.2 is sufficient when considering systems that are not too tightly focused. This section goes beyond the paraxial ap-

[7] We rearranged the formulas.

proximation and the scalar approximation. A rigorous vectorial theory of diffraction, that is valid in the tightly focused regime as well as the paraxial regime, is presented.

The theoretical development of electromagnetic diffraction of vector fields has interested researchers for over 90 years. Breakthoughs in this field were achieved by Ignatovsky [94, 95], Wolf [96], Richards and Wolf [97], and Boivin and Wolf [98], who formulated models in terms of diffraction integrals. Here, the work of [96, 97] is summarised through the formalism of Novotny and Hecht [81]. Their theory emphasises rotationally symmetric, aplanatic systems[8] and their calculations are based on the Debye approximation, in analogy to the scalar case [90]. The vector theory of diffraction can be applied to the calculation of the electric and magnetic components in the focal volume of a microscope objective.

Before we explicitely write the vector diffraction integral, the relationship between a generic far-field and its Fourier spectrum is derived via the angular spectrum representation [81]. Assuming that the beam propagates along the positive $z$-axis, the angular spectrum integral (2.29) of a vector optical field is

$$\boldsymbol{E}(x,y,z) = \iint_{-\infty}^{\infty} \widetilde{\boldsymbol{E}}(k_x,k_y;0)\,\mathrm{e}^{\mathrm{i}(k_x x+k_y y+k_z z)}\,dk_x\,dk_y, \tag{2.48}$$

where $\widetilde{\boldsymbol{E}}(k_x,k_y;0)$ represents a localised field distribution at the plane $z=0$, which is mapped onto the field distribution $\boldsymbol{E}(x,y,z)$ at other planes along $z$ by (2.48). The field at a very remote plane $\mathbf{r}$ (with infinite distance $r=(x^2+y^2+z^2)^{\frac{1}{2}}$ from the plane $z=0$), in the direction of the dimensionless unit vector $\left(\frac{x}{r},\frac{y}{r},\frac{z}{r}\right)$, is the following

$$\boldsymbol{E}_\infty\left(\frac{x}{r},\frac{y}{r},\frac{z}{r}\right) = \lim_{kr\to\infty} \iint_{\left(k_x^2+k_y^2\right)\le k_{\max}^2} \widetilde{\boldsymbol{E}}(k_x,k_y;0)\exp\left[\mathrm{i}kr\left(\frac{k_x}{k}\frac{x}{r}+\frac{k_y}{k}\frac{y}{r}+\frac{k_z}{k}\frac{z}{r}\right)\right] dk_x\,dk_y. \tag{2.49}$$

The reduced integration range is given by the fact that, because of their exponential decay, evanescent waves do not contribute to the fields at infinity. Using the method

[8] Systems fulfilling the Abbe sine condition and free from spherical aberration.

of stationary phase [78] the asymptotic behaviour of (2.49) is

$$\boldsymbol{E}_\infty\left(\frac{x}{r},\frac{y}{r},\frac{z}{r}\right)=-2\pi \mathrm{i}k\frac{z}{r}\widetilde{\boldsymbol{E}}\left(k\frac{x}{r},k\frac{y}{r};0\right)\frac{\mathrm{e}^{\mathrm{i}kr}}{r}. \tag{2.50}$$

If we replace

$$k_x\to k\frac{x}{r},\quad k_y\to k\frac{y}{r}, \tag{2.51}$$

then the far field is exclusively defined by the Fourier spectrum of the field, $\widetilde{\boldsymbol{E}}(k_x,k_y;0)$. Thus,

$$\widetilde{\boldsymbol{E}}\left(k_x,k_y;0\right)=\frac{\mathrm{i}re^{-\mathrm{i}kr}}{2\pi k_z}\boldsymbol{E}_\infty\left(k_x,k_y\right). \tag{2.52}$$

This result can be substituted into (2.48) as

$$\boldsymbol{E}(x,y,z)=\frac{\mathrm{i}re^{-\mathrm{i}kr}}{2\pi}\iint\limits_{\left(k_x^2+k_y^2\right)\le k_{\max}^2}\frac{\boldsymbol{E}_\infty\left(k_x,k_y\right)}{k_z}\mathrm{e}^{\mathrm{i}(k_xx+k_yy+k_zz)}\,dk_x\,dk_y. \tag{2.53}$$

This form of the angular spectrum integral is used below to formulate vector diffraction theory.

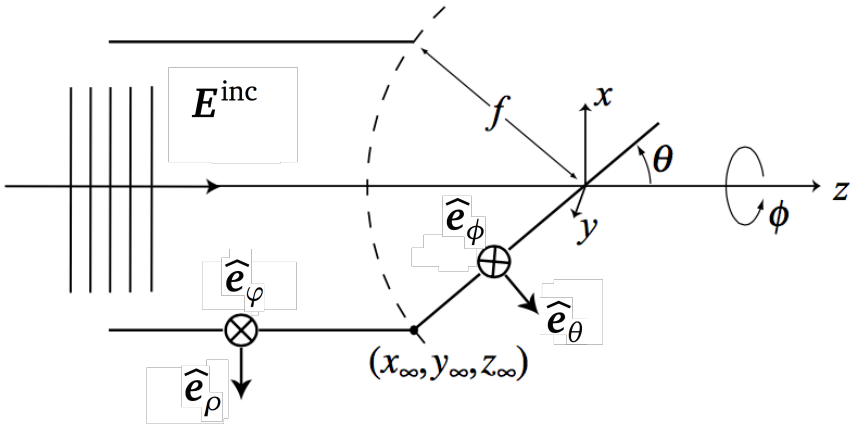


Figure 2.1: **Geometrical representation of a tightly focused field by a lens**. The paraxial field $\boldsymbol{E}^{\mathrm{inc}}$ is incident on the lens with focal length $f$, which is represented by the reference sphere of coordinates $(x_\infty,y_\infty,z_\infty)$. The refraction at this sphere maps $\widehat{\boldsymbol{e}}_\rho$ to $\widehat{\boldsymbol{e}}_\theta$, while $\widehat{\boldsymbol{e}}_\varphi=\widehat{\boldsymbol{e}}_\phi$ remains unaffected. Image adapted from [81].

We now consider a paraxial beam $\boldsymbol{E}^{\mathrm{inc}}=(E_+^{\mathrm{inc}},E_-^{\mathrm{inc}})$ incident on a lens of focal length $f$ through an aperture of radius $a$. Hence, the numerical aperture of the lens

is $\gamma = a/f$. The system is depicted in Figure 2.1. We want to evaluate the tightly focused field corresponding to $\boldsymbol{E}^{\text{inc}}$. The far-field near the optical lens at $(x_\infty, y_\infty, z_\infty)$ is calculated by the rules of geometrical optics [81], as follows. The Abbe sine condition implies that the rays incident on the reference sphere of the lens at dimensionless radius $\rho = a^{-1}\sqrt{x_\infty^2 + y_\infty^2}$ are refracted as $\rho = \gamma^{-1}\sin\theta$; the intensity law states that the energy flux along each ray is conserved, thus the refracted field satisfies $|\boldsymbol{E}^{\text{refr}}| = |\boldsymbol{E}^{\text{inc}}|\sqrt{\cos\theta}$. The refraction at the reference sphere is calculated by mapping the unit vector $\widehat{\boldsymbol{e}}_\rho$ to $\widehat{\boldsymbol{e}}_\theta$, while $\widehat{\boldsymbol{e}}_\varphi$ remains unaffected (it coincides with $\widehat{\boldsymbol{e}}_\phi$). Hence $\boldsymbol{E}^{\text{inc}} \to \boldsymbol{E}_\infty$. Note that $\boldsymbol{E}_\infty$ is the angular spectrum of the focal field, therefore it corresponds to the far-field at the reference sphere positioned at positive $z$ (Figure 2.1 does not report this). We denote[9] $\boldsymbol{E}_0 = 2k\boldsymbol{E}_\infty/k_z$, $s = 1-\gamma^2\rho^2$, where $k$ is the optical wavenumber, and rearrange the mapping in circular components as follows

$$\boldsymbol{E}_0 = \begin{pmatrix} E_+ \\ E_- \\ E_z \end{pmatrix} = \begin{pmatrix} s^{1/4}+s^{-1/4} & (s^{1/4}-s^{-1/4})\mathrm{e}^{-2\mathrm{i}\varphi} \\ (s^{1/4}-s^{-1/4})\mathrm{e}^{2\mathrm{i}\varphi} & s^{1/4}+s^{-1/4} \\ -\sqrt{2}s^{-1/4}\gamma\rho\mathrm{e}^{\mathrm{i}\varphi} & -\sqrt{2}s^{-1/4}\gamma\rho\mathrm{e}^{-\mathrm{i}\varphi} \end{pmatrix} \begin{pmatrix} E_+^{\text{inc}} \\ E_-^{\text{inc}} \end{pmatrix}. \tag{2.54}$$

When the focal length $f$ is large compared to the optical wavelength, $\boldsymbol{E}_0$ can be inserted into (2.53) to calculate the focal field $\boldsymbol{E}$. Thus, the tightly focused field is entirely determined by the far-field $\boldsymbol{E}_\infty$ on the reference sphere. All rays are refracted from the reference sphere towards the focus $(x, y, z) = (0, 0, 0)$ and no evanescent waves are involved. We use the cylindrical coordinate system $(R, \phi, z)$ in the focal volume. Since $dk_x\, dk_y = k^2\gamma^2\rho\, d\rho\, d\varphi$, the vector diffraction integral is

$$\boldsymbol{E}(R,\phi,z) = \mathrm{e}^{-\mathrm{i}kf}\,\frac{\mathrm{i}kf\gamma^2}{4\pi}\int_0^{2\pi}\!\!\int_0^1 \boldsymbol{E}_0(\rho,\varphi)\,\mathrm{e}^{\mathrm{i}k\gamma\rho R\cos(\varphi-\phi)}\mathrm{e}^{\mathrm{i}kz\sqrt{s(\rho)}}\rho\, d\rho\, d\varphi. \tag{2.55}$$

It is straightforward to derive a similar expression for the magnetic field vector in the focal volume by applying Maxwell's equation (2.4c) to the angular spectrum (2.55). As a result, the relationship $\widetilde{\boldsymbol{B}} = c^{-1}\widehat{\boldsymbol{k}} \times \widetilde{\boldsymbol{E}}$ can be used to easily derive $\boldsymbol{B}(R, \phi, z)$.

[9] Our notation differs from [81].

Efficient numerical methods for evaluating the vector diffraction integral (2.55) can be implemented. It is possible to evaluate the electromagnetic field in the focal volume by fast Fourier transform algorithms [99]. The discretisation of the reference sphere and the focal volume can be implemented in any coordinate system. We will use numerical techniques to investigate tightly focused knotted beams in the shape of a knot bundle in chapter 5 and Hopfions in chapter 6.

# 3 | Background and methods in topology

**Knots are more numerous than the stars; and equally mysterious and beautiful.**

*John Turner*

In the previous chapter, the background and the methods in optics were presented. Similarly, this chapter is an introduction to topology and its numerical methods. The first part shows how topology is applied to singular optics and mathematically defines knots, links, Hopfions and the functions describing them. Further, numerical methods for the topological analysis of scalar fields are summarised.

## 3.1 Topology in singular optics

In this section, optical vortices (§ 3.1.1) and polarisation singularities (§ 3.1.2) are analytically defined.

### 3.1.1 Optical vortices

In order to define optical vortices mathematically, light fields represented by scalar waves are considered. For example, one transverse component of the electric or magnetic field, but also the longitudinal component, where any other com-

ponent is negligible or not present at all. In particular, the scalar representation of light fields assumes that the coupling between the different components of the electric and magnetic field given by Maxwell's equations is negligible. The scalar field is defined in three dimensions and is complex valued. This function shall be represented by $\psi$, where $\psi : \mathbb{R}^3 \to \mathbb{C}$. $\psi$ can be written in terms of its modulus and argument $\chi = \mathrm{Arg}[\mathrm{Re}(\psi), \mathrm{Im}(\psi)]$ or its real and imaginary parts, as follows

$$\psi = |\psi| e^{i\chi} = \mathrm{Re}(\psi) + i\,\mathrm{Im}(\psi). \tag{3.1}$$

The *nodes* of $\psi$ are the points $\boldsymbol{r}$ in $\mathbb{R}^3$ for which $\psi(\boldsymbol{r}) = 0$. This condition can be satisfied if and only if both the real and imaginary parts of $\psi$ are zero. The zeros are also phase singularities, because the argument $\chi$ cannot be defined (is singular) on those points.

Phase singularities (or nodes) are also called optical vortices. We saw (§ 1.4) that historically they were discovered in optical fields as points around which the energy flow streamlines are closed loops. Alternatively to the circulation properties of the energy streamlines, it is more practical to define an optical vortex by its *topological charge* $\mathcal{S}$, also called *strength of the vortex*. This quantity is defined as follows

$$\mathcal{S} = \frac{1}{2\pi} \oint_C d\chi, \tag{3.2}$$

where $C$ is a closed loop along which the phase is defined everywhere, that includes the singularity. By convention the line integral is calculated in the positive direction (anticlockwise). Given that $\chi$ is a single-valued function that takes values between 0 and $2\pi$, $\mathcal{S}$ is an integer (positive, negative or zero) that is very often referred to as the *winding number* [35]. The magnitude of $\mathcal{S}$ indicates the number of $2\pi$ times the phase changes in the neighbourhood of the phase singularity and its sign indicates the direction in which the variation increases/decreases[1]. Given the properties of the

[1] In mathematical terms, the magnitude of $\mathcal{S}$ is the number of times that $C$ is wrapped around the circle $S^1$, when $\chi$ is restricted to a map from $C$ to $S^1$. The sign of $S$ indicates whether this wrapping occurs in clockwise or anticlockwise direction.

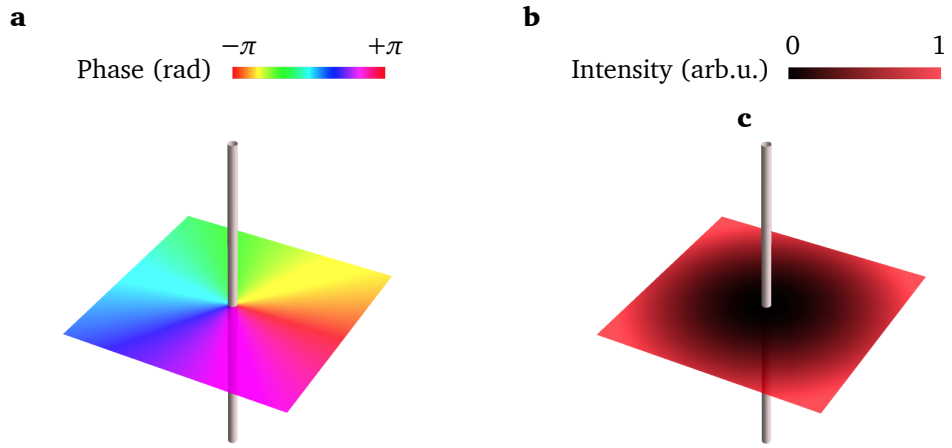


Figure 3.1: **Optical vortices representation**. Optical vortices are lines in 3D space. (a) The phase changes $2\pi$ times in a small loop around a singular point of topological charge +1. The neighbourhood of such point is colour coded with the hue wheel. (b) The intensity at the optical vortex is zero (point of darkness).

phase, we will use the *hue wheel* to represent the phase winding around a vortex, as shown in Figure 3.1.

Phase singularities are not rare in optics. They are widely used in experiments especially because they characterise Laguerre-Gaussian beams of light (§ 2.1.4). In fact, such modes show an on-axis optical vortex of charge $\mathcal{S} = \ell$ given by the phase factor $e^{i\ell\phi}$ in (2.8). Phase singularities are points in two dimensions and lines in three dimensions [35]. They can create complex patterns, as demonstrated in [100, 101], where optical vortex lines with nontrivial topology were modelled as superpositions of random plane waves. The three-dimensional nature of optical vortices and the fact that they are accessible experimentally by superpositions of optical modes make them the ideal candidates to be topologically shaped in the form of knots and links.

Two (or more) lines can intersect each other giving rise to topology-changing events. These have been studied in detail by Berry and Dennis in [15, 102] and represented in Figure 3.2. The birth and death of vortex loops were investigated as well as the reconnection events given by the intersection of one vortex line with itself or another line. These topological events were shown to be located at points where the

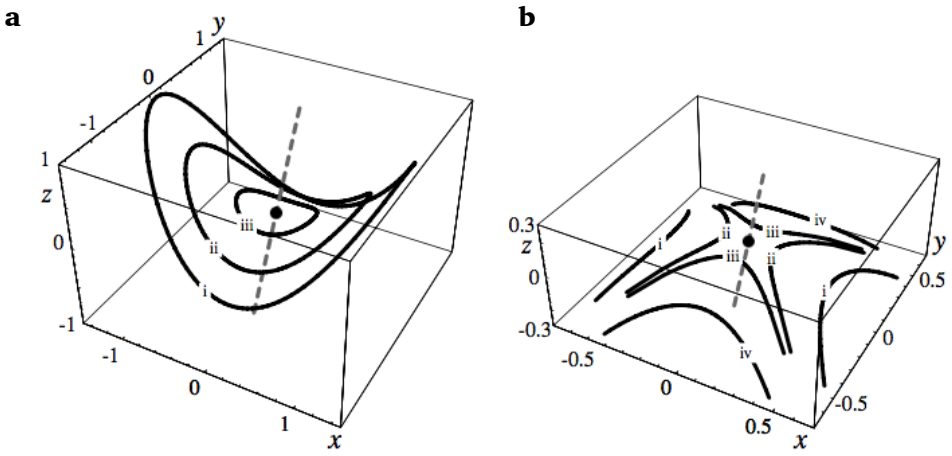


Figure 3.2: **Topology-changing events** arise when the optical vortex lines $\psi = 0$ represented by the black bold lines cross the dotted line representing $\nabla\mathrm{Re}(\psi) \times \nabla\mathrm{Im}(\psi) = 0$. (a) Vortex loop shrinking and vanishing as a parameter is changed from $i$ to $iii$. The loop disappears when it crosses the dotted line. (b) The vortex lines become closer from $i$ to $iii$ and reconnect by intersecting each other upon meeting the grey line. Image from [102].

nodal lines $\psi = 0$ intersect the lines satisfying $\nabla\mathrm{Re}(\psi) \times \nabla\mathrm{Im}(\psi) = 0$. The events were visualised by varying a single parameter in the complex field $\psi$; this is shown in Figure 3.2, were the nodal lines of two different optical fields are plotted for three different values of a parameter and labelled by $i, ii, iii$. We will use this methodology in § 4.2 and chapter 5 to analyse the topology of knotted fields by introducing topological or physical parameters to optical beam solutions.

### 3.1.2 Polarisation singularities

When the scalar representation of light is not applicable, the vectorial description of the field has to be considered. In this case, more conditions need to be satisfied for the vector field to vanish along lines. Yet another type of singularities can be studied, namely polarisation singularities, discovered and measured by Nye and Hajnal [41, 42, 103].

Polarisation singularities are points at which a quantity associated with the polar-

isation ellipse is singular. In particular, the singularities we will treat are lines along which the polarisation state of light is well defined and constant. For a 2D transverse field—whose description does not include the longitudinal component—these are *C-lines* when the polarisation is circular, and *L-surfaces* when the polarisation is linear [23]. In the case of the full 3D vector field, they are the *true* points of circular and linear polarisation. Thus they are denoted, respectively, $C^T$*-lines* and $L^T$*-lines* [103].

We present the parametrisation of such vector field singularities for the electric field below. The formalism is equivalently applicable to the magnetic field.

### C-lines and L-surfaces in transverse fields

When the longitudinal component of the electric field is negligible, the transverse component is represented by the vector field $\boldsymbol{E}^\perp : \mathbb{R}^3 \to \mathbb{C}^2$.

C-lines are the singularities of the azimuthal angle in the polarisation ellipse, or, equivalently, the azimuth $\alpha$ of the Poincaré sphere (§ 2.1.7). Their location in $\mathbb{R}^3$ is given by the following condition [35]

$$\boldsymbol{E}^\perp \cdot \boldsymbol{E}^\perp = 0. \tag{3.3}$$

Alternatively, they can be defined in terms of Stokes parameters (2.32) as the singularities of the field $\mathrm{Arg}(S_1 + \mathrm{i}S_2)$. A third condition is simply given by the loci of the zeros of the circular components of the field, which are $E_+ = 0$ and $E_- = 0$.

On the other hand, L-lines are singularities of the handedness of the polarisation ellipse [35]. They are described by the following condition

$$N = \mathrm{Re}(\boldsymbol{E}^\perp) \wedge \mathrm{Im}(\boldsymbol{E}^\perp) = 0 \tag{3.4}$$

In terms of Stokes parameters (2.32) this condition is equivalent to $S_3 = 0$.

### $\mathsf{C}^\mathsf{T}$-lines and $\mathsf{L}^\mathsf{T}$-lines in 3D vector fields

When the longitudinal component of the field is not neglected, the beam is described by the full 3D vector field $\boldsymbol{E} : \mathbb{R}^3 \to \mathbb{C}^3$. This time the polarisation singularities

cannot be defined in terms of Stokes parameters because, as previously mentioned, the Poincaré sphere does not fully determine the polarisation state of 3D vector fields.

$C^T$-lines are uniquely defined by the condition

$$\boldsymbol{E} \cdot \boldsymbol{E} = 0, \tag{3.5}$$

and $L^T$-lines by the position of the null of the vector normal to the polarisation ellipse

$$\boldsymbol{N} = \mathrm{Re}(\boldsymbol{E}) \wedge \mathrm{Im}(\boldsymbol{E}) = 0. \tag{3.6}$$

The case of intersecting $C^T$-lines and $L^T$ is very rare and corresponds to the points on which all the components of the vector field $\boldsymbol{E}$ are zero and have undefined phase.

## 3.2 Knot theory

Knots and links are studied and classified in *knot theory*, which is a branch of mathematics. In order to define knots and links, we first need to introduce the definition of *standard unit n-sphere* $S^n$, which is the set of points $(x_0, x_1, \ldots, x_n)$ in $\mathbb{R}^{n+1}$ that satisfy the equation

$$x_0^2 + x_1^2 + \ldots + x_n^2 = 1. \tag{3.7}$$

In mathematical terms, a knot is defined as the embedding of a circle $S^1$ into Euclidean 3-space $\mathbb{R}^3$ or the 3-sphere $S^3$ [104]. A link is a smooth embedding of several disjoint circles in $\mathbb{R}^3$; each knot representing the image of one of these circles is a link component [105]. A single embedding is of little interest; knots and links are a class of embeddings which are related by isotopic moves that can be carried out in 3-space without modifying the knot (isotopic embeddings) [104]. In particular, two equivalent knots are related by an *ambient isotopy*[2], which is equivalent to a homeomorphism between the complements of the two curves [106]. This map corresponds

[2] In mathematical terms, two equivalent knots $K_1$ and $K_2$ are related by an ambient isotopy, which is a continuous 1-parameter family of self-homeomorphism of $S^3$ carrying $K_1$ to $K_2$, *i.e.* $F : S^3 \times [0,1] \to S^3$ with $F(x,0) = x$ for all $x \in S^3$, $F(\cdot, t)$ a homeomorphism for all $t \in [0,1]$ and $F(K_1, 1) = K_2$.

to the smooth deformation of the curve in our intuitive picture. This makes clear why knotting is not defined for open curves; ambient isotopy transforms all such curves into the same topological object. Of course, in real world situations the concept of knottedness has been extended to curves whose ends are open, but are intuitively tangled (such as shoe laces or polymers [107]).

Knottedness of a curve can be proved (or disproved) by the use of knot diagrams (projections of a knot) and *Reidemeister moves*. Working with the three-dimensional conformations of knots is very impractical; hence, it is convenient to transfer the topological information of a knotted curve to a projection on a plane in $\mathbb{R}^3$ with its Euclidean metric, where the plane is arbitrary and the projection is usually orthogonal. Every time the line crosses it self on the plane, the 3D conformation of a line passing *over* or *under* another line is shown by a gap in the lower segment (this is a standard graphic method). Examples of such projections for the trefoil knot are shown in Figure 3.3 for two different projective planes. Each 3D knot can be represented by infinitely many diagrams; a diagram can be transformed into another one representing the same knot via Reidemeister moves [108], described in Figure 3.4. Two knot diagrams are equivalent if they are related by a finite sequence of Reidemeister moves (or their inverses). A sequence of these moves is usually applied on a specific knot diagram to give a simplified version of its projection or an intuitive information of its knot type.

Reidemeister moves are used as a practical tool to classify the large variety of knots and links based on their *minimal crossing number*. The minimal crossing number represents the number of crossings that the 'simplest' knot or link diagram can have, by which it is meant that a diagram with fewer crossings cannot be obtained under the application of Reidemeister moves. This is an *invariant of the knot*, that is a quantity that does depend only on the knot or link type and does not change under Reidemeister moves or ambient isotopies; in other words a topological invariant is the same for any geometrical conformation of the curve.

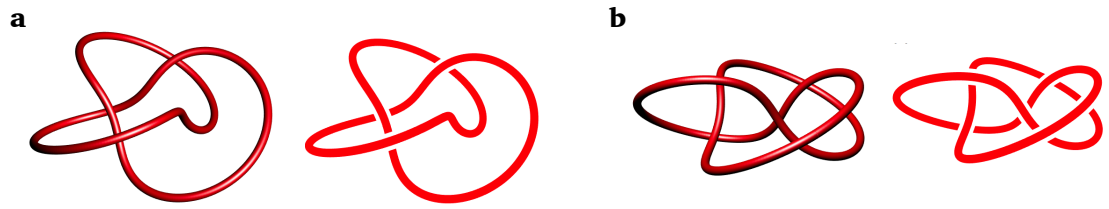


Figure 3.3: **Projections of the trefoil knot**. (a), (b) Two different orthogonal projections (right) of the same 3D curve (left). The gaps show whether a line passes over or under another line. The minimal crossing number of the curve is 3 and its knot type is $3_1$ (trefoil knot). The diagram in (b) shows 6 crossings and can be transformed into (a) via the Reidemeister moves shown in Figure 3.4.

Reidemeister moves and the minimal crossing number were the basis of the early *knot tables*. The first major work on the tabulation of knots was given by Little [109] and Tait [110], who tabulated all the knots with 10 or less crossings. Their work was extended and corrected [111, 112] and the major contribution was that of Rolfsen's table of knots [113] (which famously has a mistake corrected by Perko [114, 115]). Distinguishing knots and links by Reidemeister moves is impractical and in § 3.5.2 we will present our methods to identify the knot/link type of a three-dimensional closed curve. Our classification and notation of knots and links adopt the online *Knot Atlas* conventions [116], which contains knots and links up to the minimal crossing number 15. We adopt the Alexander-Briggs notation for the knots' identifiers: each knot is denoted by its crossing number and a subscript indicating its order amongst all knots with the same crossing number (this is arbitrary but matches most standard tabulations) [115]. For example, the trefoil knot is indicated by $3_1$. Links are denoted by the crossing number, a superscript indicating the number of components and a subscript denoting its order within the links with equivalent number of components and crossings. For example the Hopf link is indicated by $2_1^2$. A table of knots and corresponding identifiers are shown in Figure 3.5. Many researchers are currently trying to expand the tabulation of knots and links; the table of [116] is sufficient for the purpose of this thesis.

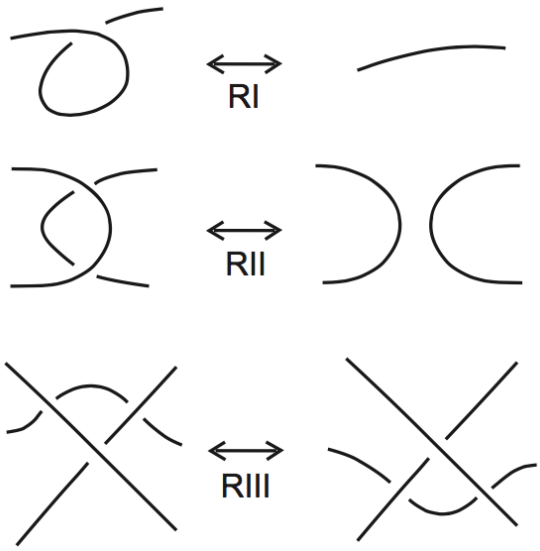


Figure 3.4: **Reidemeister moves**. The three Reidemeister moves labelled as RI, RII, RIII can be applied to a knot diagram (*e.g.* Figure 3.3) to simplify the curve's configuration without changing its knot (link) type. Image from [108].

The minimal crossing number is a widely used knot and link invariant, but, of course, it is not the only one. Another important invariant defined only for links is the *linking number*. This intuitively gives the number of times the components of a link wind about one another. We will now describe an algorithm to calculate the linking number of two linked curves $J$ and $K$ from their projections. First, it is necessary to assign an *orientation* to each knotted curve and a plus or minus sign to each crossing with the convention shown in Figure 3.6 [113]. The linking number is defined as half of the number of positive crossings minus the number of negative crossings. The linking number can also be calculated via the the Gauss linking integral [113], as follows

$$\ell k(J,K) = \oint_J \oint_K \frac{(\boldsymbol{r}_J - \boldsymbol{r}_K)\cdot(d\boldsymbol{r}_J \times d\boldsymbol{r}_K)}{|\boldsymbol{r}_J - \boldsymbol{r}_K|^3}, \tag{3.8}$$

where $\boldsymbol{r}_J$ are the points on the curve $J$ and $\boldsymbol{r}_K$ the points on the curve $K$.

Another important invariant of knots and links is the *genus* which is defined from *Seifert surfaces*. A Seifert surface is a closed connected two-dimensional surface in $\mathbb{R}^3$ whose boundary is the knot (or link) [104]. The genus of a surface can be thought of

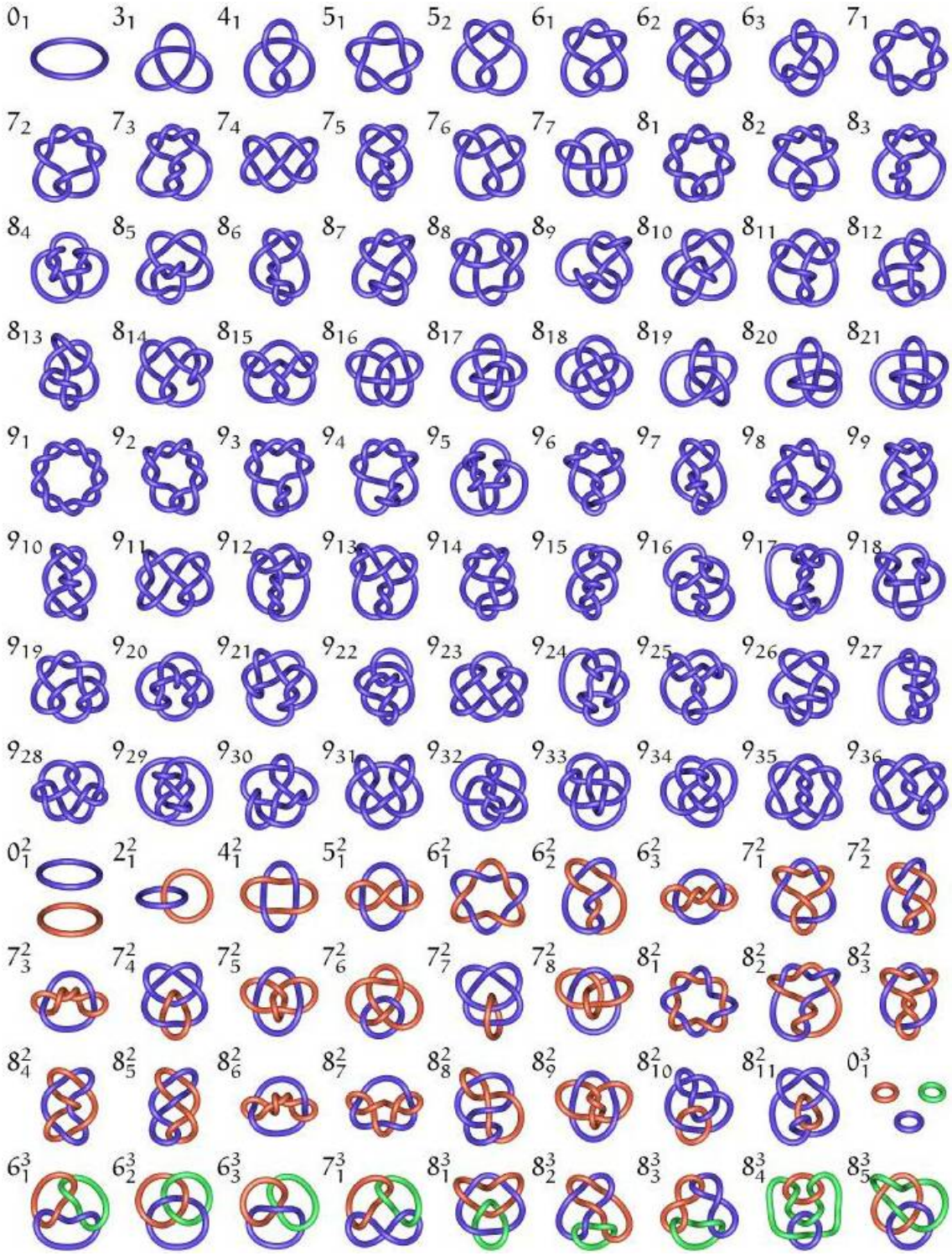


Figure 3.5: **Knot table.** The knots and links are labelled by Alexander-Briggs notation which organises them by their crossing number [Image credit Rob Scharein].


Figure 3.6: **Crossing's sign convention**. The evaluation of the linking number requires each component in the link to be oriented and each crossing to be assigned a positive or negative sign consistently with the two figures.

as the 'number of holes' on the surface. The genus $g$ of a knot (or link) is defined as the minimal genus of the Seifert surfaces of the knot (or link) [104]. Since a knotted curve is related to its equivalent class by ambient isotopies, the genus of a knot is an invariant of the knot type itself. In § 3.5.3 we will present an efficient numerical method to calculate this quantity.

An important classification of knotted curves is given by *fibred* and *non-fibred* knots/links. A knot $K$ is fibred if the complement $S^3 \setminus K$ can be represented as a fibre bundle with fibres given by the surfaces whose boundaries are the knot $K$. Such surfaces are parametrised by points in the base space $S^1$ [113]. An explicit such a fibred bundle is provided by the function $f_K : S^3 \to \mathbb{C}$, whose preimage of zero $f_K(0) = K \subseteq S^3$ is a knot or link $K$, when the derivative $\nabla \mathrm{Arg}(f_K) \neq 0$ everywhere in $S^3 \setminus K$. In this case the base space is $\mathrm{Arg}(f_K)$ and the fibres are the surfaces of constant argument corresponding to the Seifert surfaces of the knot $K$ [117]. When a knot is not fibred, there exist critical points of the phase $\mathrm{Arg}(f_K)$ in $S^3$, which satisfy $\nabla \mathrm{Arg}(f_K) = 0$ [117]. The knot $5_2$ is the simplest non-fibred knot. We will investigate the differences between fibred and non-fibred knotted optical fields in § 4.4.

An alternative way to visualise and identify knots and links is given by *braid theory*. The geometric definition of a braid is as follows. Given two lines $\{y = 0, z = 0\}$ and $\{y = 0, z = 1\}$ in $\mathbb{R}^3$ and $m$ points on each of these lines with abscissas $1, \dots m$, an $m$-strand braid is a set of $m$ non-intersecting smooth paths connecting the points on

the first line with the points on the second line, such that the projections of the paths on $Oz$ are diffeomorphisms [105]. Alexander's theorem [118] proves that any knot or link can be represented as the closure of some braid. The closure is formed by joining the two lines $\{y = 0, z = 0\}$ and $\{y = 0, z = 1\}$ around a fixed axis. Braids can be defined as algebraic objects through *Artin's relations*. In particular, the $m$-strand braid group is given by the presentation with $(m-1)$ generators $\sigma_1, \ldots, \sigma_{m-1}$, for which the Artin's relations are $\sigma_i \sigma_j = \sigma_j \sigma_i$ for $|i-j| \geq 2$ and $\sigma_i \sigma_{i+1} \sigma_i = \sigma_{i+1} \sigma_i \sigma_{i+1}$ for $1 \leq i \leq m-2$ [105]. The second Artin's relation provides an algebraic form of the third Reidemeister move (see Figure 3.4); the second Reidemeister move in this language is $\sigma_i \sigma_{i+1} = \mathbb{1}$ and the first is forbidden in the braid formalism. When the braid is scanned from $z = 1$ to $z = 0$ ($1 \leq i \leq i-1$), whenever a crossing of strands $i$ and $i+1$ is encountered, $\sigma_i$ and $\sigma_i^{-1}$ is written down, depending on whether the strand $i$ moves under or over strand $i+1$. This is depicted in Figure 3.7 [119]. In this way each braid is identified by a product of the $\sigma_i$'s and $\sigma_i^{-1}$'s, which is called the *braid word* [105].

We will use the braid formalism in § 4.2 to construct new optical knotted fields by manipulating braid words and braids' closures.

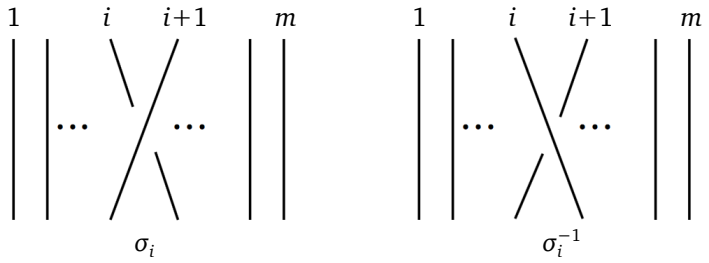


Figure 3.7: **The elementary Artin braid group generators**, adapted from [119]. The braids given by the $m$ strands show the two elementary group generators $\sigma_i$ and $\sigma_i^{-1}$, which represent the crossings of strands $i$ and $i+1$ in which the strand $i$ moves, respectively, under or over the strand $i+1$.

## 3.3 The Hopf fibration

This section defines the Hopf fibration and its mathematical properties. The Hopf fibration, named after Heinz Hopf who defined it in 1931 [120, 121] was a fundamental discovery in topology and is related to the theory of Lie groups. Here, we use the notation of [122], whose formalism requires only linear algebra and analytic geometry; a more rigorous mathematical definition is given in [123, 124]. Hopf's work [120] is an early achievement in homotopy theory. He was trying to determine the homotopy equivalence classes of maps $S^n \to S^m$, where $m \leq n$. Hopf's map is not null-homotopic, which was an unexpected discovery in this area of topology.

Given $u, v \in \mathbb{C}$ the complex coordinates for the unit three sphere $S^3$, which satisfy $|u|^2 + |v|^2 = 1$, the Hopf map is defined as the mapping $h : S^3 \to S^2$ such that

$$h(u,v) = \left(2\mathrm{Re}(u^* v), 2\mathrm{Im}(u^* v), |u|^2 - |v|^2\right). \tag{3.9}$$

The squares of the three coordinates on the right-hand side sum to 1, therefore the image of $h$ is indeed contained in $S^2$. The definition was successively extended to higher dimensions, nevertheless the original definition of Hopf will be sufficient for the purpose of this thesis.

$h$ maps multiple points in the domain to the same image element. The preimage set of $X \subset S^2$ is denoted by $h^{-1}(X)$. The Hopf map is characterised by the property that the preimage of a point on $S^2$ is a great circle on $S^3$. Each preimage set constitutes a fibre of the Hopf map; hence, the bundle of all the fibres $S^1 \hookrightarrow S^3 \to S^2$ is the *Hopf fibration*. This fibration can be visualised with a very elegant configuration in Euclidean space $\mathbb{R}^3$ which can be found via stereographic projection as follows. The stereographic projection[3] of $S^3$ on $\mathbb{R}^3$ from the point $(u, v) = (-1, 0)$ with cylindrical coordinates $(R, \phi, z)$ is

$$u = \frac{R^2 + z^2 - 1 + 2\mathrm{i}z}{R^2 + z^2 + 1}, \quad v = \frac{2R\mathrm{e}^{\mathrm{i}\phi}}{R^2 + z^2 + 1}. \tag{3.10}$$

[3]This stereographic projection is not unique. Other maps are given by transforming $u, v$ under translations, rotations and reflections of the $x, y, z$ axes.

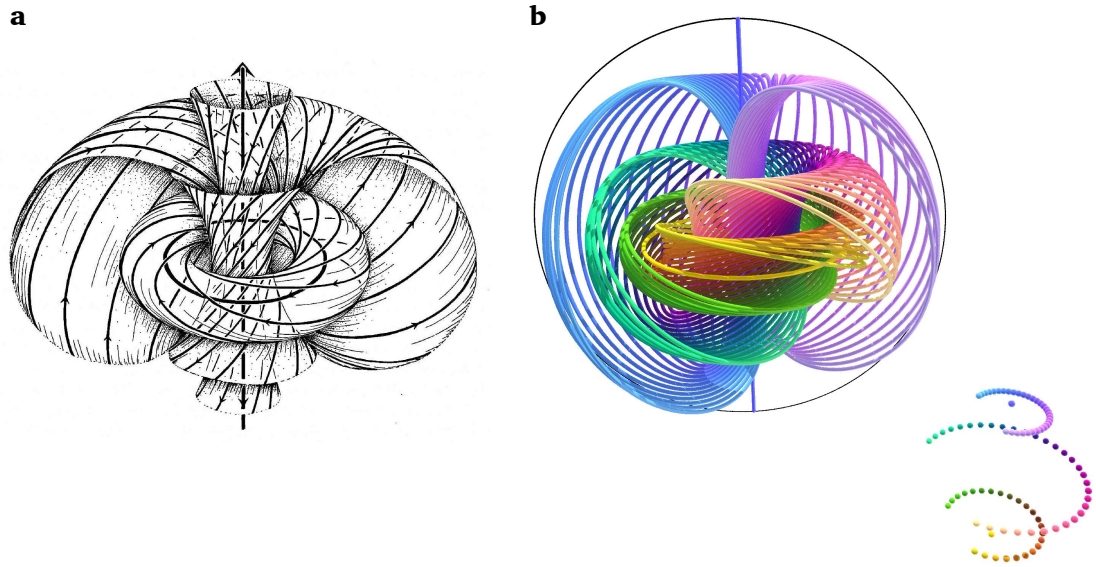


Figure 3.8: **Visualisation of the Hopf fibration** in Euclidean 3-space $\mathbb{R}^3$. Each fibre is a loop and any two distinct fibres are Hopf links. (b) The right-bottom corner shows the colour coded points on the sphere $S^2$ whose preimages are the fibres on the left. This Hopfion has Hopf index $\mathcal{H} = -1$ [Image credit (a) Roger Penrose, (b) Niles Johnson].

Figure 3.8 shows a visualisation of the Hopf fibration by (a) Penrose and (b) Johnson. The fibres span the entire 3D space. The preimages of the poles are the circle $R^2 = 1$ and the infinite line $R = 0$ (topologically this can be identified as the circle that closes at infinity); points with fixed altitude on the sphere correspond to toroidal surfaces and the set of all the points form a nested structure of tori. Any two preimages of the points on $S^2$ are in the conformation of a Hopf link; therefore the Hopf fibration is characterised by the linking number[4] (3.8) $\ell k = -1$ of any two fibres in the bundle.

For any continuous map from $S^3$ to $S^2$ the preimage sets of two regular values on $S^2$ form a link with two components in $S^3$. It turns out that the linking number (3.8) of this link is a topological invariant called the *Hopf index* $\mathcal{H}$, also called *Hopf invariant*.

[4]The sign of the linking number is determined by the orientation of each single curve. In our convention, the orientation is inherited from the structure of the Hopf fibration and is given by the topological current vector in each filament. Each fibre can be defined as the zero line of a complex scalar field, therefore the orientation of a line is determined by the 'right-hand rule': it points up for a positive topological charge on the $Rz$-plane and down for a negative topological charge.

This means that the particular choice of a pair of points on $S^2$ does not change the result and neither do continuous deformations of the map. This conserved topological quantity can be calculated with the Whitehead integral formula [125], which is often associated with electromagnetic helicity [126]. It is defined as follows

$$\mathcal{H} = \int \boldsymbol{A} \cdot \boldsymbol{B}\, dx\, dy\, dz, \tag{3.11}$$

where $\boldsymbol{B}$ is a field whose streamlines constitute the fibres (preimages of the point on the sphere) and $\boldsymbol{B} = \nabla \times \boldsymbol{A}$. Hence, $\boldsymbol{A}$ is not unique since it is determined up to gauge transformations $\boldsymbol{A} \to \boldsymbol{A} + \nabla\chi$ for some scalar field $\chi$. The explicit calculation of $\mathcal{H}$ can be laborious; in § 6.2.3 we will derive a simpler form of (3.11) suitable for optical fields. In the case of the Hopf map (3.9), the Hopf index is $\mathcal{H} = -1$ and coincides with the linking number of the preimages of any choice of points on $S^2$. The integral (3.11) can give integer values with magnitude $> 1$. These determine what we will refer to as higher order Hopfions.

## 3.4 Explicit knotted functions: Milnor polynomials for optical fields

This section describes the mathematical functions from which knotted optical fields can be derived. The existence of a complex scalar field whose nodal set is any type of knot or link is implied by the Nash-Tognoli theorem [127]; in spite of this, the explicit construction of such knotted fields is a real challenge for mathematicians and physicists. Knotted polynomials have been studied extensively by Milnor who investigated the behaviour of the nodal lines, but also the singularities of complex scalar fields in the $\mathbb{C}^2$ domain.

The first explicit polynomial maps with zero level sets in the shape of knots and links were realised for the class of *torus knots/links* by Brauner [128]. These curves lie on a toroidal surface in $\mathbb{R}^3$. They can be built explicitly by manipulating mathematical functions in $S^3$. Given $u, v$ the complex coordinates for the unit three sphere $S^3$

satisfying $|u|^2 + |v|^2 = 1$, torus knots and links are defined by the map

$$f : \mathbb{C}^2 \to \mathbb{C}, \quad f(u,v) = u^m - v^n. \tag{3.12}$$

The stereographic projection of $S^3$ on $\mathbb{R}^3$ defined by (3.10) in cylindrical coordinates $(R, \phi, z)$ gives the nodal lines of (3.12) in braid form. We will refer to this field as the Milnor polynomial[5] of the knot or link, denoted by $f_{\text{Milnor}}$. This function, expressed in Cartesian coordinates $(x, y, z)$ gives the knot or link for $f_{\text{Milnor}}(x, y, z) = 0$. For each $\phi \in [0, 2\pi]$ there are $m$ intersection points of the link with the half-plane given by a fixed value of $\phi$. This identification corresponds to $m$ diffeomorphisms between the curves that form the knot/link and the interval $[0, 2\pi]$. The nodal lines of the stereographic projection of $f$ is thus in the shape of a closed braid on $m$-strands, where the top and bottom ends of the curves have been identified. The image of a projection of these strands on the $Rz$-plane is a circle and each strand winds along the circle $n/m$ times. This configuration is the $(m, n)$-torus knot/link in Cartesian space of coordinates $(x, y, z)$. Every time either $m$ or $n$ is $\pm 1$ the nodal line is the unknot; the first nontrivial torus knots and links are the Hopf link $(2, 2)$, the double link $(2, 4)$ or $(4, 2)$, the trefoil knot $(2, 3)$ or $(3, 2)$ and the cinquefoil knot $(2, 5)$ or $(5, 2)$. Knots arise when $m$ and $n$ are coprime, otherwise the nodal lines form links.

A similar approach led Perron to explicitly construct an analogous polynomial for the simplest non-torus knot, the figure-eight $(4_1)$, which is the closure of the braid word $\sigma_1\sigma_2^{-1}\sigma_1\sigma_2^{-1}$ [129]. The projection of the closed braid associated to this knot on the $Rz$-plane does not describe a circle, but a $(1, 2)$-Lissajous figure (also known as the lemniscate of Gerono) [130]. Once the braid is constructed, the method follows exactly that of Brauner for the torus knots. Other non-torus knots can be built by repeating the basic braid of the figure-eight knot, $\sigma_1\sigma_2^{-1}$, multiple times. Similar work based on the lemniscate construction was done by Rudolph [131] and Dennis *et al.* [18, 58].

[5] Since the knotted line is given by $f_{\text{Milnor}} = 0$, the numerator of $f_{\text{Milnor}}$ is equivalently called the Milnor polynomial of the knot or link.

The mathematical construction of [18,58] was generalised to a new class of knots and links in recent work by Bode *et al*. [132]. When the new braids are projected onto the $Rz$-plane, they draw the generalised lemniscate $(1,l)$-Lissajous figure, which has $l$ lobes ($l=1$ is the circle and $l=2$ is the lemniscate of Gerono). These braids were explicitly constructed in scalar functions and their closure give *lemniscate* knots and links which correspond to the nodal lines of the fields [132]. The mathematical procedure to construct the fields associated to lemniscate knots and links is summarised below. Each curve visualised in braid space is formed by $s$ strands (analogous to $m$ for the torus knots); in 3D space each braid follows the pattern of a given braid word (§ 3.2) which is repeated $r$ times. This braid can be constructed in the complex function $p^{l,s,r}(u,h)$ in $u\in\mathbb{C}$ and periodic $h\in[0,2\pi]$, as follows

$$p^{l,s,r}(u,h)=\prod_{j=1}^{s}\Big(u-Z_j^{l,s,r}(h)\Big), \tag{3.13a}$$

$$Z_j^{l,s,r}(h)=X_j^{l,s,r}(h)+\mathrm{i}Y_j^{l,s,r}(h), \tag{3.13b}$$

$$X_j^{l,s,r}(h)=a\cos\left[\left(rh+2\pi(j-1)\right)/s\right],\quad Y_j^{l,s,r}(h)=b/l\sin\left[\left(l(rh+2\pi(j-1))\right)/s\right], \tag{3.13c}$$

where $a$ and $b$ are real parameters that stretch the lemniscate figure or its distance from the origin. From the function $p^{l,s,r}(u,h)$ it is possible to derive a semiholomorphic map $f^{l,s,r}(u,v,\overline{v})$ by replacing

$$\begin{cases}\mathrm{e}^{\mathrm{i}h}\to v\\ \mathrm{e}^{-\mathrm{i}h}\to\overline{v}.\end{cases} \tag{3.14}$$

The stereographic projection (3.10) can be used to define a polynomial map from real three-dimensional space, where the conjugate of $v$ appears as

$$\overline{v}=\frac{2R\mathrm{e}^{-\mathrm{i}\phi}}{r^2+z^2+1}, \tag{3.15}$$

ensuring $|v\overline{v}|=1$. The paper [132] proves that for appropriate choices of the parameters $a$ and $b$ the map $f^{l,s,r}(u,v,\overline{v})$ described above has the desired lemniscate knot

(link) as zero line(s). In fact, $l = 1$ corresponds to the formula of Brauner (3.12) representing torus knots and links. Various ranges of the parameters $a$ and $b$ for $l = 2$, $s = 3$, $r = 2$ give the figure-eight knot (*e.g.* $a = b = 1$). More examples of knots and links generated by this method will be given in § 4.2.

The construction of the lemniscate knots and links was generalised in [133]. This general approach proved that all knots and links can be constructed theoretically. The new construction is based on finite Fourier series in place of the Lissajous figures. However, such method introduces new critical points in the phase of the scalar field. As demonstrated in [117], the method does not seem the ideal choice for optical fields; therefore it will not be adopted in this thesis.

The mathematical functions presented in this section were used in different physical systems to create knotted fields, such as quantum or optical wavefunctions [132]. Dennis *et al*. [18, 58] showed that the maps for the torus knots and a few non-torus knots generate unique solutions to the paraxial wave equation (2.7) that coincide with the stereographically projected $f(u, v)$, *i.e.* $f_{\text{Milnor}}(x, y, z)$, at the plane $z = 0$ and have the same knot/link as the abstract mathematical function in its optical vortex line (this was briefly discussed in § 1.6). We will demonstrate this procedure explicitly in § 4.2. It is natural to ask whether the construction of Dennis *et al*. [18] extends to optical fields containing lemniscate knots and links. We will explore the success and the failure of this construction in the next chapter.

## 3.5 Numerical methods

This section presents standard numerical routines for the topological analysis of optical fields. The knots mathematically constructed in this thesis arise as zeros of complex scalar functions; § 3.5.1 shows how to extract the coordinates of the field's nodal lines. There are several different numerical algorithms to solve the task. We briefly summarise the path integral method of O'Holleran [59, 134] and Taylor [115, 135]. Further, the standardly used [115, 136] algorithms implemented by Taylor to

classify the knot or link type of entangled closed curves are described (§ 3.5.2). Finally, the method, also implemented by Taylor [137], to analyse the genus of the Seifert surfaces of the knots is summarised (§ 3.5.3).

### 3.5.1 Tracking the zeros of complex scalar fields

We present a method to extract the list of $(x, y, z)$ coordinates of the nodal lines of a complex scalar field $\psi(x, y, z)$. First, the path integral method is presented and then, an algorithm that extracts data from contour plots, implemented with the software *Mathematica* 11.

#### Vortex finding by path integrals

Optical vortices can be detected numerically by taking advantage of the topological charge given by the path integral (3.2), which implies that the complex phase winds around a singularity an integer multiple of $2\pi$ times. A discrete version of this integral can be performed using the algorithm described here, which is taken from [134]. The first step in the algorithm consists in the creation of a three-dimensional Cartesian grid of complex-valued elements; this is in practice a 3D array storing complex numbers, which can be sampled numerically from the analytic expression of a complex scalar field or experimentally from measurements. The procedure is based on a vortex finding method on the plane (a single 2D array). Each element belonging to a 2D array is considered individually, the integration path is taken around the eight cells adjacent to it, as shown in Figure 3.9; this implies that the elements at the boundaries in the 2D array are not considered at all. The sum of the phase difference between two adjacent cells in the integration path is evaluated excluding the terms whose magnitude is larger than $\pi$ (arbitrary) in order to overcome the periodic nature of the phase between 0 and $2\pi$. The closest integer of the sum divided by $2\pi$ is evaluated and the position of the elements whose result is non-zero are stored in a list. This procedure is repeated three times for each element because the path is chosen on the

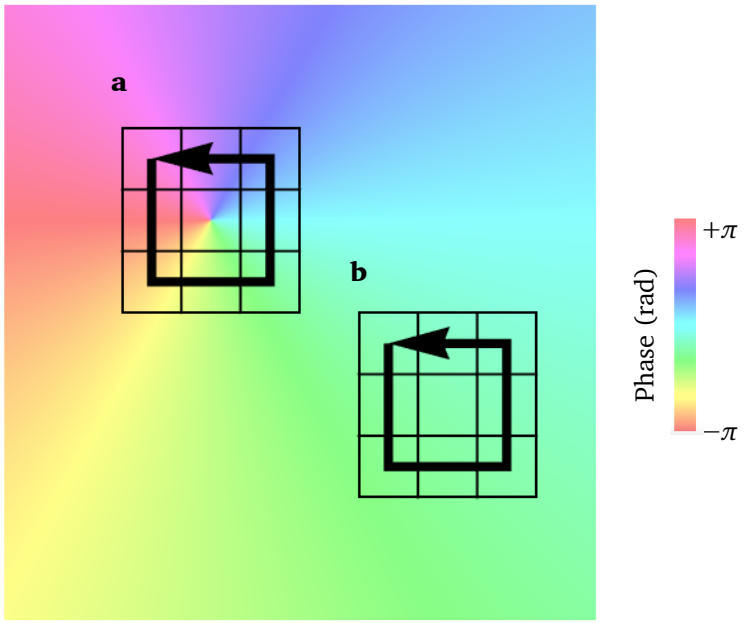


Figure 3.9: **Numerical tracking of optical vortices**. The phase of the optical field on a single plane is sampled in a 2D array. A discretised version of the topological charge $\mathcal{S}$ is calculated by following the integration path given by the eight cells adjacent to an element of the array. (a) The examined cell is identified to be a vortex. (b) The cell does not contain an optical vortex. This image was inspired by [134].

different 2D arrays associated with the three dimensions of the grid (corresponding to the $x, y, z$-directions in Cartesian space). This is necessary because the planar search method is not able to locate vortex segments which are almost 'parallel' to the 2D array under consideration (in other words when the vortex segment is located entirely in the volume between two parallel and adjacent planes). Since the detection algorithm running on a single element does not depend on the other elements, the code can be parallelised for high speed performance.

The vortex finding method by path integrals is very accurate when the resolution of the Cartesian grid representing the volume of interest is large; nevertheless, small resolutions, *e.g.* $50-100$, are sufficient to analyse simple tangles, such as the ones considered in this study. Larger resolutions improve the accuracy at the cost of the time efficiency. The numerical method is optimised in [115], by which highly complicated tangles, such as those arising in random wavefields, are analysed in details. We will

use this method in § 5.4 because it gives fast information on the topology of a beam for optimisation purposes. In chapter 6, the same method will be used to determine the location of interesting topological structures into small volumes.

#### Vortex finding by contour plots

We now present an alternative method to the vortex finding, which determines accurate results faster than the method by path integrals. This code analyses a complex scalar field $\psi(x,y,z)$, which can be defined explicitly or be interpolated from discrete data. The volume of interest is defined to be a cube. We consider a plane perpendicular to the $z$-axis and we plot the contour lines $\mathrm{Re}(\psi)=0$ and $\mathrm{Im}(\psi)=0$; we then extract the points where the two contours intersect from the graph and we store their coordinates in a list. The command can be executed $N$ times for parallel planes. We repeat this process 3 times, one for each direction $x,y,z$, in order to detect the vortex lines belonging to the volume between any two parallel and adjacent planes in the cube.

The quality of the results depends on the accuracy of the contour graph and on the resolution given by $N$. Overall, it is possible to achieve high precision in the vortex coordinates because built-in contour plot functions are extremely optimised in standard computational software. This method will be used in § 4.2 to track the complicated curves of lemniscate knots in optical fields and will also be adopted in the rest of the thesis to generate high quality plots of knotted lines.

### 3.5.2 Identifying the knot (or link) type of a curve

Most of the curves investigated in this thesis are sufficiently simple that their knot (link) type is determined by visual inspection, projections on the plane and Reidemeister moves, as described in § 3.2. However, this is unsatisfactory for complicated tangles, which require automated routines for an unambiguous classification of the curves.

We use the *pyknotid knot identification toolkit* software created by Taylor [138] to calculate a knot invariant, namely the *Alexander polynomial*, of the curves we want to classify. The Alexander polynomial, as other knot invariants, does not discriminate different knots perfectly, but it is sufficient to determine unambiguously the topology of curves characterised by low crossing number.

The code takes as the input the list of coordinates of the knotted line (multiple lists for links). The coordinates must be ordered and we do so by sampling the points with high resolution and invoking the function “FindShortestTour" in the software *Mathematica* 11 with the list of coordinate as the argument and “DistanceFunction → EuclideanDistance" in the options.

This method will be used in § 4.2 to determine the intricate topology of lemniscate knots and links.

### 3.5.3 Genus analysis

This section summarises the numerical procedure implemented by Taylor [137] to analyse the genus of the Seifert surfaces of an optical field represented by a complex scalar field whose nodal lines are knotted (or linked). The technique relies on certain standard routines for the topological analysis of surfaces.

The code takes as the input a three-dimensional array of complex numbers representing the scalar field at different points, which can either be sampled numerically or experimentally. The *marching cubes* algorithm [139] is used to extract the contour surfaces as their numerical triangulation. The connection between the continuous definition of the genus and the discrete formulation is given by the Gauss-Bonnet theorem [140]. The triangulation of each Seifert surface gives its Euler characteristic $\chi = V - E + F$, where $V$ is the number of distinct triangle vertices, $E$ is the number of distinct edges and $F$ is the number of triangle faces (distinct because the majority of vertices and edges are shared by the triangles which are not part of the surface's boundaries). The genus is $g = (b - \chi + 2)/2$, where $b$ is the number of boundary com-

ponents of the polyhedral surface. This algorithm is simple, efficient and allows the fast computation of the genus of hundreds of different Seifert surfaces from a given scalar field. The quality of the results returned by this method depends on the resolution of the input array representing the scalar field because the recovered surfaces are found from linear interpolation between the sampled points. Nevertheless, since the genus is a topological quantity, it is not affected by the errors in the approximated recovered local geometry of the field.

This numerical routine will be used in § 4.4 to analyse the genus of the Seifert surfaces arising in beams of light embedding knotted polarisation singularities. The surfaces are defined as contours of $\tan^{-1}(S_1 + \mathrm{i}\, S_2)$, which correspond to the pairs of surfaces of constant azimuth $\alpha, \alpha + \pi$ on the Poincaré sphere. The genus is an additive quantity, therefore tracing the union of these two surfaces does not affect the quality of the results; nonetheless, it simplifies the numerical performance because it avoids the introduction of unnecessary boundaries.

# 4 | Optical vortex knots and links in paraxial light

**One of the principal objects of theoretical research in any department of knowledge is to find the point of view from which the subject appears in its greatest simplicity.**

*Josiah Willard Gibbs*

Chapters 1–3 showed that, when optics and topology are combined, knotted and linked filaments made of optical vortices can be generated in scalar fields for which the paraxial approximation holds. This chapter applies the ideas presented previously to investigate and extend the theory of optical vortex knots and links. The optical knot construction is extended to the class of lemniscate knots and links. In particular, the mathematical functions described in § 3.4 are used to generate theoretically and experimentally knotted functions in light beams, with the method of polynomial beam propagation (§ 2.2.1) and numerical vortex tracking (§ 3.5.1 and § 3.5.2). Further, the methods to generate holograms for the practical implementation of optical vortex knots are presented. These involve either Laguerre-Gaussian modes (§ 2.1.4) or Zernike aperture modes (§ 2.1.5). The holograms generated by the latter functions are designed by inverting the ENZ-propagation method (§ 2.2.2). Finally, a new method to analyse the topological properties of the beams around the singular lines are introduced, based on the genus analysis described in § 3.5.3.

The contents of § 4.4 have been published in [137], in collaboration with experimentalists.

## 4.1 Extending the theory of optical vortex knots and links

This section gives the technical details concerning the formation of optical vortex knots and links [18, 58, 84], introduced in § 1.6. Berry and Dennis [14] realised knotted optical fields in the form of polynomial waves generated by long wavelength expansions of Bessel beams (§ 1.6). They successfully embedded the trefoil knot and the Hopf link in LG-modes theoretically [15] and achieved the same results in experiments a few years later [16]. Such knots were threaded by infinite vortex lines, which meant that the knotted structures were not isolated. Optical beams with isolated optical vortex knots and links were built in [18] using algebraic topology; the complex scalar fields representing these beams inherited their topologies from Milnor polynomials (§ 3.4). The theoretical predictions were generated experimentally into superpositions of Laguerre-Gaussian modes of identical waist; the experimental parameters were optimised through numerical techniques aiming to increase the intensity between two distinct optical vortex points [19].

Certain aspects of the theory of optical vortex knots in [18] have scope for further investigation. The correct knot does not always emerge in the optical field generated from a Milnor polynomial; at present, there is no proof to why the topology transfers from an abstract mathematical function, which does not satisfy the wave equation, to a polynomial optical field, which indeed does. Further, the adoption of LG-modes to embed the knotted polynomial function is justified by the fact that any Milnor polynomial multiplied by a Gaussian factor $\mathrm{e}^{-R^2/(2w^2)}$ propagates paraxially like a polynomial beam, when the waist $w$ is sufficiently large. However, nothing prevents the selection of another basis representing physical beams embedding the same nodal lines topo-

logy. The optical fields of [18] embed only torus knots falling in the class of fibred knots and links (§ 3.2). As such, the optical fields should be characterised by interested contours of the phase (the Seifert surfaces of the knots) and should not contain critical points of the phase; however, the above properties were not demonstrated from an experimental point of view.

This chapter will give new insights to the success and the failure of the paraxial evolution of Milnor functions by constructing optical fields embedding the lemniscate knots and links of [132]. Furthermore, polynomial wavefunctions embedded in Gaussian envelopes will be compared to knotted polynomials arising in generalised Airy disks. A new method for measuring and analysing the Seifert surfaces of knots and links will also be introduced.

Milnor functions (§ 3.4) are used to generate polynomial solutions $\psi$ to the paraxial wave equation (2.7) in the form of complex scalar fields with the same nodal lines topology ($\psi = 0$) of their corresponding mathematical functions [18]. The math-

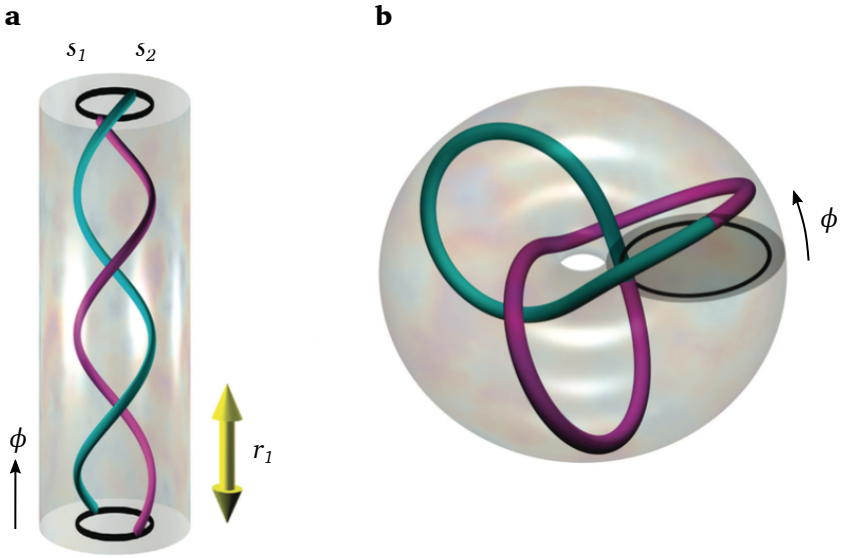


Figure 4.1: **The closure of the braid associated to the trefoil knot**. (a) The braid has $s = 2$ twisted strands. The yellow arrow indicates the basic braid word, which is repeated $r = 3$ times. (b) The knot is constructed by joining $\phi = 0$ and $\phi = 2\pi$ in a toroidal conformation. Image from [18].

ematical construction involves braids consisting of $s$ strands, whose braid word is repeated $r$ times. Figure 4.1 (a) shows the 3D-braid[1] associated with the trefoil knot, which has $s = 2$ strands and a braid word repeated $r = 3$ times. The closure of the braid is done by joining the planes $\phi = 0$ and $\phi = 2\pi$, so that the resulting conformation is a knot enclosed in a toroidal surface, as shown in Figure 4.1 (b) for the trefoil knot. The knotted curve corresponds to the nodal lines of the Milnor polynomial $f_{\text{Milnor}}(x, y, z)$. The optical field is derived from this construction by considering only the plane $z = 0$ of the Milnor polynomial. Polynomial beams are the unique solutions that coincide with Milnor polynomials at the plane $z = 0$.

Polynomial beams are a powerful tool for studying structures arising within a small volume in the optical field. Since they do not depend on additional parameters (such as the waist of the beam), they are much easier to handle analytically compared to superpositions of Laguerre-Gaussian functions. Polynomial beams (§ 2.2.1) were mathematically defined in [84] as sums of monomials in $R, \mathrm{e}^{\mathrm{i}\ell\phi}, z$, forming a basis set. It is not possible to project a generic optical wavefield onto the polynomial basis through a scalar product as they diverge at infinity ($R \to \infty$). Nevertheless, when the optical field at $z = 0$ is a complex polynomial in monomials $\mathrm{e}^{\mathrm{i}\ell\phi}R^n$, a paraxially propagating polynomial beam can be constructed explicitly by the following direct substitution

$$\mathrm{e}^{\mathrm{i}\ell\phi}R^n \to \mathrm{e}^{\mathrm{i}\ell\phi}R^{|\ell|}P^{|\ell|}_{(n-|\ell|)/2}(R, z; k), \tag{4.1}$$

where $P^{|\ell|}_{(n-|\ell|)/2}$ are the paraxial polynomials defined in (2.37). This means that it is possible to compute knotted complex scalar solutions to the paraxial wave equation in a systematic fashion simply by applying the substitution (4.1) to a Milnor polynomial. Thus, the family of polynomial beams seems to be the ideal choice to investigate knotted optical fields generated from Milnor maps. This approach will be applied in § 4.2.

[1]The definition of braid given in § 3.2 was given as a projection onto the $y = 0$ plane. In this chapter we consider three-dimensional conformations in the space of coordinates $(R, \phi, z)$.

A partial solution to the unsuccessful inheritance of the desired nodal topology was proposed by King in [58] and named *over homogenisation*. The method consists in multiplying the Milnor polynomial $f_{\text{Milnor}}(R, \phi, 0)$ by $1+R^2$, and its multiples $(1+R^2)^n$, in order to aid the desired topology transfer. The power $n$ is called *level of over homogenisation* and $n = 0$ corresponds to the unchanged Milnor map, called *standard homogenisation*. The $(5, 2)$-torus knot (cinquefoil knot) was shown to fail for the standard homogenisation case but was successfully constructed for $n = \{1, 2\}$ [58]. Since the paraxial wave equation contains derivatives of $R$ and $z$ at different orders to each other, polynomial beams contain powers of $z$ of half order with respect to the powers of $R$. On the other hand, the Milnor polynomial does not restrict the order of the powers of $z$ and has potential for more intricate nodal lines. The over homogenisation factor seems to increase the 'amount of information' transferred from the Milnor map to the paraxial function by increasing the order in $R$ and $z$ in the paraxial polynomial. In this chapter, this method will be applied to build optical wavefunctions for knots and links whose construction fails when derived from standardly homogenised Milnor functions.

Further in the chapter, the topology of knotted beams around the knotted lines will be investigated. Knotted phase singularities affect the topology of their embedding beam, whose extra topological information can be revealed by the full reconstruction of its phase contours [117]. These are the Seifert surfaces of the knot (§ 3.2), which are oriented and globally internested in a three-dimensional space filling conformation. The ability to render Seifert surfaces improves our understanding of knotted singular lines and gives insights into the behaviour of the entire optical beam. In fact, Seifert surfaces are directly related to the genus, the knot invariant corresponding to the number of bridges (holes) on a surface (§ 3.2). When the optical field $\psi$ contains three-dimensional critical points of the phase ($\nabla \text{Arg}(\psi) = 0$), its Seifert surfaces break down through these points in a conformation that locally looks like a diablo and across which the integer genus of the Seifert surfaces jumps by $\pm 1$ (in analogy to the phase

saddles of [141]). On the other hand, the total absence of these critical points gives a fibred knot [132], discussed in § 3.2.

The rest of this chapter extends the theory of paraxial optical vortex knots and links as follows. In § 4.2, optical fields whose nodal lines fall in the class of lemniscate knots and links are constructed and their properties are investigated. In § 4.3, knots and links are embedded into two different types of beams and a routine—suitable for experiments—to generate their holograms in Fourier space is presented. In § 4.4, a new method to investigate the Seifert surfaces of knots and links is introduced and their properties are studied theoretically and experimentally. The results of this chapter are discussed in § 4.5.

## 4.2 Lemniscate optical knots

This section explicitly constructs optical fields embedding the lemniscate knots described only mathematically in § 3.4. The physical interpretation of the parameters describing the lemniscate fields is given in § 4.2.1. In § 4.2.2, the construction of the optical Borromean links is shown explicitly and the topology of the corresponding optical field is analysed. More optical lemniscate knots and links are presented and anlysed in § 4.2.3.

### 4.2.1 The physical meaning of the lemniscate parameters

The family of lemniscate knots is characterised by three parameters $l$, $s$, $r$. The physical meaning of these parameters is comprehensible in braid space (§ 3.2); $l$ determines the lemniscate curve that appears by the orthogonal projection of the nodal lines onto the $Rz$-plane, $s$ is the number of separate strands that constitute the braid and $r$ is the number of repeats of the braid word in the $\phi$ direction. In order for the braid topology to be transferred correctly from the Milnor polynomials to the optical field, the optical lemniscate knots and links require the preservation of $l$, $s$, $r$ under

paraxial propagation. The mathematical fields are also characterised by the stretching factors $a$ and $b$; the lemniscate construction seems to be successful for values of $a \sim b \sim 1$ or smaller [132]. A detailed analysis of how the paraxial optical beams constructed from Milnor polynomials depend on $a$ and $b$ is discussed in § 4.2.2.

Figure 4.2 shows an example of the successful topology transfer of the lemniscate knots characterised by $l = 2$, $s = 3$, $r = \{2, 3, 4, 5\}$ and $a = b = 1$. Figure 4.2 (a)–(d) illustrates the optical knots in braid space, in which the 3 strands $s_1, s_2, s_3$ and the repetition of the basic braid word $r_1, r_2, \ldots$ are labelled for each knot; Figure 4.2 (e)–(h) reports the plots of the knotted configurations in Cartesian space. The optical field containing the figure-eight knot ($r = 2$) and the Borromean rings ($r = 3$) was constructed in [18, 58, 142], whereas the $8_{18}$ ($r = 4$) was given in [58, 132]. Figure 4.2 (d), (h) shows the same construction generalised to $r = 5$, for which the knot $10_{123}$ appears under paraxial propagation.

The topology transfer between the Milnor polynomials and the optical fields does not always occur successfully and therefore it is not possible to predict the optical vortex lines' topology forming under propagation. At times, the nodal lines do not trace the expected lemniscate figure on the $Rz$-plane: this is the case when additional strands appear, but also when the braid word associated with the optical nodal lines differs from the desired one. A way to overcome thise problem is to numerically search for values of the parameters $a$ and $b$ for which the knotted topology is inherited correctly. Alternatively, the over homogenisation method of [58] can help in many cases the topology transfer. The above methods are applied to construct optical lemniscate knots up to the minimal crossing number 10.

### 4.2.2 The case study $l = 2$, $s = 3$, $r = 3$

We now focus our investigation on the case study of the Borromean rings ($l = 2$, $s = 3$, $r = 3$) and we then apply the polynomial beam propagation (§ 2.2.1) to this lemniscate link. It is known that the Borromean rings appear under paraxial propaga-

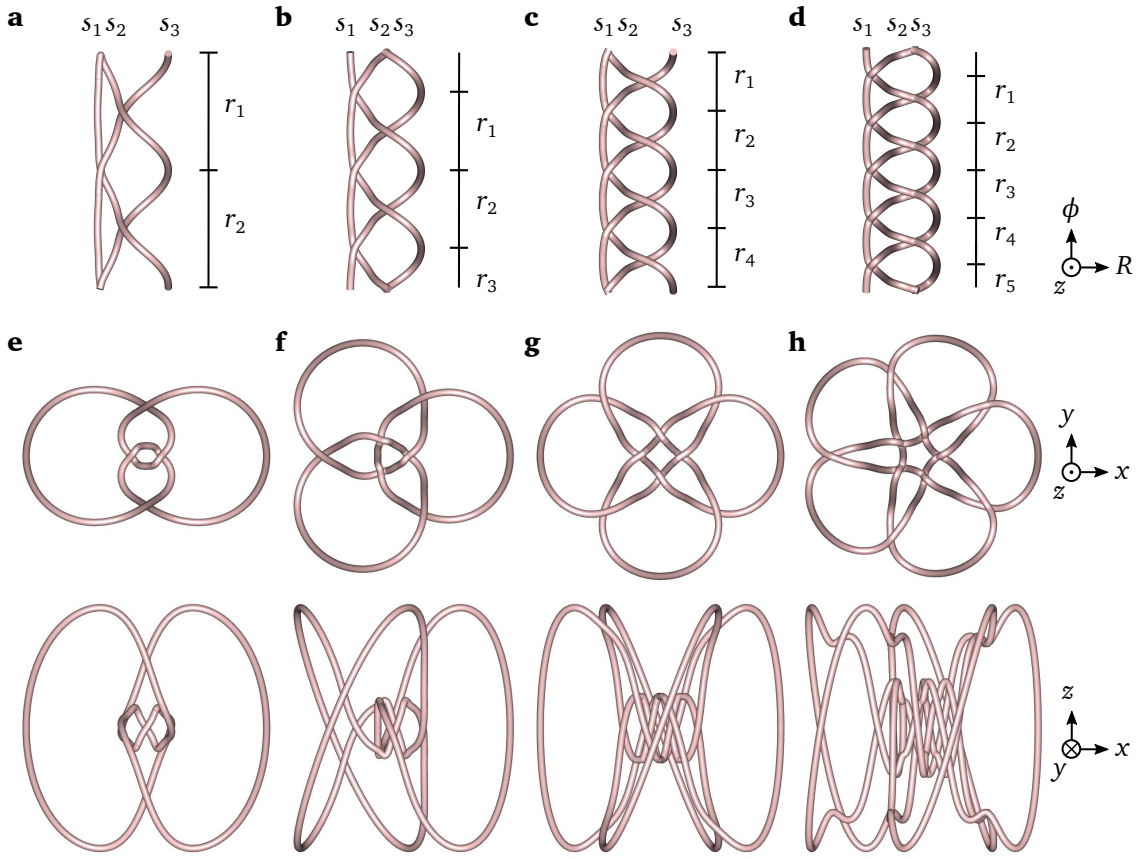


Figure 4.2: **Optical lemniscate knots** characterised by $l = 2$, $s = 3$, (a) and (e) $r = 2$, (b) and (f) $r = 3$, (c) and (g) $r = 4$, (d) and (h) $r = 5$. The stretching factors are $a = b = 1$. (a)–(d) The knots and links in braid space are formed by 3 strands $s_1$, $s_2$, $s_3$ and the braid word $\sigma_1^{-1}\sigma_2$ is repeated $r$ times. (e)–(h) Top and front view of the knots and links appearing as the nodal lines of a paraxial optical fields in Cartesian space, where (e) is the figure-eight knot, (f) the Borromean rings, (g) the knot $8_{18}$ and (h) the knot $10_{123}$.

tion of their corresponding Milnor polynomial [18, 58]. In this section we study the properties of this field by including explicitly the dependence on the stretching parameters $a$ and $b$.

We begin by substituting $l$, $s$, $r$ into the general mathematical formula for the lemniscate knots and links (3.13). Explicitly

$$\begin{aligned} f^{2,3,3}(u,v,\overline{v};a,b) = \frac{1}{64}(\overline{v}^3+v^3)\left(-8a^3-6ab^2+b^3(\overline{v}^3-v^3)\right) \\ +\frac{3}{16}\left(-4a^2+b^2+2ab(\overline{v}^3-v^3)\right)u+u^3. \end{aligned} \tag{4.2}$$

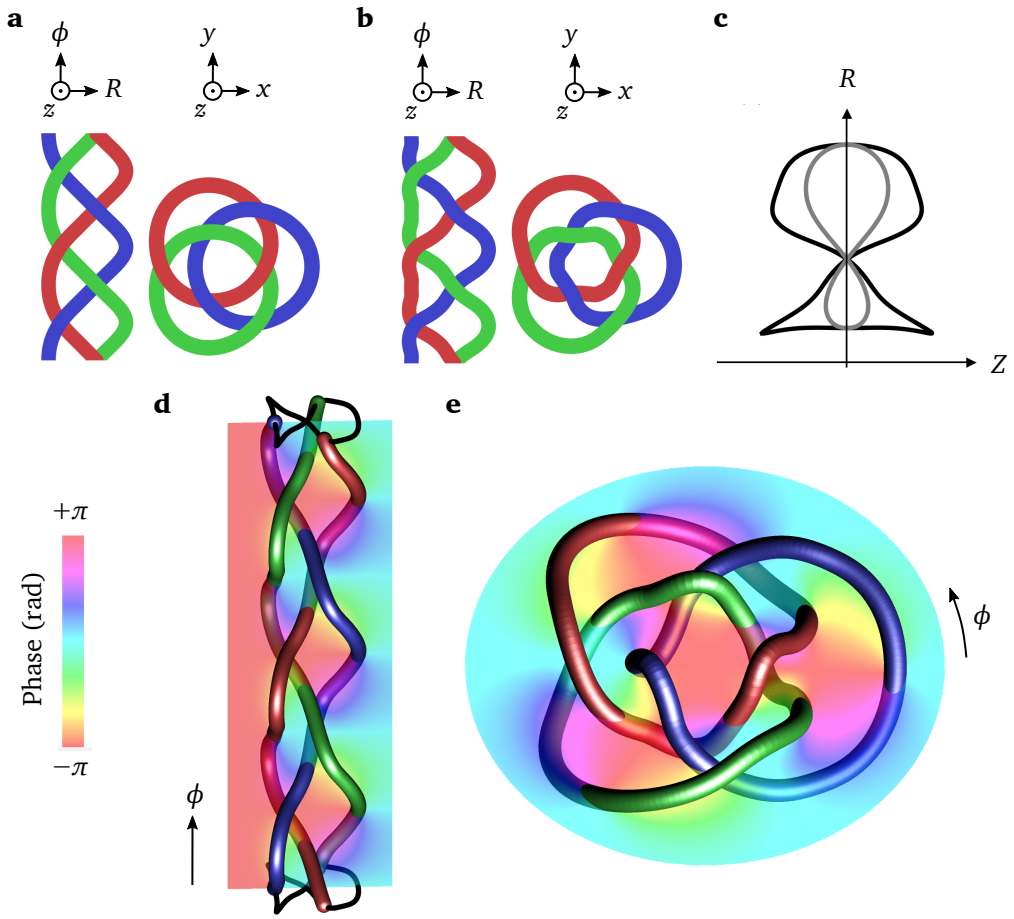


Figure 4.3: **Optical Borromean rings** corresponding to the lemniscate parameters $l = 2$, $s = 3$, $r = 3$ and stretching factors $a = b = 0.5$. A schematic version of the braid in cylindrical coordinates and the link in Cartesian coordinates are given to compare (a) the Milnor function nodal lines and (b) the optical field's nodal lines. (c) The orthogonal projection of the 3D braid onto the $RZ$-plane gives a lemniscate curve characterised by two lobes (since $l = 2$); the Milnor function is shown in grey and the optical field in black. Although the two fields share the same topology and the same $z = 0$ plane, the field at $z \gtrless 0$ is different for the mathematical function and the paraxially propagated function. (d) The 3D version of the optical braid is shown together with the corresponding lissajous figure and the phase at the plane $z = 0$. (e) The Borromean rings in Cartesian space; the phase at $z = 0$ is shown for reference.

The Milnor polynomial of the Borromean rings is calculated via stereographic projection (3.10) and (3.15) of (4.2), that is

$$f^{2,3,3}_{\text{Milnor}}(R,\phi,z;a,b) = \frac{1}{16(R^2+z^2+1)^6}\left(16b^3 e^{-6i\phi}R^6 - 16b^3 e^{6i\phi}R^6 - (R^2+z^2+1)^3\right.$$

$$\times \left(R^2+(z+\mathrm{i})^2\right)\left[12a^2(R^2+z^2+1)^2-3b^2(R^2+z^2+1)^2 \right.$$
$$\left.-16\left(R^2+(z+\mathrm{i})^2\right)^2\right]-4a\mathrm{e}^{-3\mathrm{i}\phi}R^3(R^2+z^2+1)^2\left\{4a^2(R^2+z^2+1)\right.$$
$$\left.+3b\left[b(R^2+z^2+1)-4\left(R^2+(z+\mathrm{i})^2\right)\right]\right\}-4a\mathrm{e}^{3\mathrm{i}\phi}R^3(R^2+z^2+1)^2$$
$$\times\left\{4a^2(R^2+z^2+1)+3b\left[b(R^2+z^2+1)+4\left(R^2+(z+\mathrm{i})^2\right)\right]\right\}. \tag{4.3}$$

Figure 4.3 (a) shows the braid generated as the nodal lines of (4.3) for $a=b=0.5$ and the Borromean rings appearing from the closure of such braid in Cartesian space.

As described in § 4.1, Milnor polynomials play a crucial role in generating the knotted optical fields since the initial condition for the paraxial beam to propagate along $z$ is extrapolated from the plane $z=0$ of the Milnor function. Thus, the initial condition for our case study is as follows

$$\psi_{\mathrm{2D}}^{2,3,3}(R,\phi;a,b)=-16+12a^2-3b^2+12(4a^2-b^2)R^2+3(16+20a^2-5b^2)R^4$$
$$-3(16+20a^2-5b^2)R^8-12(4a^2-b^2)R^{10}+(16-12a^2+3b^2)R^{12}$$
$$-4a\mathrm{e}^{-3\mathrm{i}\phi}R^3\left[4a^2+12b+3b^2+3(4a^2+4b+3b^2)R^2+3(4a^2-4b\right.$$
$$\left.+3b^2)R^4+(4a^2-12b+3b^2)R^6\right]-4a\mathrm{e}^{3\mathrm{i}\phi}R^3\left[4a^2-12b+3b^2\right.$$
$$\left.+3(4a^2-4b+3b^2)R^2+3(4a^2+4b+3b^2)R^4+(4a^2+12b\right.$$
$$\left.+3b^2)R^6\right]+16b^3\mathrm{e}^{-6\mathrm{i}\phi}R^6-16b^3\mathrm{e}^{6\mathrm{i}\phi}R^6. \tag{4.4}$$

The argument of the expression above is plotted in Figure 4.3 as a phase distribution in (d) cylindrical and (e) Cartesian coordinates. The optical propagating beam in 3D is found by polynomial beam propagation (§ 2.2.1): each monomial in $R$ and $\mathrm{e}^{\mathrm{i}\phi}$ is substituted in (4.4) by (4.1). Thus, a solution for the paraxial wave equation (2.7) is obtained for any value of $a$ and $b$. This takes the following form when $Z=zk^{-1}$

$$\psi_{\mathrm{par}}^{2,3,3}(R,\phi,Z;a,b)=\psi_{\mathrm{2D}}^{2,3,3}(R,\phi;a,b)+24\mathrm{i}\{(4a^2-b^2)+(16+20a^2-5b^2)R^2$$
$$-4(16+20a^2-5b^2)R^6-25(4a^2-b^2)R^8+3(16-12a^2+3b^2)R^{10}$$
$$+a\mathrm{e}^{-3\mathrm{i}\phi}R^3[-4(4a^2+4b+3b^2)-10(4a^2-4b+3b^2)R^2-6(4a^2$$
$$-12b+3b^2)R^4]+a\mathrm{e}^{3\mathrm{i}\phi}R^3[-4(4a^2-4b+3b^2)-10(4a^2+4b$$

$$
\begin{aligned}
&+3b^2)R^2-6(4a^2-12b+3b^2)R^4\ ]\ \}\,Z+24\,\{\ (-16-20a^2+5b^2)\\
&+36(16+20a^2-5b^2)R^4+400(4a^2-b^2)R^6+75(-16+12a^2-3\\
&\times b^2)R^8+a\mathrm{e}^{-3\mathrm{i}\phi}R^3\left[40(4a^2-4b+3b^2)+60(4a^2-12b+3b^2)R^2\right]\\
&+a\mathrm{e}^{3\mathrm{i}\phi}R^3\,[\ 40(4a^2+4b+3b^2)+60(4a^2+12b+3b^2)R^2\ ]\ \}\,Z^2\\
&+768\mathrm{i}\,\{\ 3(16+20a^2-5b^2)R^2+(4a^2-b^2)R^4-25(16-12a^2\\
&+3b^2)R^6+5a\mathrm{e}^{-3\mathrm{i}\phi}R^3(4a^2-12b+3b^2)+5a\mathrm{e}^{3\mathrm{i}\phi}R^3(4a^2+12b\\
&+3b^2)\ \}\,Z^3-1152\,\{\ 16+20a^2-5b^2+100(4a^2-b^2)R^2-75(16\\
&-12a^2+3b^2)R^4\ \}\,Z^4-46080\mathrm{i}\,\{\ 4a^2-b^2-3(16-12a^2\\
&+3b^2)R^2\ \}\,Z^5-46080\left\{16-12a^2+3b^2\right\}Z^6. \qquad (4.5)
\end{aligned}
$$

The topology of the lines in 3D space along which $\psi_{\mathrm{par}}^{2,3,3}$ is zero strongly depends on the parameters $a$ and $b$. By tracking the vortex lines of (4.5) as described in § 3.5.1 and by visual inspection, it is possible to determine that by selecting $a = b = 0.5$ the optical vortex lines are the Borromean rings, shown in Figure 4.3 (e). The corresponding optical braid is shown in Figure 4.3 (d) and the 3D conformation is schematised in Figure 4.3 (b). This is compared to the nodal lines of its Milnor polynomial in Figure 4.3 (a). The lemniscate figure traced on the $RZ$-plane by the optical vortices is plotted in black in Figure 4.3 (c), this overlaps with the lemniscate figure from the mathematical construction in grey. The smooth black lemniscate figure is strongly distorted in the grey figure, with the vortices executing sharp turns close to the optical axis. This indicates that the optical field is fundamentally different from its Milnor polynomial, nevertheless as predicted, they share the same topology. This properties were previously described by King in [58].

The values of $a$ and $b$ for which the optical field embeds the Borromean rings are not unique. Function (4.5) coincides with the optical field built in [18, 58] when $a = b = 1$. The nodal lines of this field are plotted in Figure 4.2 (b) and (f). Since there is no systematic rule to determine the topology of an optical beam for generic values of the stretching parameters $a$ and $b$, it is hard to determine the parameter space in which

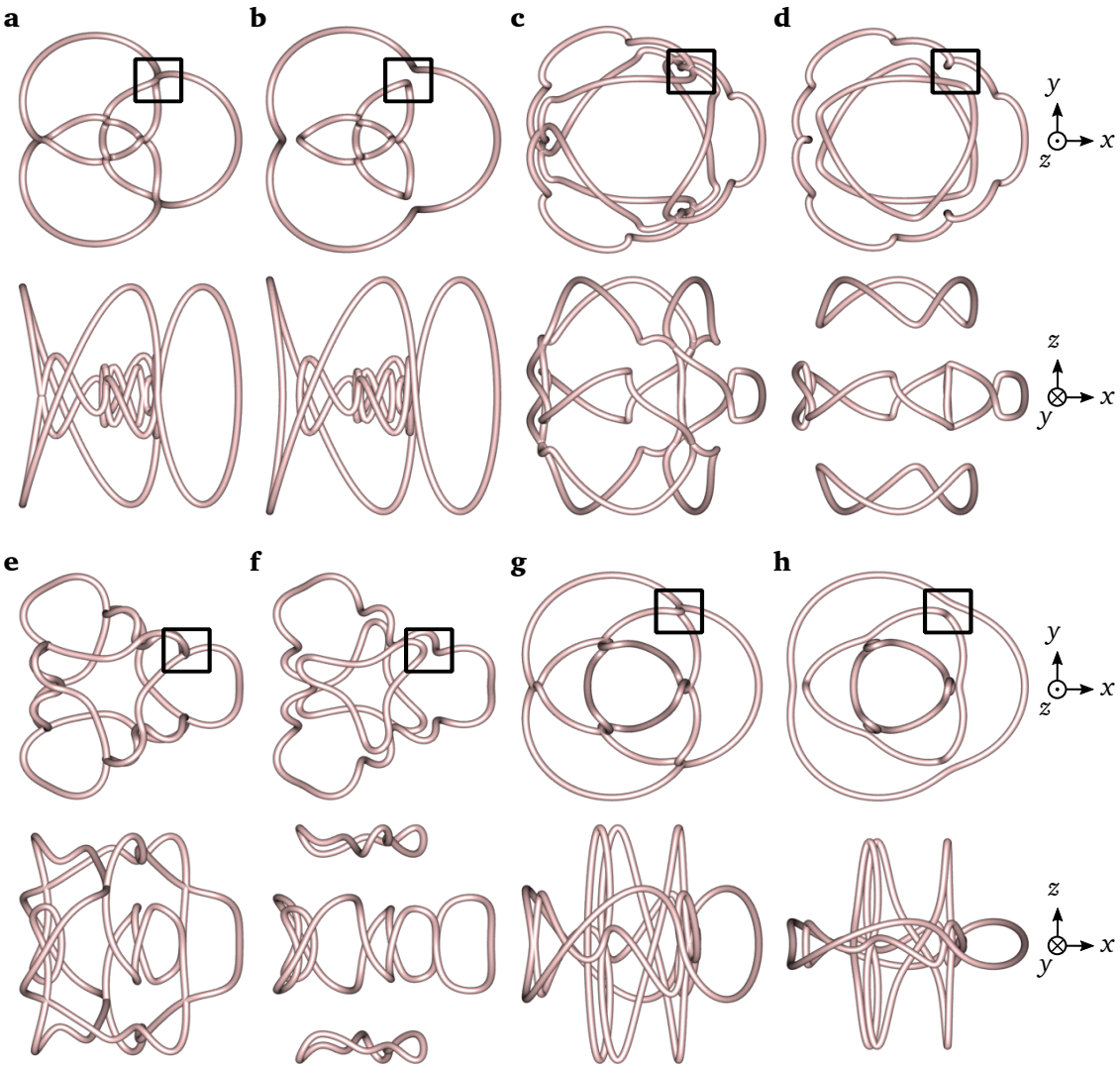


Figure 4.4: **Topological reconnections of the Borromean rings**. Top and front view of the reconnection events showing how the topology of the Borromean rings is broken up by the variation of the stretching parameters $a$ and $b$. One of the topological event has been highlighted with a black square in each plot. While keeping one parameter fixed ($b = 0.5$), $a$ is increased or decreased to a limit value: (a) when $a = 0.862$, the Borromean rings intersect at 6 points and (b) for the larger value $a = 0.890$ the Borromean rings split into 3 disjoined loops; (c) when $a = 0.169$ the rings start reconnecting and (d) for the smaller value $a = 0.148$ the loops are disjoined again. Similarly, while keeping the other parameter fixed ($a = 0.5$), $b$ is increased or decreased to a limit value: (e) when $b = 1.637$, the Borromean rings intersect at six points and (f) by increasing $b = 2.2$ three disjoined loops form; (g) when $b$ is decreased the Borromean rings reconnect when $b = 0.15$ and (h) three disjoined loops appear when $b = 0.05$.

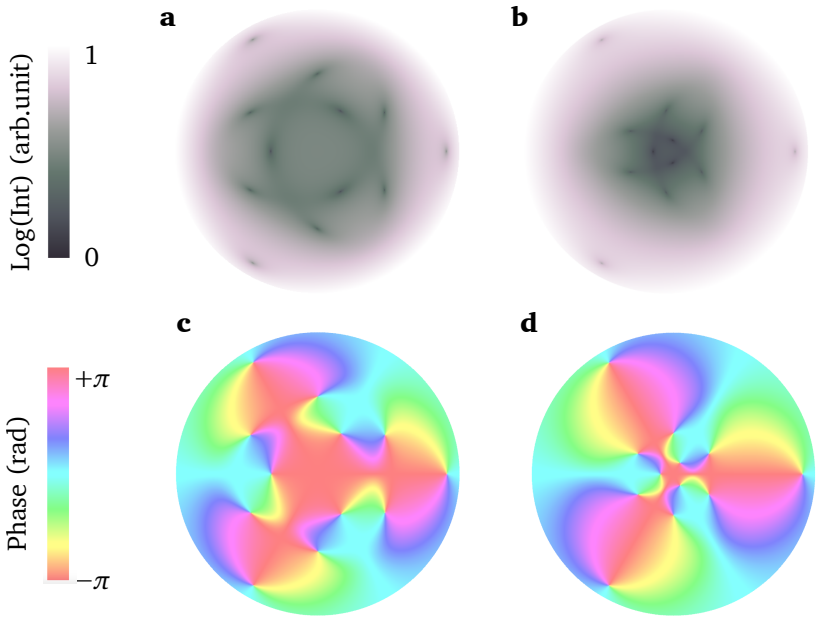


Figure 4.5: **Optimisation of the Borromean rings hologram**. Intensity and phase of the field $\psi_{2D}^{2,3,3}$, at $z = 0$. The field in (a) and (c), for which $a = b = 0.5$, is optimised compared to the field in (b) and (d), for which $a = b = 1$: the intensity between two distinct optical vortices is larger in (a) than in (b); the distances between two distinct optical vortices are larger in (c) than in (d).

the topology of the optical field is that of the desired link. The preferred approach is to track the vortex lines (§ 3.5.1) and analyse their behaviour by fixing one parameter and varying the other parameter. Such numerical search demonstrates that the topology of the Borromean rings is preserved in the following ranges: $0.169 < a < 0.862$ and $b = 0.5$, $a = 0.5$ and $0.15 < b < 1.637$. The series of events when the Borromean Rings dissolve is shown in Figure 4.4. Figures 4.4 (a)–(b) and (c)–(d) show what occurs when $a$ is largely increased or decreased when $b = 0.5$; in both cases the Borromean rings split into three unlinked loops. On the other hand, Figure 4.4 (e)–(f) and (g)–(h) show three unlinked loops in other conformations when $b$ is largely increased or decreased and $a = 0.5$.

The existence of the range for $a$ and $b$ when the topology of the links is preserved does not imply that other physical quantities, such as the intensity of the beam or the distances between the vortices, are invariant as well. We can therefore take advant-

age of such behaviour with the aim of optimising knotted optical fields and assessing the most favourable values of $a$ and $b$ for experimental implementation. From an experimental point of view, it is hard to distinguish two vortex lines close to each other since they belong to a region of darkness which can easily be in the noise levels of the CCD camera and, therefore, impossible to detect. An optimisation routine to overcome this problem was introduced in [18, 59], where a cost function-based algorithm was implemented in order to automatically search the Laguerre-Gaussian coefficients characterised by high intensity between optical vortex pairs. We propose an alternative optimisation method that consists in choosing the parameters $a$ and $b$ for which the distance between the vortex points on the focal plane $z = 0$ and the intensity around them are large. Figure 4.5 (a) shows that the intensity at $z = 0$ improves for $a = b = 0.5$ compared to Figure 4.5 (b) representing $a = b = 1$. For $a = b = 0.5$ the vortices also have larger distances. This method only takes into account the focal plane $z = 0$, but it could also be applied to the whole knotted volume. We employed this optimisation method in [137] to generate and detect the figure-eight knot ($l = 2$, $s = 3$, $r = 2$) for the first time in experiments. This function will be studied in detail in § 4.4.

### 4.2.3 The extension of the optical vortex knots table

After reporting the case study of the Borromean rings, the aim of this section is to apply the polynomial beam propagation to the rest of the lemniscate knots. Therefore, the first step is to determine the values of $a$ and $b$ for which the desired knots and links form in propagating light beams. However, our proposed construction will not always be successful and for the failing cases we will try to over homogenise the corresponding Milnor polynomial.

As an example, we consider the case $l = 2$, $s = 7$, $r = 2$. The associated Milnor polynomial embeds the lemniscate knot $8_9$ for $a = b = 1$. When its initial condition analogous to (4.4) is paraxially propagated, the forming knot is $6_2$; therefore this dif-

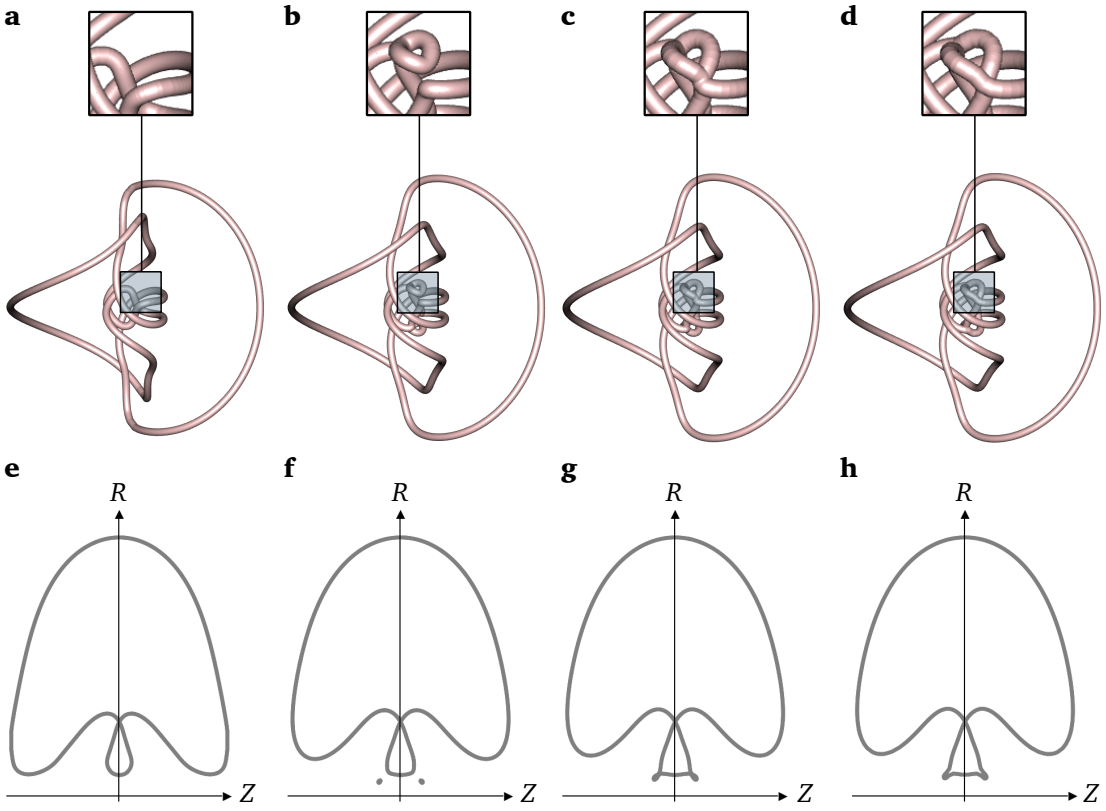


Figure 4.6: **Topological transitions induced by the over homogenisation**. (a) The optical lemniscate knot $l = 2$, $s = 7$, $r = 2$ embeds the knot $6_2$ for $a = b = 1$; the knot forming from its corresponding Milnor polynomial is the $8_9$. (d) The expected topology is generated by choosing the level of over homogenisation $n = 8$. The intermediate steps of the topology transition are (b) the formation of two loops for $n = 5$, and (c) the reconnection of such loops with the knot $6_2$ for $n = 7$. (e)–(h) The series of events is evident by looking at the orthogonal projections of the 3D lines onto the $RZ$-plane.

fers from its mathematical counterpart. The generation of the optical knot $6_2$ was not predicted by the theory of mathematical lemniscate knots of Bode. The explicit construction of new mathematical knotted fields is a promising result. Even though this type of knot cannot be explicitly constructed with the methods described in § 3.4, the knot $6_2$ falls in the definition of lemniscate knots [132]. This is due to the fact that the braid word associated with this knot is $(\sigma_1\sigma_2\sigma_3\sigma_4\sigma_2^{-1}\sigma_3^{-1})^2$, which is a characteristic of lemniscate knots. In order to generate the optical knot $8_9$, we add the multiplication factor $(1+R^2)^n$ to its corresponding Milnor polynomial and we choose the level

of over homogenisation $n = 8$. As a result, the knot $8_9$ forms under paraxial propagation. Figure 4.6 shows the topology transition between the optical knot $6_2$ and $8_9$ for increasing values of $n$. The knot $6_2$ corresponding to the standard homogenised field is shown in Figure 4.6 (a). Two additional rings appear for the level of over homogenisation $n = 5$ shown in Figure 4.6 (b), which reconnect when $n = 7$ (Figure 4.6 (c)), and form the desired topology of the knot $8_9$. Figure 4.6 (d) shows this knot when $n = 8$. Such transition is evident in Figure 4.6 (e)–(h) where the lemniscate figures on

| Milnor knot type | $l$ | $s$ | $r$ | $a = b$ | prefactor $n$ | Optical knot type |
|---|---|---|---|---|---|---|
| $4_1$ | 2 | 3 | 2 | 1 | no | same |
| $6_2^3$ | | | 3 | 1 | no | same |
| $8_{18}$ | | | 4 | 1 | no | same |
| $10_{123}$ | | | 5 | 1 | no | same |
| $6_3$ | | 5 | 2 | 1 | 5 | same |
| $8_9$ | | 7 | 2 | 1 | no | $6_2$ |
| $8_9$ | | 7 | 2 | 1 | 8 | same |
| $10_{17}$ | | 9 | 2 | 0.5 | no | $3_1$ |
| $10_{17}$ | | 9 | 2 | 1 | no | $8_7$ |
| $5_1^2$ | 3 | 4 | 2 | 0.5 | no | same |
| $9_{40}$ | | | 3 | 0.5 | no | same |
| $7_7$ | | 5 | 2 | 1 | no | same |
| $9_{31}$ | | 7 | 2 | 0.5 | no | $3_1$ |

Table 4.1: **Lemniscate knots and links.** The left column shows the knot (or link) type arising from the Milnor polynomials of [132]; $l, s, r$ are the lemniscate parameters associated to the curves; $a$ and $b$ are the stretching parameters found by numerical search; $n$ is the level of over homogenisation. The right column highlights whether the expected optical lemniscate knot (or link) appears under paraxial propagation; when the topology of the curve is different from the one arising in its Milnor counterpart, the knot (link) type is reported.

the $RZ$-plane are plotted for different values of $n$. These graphs give a good overview of what is going on, even though a satisfactory explanation of why the inclusion of the multiplying factor gives the correct topology has not been found.

The values of $a$, $b$ and $n$ corresponding to a large variety of lemniscate knots are determined and the results are reported in Table 4.1. The table shows that by exploring such parameter space it is possible to build new knotted and linked optical fields, some of which are not predicted by the mathematical theory, as for the knot $6_2$, but also for the knot $8_7$.

This section has constructed optical fields embedding lemniscate knots and links through polynomial beam propagation and has explored the parameter space in which their topology is preserved. Although polynomial optical fields satisfy the paraxial wave equation, they are not physical beams, due to the fact that they diverge at infinity and therefore cannot be reproduced in the laboratory. The next section will explore how to embed knotted polynomials into two different types of beams suitable for practical implementation.

## 4.3 Physical beams for knotted polynomials

In the previous section, optical fields embedding knotted and linked vortex lines were built explicitly in the form of polynomials. Due to superoscillations [143], any knotted polynomial beam is characterised by low amplitude in the volume where the knotted structure exists. The intensity distribution surrounding the knotted structure is very weak and the majority of the energy is concentrated around the volume of the knot. The knotted structure arising from superoscillations creates a practical challenge for whoever wants to measure such complicated structures in light beams.

A way to overcome the problem was proposed in [18], where the $z = 0$ plane of a knotted polynomial was multiplied by the Gaussian factor $\mathrm{e}^{-R^2/(2w^2)}$. It was shown that the topology of the nodal lines of the propagating beam did not change when the waist $w$ was sufficiently large. The success of the Laguerre-Gaussian basis is due to

the simplicity of its Fourier transform, given by (2.13). This property makes LG-beams suitable for experiments involving reimaging through lenses [79].

Here we show that the LG-basis is only one of the possible family of beams in which optical vortex knots can be embedded. We demonstrate that all the knots and links embedded in polynomial beams in the previous section can be created into superpositions of Bessel functions of the first kind. Even though the treatment of Bessel functions can have a complicated behaviour, in § 4.3.1 we solve the inverse problem given by the diffraction integral to evaluate the initial conditions for the knotted beams to propagate. In § 4.3.2 the trefoil knot is built explicitly into LG-modes and propagating generalised Airy disks; their corresponding holograms in Fourier space are also presented.

### 4.3.1 Solution of inverse focusing problems

A method to solve the inverse problem for focused fields is presented. This answers the question "What amplitude and phase profile are required in Fourier space to generate a beam whose behaviour around the optical axis can be represented by a polynomial?". The method is based on Nijboer's result (§ 2.1.5).

The diffraction integral (2.42) shows that a paraxial beam whose complex amplitude is represented by a Zernike aperture mode (2.14) propagates in the focal plane $z = 0$ as a Bessel function of the first kind divided by the radius. From the definition of Bessel function of the first kind

$$\mathrm{J}_n(r) = \sum_{j=0}^{\infty} \frac{(-1)^j}{(j+n)!\,j!} \left(\frac{r}{2}\right)^{n+2j}, \tag{4.6}$$

it follows that

$$\frac{\mathrm{J}_{n+1}(R)}{R} = \sum_{j=0}^{\infty} \frac{(-1)^j}{2(j+n+1)!\,j!} \left(\frac{R}{2}\right)^{n+2j}. \tag{4.7}$$

The Taylor expansion for each function (4.7) about $R = 0$ of order $N$ is

$$\frac{\mathrm{J}_{n+1}(R)}{R} \sim \sum_{j=0}^{(N-n)/2} \frac{(-1)^j}{2(j+n+1)!\,j!} \left(\frac{R}{2}\right)^{n+2j}. \tag{4.8}$$

The functions (4.8) up to order $n = N$ are the following

$$\begin{pmatrix} \frac{J_1(R)}{R} \\ \frac{J_2(R)}{R} \\ \vdots \\ \frac{J_{N+1}(R)}{R} \end{pmatrix} \sim \begin{pmatrix} 1/2 & 0 & -1/16 & 0 & \cdots & 0 & \frac{i^N 2^{-N-1}}{(N/2+1)!(N/2)!} \\ 0 & 1/8 & 0 & -1/96 & \cdots & \frac{i^{N-2}2^{-N}}{(N/2+1)!(N/2-1)!} & 0 \\ \vdots & \vdots & \vdots & \vdots & \cdots & \vdots & \vdots \\ 0 & 0 & 0 & 0 & \cdots & 0 & \frac{2^{-N-1}}{(N+1)!} \end{pmatrix} \begin{pmatrix} 1 \\ R \\ \vdots \\ R^N \end{pmatrix}. \tag{4.9}$$

The matrix associated to this linear system is upper triangular, this means that higher order Bessel functions only influence higher orders terms in $R$. It is possible to invert the system and express each power of $R$ as a finite sum of Bessel functions of the first kind. This simple mathematical result can be used to structure beams represented locally by polynomials in $R, e^{i\phi}, z$. In fact, when the polynomial describing the beam in the focal plane $z = 0$ has only powers in $R$ up to order $N-2$, it can be expressed as a finite sum of Bessel functions of the first kind by the approximation (4.9). As a consequence, the propagation integral can be inverted via the result (2.42), which gives the sum of Zernike aperture modes in Fourier space corresponding to the sum of Bessel functions describing the focal plane. This method relies on the fact that the Taylor coefficients contain local information, while the Fourier coefficients contain global information on the function [144, 145]. We will apply this method to generate the Milnor polynomial corresponding to the trefoil knot in the focal plane in the next section (§ 4.3.2).

### 4.3.2 Comparison between Gaussian envelopes and generalised Airy patterns

In order to elucidate the difference between the Laguerre-Gaussian envelope and the sum of Bessel functions, we consider the trefoil knot case as an explicative example. The Milnor polynomial function for the trefoil knot is given by the torus knots formula (3.12) in complex coordinates $(u, v)$ and the stereographic projection (3.10), where

$(n,m)=(3,2)$ and $z=0$, as follows

$$f_{\text{Milnor}}^{\text{trefoil}}(R,\phi,0)=1-R^2-R^4+R^6-8R^3\mathrm{e}^{3\mathrm{i}\phi}. \tag{4.10}$$

The 3D paraxial polynomial propagated from this function gives an optical vortex line in the form of a trefoil knot. Such polynomial was enveloped in a Gaussian beam in [18] by taking the product of (4.10) with $\mathrm{LG}_{00}(R,\phi;w)$ defined in (2.9). The polynomial field modulated by the Gaussian factor can be naturally decomposed into Laguerre-Gaussian modes characterised by the same waist. Therefore, polynomial beams correspond to superposition of LG-modes in the limit of infinitely large $w$. The details of the proof showing how a sum of Laguerre-Gaussian modes limits to the paraxial polynomial for large $w$ was reported in the supplementary information of [18]. When $w$ decreases, the optical field is strongly influenced by the Gaussian factor. If $w$ is not large enough to resemble polynomial beams, additional vortex lines appear around the knotted structure and, eventually, for smaller $w$ such lines reconnect and the knotted or linked topology is lost [18, 19]. The right balance between the undesired reconnection events of the vortex lines for small $w$ and the low intensity features of the beam for large $w$ is required to generate knotted fields whose complex amplitude is detectable in experiments. Thus, the success of the beam's topology depends on the ratio between $w$ and the size of the knot, which must be carefully chosen. The value $w=1.2$ was adopted in [18] to create the trefoil knot experimentally from an optimised version of function (4.10). Figure 4.7 (a) and (e) show, respectively, the intensity and the phase of the theoretical beam for $z=0$ and $w=1.2$; the phase singularities around the origin exhibit the desired Milnor profile, whereas the external part has a Gaussian behaviour.

For completeness, we evaluate the Fourier transform of the LG-sum from [18], which is

$$\begin{aligned}\widetilde{\psi}_{\text{trefoil}} = {} & (1-w^2-2w^4+6w^6)\mathrm{LG}_{00}(\rho,\varphi;w_0)-w^2(1+4w^2-18w^4)\mathrm{LG}_{10}(\rho,\varphi;w_0)\\ & -2w^4(1-9w^2)\mathrm{LG}_{20}(\rho,\varphi;w_0)+6w^6\mathrm{LG}_{30}(\rho,\varphi;w_0)+8\sqrt{6}\,\mathrm{i}\,\mathrm{LG}_{03}(\rho,\varphi;w_0),\end{aligned} \tag{4.11}$$

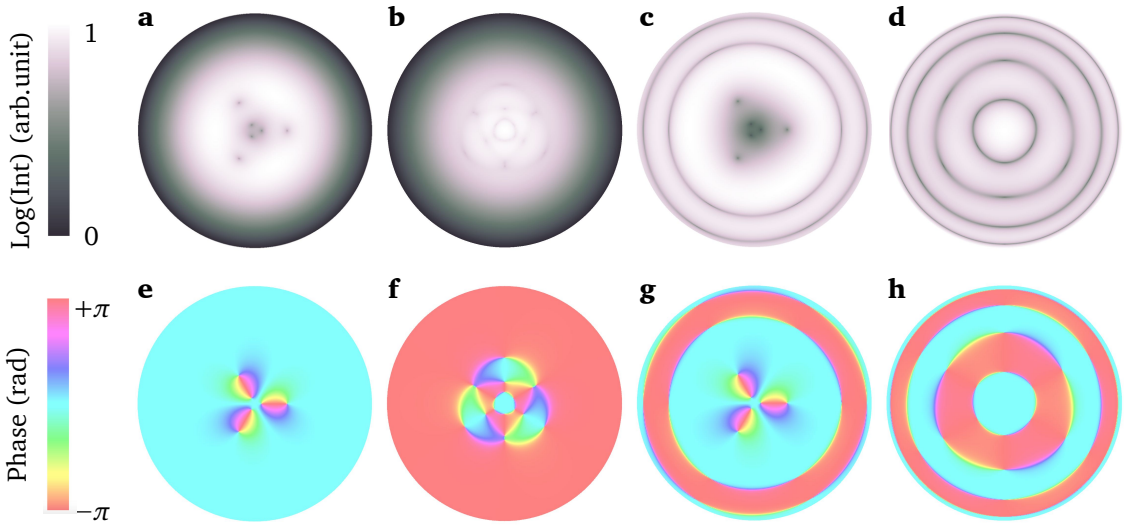


Figure 4.7: **Practical implementation of knotted polynomial beams**. The Milnor profile encoding the trefoil knot and expressed by equation (4.10) is generated locally around the optical axis of two types of beams. (a) and (e) show the intensity and phase of the Milnor pattern enveloped in a Gaussian beam [18]. (c) and (g) show the intensity and phase of the Milnor pattern in the generalised Airy pattern, represented by (4.13). These beams can be generated with holograms in Fourier space. The Gaussian envelope is generated by the LG-beams sum (4.11) with intensity (b) and phase (f). The Bessel sum is generated by the sum of Zernike polynomials (4.14) with intensity (d) and phase (h).

where the waist of the Gaussian envelope in Fourier space is $w_0 = 1/w$. The beam in Fourier space rescales with $w_0$ (note that the the coefficients of the LG-modes depend on $w$, not $w_0$). Figure 4.7 (b) and (f) show, respectively, the intensity and the phase of (4.11) for $w = 1.2$.

We now embed the Milnor profile (4.10) into a sum of Bessel functions of the first kind in the form $\mathrm{J}_{n+1}(R)/R$. Each function $\mathrm{J}_{n+1}(R)/R$ is characterised by oscillations in the amplitude similar to the Airy pattern; they incorporate an implicit lengthscale determined by the position of the first zeros in the amplitude, therefore determining a disk area around the origin. These are, effectively, the generalisation of the Airy disk. The mathematical definition of Bessel functions (4.6) does not incorporate explicit lengthscales; we can assume that lengths are expressed in units of inverse radial optical

waveumber $k_r^{-1} = 1$. A superposition of such functions also presents a disk around the origin and amplitude oscillations in the outer region. By tailoring the coefficients in the sum it is possible to structure a Milnor-like pattern inside the disk. We control the ratio between the size of the disk and the size of the trefoil knot by manually including a dimensionless scaling parameter $s$ as follows. We replace all occurrences of $R$ in (4.10) with $R/s$. Explicitly, the rescaled Milnor polynomial is

$$f_{\text{Milnor}}^{\text{trefoil}}(R,\phi;s) = 1 - \frac{R^2}{s^2} - \frac{R^4}{s^4} + \frac{R^6}{s^6} - 8\frac{R^3}{s^3}\mathrm{e}^{3\mathrm{i}\phi}. \tag{4.12}$$

The method described in § 4.3.1 is used to calculate an optical field whose Taylor expansion of order $N > 6$ about $R = 0$ is (4.12). By solving the system of equations (4.9) with $N = 8$, we evaluate the following finite sum of Bessel functions of the first kind

$$\begin{aligned}\Psi^{\text{trefoil}} = {} & 2\tfrac{\mathrm{J}_1(R)}{R} + 6(-8s^{-2}+1)\tfrac{\mathrm{J}_3(R)}{R} + 10(-384s^{-4}-24s^{-2}+1)\tfrac{\mathrm{J}_5(R)}{R} + 14(46080s^{-6} \\ & - 1920s^{-4} - 48s^{-2} + 1)\tfrac{\mathrm{J}_7(R)}{R} + 18(322560s^{-6} - 5760s^{-4} - 80s^{-2} + 1)\tfrac{\mathrm{J}_9(R)}{R} \\ & - 3072s^{-3}\mathrm{e}^{3\mathrm{i}\phi}\tfrac{\mathrm{J}_4(R)}{R} - 18432s^{-3}\mathrm{e}^{3\mathrm{i}\phi}\tfrac{\mathrm{J}_6(R)}{R} - 61440s^{-3}\mathrm{e}^{3\mathrm{i}\phi}\tfrac{\mathrm{J}_8(R)}{R}. \end{aligned} \tag{4.13}$$

Expression (4.13) shows that all the Bessel functions have fixed lengths but their superposition can be manipulated via the parameter $s$. When (4.13) is Taylor expanded in $R$ about 0 and all its occurrences in $R$ are substituted by $Rs$, the resulting expression is the polynomial (4.10) and higher order terms in $R$, which are directly proportional to $s$. This means that, when $s$ is small, the higher order terms are negligible and the field (4.13) behaves like a polynomial beam on the plane $z = 0$, but also under propagation. As mentioned previously, polynomial beams have low intensity features which make them unfavourable for experimental purposes. On the other hand when $s$ is large, the knot-pattern falls outside the generalised Airy disk and the outer oscillations dominate and destroy the topology of the optical vortices. The right balance between the small-$s$ and large-$s$ regimes gives a Milnor pattern on the focal plane enclosed in a region where the intensity is sufficiently high to be detected in experiments. The optimal value of $s$ is found as follows. It can be proved that the field (4.13) gives a

trefoil knot under propagation by inverting the diffraction integral (2.42). The Fourier transform of (4.13) is expressed as a sum of Zernike aperture modes and is defined on the disk parametrised by the dimensionless coordinates $0 \leq \rho \leq 1$, $0 \leq \varphi < 2\pi$. This is explicitly

$$\begin{aligned}\widetilde{\Psi}^{\text{trefoil}} = {} & 2s^6 \mathrm{Z}_{0,0}(\rho,\varphi) - 6s^4(-8+s^2)\mathrm{Z}_{2,0}(\rho,\varphi) + 10s^2(-384-24s^2+s^4)\mathrm{Z}_{4,0}(\rho,\varphi) \\ & - 14(46080-1920s^2-48s^4+s^6)\mathrm{Z}_{6,0}(\rho,\varphi) + 18(322560-5760s^2-80s^4 \\ & + s^6)\mathrm{Z}_{8,0}(\rho,\varphi) - 3072\mathrm{i}s^3\mathrm{Z}_{3,3}(\rho,\varphi) + 18432\mathrm{i}s^3\mathrm{Z}_{5,3}(\rho,\varphi) - 61440\mathrm{i}s^3\mathrm{Z}_{7,3}(\rho,\varphi).\end{aligned} \tag{4.14}$$

We propagate (4.14) by ENZ-theory (§ 2.2.2) via the result (2.47) and we find that the field in the focal volume embeds the trefoil knot when $s = 2.2$ (this value is not unique and could be tailored for experimental optimisation). Figure 4.7 (c) shows the intensity of $\Psi^{\text{trefoil}}$ for $s = 2.2$, its phase is plotted in Figure 4.7 (g). Figure 4.7 (d) shows the intensity of $\widetilde{\Psi}^{\text{trefoil}}$ for $s = 2.2$, its phase is plotted in Figure 4.7 (h). The Zernike sum (4.14) corresponds to a disk hologram in Fourier space which could be implemented in an experiment analogous to [18]. Similarly to the parameter $w$ in the Laguerre-Gaussian sum, the value of $s$ influences the 3D topology of the beam propagating along $z$. Larger values of $s$ could be considered if higher order Bessel functions were included in the sum (4.13) by choosing a larger $N$, this would make the area of the generalised Airy disk larger.

In this section, we demonstrated that the polynomial fields from § 4.2 can be embedded in either Laguerre-Gaussian modes or Bessel functions of the first kind for practical purposes. We showed how to solve the inverse problem for these families of beams and we have calculated their respective holograms. Only the case study of the trefoil knot was presented, but this technique generalises to all the other paraxial knots. In the next section, theory and experiments of the implementation of the figure-eight knot in Laguerre-Gaussian beams will be presented, accompanied by a new topological analysis of the structure of the beam around the knotted line.

## 4.4 Seifertometry

This section introduces the analysis of the Seifert surfaces associated to knotted beams of light, whose physical properties are analysed as topological objects in their own right in a process we call *seifertometry*.

Optical vortex knots determine the structure of the overall beam; in particular phase contours are shaped into Seifert surfaces. The reason why the experimental measurement and analysis of phase contours has not been performed yet is due to the harmonic nature of knotted light beams. In our theoretical treatment the periodicity does not appear because the term $\mathrm{e}^{\mathrm{i}(kz-\omega t)}$ is factored out (§ 2.1.3). The effect of this factor on the surfaces of constant phase can be visualised as a periodic sheeting of wavelength scale, which complicates the experimental detection. Here we demonstrate that through the method we call seifertometry it is possible to measure and analyse the Seifert surfaces of knotted beams by means of polarimetry.

The optical vortices of a homogeneously polarised beam $\psi^{\mathrm{knot}}$ become points of perfect circular polarisation, C-lines (§ 3.1.2), when the beam is circularly polarised and superimposed to a second beam of opposite handedness and free from phase singularities (such as a Gaussian beam). The optical vortex knots previously generated [16, 18] employed uniformly linearly polarised transverse beams. When a circularly polarised beam is used instead, its coherent superposition with the second beam implies that knotted lines of polarisation singularities do form. This can be understood analytically as the propagating initial condition $\boldsymbol{E}_{2\mathrm{D}} = \mathrm{e}^{-R^2/(2w^2)}\left(\psi_{2\mathrm{D}}^{\mathrm{knot}}\widehat{\boldsymbol{e}}_{\pm} + \widehat{\boldsymbol{e}}_{\mp}\right)$ that generates a knotted C-line surrounded by space-varying polarisation states in 3D space. This procedure suggests that the topological properties of the volume around polarisation knots can be revealed by means of polarimetry and, as a consequence, the Seifert surfaces bounded by the knotted line can be analysed.

Seifertometry relies on the fact that the polarisation state of each point in space can be extrapolated by the evaluation of the Stokes parameters defined in (2.32). The

Seifert surfaces correspond to the contours of the azimuthal angle $\alpha$ of the Poincaré sphere (§ 2.1.7), which indicates the orientation of the polarisation ellipse. Hence, $\alpha$ can be identified as the argument of the scalar field $S_1 + \mathrm{i}S_2$, whose singularities correspond to C-points (§ 3.1.2). Contrarily to the phase contours, the surfaces of constant $\mathrm{Arg}(S_1 + \mathrm{i}S_2)$ are not dependent on the periodic factor, meaning that they can be experimentally detected by means of polarimetry. This approach is ideal for the detection of Seifert surfaces and to reveal the undiscovered properties of knotted light beams, either theoretically or experimentally.

The polarisation knots and links and the seifertometry method described above were implemented experimentally in [137]. The generation scheme used a folded Sagnac interferometer [146, 147] to produce a beam with distinct opposite circular polarisations, one of which embedded an optical vortex knot, and the other consisting of a Gaussian beam. Each beam was structured by phase holograms displayed on a spatial light modulator, which simultaneously modulated the beams' intensity and phase profiles [18,59,148] given by $\boldsymbol{E}_{2\mathrm{D}}$. As predicted, the resulting beam embedded knotted C-lines upon free-space propagation and its polarisation state was spatially dependent. The beam's transverse polarisation distribution was reconstructed by measuring the Stokes parameters with a CCD camera. The sampled values were then used to render the Seifert surfaces through interpolation techniques. The genus of the surfaces was extrapolated for each value of the azimuthal angle $\alpha$ by the method reported in § 3.5.3 and the experimental results were compared with the theoretical predictions.

This experimental setup was used to implement seifertometry on the Hopf link, trefoil knot and cinquefoil knot, which are the torus knots previously generated as optical vortex lines [18]. The same analysis was also performed on the figure-eight knot, which is a non-torus knot. The latter was experimentally generated for the first time using a hologram function optimised with the technique reported in § 4.2. Explicitly, the figure-eight knot is the lemniscate knot $l = 2$, $s = 3$, $r = 2$ and its optical

field at $z = 0$ is given by

$$\begin{aligned}\psi_{2D}^{2,3,2}(R,\phi;a,b) = {} & 16-12a^2+3b^2-2(16+12a^2-3b^2)R^2+2a\mathrm{e}^{-2\mathrm{i}\phi}R^2(4a^2+12b \\ & +3b^2)+2a\mathrm{e}^{2\mathrm{i}\phi}R^2(4a^2-12b+3b^2)+4a\mathrm{e}^{-2\mathrm{i}\phi}R^4(4a^2+3b^2) \\ & +4a\mathrm{e}^{2\mathrm{i}\phi}R^4(4a^2+3b^2)-4b^3\mathrm{e}^{-4\mathrm{i}\phi}R^4+4b^3\mathrm{e}^{4\mathrm{i}\phi}R^4+2(16+12a^2 \\ & -3b^2)R^6+2a\mathrm{e}^{-2\mathrm{i}\phi}R^6(4a^2-12b+3b^2)+2a\mathrm{e}^{2\mathrm{i}\phi}R^6(4a^2+12b \\ & +3b^2)+(-16+12a^2-3b^2)R^8. \end{aligned} \tag{4.15}$$

The intensity and phase profiles of (4.15) are optimised for $a = 0.6$, $b = 1$ and such function was embedded in a Gaussian beam of width $w = 2.19$[2]. Figure 4.8 (a) shows the reconstructed experimental C-lines in the conformation of the figure-eight knot, and its theoretical predictions in Figure 4.8 (b),with their respective top views. The azimuthal angle $\alpha$ at $z = 0$ is plotted with a 'hue' colour map (note that so far this colour scheme was used to represent the phase of scalar fields), which gives information about the polarisation ellipse orientation on the plane. This colour representation gives an immediate analogy between C-points in polarised beams and optical vortices of generic scalar fields. More details on the experimental data of the polarisation knots and links can be found in [137].

We now compare the seifertometry results of the figure-eight knot for the propagating theoretical field and the experimental data. The rendered Seifert surfaces for values of the azimuthal angle $\alpha = \{\pm\pi, -\pi/2, 0, +\pi/2\}$ are shown in Figure 4.8 (c) for the experimental data and the theoretical field in Figure 4.8 (d). It can be observed that the experimental surfaces considerably differ from theory. The details of the Seifert surfaces topological behaviour for different values of $\alpha$ are extrapolated by calculating their genus. Figure 4.9 (a) reports the genus values as a function of the azimuthal angle in theory and experiments. Theoretically, the genus takes the minimal value of $g = 1$ for each of the Seifert surfaces, except in small intervals around $\alpha = 0 \cup \alpha = \pm\pi$ for which it is $g = 2$ (the genus is doubled when the surfaces are

[2]The definition of the Gaussian beam in [137] differs from our definition by a factor of 2, meaning that $\mathrm{e}^{-R^2/w^2}$ and $w = 1.55$.

joined as explained in the method § 3.5.3). An illustration of the genus discontinuities close to $\alpha = 0 \cup \alpha \pm \pi$ is shown in Figure 4.9 (b). As $\alpha$ increases through 0 (and $\pm\pi$), two bridges appear on the Seifert surfaces and then break through diablos situated at 3D critical points (their 2D version can be observed in Figure 4.8 (b) corresponding to

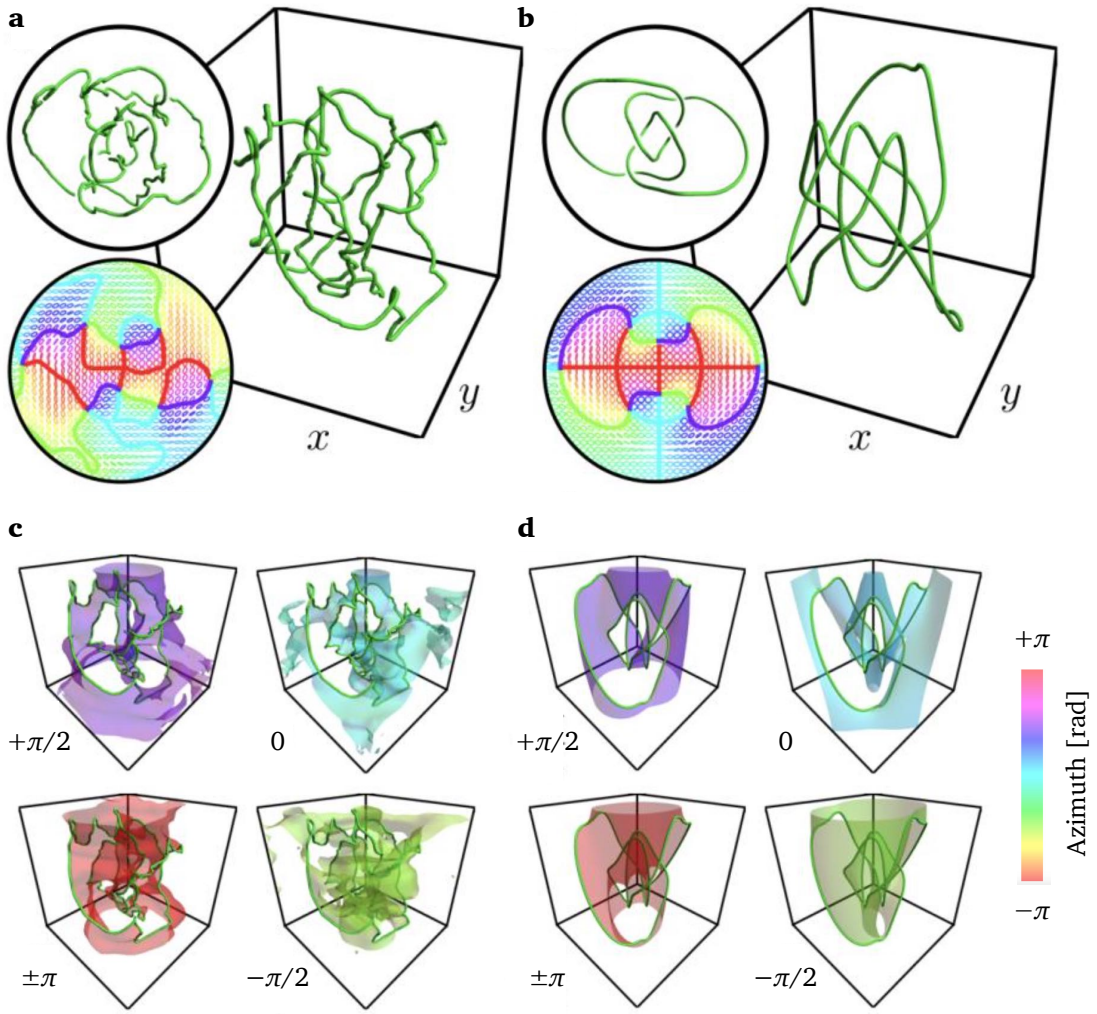


Figure 4.8: **Seifertometry of the optical figure-eight knot**. The figure-eight knot arises as the C-line of a polarised beam. (a) is reconstructed from the experimental data and (b) is the theoretical prediction. The contours $\alpha = \{\pm\pi, -\pi/2, 0, +\pi/2\}$ of the azimuthal angle at the focal plane are reported together with the colour coded polarisation ellipses and the top views of the knots. The Seifert surfaces of the experimental and theoretical knots are shown, respectively, in (c) and (d), where they are labelled by the their corresponding $\alpha$. Image from [137].

the cyan saddle points). Experimentally however, values of the genus from 2 up to 16 are measured. This indicates that the experimental Seifert surfaces are disrupted by the formation of critical points of the azimuthal angle, each of which causes the genus to increase. The formation of holes/bridges on the surfaces is caused by experimental imperfections such as aberrations, which are sufficiently small to ensure the existence of the figure-eight knot in the polarisation singularity lines, but generate critical points of the azimuth in the rest of the 3D volume.

The agreement of the experimental Seifert surfaces with the theoretical prediction seems to be even more challenging than the creation of knotted singular lines. Even

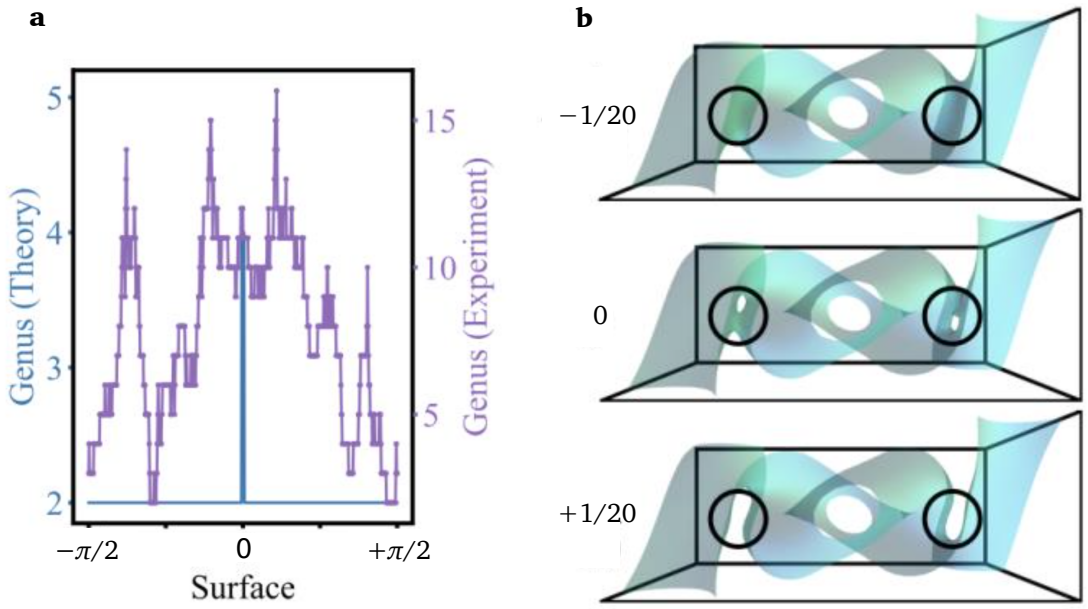


Figure 4.9: **Genus analysis of the figure-eight knot**. (a) Numerically extracted genus of the closed surfaces which are the join of pairs of Seifert surfaces with azimuth values different by $\pi$ (only a single value of $\alpha$ is shown along the horizontal axis). In the theoretical predictions, the genus remains constant except in the vicinity of the $\alpha = 0$ surface, where it spikes due to the addition of two holes in the surface. The topological event occurring in the vicinity of this value is shown in (b), where the formation of the two holes is shown by plotting the surfaces $\alpha = -1/20, 0, +1/20$. This topological event reveals the presence of a critical point of the azimuthal angle in the optical field. The experimental data shows a much more complicated behaviour. Image from [137].

though the experimental genus is not consistent with the theory, the knotted C-lines show the correct topology meaning that the knot type is preserved under the modifications of the Seifert surfaces. Seifertometry reveals the level of topological complexity of the optical field, which goes beyond the conventional reconstruction of polarisation singularity lines.

## 4.5 Discussion

In this chapter the theory of optical vortex knots in paraxial light was extended to the family of lemniscate knots and links and their properties were investigated in some detail. A new type of beam, in which knots can be embedded, was engineered with Zernike polynomials and ENZ-propagation theory. In the final part, the theory of knotted scalar fields was extended to polarised light by creating knotted C-lines in Laguerre-Gaussian superposition of beams. A topological analysis of the Seifert surfaces of these beams was also introduced.

The explicit construction of a large variety of optical vortex lines is an important step forward to fully understand the nature of these mysterious topological objects. We went beyond the paraxial optical vortex knots and links previously implemented [18,58] by applying the lemniscate knots and links algebraic functions [132] to optical fields (§ 4.2). We found that some lemniscate knots fail to appear under paraxial propagation, such as the knot $10_{17}$ ($l=2, s=9, r=2$) or the $9_{31}$ ($l=3, s=7, r=2$). We still do not have a general understanding of how and why some knots and links appear under paraxial propagation of the Milnor slice in the plane $z=0$, and some others do not. This was a problem in [18] and, despite the significant extension beyond the work of Dennis *et al.* reported in this chapter, a satisfactory explanation of why a paraxial propagating light beam generated from a Milnor function used as a hologram is still a mystery. Even though not all the lemniscate optical knots appear under propagation, the results presented in § 4.2 suggest that by improving the numerical methods and by modifying the Milnor function appropriately (analogously to

the over homogenisation method of King [58]), it could be possible to successfully construct a larger number of lemniscate knots. New knots could be generated by using an over homogenisation function that differs from $(1+R^2)^n$. For example, the factor $(c+R^2)^2$, where $c$ is a real constant, seems to aid the topology transfer between the Milnor function and the optical field for the failing cases. The vortex lines are altered by the presence of the over homogenisation factor and further investigation could reveal the relationship between this procedure and the topology of the optical fields' nodal lines.

The theory of knotted and linked phase singularities could be extended further by paraxially propagating other knots and links that do not fall in the lemniscate class, such as those constructed (only mathematically) by Bode in [133]. It is clear that the methods for the construction of optical knots and links have big potential for improvement. For instance in § 4.2.3, we generated the knots $6_2$ and $8_7$, which do not fall in the class of the mathematical lemniscate knots of Bode [132]. This shows that further investigation of knotted optical fields could suggest improvements for the mathematical construction of Milnor functions. For example, a vortex propagation dynamics approach similiar to [58, 149] could be considered. When the braids corresponding to optical knots are projected onto the $RZ$-plane (similarly to Figure 4.6 (e) for $6_2$), it is possible to analyse the strands in $(R,\phi,z)$ as the 3D trajectories of the point particles located on the $RZ$-plane, which move at velocities and accelerations depending on $\phi$. The dynamics of the motion is different for distinct strands. Such dynamical approach is not taken into consideration in the mathematical construction of [132], for which the 'particles' move at constant speed with respect to $\phi$. This indicates that the optical propagation of Milnor slices at $z=0$ gives new insights into the explicit construction of knotted and linked fields, not predicted by mathematical topology.

In § 4.3, the approach of [18] to generate knotted beams experimentally was reproposed. The method consisted in multiplying the polynomial functions described in § 4.2 by a Gaussian distribution and decomposing the result into Laguerre-Gaussian

modes. The beam's propagation resembled the polynomial functions accurately when the waist of the Gaussian $w$ was large. Then, a new type of beam that behaves like a knotted polynomial about the optical axis was introduced and was expressed analytically as a superposition of Bessel functions of the first kind. The hologram in Fourier space associated to this beam was found in terms of Zernike polynomials. The beam's polynomial behaviour was shown to be achieved correctly when the scaling parameter $s$ was small. It was observed that when the parameter $w$ was small in the LG-sum or $s$ was large in the Zernike sum, the vortex lines located around the optical axes were strongly affected by the outer part of the beam. Thus, the parameters $w$ and $s$ should be chosen appropriately from case to case for the knotted vortex lines to appear correctly. The beam solutions presented in this chapter are not the unique functions in which the polynomial behaviour can be generated. Many more functions could be explored in order to create theoretical beam solutions optimised for experiments.

The optimisation technique presented in § 4.2, which was based on the lemniscate parameters $a$ and $b$, was used to generate the hologram function (4.15). This was embedded in a Gaussian envelope and generated experimentally in a SLM [137]. This experiment was the first optical figure-eight knot ever observed in the laboratory. It would be interesting to explore how many more lemniscate knots and links could be generated experimentally by the same methods.

In § 4.4 we demonstrated that the theory and experimental procedures of knotted phase singularities can be naturally extended to knotted polarisation singularities. We generated torus knots and links, and the figure-eight knot in the form of C-lines theoretically and experimentally by means of polarimetric measurements. This allowed a detailed reconstruction of the Seifert surfaces of the knotted fields, corresponding to the contours of the azimuthal angle in the Poincaré sphere, and the evaluation of their genus. This was the basis of the topological analysis we called seifertometry. This analysis could help illuminate the difficulties in the generation of particular types of knotted fields, and for instance could be used to optimise beam parameters and

smoothing experimental imperfections by monitoring the genus of the Seifert surfaces. The critical points could be reduced to a minimum by moving them and causing annihilation reaction between each other. Our results could lead to the development of new schemes for the generation and characterisation of other optical structures that are of fundamental or applied interest, such as more complicated forms of lemniscate knots [117, 132]. The quantum nature of these knots [146] could also be explored within the framework of polarisation pattern entanglement [150, 151]. The idea of seifertometry can also be extended to random polarisation fields, whose three-dimensional singular lines were studied in [141], and in which a wide variety of knots have been found in large-scale simulations [11]. However, our results show that these events are far more delicate and subtle than controlling polarisation singularities, and their topological processes are currently not understood in optical fields.

An application of the knotted vortices and polarisation singularities described in this chapter is to imprint knots and links into photosensitive materials [152–155]. The theory of knotted optical singularities analysed so far was in the paraxial regime; the size of the knots generated experimentally in Laguerre-Gaussian beams were of the order of $w$ transversally, but of the Rayleigh distance longitudinally—in practice $\sim (1 \times 1000)$ mm. This large aspect ratio is not useful for applications involving microscale or nanoscale materials. This motivates the work presented in the next chapter.

# 5 | Singular knot bundle in non-paraxial polarised beams

**Try to imagine what the electric and magnetic fields look like at present in the space in this lecture room.**

*The Feynman Lectures on Physics, Volume II*

Chapter 4 investigated and expanded the theory of knots in the framework of paraxial light. This chapter shows how nonparaxial effects alter the structure of knotted optical singularities. For knot structures approaching the scale of wavelength, polarisation properties become non-negligible, and the electric and magnetic fields differ, leading to intertwined knotted nodal structures in the transverse and longitudinal polarisation components, which we call a knot bundle of polarisation singularities. Their structure is analysed using polynomial beam approximations (§ 2.2.1) and numerical diffraction theory (§ 2.2.3). The analysis reveals features of spin-orbit effects and polarisation topology in tightly focused geometry, and we propose an experiment to measure this phenomenon.

The contents of this chapter have been published in [156].

## 5.1 From paraxial to nonparaxial beams

Creating knotted structures in the complex amplitude patterns of structured light is a challenge for holographic beam shaping. The first theoretical constuction of optical vortex knots and links [14, 15] was described in § 1.6, as well as experiments and more recent theory [16, 18]. These schemes involved superpositions of laser modes—implemented holographically—containing optical vortices in configurations of various knots and links, within the focal volume of a paraxially propagating laser beam (§ 4.3). In § 4.4 knotted lines of circular transverse polarisation were built in paraxial beams, where the surfaces corresponding to contours of constant polarisation azimuth were resolved experimentally [137]. The study of optical knots in monochromatic fields complements the study of knotted structures realised in various other physical systems (§ 1.3), including knotted electromagnetic fields [22, 157], fluid vortex lines in water [8], knotted small molecules [5] and bio-molecules such as DNA [3], defects around colloidal structures in liquid crystals [6, 7], and knot-like structures in Bose-Einstein Condensates (BECs) [74].

In most of these other systems, energetic considerations affect the knots' stability, and exciting knotted structures in the physical medium is the main challenge. Knotted vortices in light, on the other hand, have no energy associated with them; the primary technical challenge in realising them experimentally consists in controlling the delicate parameter ranges where topological structures occur, for instance by minimising perturbations (such as aberrations) [17]. An application of such spatial configuration of vortex knots is to template knotted structures in photosensitive materials, extending previous, simpler experiments, with imprinting structured optical amplitudes into BECs [152], liquid crystals [153] and other materials [154, 155].

The theory of knotted optical singularities in light beams developed in [14–16, 18] was primarily in the paraxial regime; the superpositions of knots in Gaussian beams were of the order of the waist width $w$ transversally (of the order $10^3$–$10^4\lambda$), but of the

Rayleigh distance longitudinally ($\pi w^2 \lambda^{-1} \approx 10^6$–$10^8 \lambda$). Such an extreme aspect ratio is impractical to imprint into material systems, so it is natural to adapt this approach to create smaller knotted structures in optical fields, of a scale closer to the wavelength, whose physical aspect ratio is closer to unity.

We approach this problem by exploring, analytically and numerically, the effect of reducing the transverse size of the fields constructed in [18]. A paraxial field is one which approximately resembles a plane wave of wavelength $\lambda$ propagating in $z$ (§ 2.1.3). In the paraxial regime, the electric and magnetic part of the light field can be represented by the same complex scalar amplitude function multiplying a constant, transverse polarisation vector; the magnitude of the longitudinal components is negligible. Mathematically we show that there is, in fact, also a knotted vortex in these nearly zero components. A small vortex knot, approaching the scale of the wavelength, is outside the paraxial regime. The field around such a structure has a non-negligible longitudinal component and the electric and magnetic fields no longer agree with each other.

We will describe a regime of transverse knot size (of the order of several $\lambda$) where the focal energy is approximately evenly distributed between transverse and longitudinal components, and between electric and magnetic field components. In this regime, the paraxial field structures are perturbed by nonparaxial effects, enough to deform the knots in each component, but not so strong as to destroy the nodal knot topologies. The resulting electromagnetic field therefore displays a *bundle* of intertwined, knotted polarisation singularities (corresponding to the nodes in the various components) which we will describe in detail. We also propose an experiment in which such a knotted object might be measured. Only in the nonparaxial regime the singular bundle can be observed because, although it is already present in the paraxial regime, the electric and magnetic knots cannot be distinguished, and the longitudinal components are negligible. The size of this nonparaxial knot bundle can range from several wavelengths—both in the transverse and longitudinal directions—to subwavelengths,

which makes it ideal for light-matter imprinting.

We focus our investigation on the behaviour of the simplest knotted light field, namely that around a trefoil knot with 3-fold symmetry. As described in § 1.6, this knot evolves paraxially forwards and backwards from an initial condition in the focal plane, given by the slice $z = 0$ of a Milnor polynomial [18,132], multiplying a Gaussian of fixed width $w$. For the trefoil knot this is

$$\psi_{2D}(r,\phi) = \mathrm{e}^{-r^2/(2w^2)}(1 - r^2 - r^4 + r^6 - 8r^3\mathrm{e}^{3\mathrm{i}\phi}). \tag{5.1}$$

Fields with this transverse profile are an interesting class of structured beams for considering spin-orbit effects. This is because light carries both orbital and spin angular momentum, which are determined, respectively, by the spatial and the polarisation degrees of freedom of light [158]. Expression (5.1) is an example of a superposition of two eigenfunctions of optical orbital angular momentum (OAM): a factor proportional to $\mathrm{e}^{\mathrm{i}n\phi}$ with azimuthal index $n$, superposed with an axisymmetric factor [146]. Assuming the polarisation in the initial, focal plane is purely helical, with right or left-handed circular polarisation $\widehat{\boldsymbol{e}}_{\pm} = (\widehat{\boldsymbol{x}} \pm \mathrm{i}\widehat{\boldsymbol{y}})/\sqrt{2}$, the different OAM states propagate differently from each other, and according to the handedness of the transverse polarisation. In the quantum picture the right and left-handed circular polarisations correspond to two spin states of photons [159]. The spin-orbit interactions (SOI) of light are given by the properties of Maxwell's equations and are analogous to the SOI of electrons in solids and relativistic quantum particles. As such, intrinsic SOI phenomena occur in many optical processes that have a spatial scale of the order of the wavelength of light. The resulting polarisation structure of small knots therefore depends on the interplay of OAM and spin angular momentum [160]. In particular, we will see that the choice of helicity opposite the sense of phase increase in (5.1) is important to the structure of the polarisation bundle, and assume that the transverse amplitude (5.1) in the focal plane multiplies left-handed circularly polarised light $\widehat{\boldsymbol{e}}_{-} = (\widehat{\boldsymbol{x}} - \mathrm{i}\widehat{\boldsymbol{y}})/\sqrt{2}$.

We have seen (§ 1.6) that the trefoil function (5.1) is just one of many knot functions known to give vortices in the configurations of different kinds of knots and links

on propagation [18, 58, 132]; the behaviour of other nonparaxial propagating knot functions is broadly similar and we briefly consider some others here. We generate the $(m,n)$-torus knot/link [1] (including the trefoil knot) by taking, as the initial condition, the numerator of the fraction $u^m - v^n$, where $u = (r^2-1)/(r^2+1)$, $v = 2re^{i\phi}/(r^2+1)$ times the Gaussian factor [18, 58, 132] which are therefore superpositions of two fields with OAM indices 0 and $n$. The trefoil profile (5.1) has $(m,n) = (2,3)$, and $(3,2)$ gives a trefoil with a different spatial conformation. Other simple torus knots and links include the unknot, the Hopf link $(2,2)$, the double link $(2,4)$ or $(4,2)$, the cinquefoil knot $(2,5)$ or $(5,2)$ (the Milnor polynomial of the latter requires multiplication the over homogenisation factor $1+r^2$ (§ 4.1)).

The fields considered so far were solutions of the paraxial equation (2.7). In particular, in the paraxial regime, $k$ is large as an inverse wavelength and $|\partial_z^2 \boldsymbol{E}|$ becomes much smaller than the other terms in the reduced Helmholtz equation (2.6). Since $\nabla \cdot (\boldsymbol{E} e^{ikz}) = 0$ (from equation (2.4a)), the divergence of the transverse components of $\boldsymbol{E}$ is approximately $-ikE_z$, and since $k$ is large, the longitudinal component $E_z$ is negligible compared to the transverse components. Furthermore, the magnetic field is also polarised with the same amplitude function, and the loci of the vortex lines in the $\boldsymbol{E}$ and $\boldsymbol{B}$ coincide.

Outside the paraxial approximation the electric field $\boldsymbol{E} = \boldsymbol{E}(r,\phi,z)$ satisfies the reduced Helmholtz equation (2.6). Similarly to the paraxial regime the fields are monochromatic and the singular configurations are static. However, the longitudinal component can become comparable to the transverse components. In this regime, different components of $\boldsymbol{E}$ have optical vortices (nodal lines) in slightly different positions, whose singular structure is naturally described in terms of polarisation singularities: lines in 3D space with the same polarisation state (§ 3.1.2). The splitting of scalar vortices of transversely polarised paraxial beams into polarisation singularities has been studied in some detail [43].

The design of holograms for nonparaxial fields is very challenging, therefore it is

extremely hard to structure arbitrary polarisation singularity patterns. The problem has been mainly addressed with numerical optimisation techniques [161] and semi-analytical approaches [162, 163], but they can be hard to implement. In our analytical treatment, we consider the nonparaxial behavior of fields structured on the scale of wavelength, but where the Gaussian envelope width $w$ is fixed, using polynomial beam functions [84] (extending the scalar approach of [18] to the nonparaxial vector regime), including longitudinal polarisation. For the regime in which the Gaussian envelope is made small together with the knot, the beam is propagated numerically by evaluating the Richards-Wolf vector diffraction integral (§ 2.2.3).

The structure of the rest of this chapter is as follows. In § 5.2, we present a physical treatment of all the electromagnetic field components of the paraxial beam and the presence of knots in all the components. In § 5.3 we present a theoretical analysis of the polarisation knots that constitute the singular bundle, of the order of the wavelength, embedded in a beam with wide Gaussian envelope. In § 5.4 we optimise the bundle regime both theoretically and numerically, leading to an experiment design where the Gaussian envelope and the transverse size of the knot are of the same order and all the components of the beam have comparable amplitudes. In § 5.5 we generalise our results to torus knots by showing that the knot bundle structure can be predicted directly from Maxwell's equations. We discuss and extend our results in § 5.6.

## 5.2 Paraxial polarisation knots

This section describes paraxial beams by polynomial functions and determines the longitudinal size of optical vortex knots with respect to their transverse length; then, polarisation features to the electric field are included and the nodal lines of each of its components in the circular basis are tracked to reveal the polarisation knots.

When studying the fine structure of light, we only need to describe features of the amplitude in the region of interest. Polynomial beams (§ 2.2.1) provide an approach

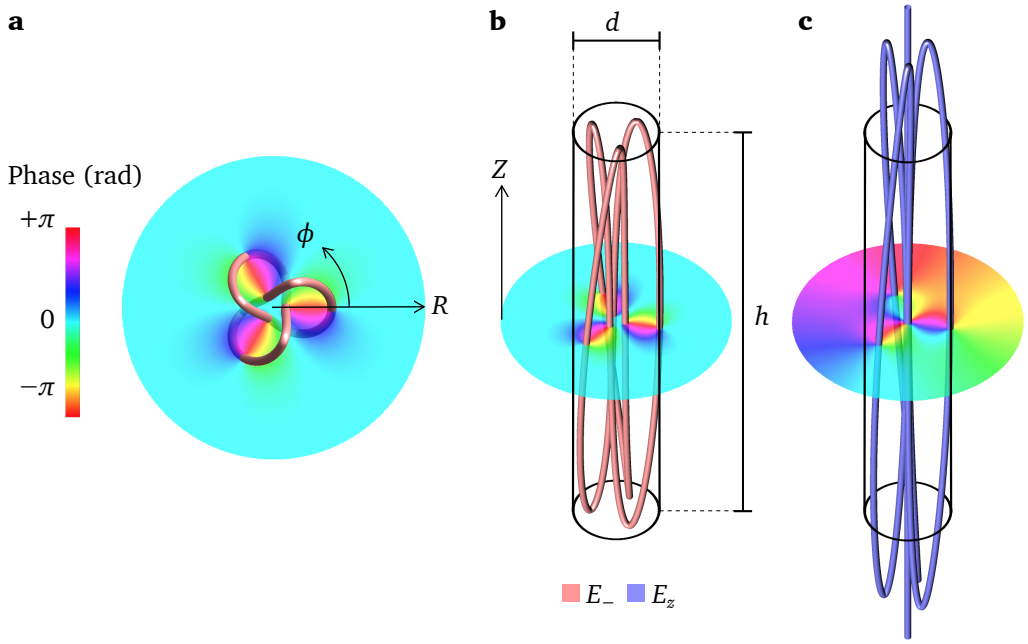


Figure 5.1: **Paraxial optical vortex trefoil knots**. (a) Phase distribution on the plane $z = 0$ of the field (5.1) which was imprinted on a hologram plate in [18] to create an optical vortex knot. (b) 3D view of the trefoil vortex knot (red) in the transverse component from (5.3). The cylinder of diameter $d$ and height $h$ encloses the knot structure. (c) 3D view of trefoil knot and axial vortex in the longitudinal component (blue) from (5.4). The same cylinder from (b) is given for reference. Physically, the knots' length along the propagation direction scales quadratically with respect to their transverse size.

to such a local study of optical amplitude structures. These are the formal, propagating solutions of the paraxial equation or reduced Helmholtz equation, which in the focal plane $z = 0$ take the form $r^{|\ell|+2p}e^{i\ell\phi}$ in cylindrical coordinates (with integer $\ell$ and $p \geq 0$). Although polynomial solutions are not satisfactory global representations of a beam—not being normalised—they arise naturally from a Taylor expansion of any beam about the origin (focal point). They can be understood as a basis for the description of superoscillatory behavior of structured low-amplitude interference embedded in a bright beam [143]; the mathematical details of the bright sidebands are lost in the asymptotic polynomial growth.

In [18], the paraxial polynomial beam containing the trefoil knot was derived

as the leading term in the expansion of a superposition of Laguerre-Gaussian beams with $1/w$ as the small parameter; in § 4.3, we showed that the same polynomial beam structure can be embedded in an envelope with *any* profile, provided the width of the envelope is large compared to the knot structure (such as a Bessel beam with small $k_r$). We will take this approach for the rest of this section, and only consider the polynomial part of (5.1), ignoring the Gaussian factor.

The form for the polynomial in (5.1) does not agree dimensionally if $r$ has the dimensions of length; this case requires a different formulation of the scaling arguments in [18]. We will now make this explicit, which is the basis of all the scaling arguments that will follow. Occurrences of $r$ in (5.1) should be replaced by the dimensionless $R \equiv krs^{-1}$, where the dimensionless scale parameter $s$ is introduced, which determines the size of the knot, similarly to § 4.3.2. This is depicted in Figure 5.1 (a), in which the six zeros of (5.1) are plotted as singularities of the phase, which occur at $r = 0.46s/k$ and $2.19s/k$ (at $\phi = 2\pi j/3$, $j = \{0,1,2\}$). The paraxial polynomial beam solution agreeing with (5.1) by $r \to s^{-1}kr$ is

$$\psi_{3\mathrm{D}}^{\mathrm{par}} = \left[1 - s^{-2}k^2r^2 - s^{-4}k^4r^4 + s^{-6}k^6r^6 - 8s^{-3}k^3r^3\mathrm{e}^{3\mathrm{i}\phi}\right] - 2\mathrm{i}\left(s^{-2} + 4s^{-4}k^2r^2 - 9s^{-6}k^4r^4\right)kz + 8\left(s^{-4} - 9s^{-6}k^2r^2\right)k^2z^2 - 48\mathrm{i}s^{-6}k^3z^3, \tag{5.2}$$

where $[\bullet]$ is independent of $z$, and corresponds to (5.1). Paraxial beams satisfy a particular scaling relation: after replacing $r$ with $R = krs^{-1}$ and $z$ with $Z \equiv kzs^{-2}$, there should be no other occurrences of $s$ and $k$ in any expression for a paraxial beam or its solutions. In the paraxial regime, $s \gg 1$, for which knots are large and elongated due to the quadratic dependence of $s$ in $Z$. We can therefore write the paraxial polynomial knotted beam as

$$E_{-}^{\mathrm{par}} = \left(1 - R^2 - R^4 + R^6 - 8\mathrm{e}^{3\mathrm{i}\phi}R^3\right) - 2\mathrm{i}Z - 8\mathrm{i}R^2Z + 18\mathrm{i}R^4Z + 8Z^2 - 72R^2Z^2 - 48\mathrm{i}Z^3. \tag{5.3}$$

It is not difficult to track the vortex lines as the complex zeros of the polynomial (5.3) using the vortex tracking routines from § 3.5.1. The identification of the knot/link type

for the simple vortex configurations we describe can be done by visual inspection, but, alternatively, one could implement the more sophisticated algorithms summarised in § 3.5.2. The 3D-vortex configuration of (5.3) is shown in Figure 5.1 (b) in red: a trefoil knot is enclosed in the cylinder with diameter $d = 0.700s\lambda$ and height $h = 0.116s^2\lambda$; from the paraxial scaling, its transverse size is proportional to $s$, and longitudinal size to $s^2$. Therefore our paraxial knot is much longer longitudinally than transversally.

It is very straightforward to perform a similar paraxial analysis for the other $(m,n)$-torus knots as described in § 1.6, but with the trefoil profile (5.1), rewritten in scaled coordinates (5.3), replaced with the appropriate section of a Milnor polynomial. The results of the paraxial dimensions for several of these knots is given in in Table 5.1.

Although the longitudinal component is negligible in the paraxial regime, it is not zero. To leading order in $k^{-1}$, $E_z = \mathrm{i}k^{-1}\nabla\cdot(E_+\widehat{\boldsymbol{e}}_+ + E_-\widehat{\boldsymbol{e}}_-)$; with the transverse polarisation fixed as $\widehat{\boldsymbol{e}}_-$, this gives the longitudinal polarisation as

$$E_z^{\mathrm{par}} = -\sqrt{2}\mathrm{i}s^{-1}R\mathrm{e}^{-\mathrm{i}\phi}\left[1+2R^2-3R^4+24R\mathrm{e}^{3\mathrm{i}\phi}+4\mathrm{i}Z\left(2-9R^2\right)+72Z^2\right]+O(s^{-2}). \tag{5.4}$$

The field $E_z^{\mathrm{par}}$ satisfies the paraxial wave equation; ignoring the prefactor and terms in $s^{-1}$ and higher, it is given purely in terms of $R$ and $Z$ and hence has the same paraxial scaling as the transverse knot. Owing to spin-orbit conversion [158], it has a negative vortex on the beam axis; otherwise the quartic polynomial in $R$ has a knotted nodal structure (shown in Figure 5.1 (c)), however with inner vortex at $R = 0.042$, almost

Table 5.1: **Paraxial scaling for different knots**. Transverse and longitudidinal sizes $d$ and $h$ for optical vortex $(m,n)$-torus knots and links in paraxial beams, generated as discussed in § 5.1. The main example in the paper is (2,3).

| Knot type | (2,2) | (2,3) | (2,4) | (2,5) | (3,2) | (4,2) | (5,2) |
|---|---|---|---|---|---|---|---|
| $d(10^{-3}s\lambda)$ | 768 | 700 | 655 | 625 | 852 | 920 | 979 |
| $h(10^{-3}s^2\lambda)$ | 205 | 116 | 79.0 | 58.7 | 173 | 152 | 113 |

at the origin. Such a knot cannot practically be measured; in § 5.3, we will consider the exact fields outside the paraxial approximation, where the vortices are separated by distances of order $s^{-1}$ (and when in fact $E_z$ is no longer negligible).

If, on the other hand, the initial transverse polarisation is chosen to be $\widehat{\boldsymbol{e}}_+$, the resulting longitudinal field is

$$E_z^{+,\mathrm{par}} = -\sqrt{2}\mathrm{i}s^{-1}R\mathrm{e}^{\mathrm{i}\phi}\left[1+2R^2-3R^4+4\mathrm{i}Z\left(2-9R^2\right)+72Z^2\right]+O(s^{-2}). \tag{5.5}$$

Unlike $E_z^{\mathrm{par}}$, the longitudinal component here is an eigenfunction of OAM with azimuthal quantum number unity; therefore there can be no other vortex structure in the longitudinal component. When the OAM of the amplitude structure has the same sign as the polarisation helicity, there is no extra knot-like interference structures in the longitudinal component. This justifies our main investigation in the topologically more interesting case of imprinting the knot with positive OAM in a field of left-handed polarisation. Apart from missing the extra azimuthal term to OAM, the radial dependence of $E_z^{+,\mathrm{par}}$ is the same as $E_z^{\mathrm{par}}$. More details are given in § 5.5.

Assuming the monochromatic magnetic field has an analogous form $\boldsymbol{B}\mathrm{e}^{\mathrm{i}(kz-\omega t)}$, Maxwell's equations can easily be solved to show, within the paraxial approximation (ignoring corrections of order $s^{-1}$ and higher), that $\boldsymbol{B} \approx \mathrm{i}c^{-1}\boldsymbol{E}$. Therefore paraxially, the nodal knots in the magnetic components exactly agree with their counterparts in the electric field, as expected [43].

We have therefore shown that in paraxial fields, the aspect ratio of a vortex knot in a transverse component scales with its transverse size, and that there is a knotted vortex structure in the negligible longitudinal component too. From the scaling laws in Table 5.1, getting a unit aspect ratio trefoil knot suggests bringing $s$ down to about $s_1 \approx 700/116 \approx 6$, which is outside the paraxial regime. As $s$ approaches unity, we need to include the $s^{-1}$-dependent terms in the components of $\boldsymbol{E}$ and $\boldsymbol{B}$ [164], suggesting the vortex lines in each of the components behave differently. We investigate this further in the next section.

## 5.3 Exact analysis of nonparaxial polarisation knot bundle

A polynomial solution of the paraxial equation can be made to solve the reduced Helmholtz equation by replacing monomials in $z$ by reverse Bessel polynomials (2.39) as shown in § 2.2.1. Doing this to our main electric field component multiplying $\widehat{\boldsymbol{e}}_-$ does not affect the initial condition in the focal plane $z = 0$, and gives

$$E_-^{\mathrm{np}} = E_-^{\mathrm{par}} + s^{-2}\left[8\mathrm{i}\left(1 + 18s^{-2} - 9R^2\right)Z + 144Z^2\right], \tag{5.6}$$

where, as in the previous section, we use $R = krs^{-1}$ and $Z = kzs^{-2}$.

Similarly, using Maxwell's equations and enforcing the polynomial beam Ansatz, we find the following full forms for the components of the nonparaxial longitudinal electric field, and the magnetic field, correctly incorporating corrections in $s^{-1}$ and higher powers,

$$E_z^{\mathrm{np}} = E_z^{\mathrm{par}} + 4\sqrt{2}\mathrm{i}R\mathrm{e}^{-\mathrm{i}\phi}s^{-3}\left[2 + 54s^{-2} - 9R^2 - 54\mathrm{i}Z\right], \tag{5.7}$$

$$B_+^{\mathrm{np}} = -4\mathrm{i}c^{-1}R^2\mathrm{e}^{-2\mathrm{i}\phi}s^{-2}\left[1 + 18s^{-2} - 3R^2 - 18\mathrm{i}Z + 24R^{-1}\mathrm{e}^{3\mathrm{i}\phi}\right], \tag{5.8}$$

$$B_-^{\mathrm{np}} = \mathrm{i}c^{-1}\left\{E_-^{\mathrm{par}} + 8s^{-2}\left[-36s^{-4} - s^{-2} + 9s^{-2}R^2 + \mathrm{i}\left(1 + 36s^{-2} - 9R^2\right)Z + 18Z^2\right]\right\}, \tag{5.9}$$

$$B_z^{\mathrm{np}} = \mathrm{i}c^{-1}\left\{E_z^{\mathrm{par}} - 4\sqrt{2}\mathrm{i}R\mathrm{e}^{-\mathrm{i}\phi}s^{-3}\left[2 + 36s^{-2} - 9R^2 - 18\mathrm{i}Z\right]\right\}. \tag{5.10}$$

The extra terms $[\bullet]$ imply the scaling laws derived in the previous section do not hold for small values of $s$, for which the beam approaches the nonparaxial regime. Tracking the nodal lines in each components can again be done easily, and the nodal knots in each component change shape when $s \ll 10$.

The exact forms (5.6)–(5.10) show how the exact optical energy is distributed around the focal volume in each component. As $s \ll 1$, the transverse knot structure becomes subwavelength, which may be considered extremely nonparaxial, within the focal volume. In this extreme nonparaxial regime, around the knot structure, $E_-^{\mathrm{np}} \propto\!\!\!\approx s^{-4}$

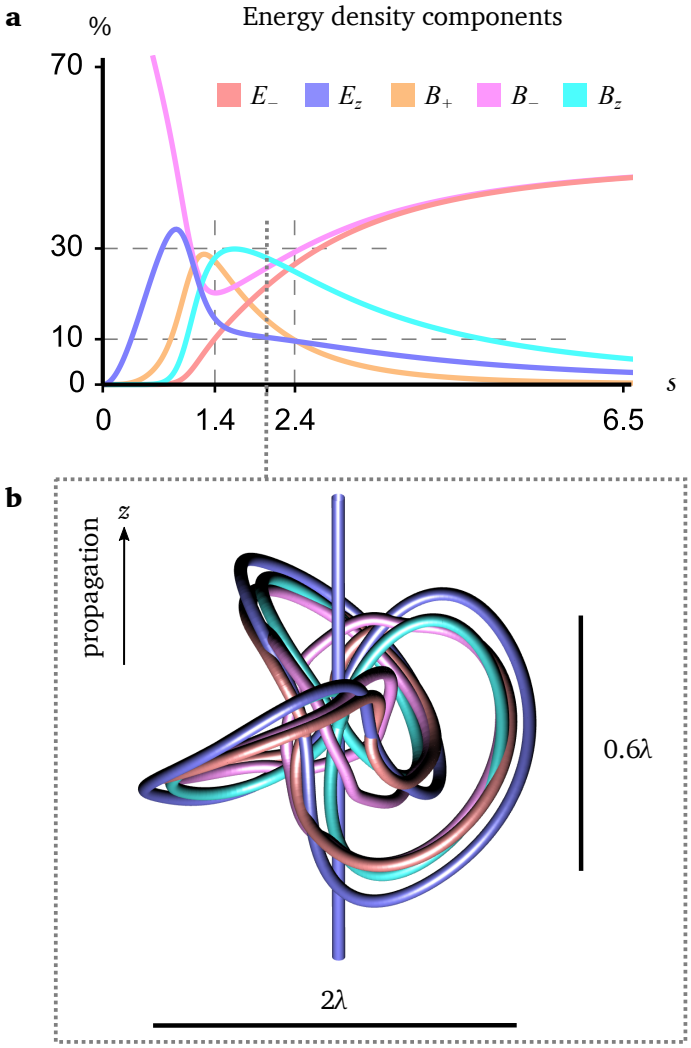


Figure 5.2: **Singular knot bundle when all components have similar focal energy**. (a) Integrated energy density in the focal disk $z = 0$, $R \leq 2.19$ for each of the components of the electromagnetic field as color coded. $E_+$ is exactly zero in the polynomial representation of the field. The dashed lines indicate that for $1.4 \leq s \leq 2.4$, each of the components (except $E_+$) has an energy between 10% and 30% of the total in the disk. (b) Singular polarisation bundle. Nodal lines in the components of $E_-, E_z, B_-, B_z$ are all entwined, each in the form of a knotted line with a similar size, which is approximately within a cylinder of diameter $2.02\lambda$ and total height $0.648\lambda$. The longitudinal components also exhibit an axial vortex.

whilst $E_z^{\rm np} \propto s^{-5}$. Analogously, $B_+^{\rm np} \propto s^{-4}$, $B_-^{\rm np} \propto s^{-6}$, $B_z^{\rm np} \propto s^{-5}$. As we will see in our more detailed analysis, the knots in each component dissolve away by reconnection when $s$ is close to unity and the field in the longitudinal components becomes large.

This phenomenon was already observed for optical vortex knots in [15, 23].

As discussed in § 5.1, there is a range of $s$ where the energy in the neighborhood of the focal point is similar in the longitudinal and transverse components. We determine the *optimal* range of $s$ for this crossover by calculating the total energy in each component in the focal plane $z = 0$, in the disk of radius $R = 2.19$ (the majority of energy, of course, being outside this). We plot the energy in this disk in each component as a function of $s$ in Figure 5.2 (a). For $1.4 \lesssim s \lesssim 2.4$ the focal energy in all four components $E_-, B_-, E_z, B_z$ is of similar order (10–30% each). This range of $s$ gives a crossover regime in which all the different vortex knots identified in the paraxial regime exist and occupy a similar volume, but are sufficiently nonparaxial for the spatial conformations of the knots to be different. The resulting system of overlapping vortex knots in the different components of the electromagnetic fields forms a *singular knot bundle*. Figure 5.2 (b) shows such remarkably complicated vectorial electromagnetic field distribution for the optimal value $s = 2.05$, where the knotted nodal lines in each of the electromagnetic field components are entwined without coinciding. Identifying and understanding this structure is the main result of this chapter.

The singular knot bundle of Figure 5.2 (b) has an aspect ratio of 0.32, smaller than unity. By numerically tracking the vortices for the nonparaxial field (5.6) for $s$ close to 6 the paraxially-estimated value for the unit aspect ratio, we find a knot of aspect ratio unity when $s = s_1 \equiv 5.75$, for which $d = h = 4.01\lambda$, shown in Figure 5.3 (a). Thus, the previously published knotting scheme [18], appropriately rescaled, does give a knot of unit aspect ratio but only when scaled to a few optical wavelengths across. The vortices in $E_z^{\rm np}, B_-^{\rm np}$ and $B_z^{\rm np}$ are shown in Figure 5.3 (b, c, d); as with the knot in $E_-^{\rm np}$, these all closely resemble their paraxial counterparts (*e.g.* the transverse components, and longitudinal components, have zeros very close, with an axial longitudinal vortex). In particular, the small $s$ corrections to the longitudinal components are sufficient to ensure the distances between the inner vortices of the longitudinal trefoil knots become comparable with their transverse size (with the vortex up the axis), but not

large enough to split the conformations of the knots in the electric and magnetic fields, which are effectively coincident.

Throughout this section, we have been considering as a thought experiment the propagation of the electromagnetic field in the neighborhood of the focal point, given that the $E_-$ component is given by (5.3) and $E_+ \equiv 0$. If $s$ is made so small that the transverse knot structure is subwavelength, we would not be surprised if nonparaxial

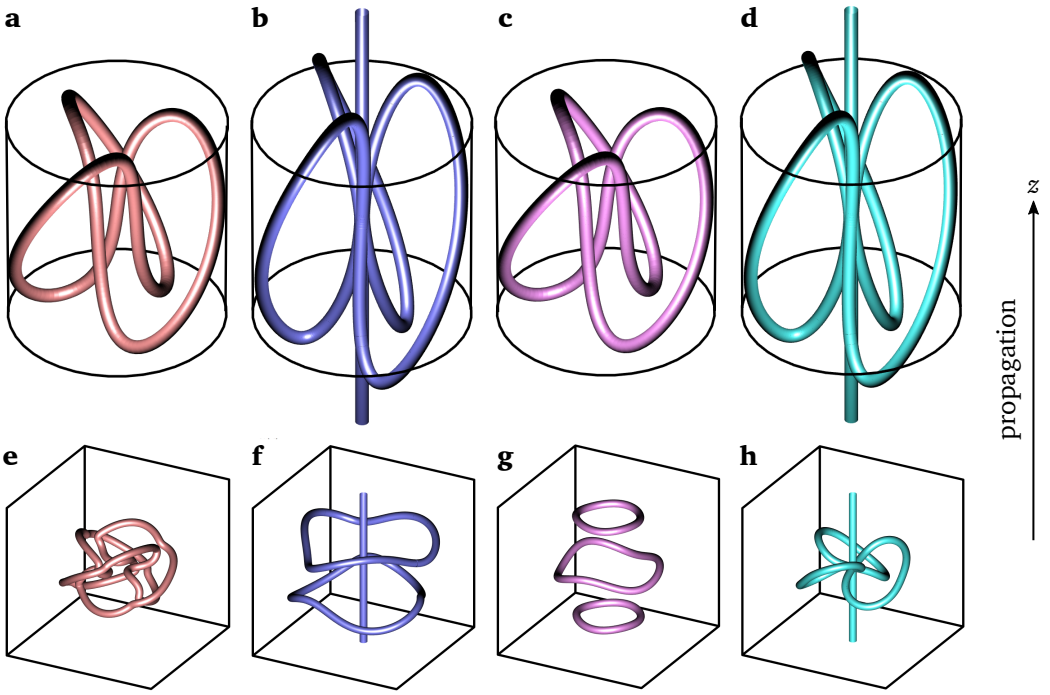


Figure 5.3: **Nonparaxial vortex knots in different components of $E$ and $B$ fields**. (a) The trefoil knot in $E_-^{\mathrm{np}}$ (a) has unit aspect ratio when $s_1 = 5.75$; the vortex lines in the other components also display a trefoil knot: (b) $E_z^{\mathrm{np}}$; (c) $B_-^{\mathrm{np}}$ (which resembles (a)); (d) $B_z^{\mathrm{np}}$ (which resembles (b)). The cylinder $d_1 = h_1 = 4.01\lambda$ is shown around each vortex configuration for comparison. (e)–(h) The corresponding vortex configurations when $s = 1.00$, drawn in a cube $\lambda^3$. (a) The knot in $E_-^{\mathrm{np}}$ corresponds to a value of $s$ just above the value where its lines reconnect, which are bounded by a cylinder of subwavelength volume $V_c \approx 0.15\lambda^3$; (f) the vortex lines in $E_z^{\mathrm{np}}$ have already reconnected to form two approximately coaxial rings, and an axial vortex; (g) vortex lines $B_-^{\mathrm{np}}$ have reconnected to give three approximately coaxial rings; (h) vortex lines in $B_z^{\mathrm{np}}$ is still a trefoil knot, threaded by a vortex line.

effects are sufficiently large to disrupt the knot topology, causing reconnections that dissolve the knot in both this and the other components [165]. The case of $s = 1.00$ is shown in Figure 5.3 (e)–(h); the knot exists in the $E_-^{\mathrm{np}}$ and $B_z^{\mathrm{np}}$ components, but have already reconnected away in the $B_-^{\mathrm{np}}$and $E_z^{\mathrm{np}}$ components. The transverse vortex knot in $E_-^{\mathrm{np}}$ (Figure 5.3 (e)) here is so small it fits within a cubic wavelength, proving that subwavelength nodal knots are supported by Maxwell's equations. The reason for the radially symmetric behavior in both $E_z$ and $B_-$ can be extrapolated by Maxwell's equations. The details of the proof are in § 5.5.

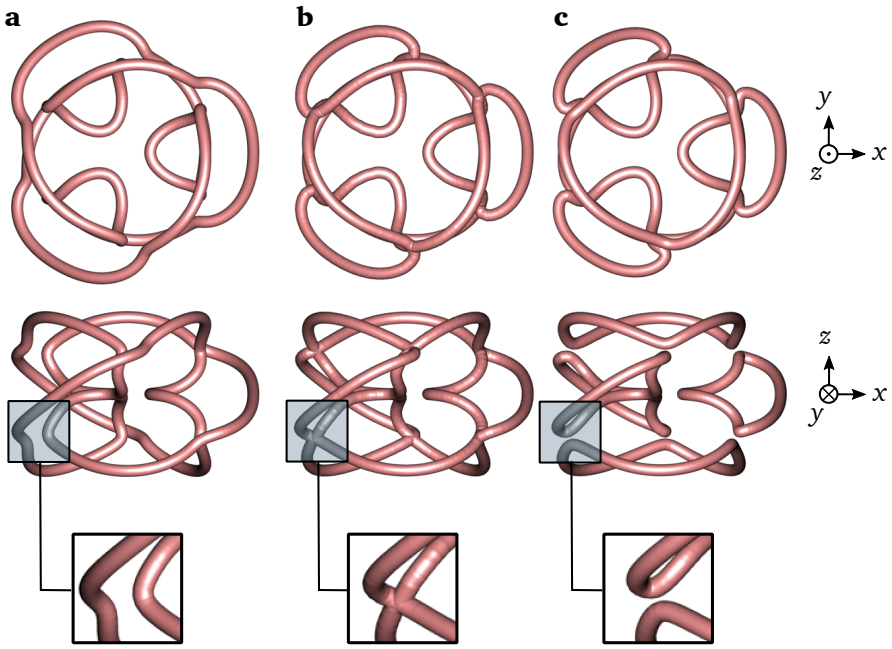


Figure 5.4: **Reconnection events destroying the vortex knot in the $E_-$ component.** The parameter $s$ is decreased from (a) $s = 1.000$, where there is a knotted vortex line, through the critical value of $s_c = 0.965$ where the vortices touch at six points. At lower values of $s$, such as (c) $s = 0.950$, the vortex configuration is five unlinked rings. In each frame, there is an axial view, a side view and an inset showing the vortex geometry.

The details of how the knot in $E_-^{\mathrm{np}}$ dissolves away by reconnections when $s < 1$ is illustrated in Figure 5.4. As the parameter $s$ reduces below unity, the vortex lines in the principal $E_-^{\mathrm{np}}$ component (Figure 5.4 (a)) approach each other at six points on the knot, and reconnect at the critical value $s_c = 0.965$. After the topology has

changed, the vortex configuration consists of five loops, one above and one below the focal plane, and three symmetrically arranged within the focal plane (Figure 5.4 (c)). The volume of a bounding cylinder around the knot at $s_c$, immediately prior to its destruction, is $V_c = 0.15\lambda^3$. The sequence of events dissolving the topology of the knots in the other components is reported in § 5.5, showing similar behaviours to $E_-$.

The topological events described in this section are not unique to the trefoil knot. The values of $s$, $d$, $h$ for unit aspect ratio and reconnection events are reported in Table 5.2 for several different torus knots and links. This characterises general optical vortex knots in the nonparaxial regime. We tracked the vortex lines of $E_z$ for other knots and we reported their knot type in Table 5.2. In § 5.5, we present similar but more general argument than in the previous sections anticipating the relationship between the knots in the various components of the polynomial beam electromagnetic field for initial conditions analogous to (5.1) for different knots.

The beams described in this section could be implemented in the laboratory by tightly focusing a paraxial beam or by constructing nanoscale resolved holograms (both equivalent to a small value of $s$ which brings the paraxial optical beam of [18] to the nonparaxial regime). However, the physical challenge of polynomial beams relies in the fact that the bulk of the energy in these beams is concentrated away from the knotted structure, and the detection of nodal knots in subwavelength volumes of extremely low intensity is a considerable challenge for experiment. Hence, a less complicated, realistic experimental design is required to potentially measure a polarisation knot bundle. In the next section, we propose an experimental design by which the singular knot bundle presented here could be observed in a physical system.

Table 5.2: **Nonparaxial torus knot bundles**. Values $s_1$ for which the aspect ratio of the knot in $E_-$ is 1 and the corresponding dimensions $d_1 = h_1$. Limiting values $s_c$ for which each knot and link dissolves and corresponding volume $V_c$ of the cylinder that encloses the nodal lines. Knot type in $E_z$ when the knot in $E_-$ has unit aspect ratio ($s_1$). The case study here is (2,3).

| $E_-$ knot type | (2,2) | (2,3) | (2,4) | (2,5) | (3,2) | (4,2) | (5,2) |
|---|---|---|---|---|---|---|---|
| $s_1$ | 3.59 | 5.75 | 7.90 | 10.2 | 4.85 | 5.80 | 8.40 |
| $d_1(\lambda)$ | 2.76 | 4.01 | 5.18 | 6.40 | 3.98 | 5.35 | 8.22 |
| $s_c$ | 0.36 | 0.97 | 3.10 | 4.50 | 0.71 | 0.88 | 3.10 |
| $V_c(\lambda^3)$ | 0.013 | 0.151 | 3.37 | 9.62 | 0.080 | 0.338 | 11.1 |
| $E_z$ knot type | unknot | (2,3) | (2,4) | (2,5) | (2,2) | (3,2) | (4,2) |

## 5.4 Experiment design to measure the bundle in tightly focused beams

Here we propose an experimental scheme that gives a singular knot bundle within the focal volume of a microscope objective of high numerical aperture. The general topological properties of the knotted fields described in the previous section are not unique to polynomial beams, and here we demonstrate the existence of the polarisation knot bundle numerically in tightly focused beams, an approach that relies on slightly different assumptions than the exact polynomial beam-based analysis of the previous section. The analytical treatment from the previous section backs up the simulations, even though the shape of the knots in the bundle are slightly different, indicating that the phenomenon we describe is general to nonparaxial beams of diverse nature. We predict that the structure we present here could be measured with the polarimetry techniques reported in [166, 167] if they were optimised for the detection of low-amplitude optical fields.

Nonparaxiality is achieved in this proposed experiment by including a high nu-

merical aperture microscope objective in the setup from [16–18], giving rise to tightly focused beams. The experimental configuration is shown in Figure 5.5. For practical purposes, the hologram plate is specified in Fourier space; the resulting structured beam has to be circularly polarised (along $\widehat{\boldsymbol{e}}_-$) before being sent to the back focal plane of the microscope objective (the polarisation setup is not included in the scheme for simplicity). When such beams with a well-defined transverse polarisation state are tightly focused, spin-orbit effects result in a non-zero field in the orthogonal transverse polarisation component $\widehat{\boldsymbol{e}}_+$ [168, 169], as well as the principal components $E_-$,

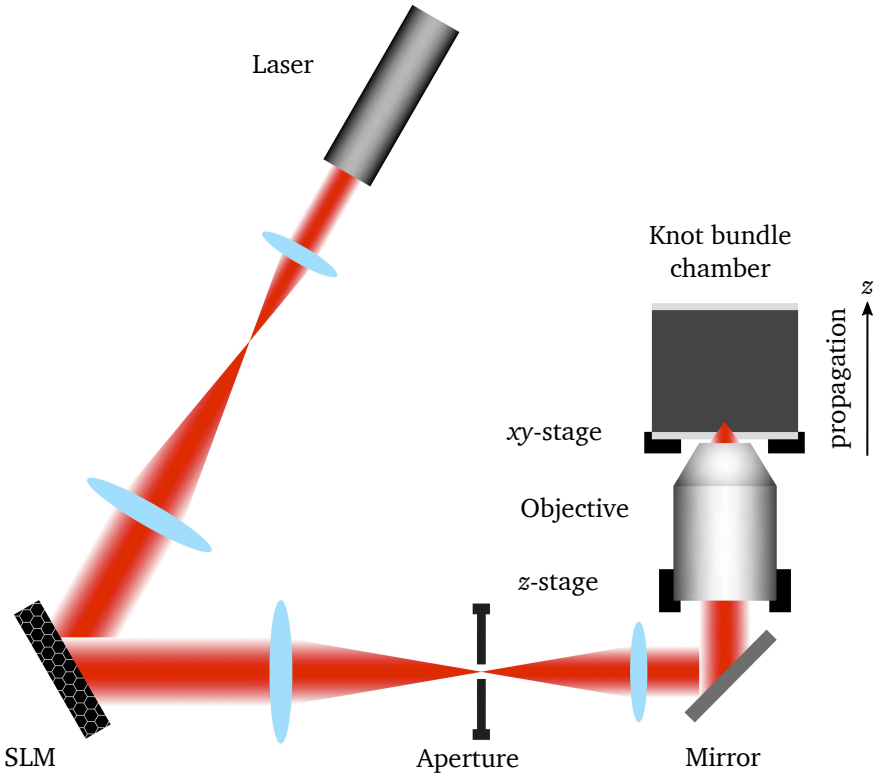


Figure 5.5: **Scheme of proposed experiment**. Experimental setup adapted from [16–18] of a tightly focused beam for the creation of the bundle of polarisation singularities. The numerical aperture of the microscope objective is $\gamma \geq 0.90$, the radius of the back focal plane is $a = 7000\lambda$. In practical experiments a uniformly circularly polarised beam acquires a weak transverse component of opposite handedness and a longitudinal component. When the hologram (5.11) is generated in the spatial light modulator (SLM), the beam in the focal volume has knotted nodal lines in each component of the electric and magnetic fields.

the longitudinal field $E_z$ and their magnetic counterparts. This redistribution of the energy between the different components is due to the aperture-lens system and is more significant for larger tight focusing.

We found that it should by possible to create a singular knot bundle in the focal volume of a microscope objective of high numerical aperture ($\gamma \geq 0.9$, assuming index of refraction 1) and radius of the back focal plane $a = 7000\lambda$. Our approach to design the hologram function consists in calculating the Fourier transform of (5.1) and discarding the terms that are not necessary for the knot bundle to appear under tight focusing. The numerically optimised Fourier hologram takes the form (in cylindrical coordinates $\rho$ and $\varphi$, in units of aperture $a$ and illuminating Gaussian of waist width $w_0$)

$$E_{-}(\rho, \varphi; w_0) = \mathrm{e}^{-\rho^2/(2w_0^2)} \left(2 + 3\,\mathrm{i}\,\rho^3 S^{-3} \mathrm{e}^{3\,\mathrm{i}\,\varphi} + 3\rho^4 S^{-4}\right). \tag{5.11}$$

The transverse size of the knot is controlled by the parameter $S$, which scales the input beam in Fourier space by analogy with the polynomial beams (a direct scaling of the focal field in real space would require more advanced methods to structure vector fields). We propagated the function in (5.11) in the focal volume by means of vector diffraction theory (§ 2.2.3). Both the paraxial and the extreme nonparaxial regimes do not give the knot bundle (as in the previous section); an appropriate balance between them is required in order to create the bundle regime. Such an overcrossing regime can be found by the careful manipulation of the focusing parameters $\gamma$, $w_0$ and $S$. In analogy to [18, 19], the tightly focused experimental scheme depends strongly on the waist of the illuminating Gaussian envelope $w_0$ incident on the backfocal plane of the microscope objective, which plays an important role in determining the topology of the beam. In fact, small $w_0$ implies that the real space beam is enveloped in a wide Gaussian; this regime clearly resembles the polynomial beam propagation that we already stated is not practical. On the other hand, large $w_0$ overfills the aperture, creating additional diffractive rings in the focal plane, around a focal volume that is too small to contain the knotted structure (we saw in the previous section that the

knot bundle cannot be made much smaller than $\lambda^3$), and tight wavefront curvature from small $1/w_0$ might further affect the knot topology, as found in the paraxial regime [18, 19].

By the analysis of the vortex lines of each component of the beam we found that the correct balance of the parameters is given by not overfilling waist of the Gaussian $w_0$, which gives an effectively smaller numerical aperture with respect to that of the microscope objective, but, more importantly, a larger focal volume in which to embed the knot bundle. The holograms given by (5.11) for different sets of parameters are plotted in Figure 5.6 (a)–(c). Such functions do not contain any phase singularities and, as mentioned, their paraxially propagating beams do not embed knotted vortex lines. This is because our optimised hologram (5.11) uses the lens-aperture system to shape the beam's interference pattern containing knotted structures.

When $\gamma = 0.90$, $S = 0.27$ and $w_0 = 0.62S$ the singular knot bundle of Figure 5.6 (d) appears in the focal volume. The numerically propagated beam contains a trefoil knot in $E_-$ (red) and $E_z$ (blue). From the spin-to-orbit effects of the input beam in the lens system, the nodal lines of the extra component $E_+$ are also trefoil knotted, threaded by an axial vortex (shown in the figure in green). Three trefoil knots appear in all the components of the magnetic field at the same position, due to the dual properties of tightly focused circularly polarised beams. The knot in $E_+$ and the mutual linear dependence of the $\boldsymbol{E}$ and $\boldsymbol{B}$ fields are the major differences from the polynomial beams predictions. The differences from the polynomial beams arise physically from the fact that the lens and the aperture system inevitably affect the input beam, and the Gaussian envelope in the focal volume is too small to behave as a polynomial beam. By evaluating the electromagnetic energy density in a disk of radius $R = 3.80\lambda$ (see previous section) we found that the energy transferred to the other components is very low, reported in Figure 5.6 (g). Specifically, only 0.01% goes to $E_+$ and 0.89% to $E_z$ (equivalently in $\boldsymbol{B}$).

In order to generate an energy distribution that could potentially be measured in

an experiment, we tightly focus the beam more in order to create the bundle regime and without destroying the topology of the knotted lines. We do so by increasing the focusing parameters $\gamma = 0.95$, $S = 0.75$ and $w_0 = 0.65S$. As a result, the knot bundle

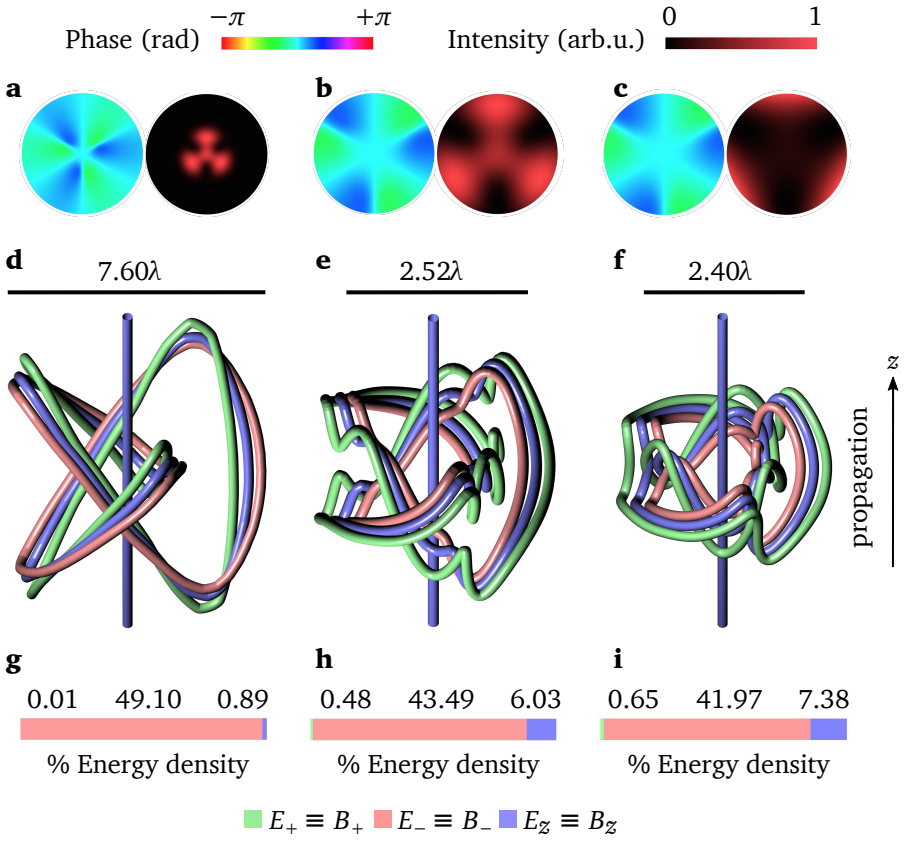


Figure 5.6: **Numerical simulations of the knot bundle**. The numerical propagation of the hologram plate (5.11) by Richards-Wolf vector diffraction theory gives the singular knot bundle, with focusing parameters $\gamma = 0.9$, $S = 0.27$, $w_0 = 0.62S$ (a, d, g); $\gamma = 0.95$, $S = 0.75$, $w_0 = 0.65S$ (b, e, h); $\gamma = 0.95$, $S = 0.90$, $w_0 = 0.90S$ (c, f, i). The beam's nodal lines in $\boldsymbol{E}$ and $\boldsymbol{B}$ are coincident, as well as their energy density distribution. (d) The focal volume has a trefoil knot in each component of the electric and magnetic fields: $E_-$, $B_-$ (red); $E_+$, $B_+$ (green) and $E_z$, $B_z$ (blue). (e) The trefoil knots are deformed and smaller for more tightly focused beams. (f) Each of the knots in $E_+$ and $E_z$ have dissolved into two separate loops because the beam is too nonparaxial, $E_-$ is still trefoil knotted. (g–i) The energy transferred from $E_-$ to $E_+$ and $E_z$ is larger for increasing tight focusing (equivalent distributions are found for the magnetic components).

of Figure 5.6 (e) and the energy distribution (h) appear. This knot bundle shows three deformed trefoil knots of smaller size compared to the previous case, which are a manifestation of the nonparaxial effects. On the other hand, the energy is larger in $E_+$ and $E_z$ which are 0.48% and 6.03% in a radius $R = 1.26\lambda$.

A further optimisation of the energy cannot be achieved because the knot bundle starts to dissolve in $E_+$ and $E_z$ when the beam is too tightly focused ($\gamma = 0.95$, $S = 0.90$, $w_0 = 0.90S$), whilst the trefoil knot is still present in $E_-$, as shown in Figure 5.6 (f). This choice of parameters has 0.65% of energy in $E_+$ and 7.38% in $E_z$ in the disk $R = 1.20\lambda$ (Figure (i)). This shows that, consistently with the theoretical results of the previous section, the knot bundle does not appear in an extreme nonparaxial regime, for which its volume is smaller than $\lambda^3$. However, the way the trefoil knots dissolve is different from the previous section: both the knots in $E_+$ and $E_z$ split only into two loops here. This is the third major difference from the knots embedded in polynomial beams.

The numerical experiment we designed can be easily extended to other knots and links. The topological behavior of the nodal lines of the different components can be predicted with polynomial beams, and the bundle regime can be approached in a high numerical aperture system by choosing the focusing parameters appropriately. As already stated in the previous section, a good balance between the energy distribution of each of the components of the field seems to be a requirement for the successful creation of knotted nodal lines in each component of the electromagnetic field. Our numerical results show that the singular knot bundle seems to be a general phenomenon of nonparaxial knotted beams in which spin to orbit effects are dominant.

## 5.5 Generalisation to other knot types

In this section we show that the symmetries required by the knot bundle can be extrapolated directly from Maxwell's equations. In particular, we consider the rela-

tionships between the different components of the electromagnetic field, assuming that one of the transverse circular components of the electric field is a Milnor-like function as discussed in § 5.1; this is straightforward for the torus knots.

We will follow the logic of § 5.2 and § 5.3, but with more general choices for the electromagnetic fields. We assume the electric field has the form

$$\boldsymbol{E} = \mathrm{e}^{\mathrm{i}(kz-\omega t)}(\psi\widehat{\boldsymbol{e}}_{\mp} + \varphi\widehat{\boldsymbol{e}}_{z}), \tag{5.12}$$

where the knot-carrying initial condition is in the transverse component $\psi$ when $z = 0$, which is either left-handed ($-$) or right-handed ($+$) circularly polarised. The corresponding magnetic field (times a factor of $c$ to ensure our scalar fields have the same physical dimension), is

$$c\boldsymbol{B} = \mathrm{e}^{\mathrm{i}(kz-\omega t)}(\overline{\psi}\widehat{\boldsymbol{e}}_{\mp} + \overline{\vartheta}\widehat{\boldsymbol{e}}_{\pm} + \overline{\varphi}\widehat{\boldsymbol{e}}_{z}), \tag{5.13}$$

which, unlike the electric field, has in general non-zero components in both right-handed and left-handed transverse components.

In keeping with § 5.3, we work in units of inverse optical wavenumber $k^{-1}$,

$$X = s^{-1}kx,\ Y = s^{-1}ky,\ Z = s^{-2}kz,$$

where $s$ is a dimensionless scaling factor, with the paraxial regime corresponding to $s \gg 1$. As we consider superposition of orbital angular momentum (OAM) eigenstates, it is further convenient to use complex helical coordinates $(\zeta, \zeta^*)$ in the transverse plane,

$$\zeta = \tfrac{1}{\sqrt{2}}(X + \mathrm{i}Y), \qquad \zeta^* = \tfrac{1}{\sqrt{2}}(X - \mathrm{i}Y) \tag{5.14}$$

$$X = \tfrac{1}{\sqrt{2}}(\zeta + \zeta^*), \qquad Y = -\tfrac{\mathrm{i}}{\sqrt{2}}(\zeta - \zeta^*). \tag{5.15}$$

From these assumptions, we can now find the relationships between the five fields $\psi, \overline{\psi}, \varphi, \overline{\varphi}, \overline{\vartheta}$ through Maxwell's equations. We assume $\psi$ is given as in § 5.3, from polynomial propagation of a polynomial initial condition at $Z = 0$. We will establish how the knotted field $\psi$ affects the symmetries of the other components in the extreme

regimes of large $s$ (paraxial) and limiting to 0 (highly nonparaxial). The symmetries of the function $\psi$ are transferred to the other components $\overline{\psi}, \varphi, \overline{\varphi}, \overline{\vartheta}$ in an overcrossing regime we call *bundle regime* and under the right assumptions each component inherits the knotted topology from $\psi$. This is demonstrated in the following.

First, from $\nabla \cdot \boldsymbol{E}$, we have

$$\varphi = \mathrm{i}s^{-1}\left[\left\{\begin{smallmatrix}\partial_\zeta \\ \partial_{\zeta^*}\end{smallmatrix}\right\}\psi + s^{-1}\partial_Z\varphi\right], \tag{5.16}$$

where the upper alternative occurs for the $\boldsymbol{E}$-field being left-handed polarised (—), and lower for right-handed polarised (+). Spin-orbit effects of course relate the helical coordinate derivatives to the helical polarisations. This equation has the solution

$$\begin{aligned}\varphi &= -s\mathrm{e}^{-\mathrm{i}s^2Z}\int^Z \mathrm{e}^{\mathrm{i}s^2Z'}\left\{\begin{smallmatrix}\partial_\zeta \\ \partial_{\zeta^*}\end{smallmatrix}\right\}\psi\mathrm{d}Z' \\ &= \frac{\mathrm{i}}{s}\left[\left\{\begin{smallmatrix}\partial_\zeta \\ \partial_{\zeta^*}\end{smallmatrix}\right\}\psi - \mathrm{e}^{-\mathrm{i}s^2Z}\int^Z \mathrm{e}^{\mathrm{i}s^2Z'}\left\{\begin{smallmatrix}\partial_\zeta \\ \partial_{\zeta^*}\end{smallmatrix}\right\}\partial_Z\psi\mathrm{d}Z'\right]\end{aligned} \tag{5.17}$$

where the second line follows by integration by parts. This step can be iterated again as needs be, introducing an extra factor of $s^{-2}$ each time; such terms are negligible in the paraxial limit, and dominant for small $s$, as discussed below.

The longitudinal component ($B_z$) of Faraday's law $\nabla \times \boldsymbol{E} + \partial_t \boldsymbol{B} = 0$ gives

$$\overline{\varphi} = \mp s^{-1}\left\{\begin{smallmatrix}\partial_\zeta \\ \partial_{\zeta^*}\end{smallmatrix}\right\}\psi, \tag{5.18}$$

which gives a direct relation between the longitudinal magnetic field and $\psi$.

The other two helical components of Faraday's law, combined with (5.18), give expressions for the remaining two fields

$$\overline{\psi} = \pm\left[\mathrm{i}\psi - s^{-1}\left\{\begin{smallmatrix}\partial_{\zeta^*} \\ \partial_\zeta\end{smallmatrix}\right\}\varphi + s^{-2}\partial_Z\psi\right], \tag{5.19}$$

$$\overline{\vartheta} = \pm s^{-1}\left\{\begin{smallmatrix}\partial_\zeta \\ \partial_{\zeta^*}\end{smallmatrix}\right\}\varphi. \tag{5.20}$$

The other Maxwell equations give no extra information. Further manipulation can be used to show all of the fields satisfy the reduced Helmholtz equation

$$0 = (\partial_\zeta\partial_{\zeta^*} + \mathrm{i}\partial_Z + \tfrac{1}{2}s^{-2}\partial_Z^2)\left\{\psi, \varphi, \overline{\psi}, \overline{\vartheta}, \overline{\varphi}\right\}, \tag{5.21}$$

as indeed they must.

We first consider the paraxial regime $s \gg 1$. (5.21) reduces to the paraxial equation $\partial_\zeta \partial_{\zeta^*} \bullet + \mathrm{i}\partial_Z \bullet = 0$. Also, (5.17) gives that $\varphi \approx \mathrm{i}s^{-1}\partial_\zeta \psi$ or $\mathrm{i}s^{-1}\partial_{\zeta^*}\psi$ and $\overline{\varphi} = \pm\mathrm{i}\varphi$. The transverse components of the magnetic field are $\overline{\psi} = \pm\mathrm{i}\psi$ and $\overline{\vartheta} \sim O(s^{-2})$. As expected, in the paraxial regime the longitudinal components of the beam ($z$) and the component of opposite handedness are negligible compared to principal transverse components and the electric and magnetic fields agree apart from a multiplicative factor that does not affect the vortex lines.

We now demonstrate that the symmetries of the torus knots' Milnor polynomials are transferred from $\psi$ to the other components of the beam. The trefoil knot field and most of the torus knot generalisations we consider have $\psi$ with the following form

$$\psi = \zeta^n + U(\zeta\zeta^*, Z), \tag{5.22}$$

where $U$ is some polynomial solution of (5.21) depending on $Z$ and $\zeta\zeta^*$. $\psi$ satisfies (5.21), since $\zeta^n$ is a solution of the 2D Laplace equation; this part of the beam does not change on propagation. For the case where $\psi$ multiplies $\widehat{\boldsymbol{e}}_+$, $\overline{\varphi}$ and paraxially $\varphi$ are proportional to $\partial_{\zeta^*}U = \zeta U'$ (with prime denoting derivative with respect to $\zeta\zeta^*$): an axisymmetric field times an axial vortex of strength 1. This shows that the sign of OAM in $\psi$ has to be opposite the sign of the transverse circular polarisation for the longitudinal component to have any degree of knot-like complexity in its amplitude structure.

On the other hand, in the case we mainly consider where $\psi$ multiplies $\widehat{\boldsymbol{e}}_-$, $\overline{\varphi}$ and paraxially $\varphi$ are proportional to $n\zeta^{n-1} + \zeta^* U' = \zeta^*[n\zeta^n + (\zeta\zeta^*)U']/(\zeta\zeta^*)$, which consists of an axial vortex of negative strength times a torus knot-like field with the same degree of rotational symmetry as $\psi$; this was indeed what was found for the trefoil knot case, and the properties generalise to the other torus knots quite directly. We have not proved that the field $n\zeta^n + (\zeta\zeta^*)U'$ has a knot in its nodal structure, although it was in our main trefoil knot example, and in the other torus knots reported in Table 2.

As $s$ varies into the nonparaxial regime, the longitudinal $B$-field retains the same relationship to $\psi$ as its derivative by (5.18). However, the relationship between the transverse and longitudinal $E$-field incurs more terms times $s^{-3}$, $s^{-5}$, .... In the extreme nonparaxial limit $s \ll 1$, from (5.17) the dominant term in $\varphi$ is proportional to $\partial_\zeta \partial_Z^N \psi$ (where $N$ is the maximum integer which gives a non-zero expression): this gives $\zeta^*$ times an axisymmetric function, agreeing with Figure 3 (f) for the case of the trefoil. An analogous argument can be made for $\overline{\psi}$ in the extreme nonparaxial limit, where $\overline{\psi} \approx -s^{-1}\partial_{\zeta^*}\varphi + s^{-2}\partial_Z \psi$, which for the knot function (5.22) is axisymmetric, represented in Figure 3 (g).

This discussion shows that the features discussed in the previous sections for the specific example of the trefoil knot are in fact more general, and apply to other torus knots whose $\psi$ function has the Milnor form (5.22), specifically that: in the paraxial regime, all non-zero components have a nodal knot that follows the same curve in space; the longitudinal components have a negative strength axial vortex for transverse polarisation $\widehat{\boldsymbol{e}}_-$, and a positive axial vortex for $\widehat{\boldsymbol{e}}_+$; the behavior of the longitudinal magnetic field is closer to the main transverse electric field component than the longitudinal electric component; in the extreme nonparaxial limit, the transverse magnetic field becomes axisymmetric, and the longitudinal electric field becomes axisymmetric times a negative vortex; where the last three cases hold for $\psi$ with positive OAM and polarisation $\widehat{\boldsymbol{e}}_-$.

These facts all support the suggestion that in the crossover regime where $s \approx 1$, there will be a nontrivial nodal topology occupying a similar focal volume in all the components. The knot-like nodal lines in this bundle regime are shown in Figure 5.7 (a) for $\varphi$, (g) for $\overline{\psi}$, and (j) for $\overline{\varphi}$ (which are trefoil knots) and $\overline{\vartheta}$ in (d) which, although possessing the right symmetries, is not knotted. Hence we anticipate a bundle structure for other kinds of torus knot; the knot type in their corresponding $E_z$ is reported in Table 2. The transition of the lines from the knot bundle topology to the topology of the extreme nonparaxial regime ($s \ll 1$) for $\varphi$, $\overline{\vartheta}$ $\overline{\psi}$, and $\overline{\varphi}$ is shown in Figure 5.7.

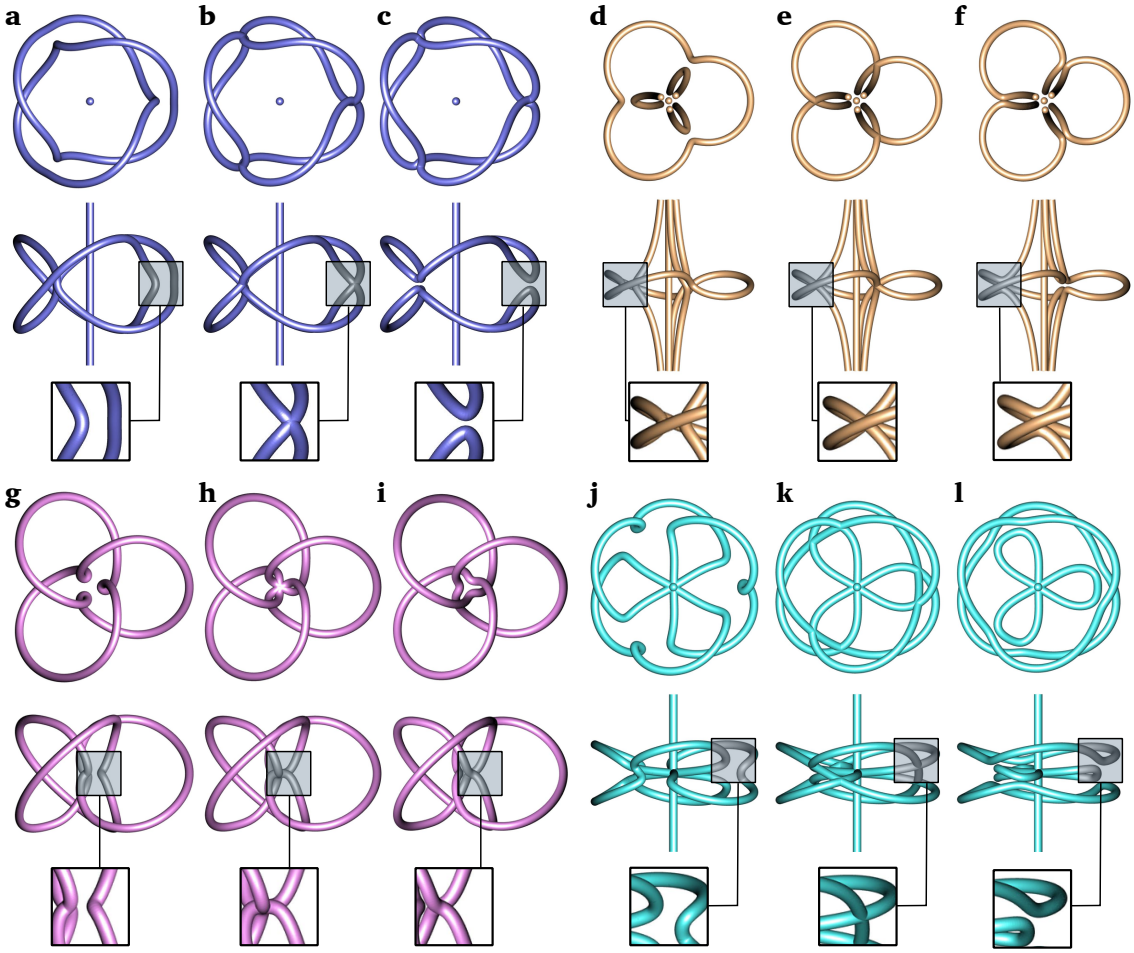


Figure 5.7: **Reconnection events transforming the vortex lines in $\varphi$, $\overline{\vartheta}$, $\overline{\psi}$, $\overline{\varphi}$ for the trefoil knot**. The parameter $s$ is decreased and topological reconnection occur at different values for the different components. (a) The trefoil knot in $\varphi$ at $s = 1.200$ (b) touches at three points at $s = 1.163$ and (c) splits into two circles showed at $s = 1.115$. The nodal lines of $\overline{\vartheta}$ are not knotted at any value of $s$, however (e) topological reconnections occur at $s = 0.911$; the dynamic of the events is shown for (d) $s = 0.920$ and (f) $s = 0.900$. (g) The trefoil knot in $\overline{\psi}$ at $s = 2.680$, (h) reconnects at the origin for $s = 2.647$ and (i) transforms into three linked rings, shown at $s = 2.620$. (j) The trefoil structure in $\overline{\varphi}$ at $s = 0.610$, (k) reconnects at $s = 0.556$ and (l) splits into another trefoil-like knot and two loops shown at $s = 0.535$.

The reconnections happen at different values of $s$ for the different components.

A slightly more general field, including the (3,2), (4,2) and (5,2) examples in Table 2, has the form $\zeta^m V(\zeta\zeta^*, Z) + U(\zeta\zeta^*, Z)$. Fields with a knotted $\psi$ of this form do

not quite have all the properties described above. In particular, the axial component may be complicated and even knotted for $\psi$ if this form combined with $\widehat{\boldsymbol{e}}_+$. In the examples in the table, the knot in the longitudinal component $\varphi$ is of a simpler torus knot type than the transverse field, reflecting the effects of $V(\zeta\zeta^*, Z)$ on the field. We will not describe the properties of these fields further here, but it is straightforward to do so using similar analysis.

Finally, we note that our analysis here may be used to approach the problem described recently in [170], which may be paraphrased in the present terminology as "how can we determine $\psi$ such that $\varphi$ is a desired knotted field?" Taking the desired $\varphi$ to be (5.22), we can see immediately from (5.16) that, for $\widehat{\boldsymbol{e}}_-$ polarisation,

$$\psi = -\int^{\zeta} (\mathrm{i}s\varphi + s^{-1}\partial_Z\varphi)\mathrm{d}\zeta', \tag{5.23}$$

which can be calculated directly from our polynomial $\varphi$. A cursory numerical investigation of this $\psi$ has an axial vortex and a nodal knot (as it must) for large $s$, but the knot structure breaks down for $s \approx 1$, leading to a system of concentric rings around the axial vortex. We note that the approach in [170] assumed the transverse polarisation was linear, hence the analysis there is somewhat more complicated, and the present approach based on helical states can readily be adapted to the linear transverse polarisation case.

## 5.6 Discussion

We have shown how nonparaxiality and tight focusing affects the optical vortex torus knots of [18]. At small sizes, polarisation effects become important, revealing a new sort of knotted optical field enclosing a complicated structure we call a singular knot bundle. In order to establish the generality of the knot bundle, we investigated two different kinds of nonparaxial electromagnetic fields. Polynomial beams [84] give an analytic expression in the neighborhood of the knot, thereby revealing general behavior of the optical vortex topology, whereas numerically propagated tightly focused

Laguerre-Gaussian beams [81,97] describe a more physically accessible situation realisable in experiments. Although we mainly focused on the specific example of the trefoil knot, in § 5.5 we outline a general argument establishing bundles of torus knotted polarisation singularities as general in appropriate superpositions of nonparaxial, circular polarised beams. The bundle is a topological object, where the nodal lines in each component of the electric and magnetic fields are simultaneously knotted in a similar volume (the knots are not necessarily of the same type). Its presence is hidden in the paraxial regime in which electric and magnetic vortex knots collapse and some components are negligible, so the knot bundle effectively behaves like one single vortex line. We identified a particular regime—the bundle regime—in which all the different knots become entities in their own right because the electromagnetic energy is distributed equivalently in all the components. We expect this phenomenon to extend to other, more complicated knots (including non-torus knots such as the figure-eight knot), suggesting this nonparaxial polarisation structure adds to the menagerie of knotted electromagnetic fields. In particular, other knotted physical quantities related to knotted light are the time-dependent electromagnetic field lines and their related null lines [20,21] and the static optical vortex lines of complex scalar fields [14–16,18] (the latter construction was extended to the longitudinal component of nonparaxial beams in [170]).

Instead of tracking the nodal lines of each component of the electric and magnetic field in the canonical helical basis, our topological tools could be used to account for singularities that are independent of the choice of basis, such as $\mathrm{C}^{\mathrm{T}}$ lines and $\mathrm{L}^{\mathrm{T}}$ lines [103]. It is known that in the perfect paraxial regime C and $\mathrm{C}^{\mathrm{T}}$ lines sit together and as they move to the nonparaxial regime they form clusters of polarisation singularities [43]. In the polynomial beams, we assumed $E_+$ to be exactly zero everywhere and the longitudinal component to be non-negligible; with these assumptions the nodal lines of $E_-$ are $\mathrm{L}^{\mathrm{T}}$ lines (the electric field is only longitudinal along those lines) and the nodal lines of $E_z$ are $\mathrm{C}^{\mathrm{T}}$ lines (the electric field is purely left-handed

circular along those lines). On the other hand, the magnetic field has also a right-handed component; hence, its polarisation singularities are not *true* with respect to the 3D vector and the nodal lines of $B_+$ and $B_-$ are C lines (only the transverse vector is circularly polarised) and the nodal lines of $B_z$ are points along which the field is purely transverse (mixture of right and left-handed polarisation states). The polarisation on the optical axis is purely left-handed circular for both $\boldsymbol{E}$ and $\boldsymbol{B}$ since all the other components are null (it truly behaves like an optical vortex line). However, in tightly focused beams the topology of $C^T$ and $L^T$ lines is not this obvious. A preliminary analysis of the $C^T$ lines of our numerically propagated fields do not show knots, but other interesting conformations such as loops and lines intertwining the optical axis. On the other hand, the $L^T$ lines do not present any topology of interest, mainly because the knotted condition is extremely hard to achieve for these type of singularities. Overall our results indicate that the topology of tightly focused beams is very rich and much more could be revealed by the topological analysis of the singularities of other physical quantities. Beam parameters could potentially be optimised to structure these various kinds of polarisation singularities, such as the time averaged and instantaneous Poynting vector, optical field lines and the Riemann-Silberstein vector.

Our theoretical analysis revealed the presence of a bundle regime, for which the energy is approximately equally distributed between all the components of the beam. Since no component has a negligible amplitude distribution, this range seems to be ideal not only from the point of view of topology but also that of experiments. We proposed an experimental scheme to generate the bundle regime and we highlighted the difficulties to create the right balance between the experimental parameters for the generation of the singular knot bundle. Our experimental setup was adapted from that of previous paraxial optical vortex knot experiments [18], with the difference that the beam is tightly focused by a microscope objective and its initial polarisation state is circular. As with all experiments shaping superoscillatory phenomena [143], the beam should be accurately structured at subwavelength scale and imperfections such as ab-

errations should be reduced to a minimum, and the low amplitude around the nodal structures needs to be resolved and distinguished from the CCD camera noise. Measuring the 3D structure of the 3D polarisation field in the focal volume also presents an experimental challenge; this might be approached via 3D nano-tomography similar to [171]. An alternative way to generate and detect these optical knotted fields could be via single photon measurements; the experimental methods of [146, 172] could be adapted to the nonparaxial regime.

The knotted structures we describe, for the $(m, n)$-torus knots, occur in superpositions of two OAM eigenstates $\ell = 0$ and $\ell = n$, and knots in similar fields, at the single photon level, were previously used as a basis for spatial measures of quantum entanglement [146]. In nonparaxial propagation, azimuth-dependent effects ('orbital') becomes strongly coupled with polarisation ('spin') [158]. The singular knot bundle may therefore be considered as a particular macroscopic 3D manifestation of optical spin-orbit interaction, when the OAM has an opposite sign from the spin. This kind of structured, tightly focused light might be used to induce circular dichroism into chiral and nonchiral structures in order to provide morphological information of certain nanoscale structures, such as proteins [173] , metamaterials [174] and plasmonic systems [175, 176].

Our investigation of small optical vortex knots, originally motivated by imprinting optical knots into matter, has led to the discovery of the polarisation bundle as a quite general phenomenon in knotted light fields where the aspect ratio of the knot is approximately unity. The singular knot bundle's stability in various nonparaxial beams demonstrates its robustness to perturbations of diverse origins and is worth investigating further. It would be interesting to investigate how such 3D spatially-varying polarisation fields affect materials that reorient with respect to the polarisation direction, such as azobenzene polymers [177–179]. Embedding the singular knot bundle into soft-materials or quantum physical systems might reveal new features of light-matter interaction and could be used to store topological states [180]. Since photons

are robust, fast, and readily available, they represent ideal carriers of quantum information. On the other hand, atoms are long-lived and reliable storage and processing units. Hence, the challenge is to develop a technique for coherent transfer of quantum information carried by light to atoms and vice versa [181].

The theoretical methods presented in this chapter aim to be as close as possible to the experimental routines currently used in structured light where Laguerre-Gaussian modes seem to be the basis of preference. Nevertheless, we reported in § 4.3 that polynomial beams could effectively represent superoscillatory interference structures close to the axis within a beam with a wide envelope, not only a Gaussian, but also, for instance Bessel beams [55, 56], and alternative envelopes could be designed to fit a specific experimental setup. For example, by exploring Richards-Wolf propagation theory further, the inverse problem could be solved in a more sophisticated way to generate new holograms for knotted beams. This motivates the work presented in the next chapter, in which we adopt Bessel functions and Zernike aperture modes as tools to structure tightly focused fields.

# 6 | Knotted Hopfions in 3D polarisation textures

**...the results to which they lead us, shew strikingly how small foundation there was for the original objection to the undulatory theory of light, viz. that if waves spread equally in all directions, ther could be no such thing as darkness.**

*George Biddell Airy*

In § 4.3, Zernike modes were used to structure efficiently optical fields diffracted from an aperture. In chapter 5, a bundle of entwined knots corresponding to the nodal lines of the electric and magnetic field components was shown to arise in the focal volume of tightly focused beams. In this chapter, the behaviour of the Zernike aperture modes in the tightly focused regime is explored. Hopf fibrations, which are characterised by integer Hopf indices, are shown to manifes 'naturally' in the polarisation texture of dark beams. Further, optical Hopfions are engineered in the paraxial regime and an experiment to confirm our predictions is presented[1]. Additional properties of Hopf fibrations and the physical systems in which they are found were described in previous chapters, respectively, in § 3.3 and § 1.7.

[1]The experimental system was designed and respective experimental results were achieved in collaboration with Ramon Runde and Eileen Otte of the group of Prof. Cornelia Denz, Institute of Applied Physics, University of Münster, Germany. R. Runde performed the measurements.

## 6.1 Dark focus: a diffraction phenomenon

Nontrivial knotted singular structures can arise in the focal volume of a high numerical aperture aplanatic system (chapter 5), which is characterised by a vectorial behaviour (§ 2.2.3). This chapter further explores the topology of tightly focused beams, with particular attention to the diffraction patterns originated from a circular aperture illuminated with non-uniform intensities.

When polarised beams are tightly focused, the focal volume is filled with inhomogeneous polarisation distributions; this means that the electric and magnetic vector fields are characterised by polarisation states that differ from point to point in the focal volume. Hence, the polarisation distribution in the focal volume does not usually present an ordered pattern. Cases of ordered distribution of polarisation states exist and they are denoted *polarisation textures*. An example of a polarisation texture is given by the class of full Poincaré (FP) beams [182,183]. They are optical fields whose polarisation at any transverse plane spans a disk-like region showing all the possible states represented by the Poincaré sphere (§ 2.1.7). The Poincaré sphere collapses into a disk that either rotates, expands or contracts under propagation. Another 2D polarisation texture is given in [184] in the form of a topological soliton.

Here, the topology of 3D polarisation textures arising in the focal volume of tightly focused Zernike aperture modes (§ 2.1.5) is analysed. These beams embed a whole family of Hopf fibrations differentiated by the value of the Hopf index (§ 3.3). The maps fibres are defined as the preimages of the points on the Poincaré sphere (lines characterised by the same polarisation state) and correspond to the torus knots and links. These topological objects are *knotted Hopfions in polarisation textures*. Figure 6.1 shows the toroidal surface generated by the linear polarisation states of the tightly focused Zernike mode $Z_{6,0}$. This is part of a volume filling Hopfion whose fibres are trefoil knots. The figure reports the intensity distributions on the faces of a cube with edge size $2\lambda$, on which the dark features of the focus can be observed. The phys-

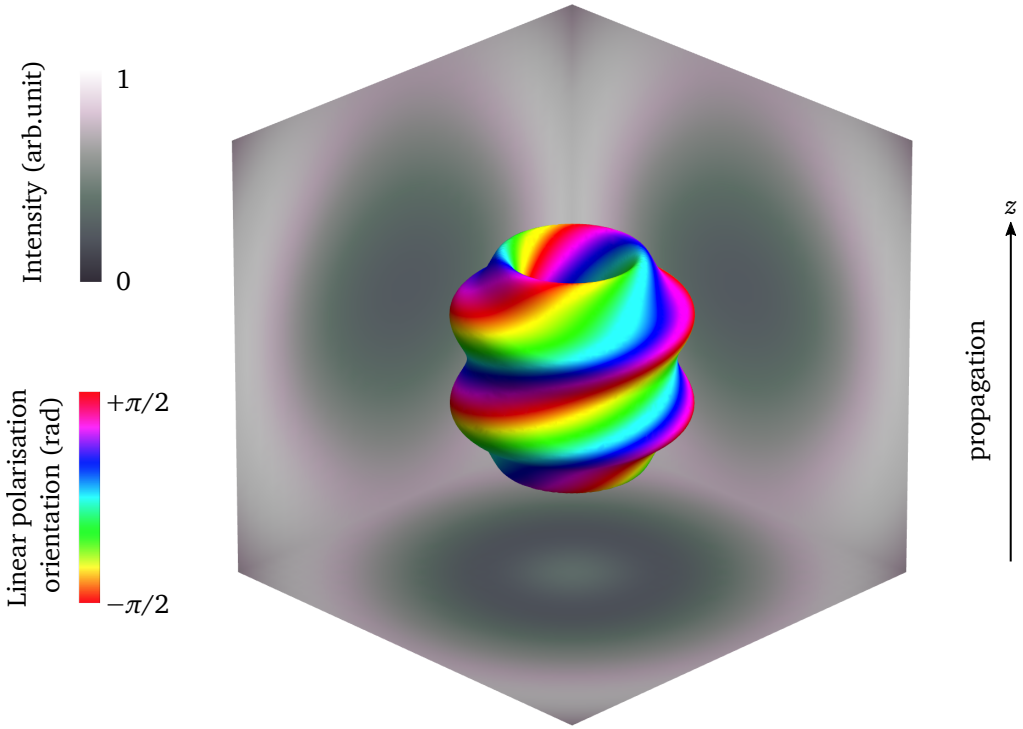


Figure 6.1: **Trefoil-knotted Hopfion in the polarisation texture of a dark beam**. A subwavelength Hopf fibration is found in the 3D polarisation distribution of the focal volume of a tightly focused Zernike mode. The plot shows the intensity at the faces of a cube of volume $(2\lambda)^3$. The hue colours represent the orientation of the linear polarisation states. This volume filling topological structure is a manifestation of superoscillations in dark beams, similar to optical vortex knots.

ical system in which this Hopfion is found is schematised in Figure 6.2. A beam with azimuthally-symmetric amplitude distribution given by $Z_{6,0}$ and uniform circular polarisation is sent to the backfocal plane of a microscope objective with high numerical aperture. The 3D focal volume originated by the tight focusing of such beam profile is characterised by a dark region whose topology is that of the Hopf fibration. The full focal volume generated by the tight focusing of single Zernike polynomials will be determined and an analytic model to describe the Hopf fibrations will be presented. We will introduce analytic propagation methods based on Richards and Wolf vector diffraction theory (§ 2.2.3) and ENZ-theory (§ 2.2.2).

The dark features of a tightly focused Zernike mode can be thought of as a *dark*

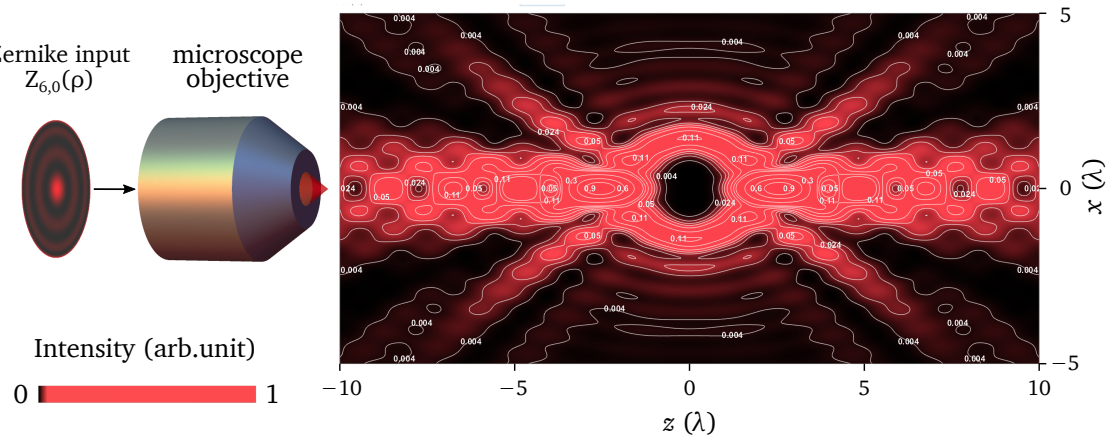


Figure 6.2: **Dark focus generated by a tightly focused Zernike polynomial.** A beam with amplitude given by the Zernike polynomial $Z_{6,0}(\rho)$ and characterised by uniform circular polarisation is sent to the back focal plane of a microscope objective of high numerical aperture ($\gamma = 0.9$). The beam is tightly focused in the $z$ direction. The volume around the focal point ($x = y = 0$) is a dark focus of a few wavelengths in size, which is characterised by a much lower intensity compared to the outer region. The total intensity distribution in the $xz$-plane is plotted, as well as the white lines representing its contours.

*focus*, in contrast with the bright focus arising from a tightly focused plane wave. In fact, when the Zernike modes are incident on the aperture of a lens and propagated paraxially, they generate a family of dark beams represented by Bessel functions of the first kind $J_{n+1}(R)/R$, with $n > 0$ (§ 2.2.2). These are the simplest examples of dark beams because they are characterised by intensity distributions that are zero at $R = 0$. Propagating Zernike modes preserve their dark features in the tightly focused regime (as shown by Figure 6.2). The spin to orbit conversion given by the lens system perturbs the dark foci and generates Hopfion-like structures in the focal volume. This demonstrates that the *natural knotting* of azimuthally-symmetric Zernike modes is induced by the spherical geometry of the lens, which introduces azimuth-dependent components to the vector field. This is analogous to the singular knot bundle presented in the previous chapter, where the interplay between the orbital angular momentum and spin angular momentum was shown to play an important role in the formation

of Milnor-like knotted optical fields. Therefore, Hopfions arise as the effect of the spin-orbit conversion in tightly focused circularly polarised dark beams.

The Zernike polynomial with $n = 0$ does not generate a dark beam under propagation, but simply corresponds to a plane wave incident on the aperture of the lens. Airy's classical result [185] shows that the corresponding light distribution in the focal plane is given by the Fraunhofer diffraction on the aperture of the lens. This is mathematically represented by the Bessel function $J_1(R)/R$ in the paraxial regime [30], which corresponds to a bright focus. The full three-dimensional light distribution near the focus (out-of-focus) for the diffracted plane wave was first calculated in detail by Lommel in [186, 187]. Similar analysis were published by Struve and Schwarzschild [30], but the most famous treatment of this problem was given by Debye in 1909 [90, 91]. The intensity and phase derived by these calculation was treated in detail in [30]. The bright focus arising from the Zernike $Z_{0,0}$ does not show any topology of interest, as demonstrated by the original plots of Wolfs reported in Figure 6.3.

The restriction of uniform amplitude from Lommel's treatment was removed by Hopkins in 1949 [188]. The diffraction theory of light by an aperture was remarkably advanced in the 1930-1940's by the joint work of Zernike and Nijboer. However, Zernike and Nijboer did not think of Zernike polynomials in the terms described above. They used Zernike polynomials to represent the wavefront aberration of a focused beam. They derived the complex amplitude distribution in the focal plane by their integral result (2.19) and balanced the undesired aberrations. Here, Zernike polynomials are considered as light modes in their own right. The diffraction pattern associated with a single Zernike aberration was analysed by Wolf [30]. However, the aberration representing a little deviation of the wavefront from a sphere was small and was represented by an exponential function in which Zernike polynomials were included in the exponent. These limits in the aberration function were removed by Janssen in 2002, who extended the Nijboer-Zernike diffraction theory to arbitrary large aberrations [89] and established ENZ-theory (§ 2.2.2). The major contribution

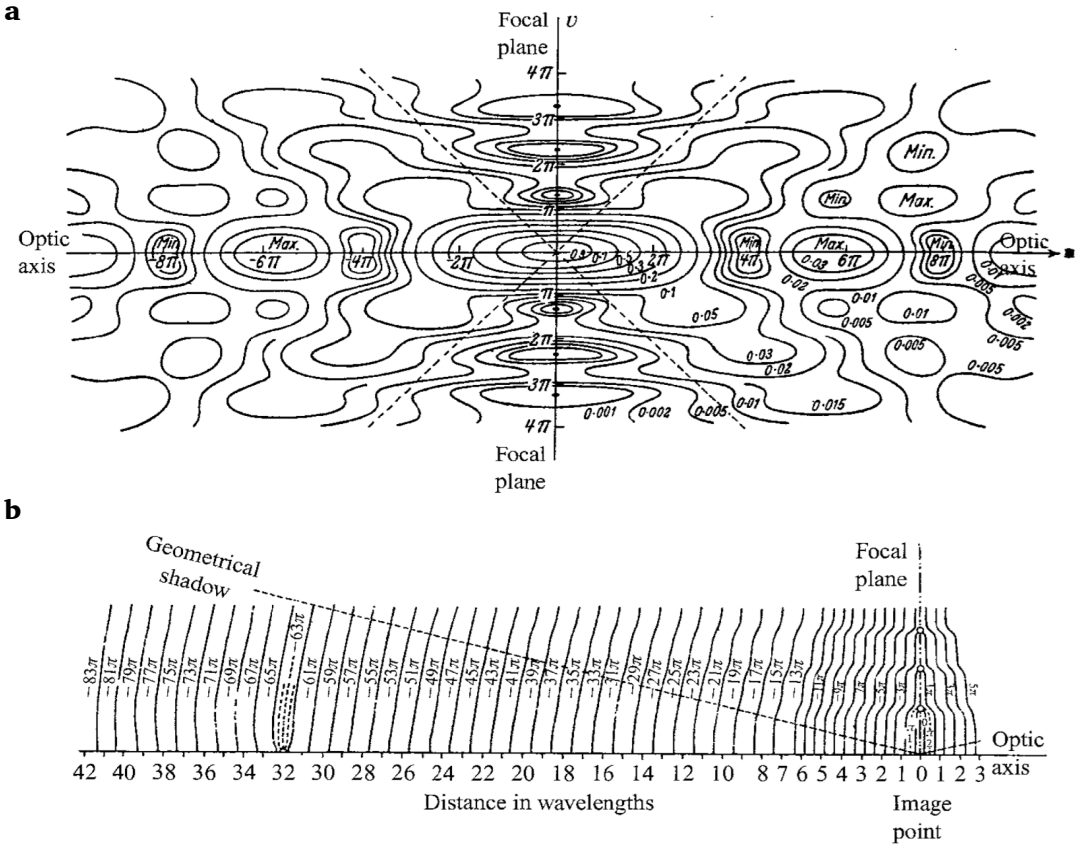


Figure 6.3: **Propagating Airy pattern**. The paraxial propagation of a plane wave incident on a circular aperture gives a diffraction pattern showing a bright focus. This is surrounded by the Airy dark rings, which lie on the focal plane. (a) The contours of the intensity and (b) the phase of the focused field at the $xz$-plane ($uv$ in the graphs) are plotted. Images from [30].

of Janssen was to remove the Zernike polynomials from the exponential and use them as a basis to express the complex amplitude of the field. ENZ-theory includes a treatment of the 3D paraxial propagation of single Zernike aperture modes in [89, 93].

Diffraction patterns arising from circular apertures are still topic of modern research. Dark beams of light were studied by Bokor and Davidson, who described a method to generate a dark focal spot surrounded by light intensity in all directions [189]. Lekner defined a new type of beam whose complex function has rings of zeros in the focal plane [190]. The topology of phase and polarisation singularities in focal regions was discussed in some detail in [191]. However, in most of these

applications of diffraction theory to optics, light is considered as a scalar wave phenomenon and the polarised nature of light around the focus is ignored. Tightly focused Zernike aperture modes were considered in [162, 192] where, however, the topology of a single polynomial has not been investigated.

The rest of this chapter is structured as follows. § 6.2 presents the topological and optical analytic tools developed to analyse 3D polarisation textures in dark beams of light. § 6.3 presents a whole family of knotted and linked Hopfions arising naturally from tightly focused Zernike aperture modes. The numerical results and a topological model of the beams are reported. § 6.4 generalises the findings to paraxial Hopfions to shape the polarisation texture of transverse light by using algebraic topology. Furthermore, preliminary experimental results based on the theoretical predictions are proposed. § 6.5 contains the discussion of the outcomes.

## 6.2 Theoretical methods

This section develops the theoretical methods used in § 6.3 and § 6.4 to analyse the topology of optical knotted Hopfions in the tightly focused and paraxial regimes. Section § 6.2.1 reports an analytic solution to Richards and Wolf vector diffraction integral (2.55) in a method we call SWAS theory. Another solution to the same vector integral is given in § 6.2.2: the method is the nonparaxial version of ENZ-theory (§ 2.2.2). In § 6.2.3, a compact and simple formula for the calculation of the Hopf index (§ 3.3) is presented.

### 6.2.1 The Spin-Weighted Angular Spectrum (SWAS) theory of focusing

Historically, before the Debye–Wolf integral was rearranged into a fast Fourier transform (FFT) form, which can be computed at high speed [99], the evaluation of the vector diffraction integral (2.53) was a rather time-consuming assignment. Series

expansion methods have been proposed to avoid the evaluation of the integral. The most known and used theory of focusing was introduced by Sheppard and Török [193] and consists in a multipole expansion; further information can be found in [194]. The method has been used in the calculation of Mie scattering by nanoparticles [195] accompanied by experimental applications [166]. This was a major breakthrough in the experimental detection of electromagnetic vector fields in subwavelength scale focal volumes [171].

### Multipole expansion of vector plane waves

Multipoles can be defined in different ways depending on the definition of the vector spherical harmonics; the formalism of [196] is used here. Spherical harmonics are defined in the spherical angular coordinates $0 \leq \varphi < 2\pi$, $0 \leq \vartheta \leq \pi$ as follows

$$Y_{\ell m}(\vartheta, \varphi) = \sqrt{\frac{2\ell+1}{4\pi}\frac{(\ell-m)!}{(\ell+m)!}} P_\ell^m(\cos\vartheta) \mathrm{e}^{\mathrm{i}m\varphi}, \tag{6.1}$$

where $P_\ell^m(z)$ is an associated Legendre polynomial of indices[2] $\ell$ and $m$. Vector spherical harmonics are defined as [196]

$$\boldsymbol{Y}_{\ell m} = \sqrt{\frac{1}{\ell(\ell+1)}} \boldsymbol{L} Y_{\ell m} \tag{6.2}$$

with $\ell \neq 0$ and the angular momentum operator $\boldsymbol{L} = -\mathrm{i}\boldsymbol{r} \times \boldsymbol{\nabla}$ in units of $\hbar$. The magnetic multipole fields, also called transverse electric (TE) fields (since the radial electric field vanishes), are defined as

$$\boldsymbol{M}_{\ell m}(r, \vartheta, \varphi) = j_\ell(kr) \boldsymbol{Y}_{\ell m}(\vartheta, \varphi), \tag{6.3}$$

where $r$ is the radial spherical coordinate, $k$ is the optical wavenumber and $j_\ell(kr)$ is a regular spherical Bessel function $j_\ell(z) = \sqrt{\pi/(2z)} J_{\ell+1/2}(z)$. The electric multipole fields, also called transverse magnetic (TM) fields, are defined as

$$\boldsymbol{N}_{\ell m}(r, \vartheta, \varphi) = -\frac{\mathrm{i}}{k} \boldsymbol{\nabla} \times \boldsymbol{M}_{\ell m}(r, \vartheta, \varphi). \tag{6.4}$$

[2] In order to be consistent with the literature, the index $\ell$ corresponds to the total angular momentum, unlike the previous chapters where $\ell$ was associated with the orbital angular momentum of optical beams.

As mentioned above, it is known that a tightly focused field can be expanded in electric and magnetic multipoles [193]. Given the angular spectrum (2.29), it is reasonable to ask what the plane wave decomposition of the multipoles looks like. Scalar plane waves are expressed as sums of spherical waves via the following Rayleigh expansion

$$\mathrm{e}^{\mathrm{i}\boldsymbol{k}\cdot\boldsymbol{r}} = 4\pi \sum_{\ell m} \mathrm{i}^{\ell} j_{\ell}(kr) Y^{*}_{\ell m}(\widehat{\boldsymbol{k}}) Y_{\ell m}(\widehat{\boldsymbol{r}}). \tag{6.5}$$

The vectorial analog to this expansion can be defined in different ways. A particular treatment is given in [197], but the formalism of [196] is used here. The multipole expansion of vector plane waves is found directly by coupling in the spin-1 basis functions using the Wigner coefficients. The expansion is given in the helical basis[3] $\widehat{\boldsymbol{\xi}}_p = \sqrt{1/2}(\widehat{\boldsymbol{e}}_{\vartheta} + \mathrm{i}p\widehat{\boldsymbol{e}}_{\varphi})$ where $p$ takes values $\pm 1$, as follows

$$\mathrm{e}^{\mathrm{i}\boldsymbol{k}\cdot\boldsymbol{r}}\widehat{\boldsymbol{\xi}}_p = \sum_{\ell=1}^{\infty}\sum_{m=-\ell}^{\ell} \mathrm{i}^{\ell}\sqrt{2\pi(2\ell+1)} D^{\ell}_{mp}(\varphi,\vartheta,0)\left[\boldsymbol{M}_{\ell m}(\boldsymbol{r}) + \mathrm{i}p\boldsymbol{N}_{\ell m}(\boldsymbol{r})\right], \tag{6.6}$$

where $D^{\ell}_{mp}(\varphi,\vartheta,0)$ are Wigner $D$-functions $D^{\ell}_{ms}$ defined in terms of the Euler angles with the conventions of [196, 198–200] as[4]

$$D^{\ell}_{ms}(\varphi,\vartheta,\psi) = \mathrm{e}^{-\mathrm{i}m\varphi} d^{\ell}_{ms}(\vartheta)\mathrm{e}^{-\mathrm{i}s\psi}, \tag{6.7}$$

$$\begin{aligned} d^{\ell}_{ms}(\vartheta) = (-1)^{m-s}&\sqrt{(\ell+s)!(\ell-s)!(\ell+m)!(\ell-m)!} \\ &\times \sum_{j=\max(0,m-s)}^{\min(\ell+s,\ell-m)} (-1)^{j} \frac{\cos^{2\ell+s-m-2j}\left(\frac{\vartheta}{2}\right)\sin^{m-s+2j}\left(\frac{\vartheta}{2}\right)}{(m-s+j)!(\ell+s-j)!(\ell-m-j)!j!}, \end{aligned} \tag{6.8}$$

where $s$ is the spin weight, which is $\pm 1$ in our optical systems.

Our treatment consists in rearranging (6.6) in the same form as its scalar version (6.5). We start by noticing that the Wigner $D$-functions hold an important relationship with a family of functions called spin-weighted spherical harmonics ${}_sY_{\ell m}$, which are a complete orthonormal basis [201]. As such, they are orthogonal over the entire sphere

$$\int_0^{\pi}\int_0^{2\pi} {}_sY_{\ell m}(\vartheta,\varphi)\,{}_sY^{*}_{\ell' m'}(\vartheta,\varphi)\sin\vartheta\, d\varphi\, d\vartheta = \delta_{\ell\ell'}\delta_{mm'} \tag{6.9}$$

[3] Our definition of $\widehat{\boldsymbol{\xi}}_p$ equals that of [196] by a multiplication factor $-p$.

[4] Our convention adopts the Condon-Shorley phase for the spherical harmonics.

and they satisfy the completeness relation. The relationship between the spin-weighted spherical harmonics and the Wigner $D$-functions is

$$ {}_sY_{\ell m}(\vartheta,\varphi) = (-1)^m \sqrt{\frac{2\ell+1}{4\pi}} D^{\ell}_{-ms}(\varphi,\vartheta,-\psi)\mathrm{e}^{-\mathrm{i}s\psi}. \tag{6.10} $$

Since ${}_sY_{\ell m}(\vartheta,\varphi)^* = (-1)^{s+m}\,{}_{-s}Y_{\ell -m}(\vartheta,\varphi)$ we can rearrange (6.10) as

$$ {}_sY^*_{\ell m}(\vartheta,\varphi) = (-1)^s \sqrt{\frac{2\ell+1}{4\pi}} D^{\ell}_{m-s}(\varphi,\vartheta,\psi)\mathrm{e}^{-\mathrm{i}s\psi}. \tag{6.11} $$

This expression was derived by Challinor *et al.* in [202].

We then define a new basis set given by mixed vector spherical harmonics in a similar fashion to [203]. Expression (6.6) suggests that a convenient superposition is

$$ \boldsymbol{CK}^p_{\ell m} = \frac{1}{\sqrt{2}}\left(\boldsymbol{M}_{\ell m} + \mathrm{i}p\boldsymbol{N}_{\ell m}\right). \tag{6.12} $$

We denote the basis by $\boldsymbol{CK}^p_{\ell m}$ because it corresponds to a well known set of eigenfunctions of the curl operator called Chandrasekhar-Kendall states [204]. As such, they satisfy the following

$$ \boldsymbol{\nabla}\times\boldsymbol{CK}^p_{\ell m} = pk\boldsymbol{CK}^p_{\ell m}, \tag{6.13} $$

where the eigenvalue is given by positive or negative wavenumber. These states are very important in plasma physics [205] and fluid dynamics [206], and they have been used more recently to represent optical knotted field lines [20]. A vector plane wave expansion in CK-eigenfunctions with coefficients proportional to the spin-weighted spherical harmonics is obtained by inserting (6.11) and (6.12) into (6.6), as follows

$$ \mathrm{e}^{\mathrm{i}\boldsymbol{k}\cdot\boldsymbol{r}}\widehat{\boldsymbol{\xi}}_p = -4\pi\sum_{\ell m}\mathrm{i}^{\ell}\,{}_{-p}Y^*_{\ell m}(\widehat{\boldsymbol{k}})\boldsymbol{CK}^p_{\ell m}(\boldsymbol{r}). \tag{6.14} $$

### Analytic solution to Richards-Wolf vector diffraction integral

The result (6.14) is applied to Richards and Wolfs vector diffraction integral (§ 2.2.3). This gives an analytic solution expressed as a superposition of CK-eigenfunctions. An aplanatic optical system of numerical aperture $\gamma$ is considered

here. $\boldsymbol{E}_\infty$ is the angular spectrum corresponding to the paraxial field $\boldsymbol{E}^{\text{inc}}$ incident on the aperture of the lens, $k$ is the wavenumber. We start by rearranging the vector diffraction integral (2.55) in spherical coordinates $\boldsymbol{r} = (r, \theta, \phi)$ and $\boldsymbol{k} = (k, \vartheta, \varphi)$. Since $dk_x\, dk_y = k^2 \cos\vartheta \sin\vartheta d\varphi\, d\vartheta$, this is

$$\boldsymbol{E}(r, \theta, \phi) = \mathrm{e}^{-\mathrm{i}kf} \frac{\mathrm{i}kf}{2\pi} \int_0^{\vartheta_{\max}} \int_0^{2\pi} \boldsymbol{E}_\infty(\vartheta, \varphi)\, \mathrm{e}^{\mathrm{i}kr\cos(\varphi-\phi)\sin\vartheta\sin\theta} \mathrm{e}^{\mathrm{i}kr\cos\vartheta\cos\theta} \sin\vartheta\, d\varphi\, d\vartheta, \tag{6.15}$$

where $\vartheta_{\max} = \sin^{-1}\gamma$ is the one-half angular aperture of the lens. It is also convenient to rearrange the angular spectrum in helical components $\widehat{\boldsymbol{\xi}}_\pm$. This is because they appear in (6.14), but more importantly the angular spectrum is a vector field tangent to the reference sphere, therefore it can be represented in helical components as $\boldsymbol{E}_\infty = \sum_p (E_\vartheta - \mathrm{i}pE_\varphi)\widehat{\boldsymbol{\xi}}_p$. In the helical basis the relationship between and the angular spectrum and the incident field (2.54) simplifies to

$$\boldsymbol{E}_\infty = \begin{pmatrix} \xi_+ \\ \xi_- \end{pmatrix} = \sqrt{\cos\vartheta} \begin{pmatrix} \mathrm{e}^{\mathrm{i}\varphi} & 0 \\ 0 & \mathrm{e}^{-\mathrm{i}\varphi} \end{pmatrix} \begin{pmatrix} E_+^{\text{inc}} \\ E_-^{\text{inc}} \end{pmatrix}. \tag{6.16}$$

When the incident beam is either right-handed or left-handed circularly polarised, the angular spectrum $\boldsymbol{E}_\infty = \xi_p \widehat{\boldsymbol{\xi}}_p$ can be expressed in terms of a scalar function $\varepsilon$ defined over the entire semisphere as

$$\varepsilon(\vartheta, \varphi) = \begin{cases} \xi_p & \text{if } \sin\vartheta < \gamma \\ 0 & \text{otherwise.} \end{cases} \tag{6.17}$$

This function can be decomposed into spin-weighted spherical harmonics, as follows

$$\varepsilon(\vartheta, \varphi) = \sum_{\ell m} c_{\ell m}\, {}_{-p}Y_{\ell m}(\vartheta, \varphi), \tag{6.18}$$

where

$$c_{\ell m} = \int_0^{\pi} \int_0^{2\pi} \varepsilon(\vartheta, \varphi)\, {}_{-p}Y^*_{\ell m}(\vartheta, \varphi) \sin\vartheta\, d\varphi\, d\vartheta. \tag{6.19}$$

The dependence of (6.15) on the helical basis can be factored out. Then, the result (6.14) is inserted in the integral, which is rearranged as follows

$$\begin{aligned}\boldsymbol{E}(r,\theta,\phi) &= \mathrm{e}^{-\mathrm{i}kf}\frac{\mathrm{i}kf}{2\pi}\int_0^{\pi}\int_0^{2\pi}\varepsilon(\vartheta,\varphi)\widehat{\boldsymbol{\xi}}_p\,\mathrm{e}^{\mathrm{i}kr\cos(\varphi-\phi)\sin\vartheta\sin\theta}\mathrm{e}^{\mathrm{i}kr\cos\vartheta\cos\theta}\sin\vartheta\,d\varphi\,d\vartheta,\\ &= -2\mathrm{i}kf\,\mathrm{e}^{-\mathrm{i}kf}\sum_{\ell m}\mathrm{i}^{\ell}\left[\int_0^{\pi}\int_0^{2\pi}\varepsilon(\vartheta,\varphi)\,{}_{-p}Y^{*}_{\ell m}(\vartheta,\varphi)\sin\vartheta\,d\varphi\,d\vartheta\right]\boldsymbol{CK}^{p}_{\ell m}(r,\theta,\phi).\end{aligned} \tag{6.20}$$

The term $[\bullet]$ can be identified as the coefficients $c_{\ell m}$ defined in (6.19) which, when substituted into (6.20), give the following compact solution to Richards-Wolf vector diffraction integral

$$\boldsymbol{E}(r,\theta,\phi) = -2\mathrm{i}kf\,\mathrm{e}^{-\mathrm{i}kf}\sum_{\ell m}\mathrm{i}^{\ell}c_{\ell m}\boldsymbol{CK}^{p}_{\ell m}(r,\theta,\phi). \tag{6.21}$$

This result is fundamentally important because it expresses the field in the focal volume of an aplanatic lens as an infinite sum of Chandrasekhar-Kendall eigenfunctions $\boldsymbol{CK}^{p}_{\ell m}$. Further, the coefficients $c_{\ell m}$ are simply derived by expanding the angular spectrum in the helical basis into a superposition of spin-weighted spherical harmonics ${}_{-p}Y_{\ell m}(\vartheta,\varphi)$. Since the CK-functions are eigenstates of the curl operator, this also applies to the focal field which satisfies $\boldsymbol{\nabla}\times\boldsymbol{E} = pk\boldsymbol{E}$. By using Maxwell's equation (2.4c), it is easy to show that also the magnetic field in the focal volume is a curl eigenstate, given by $\boldsymbol{B} = -\mathrm{i}p\boldsymbol{E}/c$.

Expression (6.21) has the form of a series of CK-states. For practical purposes this infinite sum can be truncated at the finite value $N$. This is because the dependence of $\boldsymbol{E}$ on $\phi$ can be separated from that on $r$ and $\theta$. The minimum power of $r$ in each state $\boldsymbol{CK}^{p}_{\ell m}$ is always $m$. This implies that since a small sphere centred at the focal point is not affected by high order terms in $r$, the electric and magnetic fields in such a focal volume can be represented by a finite number $N$ of CK-states. A focal volume characterised by large radius requires a larger $N$ compared to the function describing a smaller sphere. When analysing a specific focal field, it is convenient to consider only the

Taylor expansion of each CK-eigefunction of order $N$ in $r$ about $r = 0$. The SWAS theory of propagation implies that the explicit evaluation of the vector diffraction integral is not required. Instead, the coefficients $c_{\ell m}$ are evaluated; this is the laborious step in the method. Spin-weighted spherical harmonics seem to be built naturally for vector fields expressed in the helical basis. If the electric and magnetic fields are helicity eigenstates, the angular spectrum expansion into spin-weighted spherical harmonics generates simple analytic forms for the focal electromagnetic field. This is in contrast to standard vector spherical harmonic expansions, which do not generate simple analytic expressions. This justifies why we will use SWAS-theory to perform the topological analysis of tightly focused knotted fields. In the previous chapters we expressed knotted optical fields in cylindrical coordinates as polynomials in $R, \mathrm{e}^{\mathrm{i}\phi}, z$. When the Taylor expansion of a CK-sum is expressed in cylindrical coordinates $(R, \phi, z)$, it has very often a simple analytic form. For this reason, we will use superpositions of CK-eigenfunctions to represent optical knotted Hopfions in § 6.3.2.

### 6.2.2 Nonparaxial (adapted) ENZ

The nonparaxial version of ENZ-theory (§ 2.2.2) was given in [162]. However, the approach was not presented in a mathematical elegant form. Here, we consider a similar but simpler approach to nonparaxial ENZ. Our contribution, inspired by the polynomial beam propagation of [84] (§ 2.2.1) is to expand the exponential factor of the diffraction integral (2.55) into reverse Bessel functions.

As for the nonparaxial polynomials, we substitute the nonparaxial exponential in the angular spectrum (2.55) with the exponential generating function (2.38), as follows

$$\mathrm{e}^{\mathrm{i}kz\sqrt{1-\gamma^2\rho^2}} = \mathrm{e}^{\mathrm{i}kz}\mathrm{e}^{-\mathrm{i}kz\left(1-\sqrt{1-\gamma^2\rho^2}\right)} = \mathrm{e}^{\mathrm{i}kz}\sum_{j=0}^{\infty}\frac{(\gamma\rho)^{2j}}{2^j j!}\theta_j^-(-\mathrm{i}kz)\,. \tag{6.22}$$

Expression (6.22) is substituted into (2.55), as follows

$$\boldsymbol{E}(R,\phi,z) = \mathrm{e}^{-\mathrm{i}kf}\,\frac{\mathrm{i}kf\gamma^2}{4\pi}\mathrm{e}^{\mathrm{i}kz}\sum_{j=0}^{\infty}\frac{\gamma^{2j}}{2^j j!}\theta_j^-(-\mathrm{i}kz)\int_0^1\int_0^{2\pi}\rho^{2j}\boldsymbol{E}_0(\rho,\varphi;\gamma)\,e^{\mathrm{i}k\gamma\rho R\cos(\varphi-\phi)}\rho\,d\varphi\,d\rho. \tag{6.23}$$

The integral can be solved by expanding each component of $\rho^{2j}\boldsymbol{E}_0$ labelled $i = \{+,-,z\}$ into Zernike polynomials, as shown in § 2.1.5. Therefore

$$\rho^{2j}E_i(\rho,\varphi;\gamma) = \sum_{n\ell}\beta^i_{n\ell}(\gamma,j)\mathrm{Z}_{n\ell}(\rho,\varphi), \tag{6.24}$$

where

$$\beta^i_{n\ell}(\gamma,j) = \frac{n+1}{\pi}\int_0^1\int_0^{2\pi}\rho^{2j}E_i(\rho,\varphi;\gamma)\mathrm{R}_n^{|\ell|}(\rho)\mathrm{e}^{-\mathrm{i}\ell\varphi}\rho\,d\varphi\,d\rho. \tag{6.25}$$

The $\beta^i_{n\ell}(\gamma,j)$ coefficients can be found with a numerical software, such as *Mathematica* 11. Thus, each component of $\boldsymbol{E}$ in (6.23) becomes

$$\begin{aligned}E_i(R,\phi,z) = \mathrm{e}^{-\mathrm{i}kf}\,\frac{\mathrm{i}kf\gamma^2}{4\pi}\mathrm{e}^{\mathrm{i}kz}\sum_{j=0}^{\infty}\frac{\gamma^{2j}}{2^j j!}\theta_j^-(-\mathrm{i}kz)\sum_{n\ell}\beta^i_{n\ell}(\gamma,j)\\ \times\int_0^1\int_0^{2\pi}\mathrm{Z}_{n\ell}(\rho,\varphi)\,e^{\mathrm{i}k\gamma\rho R\cos(\varphi-\phi)}\rho\,d\varphi\,d\rho.\end{aligned} \tag{6.26}$$

The ENZ result (2.42) can be inserted into the second line of (6.26) and the expression can be rearranged as follows

$$E_i(R,\phi,z) = \mathrm{e}^{-\mathrm{i}kf}\,\frac{\mathrm{i}kf\gamma^2}{2}\mathrm{e}^{\mathrm{i}kz}\sum_{j=0}^{\infty}\frac{\gamma^{2j}}{2^j j!}\theta_j^-(-\mathrm{i}kz)\sum_{n\ell}\beta^i_{n\ell}(\gamma,j)\mathrm{i}^n\frac{\mathrm{J}_{n+1}(k\gamma R)}{k\gamma R}\mathrm{e}^{\mathrm{i}\ell\varphi}. \tag{6.27}$$

This result is a double series expansion in $n$ and $j$, which, respectively determine the order of the powers in $R$ and the order of the powers in $z$. The infinite sums can be truncated with respect to the focal volume of interest. Due to the same reason, each $\mathrm{J}_{n+1}(k\gamma R)$ can be Taylor expanded about 0 in $k\gamma R$ up to the same order of the truncation in $n$. This means that (6.27) is a polynomial solution to Richards-Wolf vector diffraction integral analogous to the polynomial beams of section § 2.2.1. The

paraxial analogue of this solution is given by small values of $\gamma$, which can be obtained by expanding the solution in $\gamma$ about 0.

The nonparaxial ENZ will be used to evaluate topological invariants of tightly focused Zernike polynomials in § 6.3.3.

### 6.2.3 Hopf index calculations

The Hopf index was introduced in § 3.3 as a topological property of a suitable map from $\mathbb{R}^3$ to $S^2$. This section presents a formula to calculate the Hopf index of a vector field $\boldsymbol{E} = (E_+, E_-)$. This method is adapted from [126].

A generic vector field $\boldsymbol{B}$ tangent to the level curves of a complex scalar field $\psi$ is defined as follows

$$\boldsymbol{B} = \frac{1}{2\pi \mathrm{i}} \cdot \frac{\nabla\psi^* \times \nabla\psi}{(1+\psi\psi^*)^2}. \tag{6.28}$$

When the level sets of $\psi$ are knotted, the vector $\boldsymbol{E}$ constructed from $\psi$, as explained below, has nontrivial helicity (§ 3.3) given by

$$\mathcal{H} = \int \boldsymbol{A} \cdot \boldsymbol{B}\, d^3x. \tag{6.29}$$

$\boldsymbol{A}$ is a vector potential such that $\nabla \times \boldsymbol{A} = \boldsymbol{B}$. The explicit calculation of $\mathcal{H}$ implies that the vector potential has to be found explicitly, but it is defined up to a gauge. It is shown in [126] that the optimal choice of the gauge transformation can be done by using the rational map $\psi = E_+/E_-$ and Euler potentials. $E_+$ and $E_-$ are two complex valued polynomials. It follows that

$$\boldsymbol{A} = \frac{1}{4\pi \mathrm{i}} \times \frac{|E_+|^2 \nabla \log\left(E_+/E_+^*\right) + |E_-|^2 \nabla \log\left(E_-/E_-^*\right)}{|E_+|^2 + |E_-|^2}. \tag{6.30}$$

By inserting (6.30) and (6.28) into (6.29) we find

$$\mathcal{H} = \frac{1}{16\pi^2} \int \frac{\boldsymbol{J}_+ \cdot (\nabla \times \boldsymbol{J}_-) + \boldsymbol{J}_- \cdot (\nabla \times \boldsymbol{J}_+)}{(|E_+|^2 + |E_-|^2)^2}\, d^3x, \tag{6.31}$$

where $\mathbf{J}_\pm = \mathrm{Im}(E_\pm^* \nabla E_\pm)$. The Whitehead integral [125, 207] shows that this helicity is equivalent to the Hopf invariant of the two-component vector $\boldsymbol{E} = (E_+, E_-)$.

Expression (6.31) can be proved by rewriting $\boldsymbol{B}$ using Euler potentials as [126]

$$\boldsymbol{B} = \nabla\left(\frac{\psi\psi^*}{1+\psi\psi^*}\right) \times \frac{1}{4\pi \mathrm{i}} \nabla \log\left(\frac{\psi}{\psi^*}\right), \tag{6.32}$$

and

$$\boldsymbol{\mathcal{A}} = \frac{1}{4\pi \mathrm{i}}\left(\frac{\psi\psi^*}{1+\psi\psi^*}\right) \nabla \log\left(\frac{\psi}{\psi^*}\right) = \boldsymbol{A} - \nabla \log\left(\frac{\psi_-}{\psi_-^*}\right). \tag{6.33}$$

The term $\nabla \log\left(E_-/E_-^*\right)$ is singular at $E_- = 0$, therefore the gauge transformation $\boldsymbol{A} = \boldsymbol{\mathcal{A}} + 1/(4\pi \mathrm{i}) \nabla \log\left(E_-/E_-^*\right)$ is applied to remove the singularity. This allows the helicity (6.29) to be evaluated directly.

The integral form (6.31) will be used in § 6.3 and § 6.4 to prove the presence of Hopf fibrations in focused optical beams.

## 6.3 Hopf fibrations in tightly focused Zernike polynomials

This section presents torus-knotted Hopfions arising naturally in the polarisation texture of tightly focused Zernike aperture modes. First, the topological properties of the focal volume are analysed numerically by considering the case study of the trefoil-knotted Hopfion (§ 6.3.1). Then, an analytical model for the focused field is given in § 6.3.2; this is based on SWAS-theory (§ 6.2.1). Further, the Hopf index of the optical Hopf fibration is calculated in § 6.3.3 via the procedures described in § 6.2.2 and § 6.2.3. Finally, the whole family of knotted and linked Hopfions arising from the Zernike modes are presented in § 6.3.4.

### 6.3.1 Trefoil-knotted Hopfion

The case study of the Zernike $\mathrm{Z}_{6,0}$ aperture mode is considered. This generates a trefoil-knotted Hopfion in the focal volume under tight focusing.

The incident beam on the lens is right-handed circularly polarised and its complex amplitude on the aperture plane, which is parametrised by the dimensionless coordin-

ates $0 \leq \rho \leq 1$ and $0 \leq \varphi < 2\pi$, is represented by the following Zernike polynomial (2.14)

$$\mathrm{Z}_{6,0}(\rho) = -1 + 12\rho^2 - 30\rho^4 + 20\rho^6. \tag{6.34}$$

The propagating beam is computed by the numerical evaluation of Richards-Wolf vector diffraction integral (§ 2.2.3). The lens has numerical aperture $\gamma = 0.9$, lengths are expressed in units of the optical wavelength $\lambda$. In these units the radius of the aperture is $a = 6600\lambda$; this value does not influence the topology in the focal volume as long as it is large compared to the optical wavelength. The focal volume under investigation is a cube of length $2\lambda$.

The numerical results generated by the tightly focused Zernike mode (6.34) show that: the $E_+$ component has an azimuthally-symmetric intensity profile at the focal plane, on which nodal lines in the form of concentric loops are found; $E_-$ has a vortex of strength 2 at the focal point and $E_z$ has a vortex of strength 1 at the same point. The complex amplitudes corresponding to the $E_x$ and $E_y$ transverse components present four phase singularities each, two along the $x$-axes and two along the $y$-axes. The pattern in $E_x$ is $\pi/2$ rotated with respect to the pattern in $E_y$ and they both show similar features to the Milnor functions (§ 3.4) corresponding to the $(m, 2)$-torus knots at $z = 0$. This suggests that knotted lines could arise in the focal volume. Thus, it is natural to track the 3D nodal lines of the Cartesian components in the focal volume through the numerical algorithm of § 3.5.1. Such topological analysis reveals that there are indeed two identical trefoil knots, corresponding to the $(3, 2)$-torus knot, rotated by $\pi/2$ with respect to each other. The corresponding knot diagrams are shown in Figure 6.4 (a).

A more accurate analysis of the 3D topology of the other linear polarisation states shows that they all are trefoil knots. They are given by the preimages associated to the equatorial points of the Poincaré sphere. The latter is shown in Figure 6.4 (d). Figure 6.4 (b) shows the line representing the horizontal polarisation in red ($E_y = 0$), the vertical in cyan ($E_x = 0$) and the diagonal states in green ($E_x - E_y = 0$) and purple

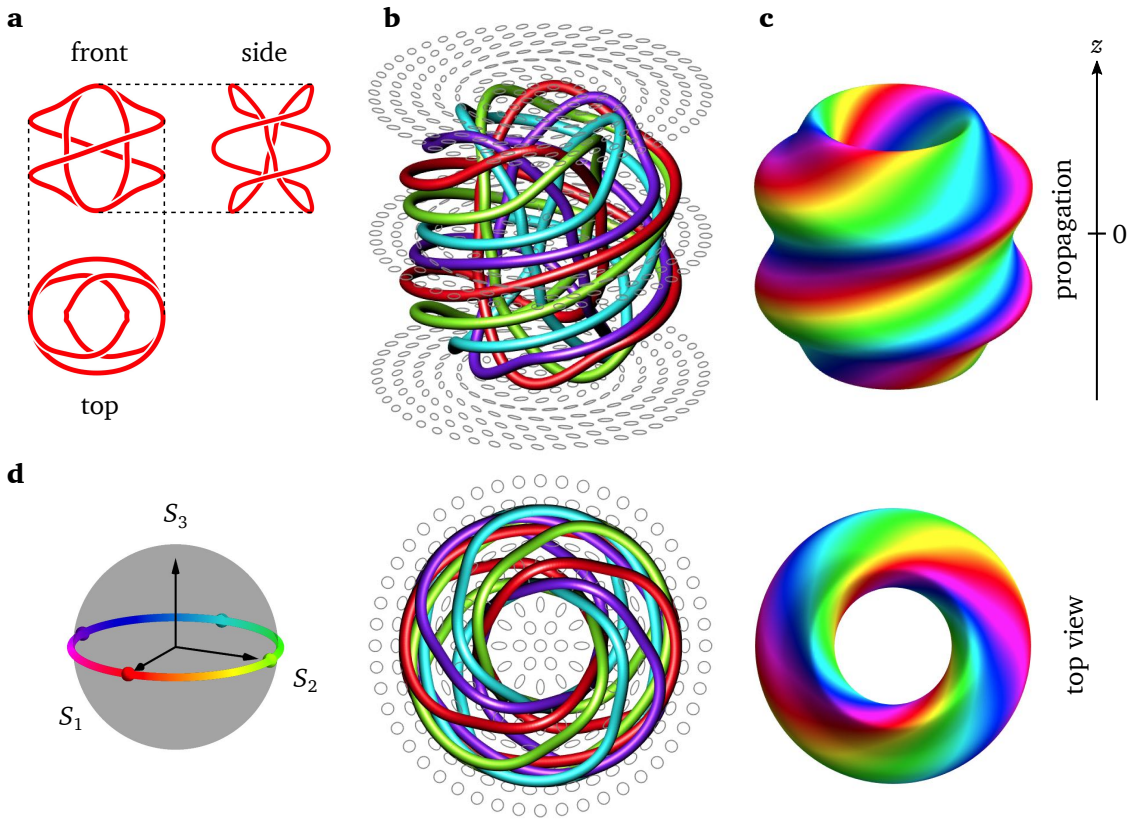


Figure 6.4: **Linear polarisation states in the trefoil-knotted Hopfion**. The tightly focused Zernike mode $Z_{6,0}$ generates a Hopf fibration in the focal polarisation texture ($\gamma = 0.9$). (d) The linear polarisation states, that are mapped to the equator in the Poincaré sphere, are represented by the hue colour wheel. (a) Each state takes the form of the same trefoil knot. (b) Trefoil knots corresponding to different linear polarisation states form a fibred bundle: horizontal in red ($E_y = 0$), vertical in cyan ($E_x = 0$), $\pi/4$ green ($E_x - E_y = 0$) and $3\pi/4$ purple ($E_x + E_y = 0$). (c) The set of all the linear polarisation states sweeps out a continuous L-surface in the shape of a torus of width $1.03\lambda$ and height $0.97\lambda$.

($E_x + E_y = 0$). For reference, also the polarisation ellipses at three different values of $z$ are plotted. The top view of the structure in Figure 6.4 (b) shows that the trefoil knots' orientation in space is half the azimuthal angle $\alpha$ in the Poincaré sphere. The whole set of linear polarisation states sweeps out a toroidal surface (the surface of revolution of a single trefoil knot) of width $1.03\lambda$ and height $0.97\lambda$. Figure 6.4 (c) shows this torus, where the hue wheel of colours is mapped to the angle $\alpha$ of the Poincaré sphere,

analogously to § 4.4. The trefoil knots corresponding to the linear polarisation states are analogous to the fibres in the Hopf fibration.

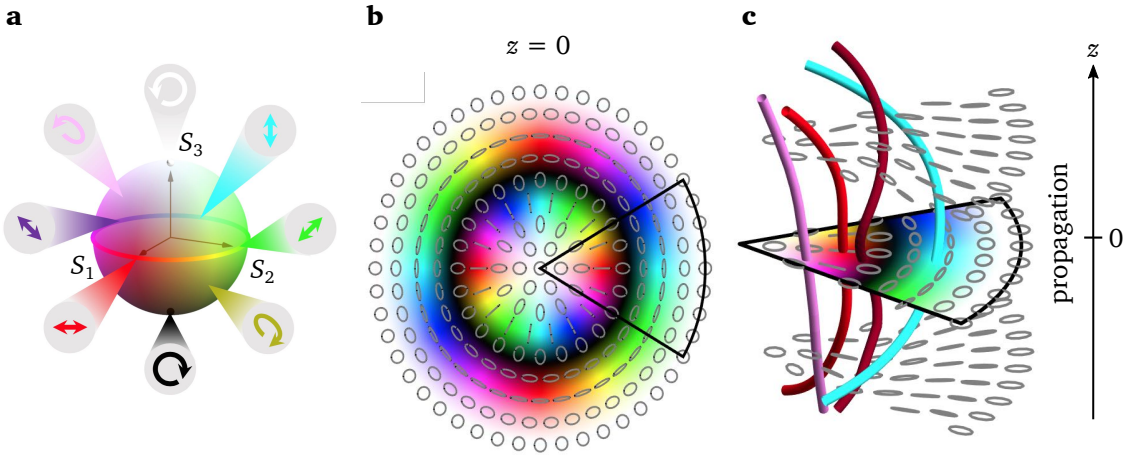


Figure 6.5: **Topological analysis of a 3D polarisation texture**. The polarisation structure in the focal volume of a tightly focused beam is analysed by colour coding the Poincaré sphere and the corresponding polarisation states equivalently. (a) The azimuthal angle of the Poincaré sphere is mapped to the hue wheel and the elevation angle to the saturation level. (b) The focal plane $z = 0$ of the tightly focused Zernike mode $Z_{6,0}$ is colour coded and overlapped with the polarisation ellipses distribution. (c) Lines characterised by the same polarisation state can be tracked in the focal volume. Visual examples (red, cyan, pink and dark pink lines) are plotted, as well as the polarisation ellipses at three different planes of fixed $z$.

The rest of the polarisation texture in the focal volume is revealed by mapping each point in the volume to the Poincaré sphere through the Stokes parameters (§ 2.1.7). This is an ordered texture in the form of a Hopf fibration. In order to visualise such a complicated three-dimensional structure, we construct the function that takes the points on the Poincaré sphere to the lines in the focal volume characterised by the same polarisation state. Given the transverse optical field in the circular basis $(E_+, E_-)$, a complex scalar field $\Psi$ is defined for each fixed point on the Poincaré sphere. This is parametrised by the azimuthal angle $\alpha$ and the elevation angle $\beta$ as

follows

$$\Psi(\alpha,\beta)=\left[\cos\left(\frac{\beta}{2}\right)-\sin\left(\frac{\beta}{2}\right)\right]\mathrm{e}^{\mathrm{i}\alpha/2}E_{+}-\left[\cos\left(\frac{\beta}{2}\right)+\sin\left(\frac{\beta}{2}\right)\right]\mathrm{e}^{-\mathrm{i}\alpha/2}E_{-}. \quad (6.35)$$

The zero lines of $\Psi$ for fixed values of $\alpha$ and $\beta$ correspond to lines in three dimensions characterised by the same polarisation state. In other words, the level sets of $\psi = E_+/E_-$ are lines along which the polarisation state is constant; therefore the polarisation ellipses are characterised by the same orientation $\alpha/2$ and eccentricity $\beta/2$ (§ 2.1.7) on the nodal lines of $\Psi$. We track the zeros of $\Psi$ for different values of the parameters by mapping the entire Poincaré sphere to the colour map illustrated in Figure 6.5 (a). This indicates the polarisation state of each point in the focal volume. As above, the longitude (the orientation of the polarisation ellipse) is represented by the colours of the hue wheel and the latitude (the eccentricity of the polarisation ellipse) is represented by the saturation level, where darker and lighter colours correspond, respectively, to the southern and northern hemisphere. Figure 6.5 (b) shows the colour coded focal plane of the tightly focused Zernike mode represented by (6.34). The linearly polarised states are identified by the non-saturated hue colours, the right-handed states are white, the left-handed states are black, the colours in between represent elliptic polarisation. This procedure is used to track lines characterised by the same polarisation state in 3D space. These are shown in in Figure 6.5 (c), where four lines with fixed $\alpha$ and $\beta$ have been partially plotted.

The topological analysis of the full three-dimensional focal volume shows that the polarisation texture in the focal volume embeds a volume filling topological object composed of internested tori given by the contour surfaces of the Stokes parameter $S_3$. A tomography of this structure is shown in Figure 6.6 (b) and (c), where the left-handed states are three rings coloured in black and the right-handed states are positioned along the optical axes and plotted in white. Figure 6.6 (d) shows the loci of focal points corresponding to $S_3 = 0.730$, which is a larger torus compared to $S_3 = 0$ representing linearly polarised states (Figure 6.6 (e)). A more detailed analysis shows that when $S_3$ decreases to negative values, the corresponding preimages are smaller

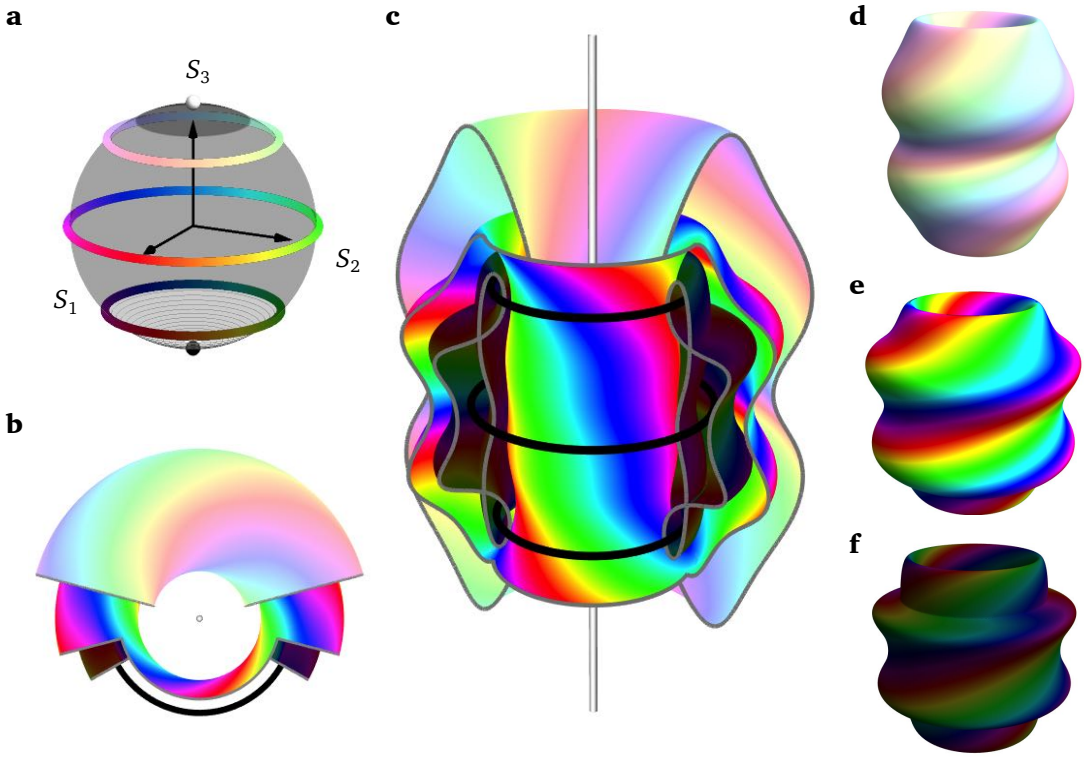


Figure 6.6: **Nested tori conformation in the trefoil-knotted Hopfion**. Fixed values of $S_3$ on the Poincaré sphere correspond to toroidal contour surfaces in the focal volume, which form a nested structure of tori. (a) Colour coded loops on the Poincaré sphere corresponding to $S_3 = \{0.730, 0, -0.712\}$. Tomography (b) top view and (c) 3D view of the polarisation texture of the tightly focused Zernike mode $Z_{6,0}$ in focal volume ($\gamma = 0.9$). The points corresponding to $S_3 = 1$ and $S_3 = -1$ are located, respectively, at the optical axes (the torus closing at infinity) and along three disconnected circles. Torus corresponding to (d) $S_3 = 0.730$, (e) $S_3 = 0$, (f) $S_3^{\text{split}} = -0.712$. The latter shows the topological event in which a single toroidal surface splits into three disconnected tori.

tori and eventually the torus corresponding to $S_3^{\text{split}} = -0.712$ (Figure 6.6 (f)) splits into three different tori. The critical points are clearer in the tomography of Figure 6.6 (c).

The mathematical map that acts from the focal optical field $(E_+, E_-)$ to the Stokes parameters $(S_1, S_2, S_3)$ is a Hopf map. However, the tightly focused Zernike mode $Z_{6,0}$ does not generate a perfect Hopf fibration, because there exists a value $S_3^{\text{crit}} = 0.885$

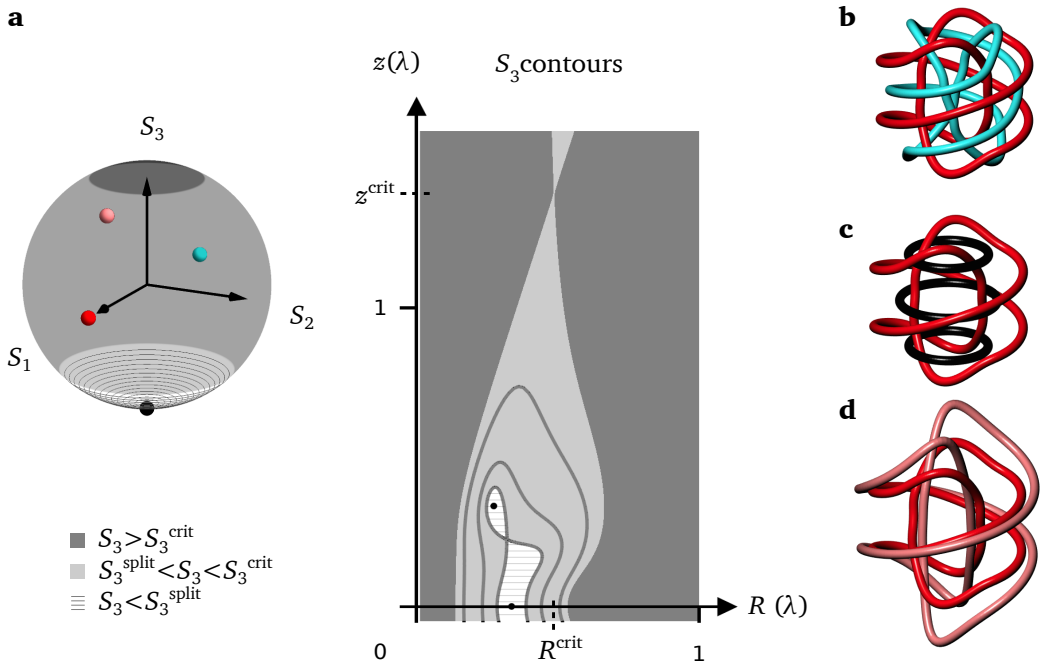


Figure 6.7: **Linking number around the focus.** (a) The focal volume generated by the Zernike mode $Z_{6,0}$ can be divided in three topological regions: the volume around the black C-lines (white striped), where the contours of $S_3 < S_3^{\text{split}}$ are three tori with disconnected loops as fibres; a finite volume (grey), where each contour of $S_3^{\text{split}} < S_3 < S_3^{\text{crit}}$ is a single torus with trefoil knots as fibres; the outer region $S_3 > S_3^{\text{crit}}$ (dark grey), where the Hopfion topology is lost. The torus reconnects with outer surfaces at $(R^{\text{crit}}, z^{\text{crit}})$. (b)–(d) The curves are the preimages of the points on the Poincaré sphere drawn in (a) with coordinates $(S_1, S_2, S_3)$: $(1,0,0)$ in red, $(-1,0,0)$ in cyan, $(1,0,0.730)$ in pink and $(0,0,-1)$ in black. These are trefoil knots or sets of three disconnected loops. The linking number between two distinct curves is $-6$ for all the points mapped to $S_3 < S_3^{\text{crit}}$; this quantity coincides with the Hopf index in the small $\gamma$ regime (§ 6.3.3).

for which the surface contour of $S_3$ reconnects with surfaces from the outer regions. This is shown in Figure 6.7 (a) where the contours of $S_3$ in the positive $Rz$-plane are plotted (note that the contours of $S_3$ are azimuthally-symmetric and $z$ symmetric). Dark grey indicates the focal area in which the Hopf fibration features are lost, the corresponding points on the Poincaré sphere $S_3 > S_3^{\text{crit}}$ are also indicated with the same colour. The rest of the focal volume shows interesting topological properties. The preimages of the points on the Poincaré sphere $S_3^{\text{split}} < S_3 < S_3^{\text{crit}}$ are trefoil knots

and the preimages of the points $S_3 < S_3^{\text{split}}$ are three disconnected loops. The most significant property of the preimages in the region $S_3 < S_3^{\text{crit}}$ is that any two knots, or any two pairs of three loops, or a knot and three loops, always have linking number (3.8) $\ell k = -6$. The sign of the linking number is determined by the orientation of each single fibre, which is not arbitrary in a 3D polarisation texture. In particular, the orientation is inherited from the structure of the field and is given by the topological current vector in each filament. Each polarisation state is found as the nodal line of a complex scalar field, therefore the topological current vector assigned to this line is determined by the 'right-hand rule': it points up for a positive topological charge on the $Rz$-plane and down for a negative topological charge. Some examples of linked curves are shown in Figure 6.7 (b)–(d). The invariant linking number for any pair of fibres corresponding to a mathematical map is the signature property of a Hopf fibration.

Given that the outer region does not have the required topological properties, the tightly focused field generated by the Zernike mode $\mathrm{Z}_{6,0}$ is not a perfect Hopf fibration in the mathematical sense, nevertheless the analogy between the mathematical model and our simulation is clear. When the Zernike mode $\mathrm{Z}_{6,0}$ is propagated with different values of the numerical aperture $\gamma$, the Hopfion structure is present for any value of the parameter. The values of $S_3^{\text{crit}}$ and $S_3^{\text{split}}$ vary when $\gamma$ is varied. Therefore, the Hopfion is topologically robust to variation of the focusing parameter.

When the same analysis is performed with a left-handed polarised input beam, the component which carries the azimuthally-symmetric profile is $E_-$ and the signs of the vortices in $E_+$ and $E_z$ are negative with respective strength $-2$ and $-1$. The Hopfion is identical to the one described above with the difference that the overall handedness changes; thus, the linking number of two distinct preimages of $S_3 < S_3^{\text{crit}}$ is $\ell k = 6$. We will see in § 6.3.3 that such configuration is characterised by apositive Hopf index $\mathcal{H} = 6$.

### 6.3.2 Analytic representation

In this section, SWAS theory (§ 6.2.1) is applied to the tight focusing of the Zernike mode $Z_{6,0}$ and the analytic representation of the trefoil-knotted Hopf fibration is evaluated in the focal volume.

A circularly polarised paraxial beam is incident on the aperture of the lens of radius $a = \gamma f$, whose points are parametrised by the dimensionless variables $0 \leq \rho \leq 1$ and $0 \leq \varphi < 2\pi$. The field has the complex amplitude profile of the Zernike $Z_{6,0}$ in the aperture plane and is represented by the vector $\boldsymbol{E}^{\text{inc}}(\rho, \varphi) = R_6^0(\rho)\widehat{\boldsymbol{e}}_+$. The angular spectrum of the field $\boldsymbol{E}_\infty$ is a vector field tangent to the reference sphere of the lens at any point and is given by (6.16) in the helical basis. Since the incident field is uniquely right-handed polarised, the angular spectrum can be expressed in terms of a complex scalar field in the positive helical component, $\boldsymbol{E}_\infty = \xi_+ \widehat{\boldsymbol{\xi}}_+$. It is convenient to define the complex scalar field $\varepsilon$ over the entire semisphere by (6.17), which, in spherical coordinates $(\vartheta, \varphi)$ (in this coordinate system $\rho = \sin\vartheta/\gamma$), is

$$\varepsilon(\vartheta, \varphi; \gamma) = \begin{cases} \sqrt{\cos\vartheta}\, e^{i\varphi} R_6^0\left(\frac{\sin\vartheta}{\gamma}\right) & \text{if } \sin\vartheta < \gamma \\ 0 & \text{otherwise.} \end{cases} \tag{6.36}$$

Expression (6.36) is decomposed into spin weighted spherical harmonics ${}_{-p}Y_{\ell m}(\vartheta, \varphi)$, as defined by (6.18). The helicity[5] sign gives $p = +1$. The corresponding coefficients in the sum are given by (6.19). It is straightforward to see that the coefficients are not zero only when $m = +1$, because of the presence of the term $e^{i\varphi}$ in (6.36). Thus

$$\varepsilon(\vartheta, \varphi; \gamma) = \sum_\ell c_{\ell 1}(\gamma)\, {}_{-1}Y_{\ell 1}(\vartheta, \varphi). \tag{6.37}$$

The coefficients $c_{\ell 1}$ can be evaluated with their explicit dependence on $\gamma$ with the software *Mathematica* 11.

The angular spectrum expressed as a sum of spin weighted spherical harmonics

[5]The helicity given by the sense of circular polarisation is not the topological helicity discussed in § 6.2.3.

Table 6.1: **Analytic representation of the tightly focused $Z_{6,0}$ with SWAS theory**. A right-handed polarised beam with the amplitude profile of the Zernike mode $Z_{6,0}$ generates an angular spectrum which can be approximated by a sum of ${}_{-1}Y_{\ell 1}(\vartheta,\varphi)$ functions with coefficients $c_{\ell 1}$. The same coefficients are used to represent the corresponding tightly focused beam around the focal point, which is given by a superposition of Chandrasekhar-Kendall eigenfunctions as defined by (6.38). The coefficients are tabled for the numerical aperture $\gamma = 0.9$.

| $\ell$ | 1 | 2 | 3 | 4 | 5 | 6 | 7 | 8 |
|---|---|---|---|---|---|---|---|---|
| $c_{\ell 1}$ | -0.016 | 0.049 | -0.030 | -0.124 | 0.206 | 1.232 | 2.569 | 3.280 |
| $\ell$ | 9 | 10 | 11 | 12 | 13 | 14 | 15 | 16 |
| $c_{\ell 1}$ | 2.641 | 0.890 | -0.833 | -1.397 | -0.642 | 0.523 | 0.987 | 0.438 |
| $\ell$ | 17 | 18 | 19 | 20 | 21 | 22 | 23 | 24 |
| $c_{\ell 1}$ | -0.451 | -0.772 | -0.281 | 0.435 | 0.627 | 0.155 | -0.431 | -0.513 |
| $\ell$ | 25 | 26 | 27 | 28 | 29 | 30 | 31 | 32 |
| $c_{\ell 1}$ | -0.051 | 0.425 | 0.4147 | -0.035 | -0.413 | -0.324 | 0.106 | 0.039 |

simplifies the evaluation of the diffraction integral (6.15). The focused field can be represented by a superposition of Chandrasekhar-Kendall eigenfunctions (6.12) via the result (6.21), as follows

$$\boldsymbol{E}(r,\theta,\phi) = -2ikf\,\mathrm{e}^{-ikf}\sum_{\ell}\mathrm{i}^{\ell}c_{\ell 1}(\gamma)\boldsymbol{C}\boldsymbol{K}^{1}_{\ell 1}(r,\theta,\phi). \tag{6.38}$$

Higher order CK-states influence the field only at large distances from the focus (§ 6.2.1). Therefore, the order of truncation in the expansion depends on the size of the focal volume to be represented. Since the numerical aperture $\gamma$ of the lens scales the size of the focal volume (weaker lenses give rise to larger images in the focal area), the order of truncation depends also on the lens system considered. Figure 6.7 (a), for which $\gamma = 0.9$, shows that the outer region, in which there is no presence of the hopfion-like behaviour, are placed at distances larger than $2\lambda$. We represent analytically only the volume in which the Hopfion is confined. When $\gamma = 0.9$, the

Taylor expansion of order $N = 32$ about $r = 0$ of the CK-sum (6.38) with $N$ terms gives an accurate representation of the focal field in a sphere of radius $2\lambda$. The values of $c_{\ell 1}$ for $\gamma = 0.9$ up to $N = 32$ are reported in Table 6.1.

Our analytic representation of the tightly focused Zernike $\mathrm{Z}_{6,0}$ in terms of CK-eigenfunctions is consistent with the numerical evaluation of Richards-Wolf vector diffraction integral in a sphere of radius $2\lambda$. The numerical data was derived from a highly resolved aperture plane ($7000 \times 7000$ array) and high performance computers. The plots in Figure 6.8 show the real and imaginary parts of all the focal field components $E_+, E_-, E_z$ in the region $0 < R < \lambda, \phi = 0$ and $z = (0, 1/4, 1/2, 1)\lambda$. The plots compare analytic SWAS theory with the discrete numerical data evaluated with standard Richards-Wolf theory. A larger focal volume could be represented accurately by a sum of CK functions that includes higher order terms. However, the larger the order, the harder it is to evaluate the field and the smaller the time efficiency of the method.

### 6.3.3 The Hopf index of dark beams

Since a Hopfion is a topological object characterised by an integer value of the Hopf index, we present a model showing that the focused Zernike mode $\mathrm{Z}_{6,0}$ has topological invariant $\mathcal{H} = -6$. The results are found by using the nonparaxial ENZ-method of § 6.2.2.

Similarly to § 6.3.2, the incident beam on the lens is represented by the vector $\boldsymbol{E}^{\mathrm{inc}}(\rho, \varphi) = \mathrm{R}_6^0(\rho)\widehat{\boldsymbol{e}}_+$. Here, the angular spectrum $\boldsymbol{E}_\infty = k_z \boldsymbol{E}_0/(2k)$ is expressed in circular components. $\boldsymbol{E}_0$ is given by (2.54), as follows

$$\boldsymbol{E}_0(\rho, \varphi; \gamma) = \begin{pmatrix} s^{1/4} + s^{-1/4} \\ (s^{1/4} - s^{-1/4})\mathrm{e}^{2\mathrm{i}\varphi} \\ -\sqrt{2} s^{-1/4} \gamma \rho \mathrm{e}^{\mathrm{i}\varphi} \end{pmatrix} \mathrm{R}_6^0(\rho), \tag{6.39}$$

with $s = 1 - \gamma^2 \rho^2$. In order to find the focal field, the function $\rho^{2j} \boldsymbol{E}_0(\rho, \varphi; \gamma)$ is decomposed into the Zernike polynomial basis, as given by (6.24). The coefficients $\beta_{n\ell}^i(\gamma, j)$ are expressed by (6.25). The analytic form of the coefficients is a sum of

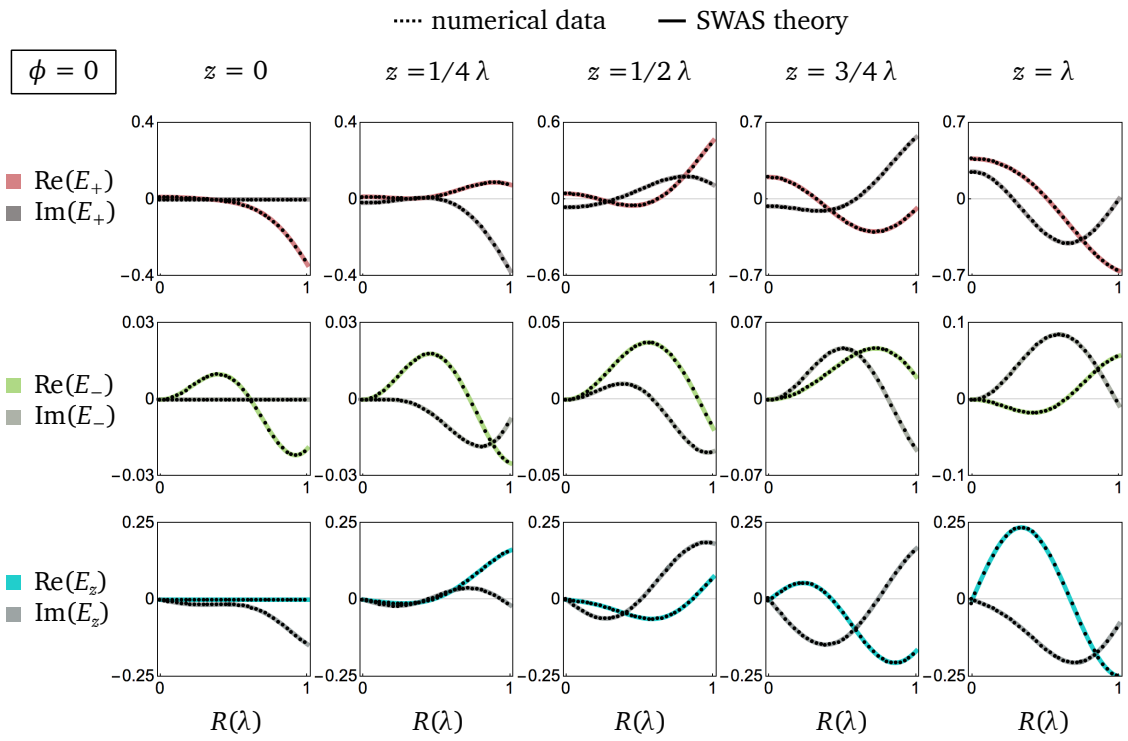


Figure 6.8: **Vector diffraction integral with SWAS theory and numerical data**. SWAS theory enables the analytical evaluation of Richards-Wolf vector diffraction integral in the form of a sum of Chandrasekhar-Kendall eigenfucntions. The focal field coefficients of the tightly focused Zernike mode $Z_{6,0}$ are given in Table 6.1. The sum has 32 CK-functions. The theoretical expression is consistent with the numerical results in a sphere of radius $2\lambda$ centred at the focus. The plots show the real and imaginary parts of the components of the electric field in the region $0 < R < \lambda, \phi = 0$ and $z = (0, 1/4, 1/2, 1)\lambda$.

Gaussian (ordinary) hypergeometric functions [208], which depends on the numerical aperture $\gamma$ and the index $j$ and can be calculated with *Mathematica* 11. The coefficients are inserted into formula (6.27) to determine the focal field $\boldsymbol{E} = (E_+, E_-, E_z)$ as an expansion in Bessel functions of the first kind labelled by $n$, multiplying reverse Bessel functions labelled by $j$. The truncation values for $n$ and $j$ can be found as follows. The term $ikf\gamma^2 e^{ik(z-f)}/2$ is factored out from the focal field $\boldsymbol{E}$ and the result is expanded in $\gamma$ about $\gamma = 0$. Only the first non-zero term is kept. The transverse components of

the truncated focal field are of order 6 in $\gamma$. In units of length $k^{-1}=1$, they are

$$E_{+}^{n=6}(R,\phi,z)=\frac{1}{630\times 2^{9}}\left(72-18R^{2}-R^{6}-18\mathrm{i}(10-4R^{2}+R^{4})z\right.$$
$$\left.+72(-2+R^{2})z^{2}+48\mathrm{i}z^{3}\right)\gamma^{6}, \tag{6.40a}$$
$$E_{-}^{n=6}(R,\phi,z)=\frac{1}{420\times 2^{7}}R^{2}\mathrm{e}^{2\mathrm{i}\phi}\left(6-R^{2}-6\mathrm{i}z\right)\gamma^{6}. \tag{6.40b}$$

For completeness, the first non-zero terms of the longitudinal component are calculated up to the same order in $\gamma$. Thus

$$E_{z}^{n=6}(R,\phi,z)=\frac{\mathrm{i}}{4\sqrt{2}}R\mathrm{e}^{\mathrm{i}\phi}\left(-\gamma^{2}+\frac{1}{12}(-2+R^{2}+4\mathrm{i}z)\gamma^{4}\right.$$
$$\left.+\frac{1}{384}\left(-30+6R^{2}-R^{4}+\mathrm{i}(48-12R^{2})z+24z^{2}\right)\gamma^{6}\right). \tag{6.41}$$

However, this component is not involved in the Hopf fibration.

When the field expression (6.40) is inserted into (6.35), it gives a complex scalar field $\Psi(\alpha,\beta)$ that has nodal lines in the shape of a trefoil knot or three disjoint loops. Each line corresponds to the preimage of the point on the Poincaré sphere with coordinates $\alpha,\beta$; every pair of distinct preimages has linking number $\ell k=-6$. It is easy to show that the transverse components (6.40) originate a vector field $\boldsymbol{E}=(E_{+}^{n=6},E_{-}^{n=6})$ in the form of a mathematical Hopf fibration. The Hopf index (6.31) for this vector is $\mathcal{H}=-6$ and does not depend on the parameter $\gamma$. Expressions (6.40) and (6.41) are derived as the first non-zero terms in the field expansion of order 6 about $\gamma=0$ and satisfy the paraxial wave equation. They physically correspond to the paraxial approximation for the vector field in the focal volume. The perturbation in $\gamma$ must be large enough to trigger the vector behaviour of the field, so that the $E_{-}$ component is not negligible.

The value of the Hopf index indicates that the Zernike mode $\mathrm{Z}_{6,0}$ is transformed by the lens system into a new field which is a perfect mathematical Hopfion in the small $\gamma$, paraxial, regime. However, all the calculations were performed in the tightly focused regime in § 6.3.1. This means that higher order terms in $\gamma$ should be included in the focal field analytic representation. When such terms are considered, the Hopf

index does not take integer values. This is because the integral (6.31) is performed over an infinite volume and it was observed (§ 6.3.1) that the Hopfion topology is lost in regions far from the focus. Hence, the field in the tightly focused regime is not a perfect Hopfion but embeds a Hopf fibration in its first non-zero terms in $\gamma$, given by (6.40). The Hopfion-like structure is clearly present in the focal volume. This is demonstrated by the fact that the linking number of any two distinct preimages of $S_3 < S_3^{\text{crit}}$ is $-6$.

### 6.3.4 A family of knotted Hopfions for tailoring topological invariants

The topological analysis performed in § 6.3.1–§ 6.3.3 on the tightly focused Zernike mode $Z_{6,0}$ is extended to the other Zernike modes: a whole family of knotted Hopfions whose fibres are torus knots and links is presented.

SWAS theory is used to calculate the analytic expressions for vector fields in the focal volume with high accuracy and speed. In our analysis the value of the numerical aperture is fixed to $\gamma = 0.9$, similarly to the case study $n = 6$. It is found that the Zernike modes of index $n = \{2, 4, 6, 8, 10\}$ give rise to Hopf fibrations whose fibres are the $(m, 2)$-torus knots or links, with $m = n/2$. Each of these fibrations is characterised by a value $S_3^{\text{crit}}$ for which the contour toroidal surface reconnects with outer surfaces, as described in § 6.3.1 for the case study. The values of $S_3^{\text{crit}}$ and the coordinates $(R^{\text{crit}}, z^{\text{crit}})$ at which the topological event occurs are reported in Table 6.2. Furthermore, each tightly focused field is characterised by one or more values $S_3^{\text{split}}$ for which the corresponding contour toroidal surface splits into 2 or 3 tori as the $S_3$ parameter is decreased. The values $S_3^{\text{split}}$ are reported in Table 6.2, as well as the corresponding number of total tori appearing for that fixed value of $S_3^{\text{split}}$.

Figure 6.9 (b)–(f) shows the $Rz$-plane of the tightly focused Zernike modes of index $n = \{2, 4, 6, 8, 10\}$ with $\gamma = \{0.95, 0.95, 0.9, 0.9, 0.9\}$. The polarisation state distribution is colour coded with the map in Figure 6.9 (a), similarly to § 6.3.1. The

Table 6.2: **Properties of the Hopfions originated from the Zernike modes**. Tightly focused Zernike modes $Z_{n,0}$ generate Hopf fibrations in the focal voume. Each field is characterised by fibres which are torus knots or links of a type depending on the index $n$. For high values of the numerical aperture $\gamma$, the Hopfion topology is only preserved near the focus and is lost in the outer region (as shown in Figure 6.7 for $Z_{6,0}$). The values of $S_3, R, z$ (critical) for which this topological event happens are reported for $\gamma = 0.9$. Each Hopfion is characterised by one or multiple values of $S_3$ (split) for which the corresponding contour surface splits into two or more tori. They are also reported for $\gamma = 0.9$. The number of total tori present in the focal volume after the topological event is reported in the brackets. Note that, since for $n = 2$ there is only one torus present, there is no value of $S_3^{\text{split}}$. Topological quantities, such as the Hopf index in the small $\gamma$ regime and the topological charge of $\text{Arg}(S_1 + \text{i}S_2)$ on the $Rz$-plane, are integers.

| Zernike index $n$ | 2 | 4 | 6 | 8 | 10 |
|---|---|---|---|---|---|
| Knot type | (2,2) | (4,2) | (6,2) | (8,2) | (10,2) |
| $S_3^{\text{crit}}$ | 0.945 | 0.919 | 0.885 | 0.856 | 0.832 |
| $R^{\text{crit}}(\lambda)$ | 0.4 | 0.5 | 0.5 | 0.5 | 0.5 |
| $z^{\text{crit}}(\lambda)$ | 0.2 | 0.8 | ±1.4 | ±1.9 | ±2.4 |
| $S_3^{\text{split}}$ (number of tori) | (1) | 0.040 (2) | −0.712 (3) | −0.871 (2)<br>−0.898(4)<br>−0.924 (6) | −0.463 (3)<br>−0.649 (5)<br>−0.957 (7) |
| $\mathcal{H}$ | −2 | −4 | −6 | −8 | −10 |
| $\text{Arg}(S_1 + \text{i}S_2)$ charge | −1 | −2 | −3 | −4 | −5 |

red curves correspond to the horizontal polarisation states which are the $(m, 2)$-torus knots; the $E_-$ polarisation states ($E_+ = 0$) are also plotted and they are disconnected loops in each case. The total topological charge given by these loops, which can be evaluated from the phase of $\text{Arg}(S_1 + \text{i}S_2)$ on the $Rz$-plane, is $-n/2$. This is an important observation because a Zernike mode of index $n$ generates a dark focus $J_{n+1}(R)/R$ in the perfect paraxial regime. It seems that, under the spin-orbit effects generated

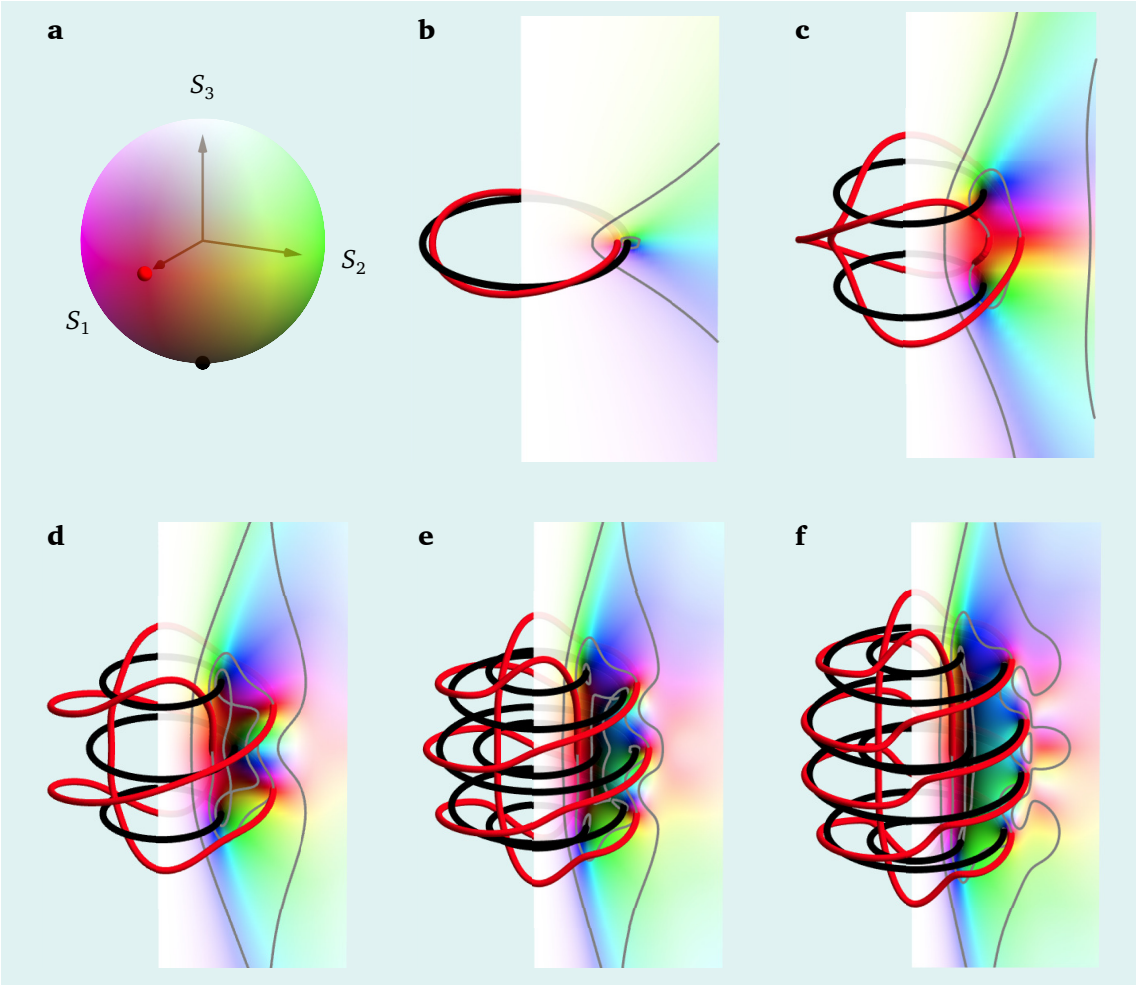


Figure 6.9: **Family of Hopfions originated from the Zernike modes**. When the Zernike aperture modes $Z_{n,0}$ with $n$ = (b) 2, (c) 4, (d) 6, (e) 8, (f) 10 are tightly focused with numerical aperture $\gamma$ = (b),(c) 0.95, (d)–(f) 0.9, they give rise to dark foci embedding Hopfions in the focal volume. Their topology is revealed by colour coding the points characterised by the same polarisation state. (a) Poincaré sphere colour map. (b)–(f) The $Rz$-plane ($\phi = 0$) shows the colour coded polarisation textures and the contours $S_3^{\text{split}}, 0, S_3^{\text{crit}}$ of $S_3$. The 3D horizontal polarisation states are the $(n/2, 2)$-torus knots and links (red lines). The singular lines of $\text{Arg}(S_1 + \text{i}S_2)$ are C-lines in the shape of disconnected loops (black lines), determining a total topological charge at the $Rz$-plane of $-n/2$.

in the lens system, the scalar dark focus splits into nodal rings of charge $-n/2$. This perturbed configuration in $E_+$ combines with the $E_-$ component, which carries an optical vortex of charge 2 (OAM $\ell = 2$), to give rise to $(m, 2)$-torus knots (links) in the

3D polarisation texture.

The Hopf index of the focal fields originated from the family of Zernike aperture modes is calculated similarly to § 6.3.3. Each Hopf fibration generated by the field given by $\mathrm{Z}_{n,0}$ is characterised by an integer Hopf index $\mathcal{H} = -n$. Each field is propagated by nonparaxial ENZ-theory and is represented by its first non-zero term of the Taylor expansion in $\gamma$ about $\gamma = 0$. The formulae for the Hopf fibrations in the small $\gamma$ regime are the following.

$$E_+^{n=2}(R,\phi,z) = -\frac{1}{24}\left(R^2 + 2\mathrm{i}z\right)\gamma^2 + \frac{1}{384}\left(2 - 8\mathrm{i}(1-R^2)z\right)\gamma^4, \tag{6.42a}$$

$$E_-^{n=2}(R,\phi,z) = \frac{1}{192}R^2\mathrm{e}^{2\mathrm{i}\phi}\gamma^4, \tag{6.42b}$$

$$E_+^{n=4}(R,\phi,z) = \frac{1}{15\times 2^7}\left(2 + R^4 - 8\mathrm{i}(1-R^2)z - 8z^2\right)\gamma^4, \tag{6.42c}$$

$$E_-^{n=4}(R,\phi,z) = \frac{1}{15\times 2^6}R^2\mathrm{e}^{2\mathrm{i}\phi}\gamma^4, \tag{6.42d}$$

$$\begin{aligned} E_+^{n=8}(R,\phi,z) = \frac{1}{35\times 2^{15}3^4}\big(&4248 - 1152R^2 + 72R^4 + R^8 + 32\mathrm{i}(-270 + 90R^2 - 9R^4 \\ &+R^6)z - 288(22 - 8R^2 + R^4)z^2 - 768\mathrm{i}(-3 + R^2)z^3 + 384z^4\big)\gamma^8, \end{aligned} \tag{6.42e}$$

$$E_-^{n=8}(R,\phi,z) = \frac{1}{35\times 2^{13}3^3}R^2\mathrm{e}^{2\mathrm{i}\phi}\left(132 - 16R^2 + R^4 + 16\mathrm{i}(-9 + R^2)z - 48z^2\right)\gamma^8, \tag{6.42f}$$

$$\begin{aligned} E_+^{n=10}(R,\phi,z) = \frac{1}{77\times 2^{18}3^45^2}\big(&388800 - 106200R^2 + 7200R^4 - 200R^6 - R^{10} \\ &- 50\mathrm{i}(14040 - 4320R^2 + 360R^4 - 16R^6 + R^8)z + 800(-612 + 198R^2 \\ &-18R^4 + R^6)z^2 + 4800\mathrm{i}(38 - 12R^2 + R^4)z^3 - 9600(-4 + R^2)z^4\big)\gamma^{10}, \end{aligned} \tag{6.42g}$$

$$\begin{aligned} E_-^{n=10}(R,\phi,z) = \frac{1}{385\times 2^{16}3^4}R^2\mathrm{e}^{2\mathrm{i}\phi}\big(&6120 - 660R^2 + 30R^4 - R^6 - 30\mathrm{i}(228 - 24R^2 \\ &+R^4)z + 240(-12 + R^2)z^2 + 480\mathrm{i}z^3\big)\gamma^{10}. \end{aligned} \tag{6.42h}$$

The analytic expressions (6.42) describing the family of Hopf fibrations show that they all share the common property that the $E_+$ and $E_-$ scalar components are polynomials in $R$ and $z$ and have, respectively, OAM $\ell = 0$ and $\ell = 2$. All the fields, except the case $n = 2$, are of order $n$ in $\gamma$ and $R$. The case $n = 2$ is an exception because the $E_-$ component is characterised by a zero term of order 2 in $\gamma$, meaning that the first

non-zero term is of order 4. This implies that the Hopf index for $n = 2$ depends on $\gamma$ and is not exactly $-n$. Nevertheless, by keeping only powers of $R$ up to order 2, we observe that the Hopf index is 2 only if the value of $\gamma$ is large enough to include the powers of order 4.

Similarly to the case study $n = 6$, the Hopf indices of the other Zernike modes have non-integer values when higher order terms in $\gamma$ are included in the fields' representation. This effect is confirmed by the existence of the $S^{\text{crit}}$ values for which the corresponding toroidal surfaces reconnect with outer surfaces. Nevertheless, in each case the focal volume embeds a Hopfion-like structures for which the linking number of two distinct polarisation states is $-n$ and coincides with the Hopf index in the small $\gamma$ regime.

## 6.4 Optical Hopfions associated to torus knots and links

This section generalises the results of § 6.3 to optical Hopfions engineered in paraxial beam solutions. The fibres associated to these fields are the $(m, n)$-torus knots and links. In § 6.4.1, 3D polarisation textures are engineered in paraxial vector fields by adapting the algebraic topology methods used in (§ 3.4) to generate optical vortex knots in scalar fields. § 6.4.2 presents the preliminary results on optical Hopfions generated experimentally in superpositions of polarised Laguerre-Gaussian beams.

### 6.4.1 Engineering Hopf fibrations in optical beams

The simplest Hopf fibration is mathematically described by the Hopf map $h$ (3.9) acting on the vector field $(u, v)$, where $u, v$ are complex coordinates on the unit 3-sphere (§ 3.3). The set of preimages constitute the fibre bundle of the Hopf fibration, which can be found by the stereographic projection (3.10). Each fibre is in the conformation of a circle and the preimages corresponding to every two distinct points on

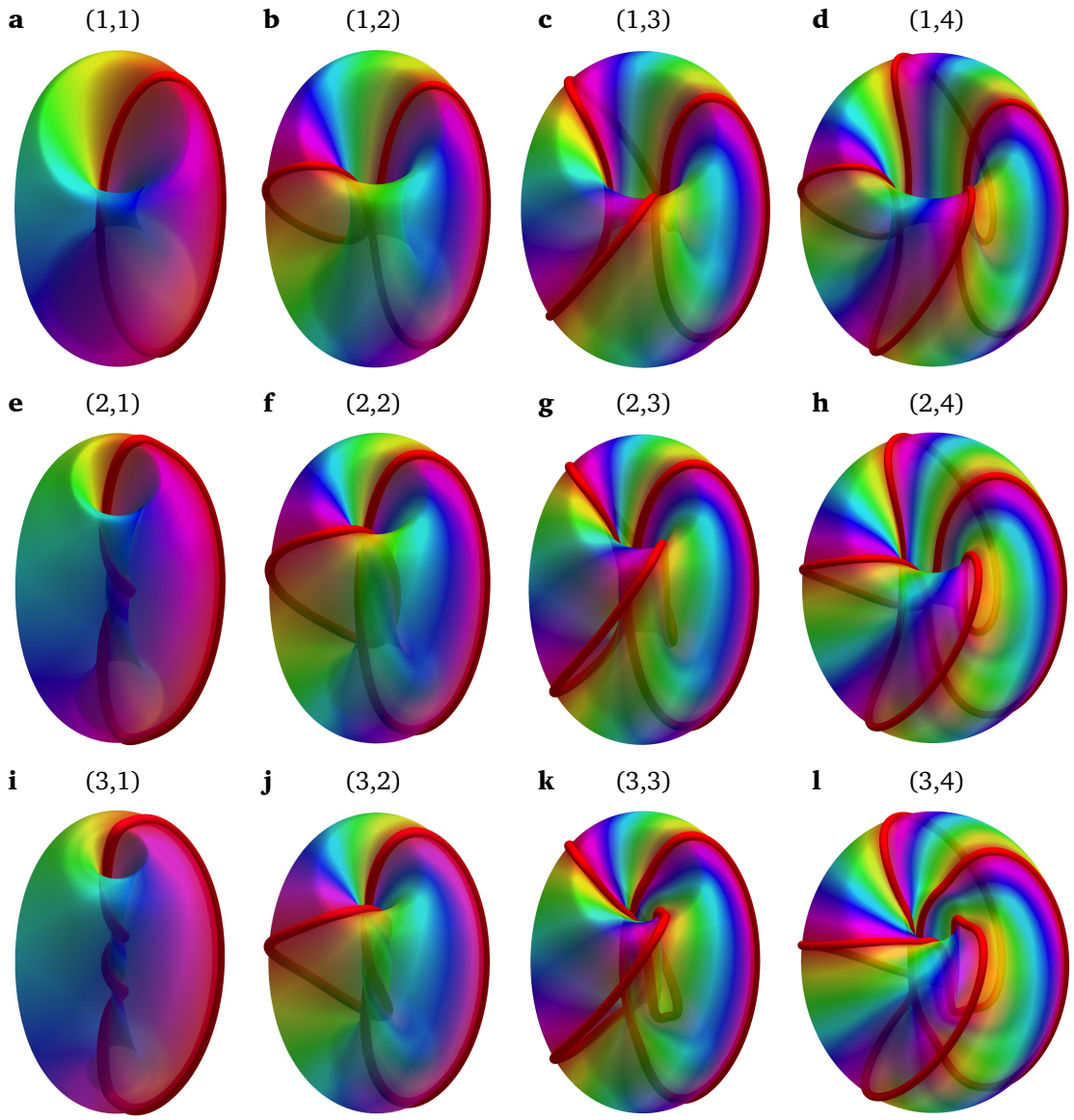


Figure 6.10: **$(m,n)$-torus-knotted Hopfions in paraxial light**. The mathematical vector field $(u^m, v^n)$ generate the initial conditions to construct paraxial polarised fields $(E_+^{\text{par}}, E_-^{\text{par}})_{m,n}$ in the form of Hopf fibrations of Hopf index $\mathcal{H} = -mn$. (a)–(l) The majority of the fibres in the Hopfions are $(m,n)$-torus knots or links (the plots are labelled with their corresponding values of $(m,n)$). The horizontal polarisation state is emphasised with a red thick tube in each plot. The linearly polarised states of each optical Hopfion sweep out a torus.

the target space ($S^2$) are Hopf links. This conformation has Hopf index $= -1$. Such mathematical construction can be generalised to Hopf fibrations with higher order

Hopf index by considering the vector field $(u^m, v^n)$. In fact, the Hopf map $h(u^m, v^n)$ generates Hopfions in Cartesian space characterised by Hopf index $\mathcal{H} = -mn$. Most of the fibres generated by each map are $(m, n)$-torus knots (or links), while the rest of the preimages are disconnected loops, which do not affect the value of the Hopf invariant.

The work of Kobayashi and Nitta [209, 210] clarified the direct connection between Hopfions and torus knots. They presented Hopfions as stable and static solutions of the extended Faddeev–Skyrme model, which they describe as toroidal domain walls where the $U(1)$ modulus of the domain wall is twisted along the toroidal and poloidal cycles of the torus, respectively, $n$ and $m$ times. The Hopf charge was found to be the product $nm$ of the two topological charges.

Here, Hopf fibrations generated from $h(u^m, v^n)$ are employed to transfer the Hopfion topology form the mathematical maps into polarised optical fields. The results are presented by considering the case study of the torus-knotted Hopfion characterised by $(m, n) = (1, 1)$. The corresponding mathematical vector field has the following form in Cartesian space, given by expression (3.10)

$$(u, v) = \left( \frac{R^2 - 1 + 2\mathrm{i}z + z^2}{R^2 + z^2 + 1}, \frac{2R\mathrm{e}^{\mathrm{i}\phi}}{R^2 + z^2 + 1} \right), \tag{6.43}$$

where the two components are characterised by azimuthal dependence 0 and 1. The numerator of the mixed state $u \pm v$ is in the form of a Milnor polynomial whose zero line is the $(1, 1)$-torus knot (the unknot), where the sign $\pm$ determines the orientation in space of the nodal line. This is straightforward from the formula (3.12) describing torus knots. The $z = 0$ slice of such a Milnor polynomial contains terms with orbital angular momentum (OAM) indices $\ell = 0$ and $\ell = 1$. The method requires to separate the terms with different OAM into the vector field $(E_+^{2\mathrm{D}}, E_-^{2\mathrm{D}})$, as follows

$$\left(E_+^{2\mathrm{D}}, E_-^{2\mathrm{D}}\right) = \left(-1 + R^2, 2R\mathrm{e}^{\mathrm{i}\phi}\right). \tag{6.44}$$

This is equivalent to multiply $u$ and $v$ with their least common denominator and take the $z = 0$ slice of the result. Each component of (6.44) can be propagated paraxially

similarly to [18] (§ 1.6) via polynomial beam propagation (§ 2.2.1). The paraxially propagating field $(E_+^{\text{par}}, E_-^{\text{par}})_{m,n}$ originated from (6.44) is

$$\left(E_+^{\text{par}}, E_-^{\text{par}}\right)_{1,1} = \left(-1 + R^2 + 2\mathrm{i}z, 2R\mathrm{e}^{\mathrm{i}\phi}\right). \tag{6.45}$$

Likewise, the case $(m,n) = (2,1)$ gives the following paraxial field

$$\left(E_+^{\text{par}}, E_-^{\text{par}}\right)_{2,1} = \left(1 - R^2 + R^4 - \frac{2}{3}\mathrm{i}(1-2R^2)z - \frac{2}{9}z^2, 2R\mathrm{e}^{\mathrm{i}\phi}(1 + R^2 + \frac{2}{3}\mathrm{i}z)\right). \tag{6.46}$$

Similarly to the optical vortex knots generated in chapter 4, the optical fields (6.45) and (6.46) coincide with their mathematical counterpart at $z = 0$, but they have a different behaviour in the powers of $z$.

The field $(E_+^{\text{par}}, E_-^{\text{par}})_{m,n}$ is mapped to its Stokes parameters. The topological analysis of the polarisation texture generated from the preimages of the Poincaré sphere demonstrates that (6.45) and (6.46) are Hopf fibrations with topological charge, respectively, $\mathcal{H} = -1$ and $\mathcal{H} = -2$. Figure 6.10 (a) and (b) show the tori formed by the linearly polarised states ($S_3 = 0$) of (6.45) and (6.46). The fibre associated to $(S1, S2, S3) = (1, 0, 0)$ is enlightened and corresponds to the unknot.

This approach is used to generate the Hopf fibrations corresponding to the $(m,n)$-torus knots with $m = \{1,2,3\}$ and $n = \{1,\ldots,4\}$. Figure 6.10 shows the linear polarisation states of each Hopfion as the toroidal surface and its corresponding $(m,n)$-torus knot (link) as the red tube. It is straightforward to show that these Hopf fibrations have a values of $S_3^{\text{split}}$ for which the corresponding toroidal surface splits into more tori analogously to § 6.3. Dissimilarly, there is no presence of a critical value $S_3^{\text{crit}}$ for which the toroidal shells are destroyed in the outer region. Thus, the optical fields generated from the map $h(u^m, v^n)$ are perfect mathematical Hopfions and their Hopf index is $\mathcal{H} = -mn$.

The limited cases of $m$ and $n$ values studied here do not give a generalisation for every $(m,n)$-torus knot and link, and some cases might fail to work. For example, we observe that the case $(m,n) = (5,2)$ does not generate a Hopfion unless the vector field $(E_+^{\text{2D}}, E_-^{\text{2D}})$ is over homogenised with the function $1 + R^2$, with level of over ho-

mogenisation 1. This method is reproposed from the generation of the optical vortex cinquefoil knot (§ 4.1).

### 6.4.2 Experimental realisation of paraxial Hopfions

An experiment to generate paraxial Hopfions in the laboratory is presented. The method consists in realising the Hopfions in a superposition of Laguerre-Gaussian modes. This is done by multiplying each component of the vector field $(E_+^{2D}, E_-^{2D})$ with a Gaussian factor, in analogy to the generation of optical vortex knots (§ 4.3). Optical Hopfions are dark beams and as such, they are very hard to generate and detect experimentally. It is already complicated to generate a single knotted vortex line. The experimental generation of an Hopfion-like optical field requires the full control of the 3D texture of polarisation states, which is extremely challenging from an experimental point of view.

The amplitude profiles of the components of the vector $LG_{00}(R,\phi;w)(E_+^{2D}, E_-^{2D})$ are imposed in the $z=0$ plane of a superposition of two LG-beams of waist $w$ (§ 2.1.4 ) and opposite polarisation. The hologram plate of the $(1,1)$-torus knotted Hopfion is calculated as follows. Expression (6.45) at $z=0$ is enveloped in a Gaussian, where the dimensionless parameters are included for practical purposes: $s$ scales the transverse size of the Hopfion in the same way it scales the optical vortex knots in chapter 5, $a, b, c$ are included to optimise the intensity of the beam by taking small steps from the initial values $a=b=c=1$. Thus, the field on the focal plane is given by

$$E_+ = (-a + bR^2 s^{-2}) LG_{00}(R,\phi;w), \tag{6.47a}$$

$$E_- = 2cRs^{-1} e^{i\phi} LG_{00}(R,\phi;w). \tag{6.47b}$$

The Fourier transform in the variables $\rho, \varphi$ is

$$E_+ = \left(-a + 2bw^2 s^{-2} - bw^2 s^{-2}\rho^2 w_0^{-2}\right) LG_{00}(\rho,\varphi;w_0), \tag{6.48a}$$

$$E_- = -2ice^{i\varphi} ws^{-1}\rho w_0^{-1} LG_{00}(\rho,\varphi;w_0). \tag{6.48b}$$

[6] Institute of Applied Physics, University of Münster (Germany).

The parameter $w_0$ is the waist of the Gaussian envelope in Fourier space.

The theoretical analysis of the propagating LG-superpositions indicates that (6.48) does not generate a perfect Hopf fibration with integer Hopf index, unless the waist of the beam $w$ in real space is large. For practical purposes, the beam needs to have a waist comparable to the size of the Hopfion, where the latter can be defined as the length of the torus originated by the linearly polarised states at $z = 0$. The difficulties arising in the experimental realisation of paraxial Hopfions are similar to those encountered in the optical vortex knots. In fact, a Laguerre-Gaussian superposition of modes with large waist gives a dark beam which cannot be detected. On the other hand, a small waist destroys completely the nature of the superoscillations generating the Hopfion. The value of $w$ is determined by fixing $w_0$ in practice, this parameter needs to be chosen appropriately so that, even though the Gaussian envelope dom-

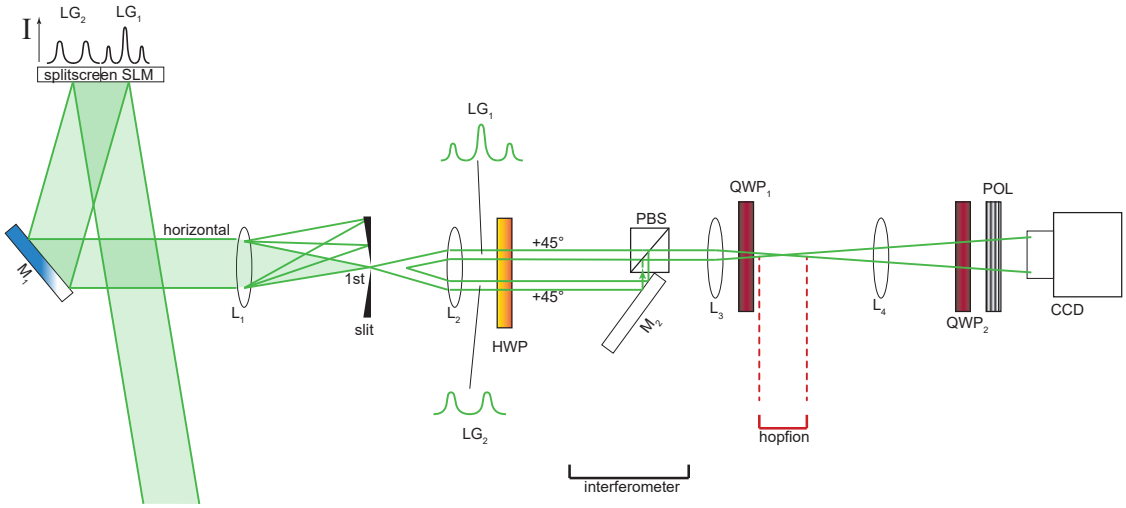


Figure 6.11: **Experimental setup for Hopfions in the polarisation texture**. This scheme represents the experimental setup for the generation of two overlapping superpositions of LG-beams: one is right-handed polarised and azimuthally symmetric, the other is left-handed polarised and carrying non-zero OAM. The holograms are generated in Fourier space on a SLM. The beams are overlapped in the focal volume of the lens $L_3$, giving rise to a Hopf fibration enveloped by a Gaussian. The Stokes parameters of the polarisation texture are detected via polarimetric measurements by a CCD camera [Image credit R. Runde[6], article in preparation].

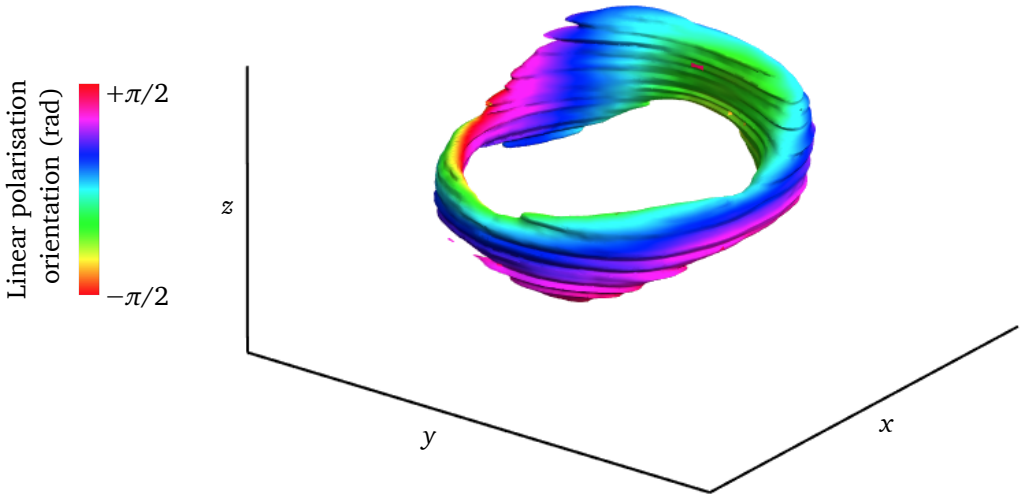


Figure 6.12: **Preliminary experimental results for an optical Hopfion**. The analysis of the Stokes parameters experimentally detected in the focal volume of the lens $L_3$, schematised in Figure 6.11, indicates the presence of the $(1,1)$-torus knotted Hopfion in a superposition of LG-beams. This is generated from the SLM which is shaped with the field (6.48) in Fourier space. The image represents the points $S_3 = 0$ corresponding to the linear polarised states, which form a toroidal surface [Experimental data by R. Runde[6], article in preparation].

inates the beam for large $R$, the volume around the optical axes truly behaves like polynomial beams and the topology of the Hopf fibration manifests itself locally. This characteristic is similar to the Hopfions that arise from tightly focused Zernike aperture modes (§ 6.3). In fact, similarly to the Airy rings appearing in the outer region of tightly focused Zernike modes, the Gaussian envelope influences the outer structure of the Hopf fibration.

The experiment design by Otte and Runde is shown in Figure 6.11. The intensity, the phase and the polarisation of two beams are shaped in Fourier space with the profile of the components (6.48) and the parameters $a, b, c, s, w_0$ chosen appropriately. The propagating beams of opposite circular polarisation are overlapped in real space and the 3D polarisation texture is detected by polarimetric measurements of the Stokes parameters. The preliminary analysis of the experimental data indicates that a

Hopfion-like structure of Hopf index $\mathcal{H} = -1$ appears in the focal volume in the position shown in Figure 6.11. This is in good agreement with the theoretical predictions. Figure 6.12 shows the toroidal surface formed by the discrete data representing the contour $S_3 = 0$. Further analysis in required to determine whether the Hopfion has formed all over the three-dimensional polarisation texture.

## 6.5 Discussion

Hopfions arising naturally in the polarisation texture of tightly focused Zernike modes were described. Each mode with index $n$ generates a Hopf fibration whose fibres are the $(n/2, 2)$ torus knots (or links). The construction was generalised to $(m, n)$-torus knotted Hopfions[7] by engineering paraxial optical fields with the aid of algebraic topology. The theoretical predictions have been implemented experimentally in a superposition of Laguerre-Gaussian polarised beams.

An optical Hopf fibration is represented mathematically by a transverse beam whose components $E_+, E_-$ are characterised, respectively, by orbital angular momentum 0 and $\ell$. This vector field is mapped to the Poincaré sphere through the Stokes parameters. The preimages of the sphere are lines characterised by the same polarisation state in Cartesian space and they can form $(m, n)$-torus knotted or linked configurations or disconnected loops, with $n = \ell$. In our theoretical model every two distinct preimages have linking number $-mn$, which is also the Hopf index $\mathcal{H}$ of the map. This topological invariant is the signature feature of a Hopfion.

It is important to emphasise that the topological objects arising from the Zernike family of modes occur naturally from the spin to orbit conversion in the lens system; it is not necessary to engineer the beam's structure. The input beam's intensity profile is an azimuthally-symmetric polynomial of order $n$ given by a Zernike aperture mode. When the perturbation caused by the geometry of the lens is not considered, focused Zernike modes generates a dark focus $\mathrm{J}_{n+1}(R)/R$. On the other hand, when the per-

[7] In this generalisation $n$ is not related to the index of the Zernike aperture mode mentioned before.

turbation is considered, the dark focus splits into nodal rings and the total topological charge is $-n/2$ in the $Rz$-plane. When the input beam is right-handed polarised, the geometry of the lens generates an OAM $\ell = 2$ in the left-handed component. The interaction of the principal right-handed component of the focal beam with the opposite component carrying orbital angular momentum generates a highly symmetric polarisation texture in the conformation of a Hopfion of Hopf charge $-n$. Note that similar results with inverted signs are found for a left-handed input beam. As a consequence the handedness of the Hopfion also changes. This phenomenon resembles the first construction of optical vortex lines in the shape of torus knots and links by Berry and Dennis [14]. It was shown that, under a small perturbation, a vortex ring of strength $m$ and a vortex line of strength $n$ which, unfold into the $(m,n)$-torus knots for $m$ and $n$ coprime or the $(m,n)$-torus links, otherwise. The closed curve was threaded by $n$ distinct lines. The resulting conformation was a stable structure made of strength $\mathcal{S} = 1$ optical vortex lines. Further investigation is required to prove that any Zernike mode of index $n$ generates a $(n/2,2)$-torus knotted Hopfion.

The family of Hopfions constitutes new topological states of light in a dark focus, robust under the perturbation of the focusing parameters. In fact, the Hopfions arise for all values of the numerical aperture $\gamma$. In the limit $\gamma \to 0$, which corresponds to a paraxially propagating scalar field, each Hopfion texture collapses into the dark focus and is only revealed when a small $\gamma$ perturbation is included. This condition is sufficient to create optical fields satisfying the paraxial wave equation and embedding perfect mathematical Hopfions in the polarisation texture. It seems that higher order terms in $\gamma$, corresponding to nonparaxial effects and lens geometrical effects, alter the structure of the topology in the outer region, leading to non integer values of the Hopf index. Nevertheless, high values of $\gamma$ still embed Hopfion-like structures in the focal volume. This is demonstrated by the fact that the linking number of two distinct polarisation states coincides with the Hopf index in the small $\gamma$ regime. An alternative method to quantify this topological invariant in a finite volume could give new insights

into the Hopf fibrations generated spontaneously into tightly focused Zernike modes. For instance, in [211] the Hopf index of a chiral magnet nanodisk is evaluated numerically in a finite volume showing that the result converges quickly when the total number of grid points is increased. Yet, we cannot apply the same method because the optical Hopfions are not entirely contained in a finite volume. This is because the outer rings belonging to the generalised Airy disks destroy their topology. In order to have a localised Hopfion, there would be an extended volume characterised by right-handed polarisation [212], which however is not the case. Optimisation techniques could be implemented to generate such localised Hopfions of integer Hopf charge in tightly focused beams.

Hopfions generated by the Zernike aperture modes were represented by a sum of Chandrasekhar-Kendall eigenstates in § 6.3.2. When the input beam is right/left-handed circularly polarised, the vector focal field is a curl eigenstate characterised by a well defined positive/negative helicity. CK-eigenstates were already adopted to describe optical Hopfions whose fibres are the electromagnetic field lines in [20]. Even though our fields manifest the same topology and are described by the same eigenbasis, the polarisation textures we describe do not have knotted field lines and, therefore, do not share the same physical nature of the fields described by Irvine and Bouwmeester in [20]. Nevertheless, curl eigenstates are of broad importance in plasma physics [205] and fluid dynamics [206]. The fact that our polarisation Hopfions have similar features could bring new insights to the context of structured light and singular optics.

In § 1.7, it was mentioned that Hopfions are very often associated to Skyrmions. These are characterised by a topological quantity called *Skyrmion number* (or winding number) [212]. Skyrmions may be considered generalisations of the Hopf fibration where an overall phase factor is included in the vector field representing the physical field. Recent results [184] showed that 2D Skyrmions can be generated from the superposition of two Laguerre-Gaussian beams with OAM $\ell = 0$ and $\ell = \pm 1$. In some

areas, such as particle physics, these solitons are called *baby Skyrmions* to distinguish their 2D nature from the 3D nature of "true" Skyrmions. It seems that the topological objects of [184] are equivalent to the paraxial Hopfions presented in § 6.4 at the slice $z = 0$. Hence, our results should be their 3D counterpart. Further investigation will reveal whether there is a deeper connection between our optical Hopfions and 3D Skyrmions. An evident difference is that the optical Hopfions describe here do not arise from minimising the energy functional.

The generation of tightly focused Zernike aperture modes does not require particular skills in hologram shaping, as the Hopfions arise spontaneously in the focal volume. However, the dark features of polarisation Hopfions indicate that the major experimental difficulty is the detection of the beam. Recent work is moving in the direction of optimising the detection of vector fields at the nanoscale [166], albeit with little interest in low amplitude (dark) fields. The experimental realisation of paraxial Hopfions (§ 6.4) has been possible because their size is much larger than their tightly focused analogues. Nonetheless, also the paraxial experiment is very difficult because the polarisation texture of the entire focal volume needs to be controlled with accuracy. Optimisation of the experimental methods is required to generate Hopfions of higher order Hopf index.

If Hopfions in the polarisation texture of optical beams were to be implemented, robust topological structures with big potential for applications could be accessed. Dark beams have been used in the past as bottle beams generated from the interference of two fundamental Gaussian beams with different waists [213]. This type of beam is used to trap cold atoms. Optical Hopfions have similar features and could be applied into atom traps to trigger curious topological driving dynamics. Recent work [214, 215] showed that the spin texture of topological insulators depends on changes in the polarisation of the incident light. Other examples of skyrmionic spin texture created experimentally within an optically trapped and spin-polarised ferromagnet was given in [216]. Other applications could involve magnetic nanostructures which are useful

for data storage, sensing and biomedicine. Patterned nanomagnets were traditionally two-dimensional planar structures, but recent work has expanded nanomagnets into three dimensions, where more complex configurations become possible [217], such as Hopf fibrations [211]. Other applications have been shown in the emission from the polariton condensate [184] in planar systems.

# 7 | Conclusions

**In light of knowledge attained, the happy achievement seems almost a matter of course, and any intelligent student can grasp it without too much trouble. But the years of anxious searching in the dark, with their intense longing, their alterations of confidence and exhaustion and the final emergence into the light – only those who have experienced it can understand it.**

*Albert Einstein*

This thesis investigated optical fields whose spatial conformations have the form of knots and links. We showed that nontrivial topological states manifest naturally in the dark focus of light beams. The explicit construction of optical wavefunctions characterised by knotted and linked optical vortices had already been established in the literature. We investigated these fields in detail and brought a new level of analysis to optical beams, given by volume filling configurations corresponding to knotted textures of polarisation states.

Our investigation started by considering optical vortex knots and links in paraxial scalar fields. The study was based on previous results in which algebraic topology (specifically Milnor polynomials) was adopted to design knotted optical wavefunctions (§ 4.1). Similarly, the mathematical functions corresponding to the family of lemniscate knots and links were used in § 4.2 to build the same type of curves in optical fields. The experimental realisation of these optical vortex knots in superpositions of Laguerre-Gaussian beams requires the design of holographic plates. A

similar method based on the ENZ-theory of propagation and involving superpositions of Zernike aperture modes was proposed in § 4.3. We then demonstrated that the analysis of beams with space-varying polarisation properties gives new insights into the understanding of topological optics. Knotted C-lines were generated theoretically and experimentally in superpositions of LG-modes, and the topological analysis of the Seifert surfaces (seifertometry) was performed on these beams (§ 4.4).

We continued to explore vector fields in § 5.1, by bringing knots and links to the nonparaxial regime, in which the polarised nature of light was non-negligible. The scaling rules of paraxial beams were analysed in § 5.2 and the effects of nonparaxiality on knotted optical vortex lines were investigated in § 5.3. The full analyses of the electric and magnetic fields were performed and a singular bundle of knotted components in an optimal nonparaxial regime was presented. The realisation of this singular topological object was proposed in an experiment involving tightly focused Laguerre-Gaussian modes (§ 5.4). In addition, we showed that knot bundles corresponding to the torus knots can be found in the nonparaxial regime (§ 5.5).

We pursued the investigation of tightly focused beams by considering dark foci arising from diffracted Zernike modes (§ 6.1). First, the analytical tools to analyse such beams were developed: they were the SWAS theory of propagation, the nonparaxial ENZ-theory and the simplified Hopf index integral (§ 6.2). Further, our results concerning the family of Hopfions in the polarisation texture of tightly focused Zernike aperture modes were presented (§ 6.3). These embedded the torus knots as lines of fixed polarisation. The results were extended to the paraxial regime, showing that not only can Hopfions manifest in tightly focused Zernike modes, but they can also characterise other optical fields represented by vector fields with certain OAM properties. We presented preliminary results on the experimental realisation of Hopfions engineered in LG-modes (§ 6.4).

Our results leave space for immediate considerations. They show the connection between singular and topological optics: the first investigates singular physical quant-

ities in light fields, such as phase singularities, the second associates the field with topological quantities, such as the Skyrmion number. We demonstrated that singular optics is deeply connected with the polarisation texture of focused fields. This was explicitly demonstrated by our results, since Seifert surfaces were reconstructed from polarimetry around C-lines, the singular knot bundles arose from the tight focusing of optical vortex knots and the optical Hopfions collapsed into optical vortex rings in the scalar paraxial regime. The phase and polarisation singularities of an optical field form a 'skeleton' supporting the topology of the beam. We developed the results in this study by taking a journey form optical vortices to C-lines and L-surfaces, and finally to lines of constant polarisation. This new direction led to the discovery of three-dimensional polarisation textures in the form of Hopf fibrations and Skyrmions.

The study of complicated topological conformations required the development and adaptation of numerical and analytical propagation methods for the description of the geometric structure of light fields in regions of low intensity. At the same time, these theoretical techniques aimed to be practical approximations that are consistent with standard routines of experimental optics. This was demonstrated by the several experiment designs proposed throughout the different chapters, two of which (seifertometry and paraxial Hopfions) were realised in the laboratory. Further advances of experimental techniques in topological optics could be used to imprint stable topological states into matter systems.

Our results indicate a new way of thinking about knotted light. The similarities between dislocations in crystal lattices and scalar optical fields, which historically started the 'realm' of singular optics, seems to reappear in the context of 3D polarisation textures. Our results concerning optical Hopfions, characterised by invariant Hopf index, emphasise the mathematical connections between optics and nuclear physics or soft matter. It is natural to ask whether there are more optical phenomena, different from dark foci, that embed nontrivial and undiscovered geometric configurations. For example, near-field optics could represent an alternative framework for applied

topology.

A natural direction for future work is to construct knotted and linked vortex lines into acoustic beams. In principle, this would be possible because the wavefunctions describing sound satisfy the scalar Helmholtz equation as well as optical wavefunctions. Therefore, the theoretical and numerical methods used throughout this thesis could be equivalently applied to knots of 'silence'. The recent construction of single-sided ultrasonic emitters to generate acoustic structures [218] suggests that these elements could have the same role of SLMs for light. The emitters are computer-controlled devices generating phase delays in an array of transducers. Sound has already been used to generate 3D acoustic trapping, translation and rotation of levitated particles in air [218]. The same method could also operate in water or tissue. It is predicted that acoustic tweezers could become the larger-scale counterparts of optical tweezers. Furthermore, acoustically-controlled machines have the advantage of not interfering with the magnetic field present in a physical system. This property favours topological applications on magnetic materials.

# Bibliography


[1] L. H. Kauffman, *Knots and Physics* (World Scientific, 2001), 4th ed.

[2] M. D. Frank-Kamenetskii, A. V. Lukashin, and A. V. Vologodskii, "Statistical mechanics and topology of polymer chains", *Nature* **258**, 398–402 (1975).

[3] L. F. Liu, J. L. Davis, and R. Calendar, "Novel topologically knotted DNA from bacteriophage P4 capsids: studies with DNA topoisomerases", *Nucleic Acids Res.* **9**, 3979–3989 (1981).

[4] N. C. H. Lim and S. E. Jackson, "Molecular knots in biology and chemistry", *J. Phys.: Condens. Matter* **27**, 354101 (2015).

[5] J. J. Danon, A. Krüger, D. A. Leigh, J.-F. Lemonnier, A. J. Stephens, I. J. Vitorica-Yrezabal, and S. L. Woltering, "Braiding a molecular knot with eight crossings", *Science* **355**, 159–162 (2017).

[6] U. Tkalec, M. Ravnik, S. Čopar, S. Žumer, and I. Muševič, "Reconfigurable knots and links in chiral nematic colloids", *Science* **333**, 62–65 (2011).

[7] A. Martinez, M. Ravnik, B. Lucero, R. Visvanathan, S. Žumer, and I. I. Smalyukh, "Mutually tangled colloidal knots and induced defect loops in nematic fields", *Nat. Mater.* **13**, 258–263 (2014).

[8] D. Kleckner and W. T. M. Irvine, "Creation and dynamics of knotted vortices", *Nat. Phys.* **9**, 253–258 (2013).

[9] M. V. Berry, "Knotted zeros in the quantum states of hydrogen", *Found. Phys.* **31**, 659–667 (2001).

[10] A. Enciso, D. Hartley, and D. Peralta-Salas, "A problem of Berry and knotted zeros in the eigenfunctions of the harmonic oscillator", *J. Eur. Math. Soc.* **20**, 301–314 (2018).

[11] A. J. Taylor and M. R. Dennis, "Vortex knots in tangled quantum eigenfunctions", *Nat. Commun.* **7**, 12346 (2016).

[12] D. Proment, M. Onorato, and C. F. Barenghi, "Vortex knots in a Bose-Einstein condensate", *Phys. Rev. E* **85**, 036306 (2012).

[13] P. M. Sutcliffe and A. T. Winfree, "Stability of knots in excitable media", *Phys. Rev. E* **68**, 016218 (2003).

[14] M. V. Berry and M. R. Dennis, "Knotted and linked phase singularities in monochromatic waves", *Proc. R. Soc. A* **457**, 2251–2263 (2001).

[15] M. V. Berry and M. R. Dennis, "Knotting and unknotting of phase singularities: Helmholtz waves, paraxial waves and waves in 2+1 spacetime", *J. Phys. A* **34**, 8877–8888 (2001).

[16] J. Leach, M. R. Dennis, J. Courtial, and M. J. Padgett, "Laser beams: Knotted threads of darkness", *Nature* **432**, 165–165 (2004).

[17] J. Leach, M. R. Dennis, J. Courtial, and M. J. Padgett, "Vortex knots in light", *New J. Phys.* **7**, 55 (2005).

[18] M. R. Dennis, R. P. King, B. Jack, K. O'Holleran, and M. J. Padgett, "Isolated optical vortex knots", *Nat. Phys.* **6**, 118–121 (2010).

[19] M. J. Padgett, K. O'Holleran, R. P. King, and M. R. Dennis, "Knotted and tangled threads of darkness in light beams", *Contemp. Phys.* **52**, 265–279 (2011).

[20] W. T. M. Irvine and D. Bouwmeester, "Linked and knotted beams of light", *Nat. Phys.* **4**, 817–817 (2008).

[21] H. Kedia, I. Bialynicki-Birula, D. Peralta-Salas, and W. T. M. Irvine, "Tying knots in light fields", *Phys. Rev. Lett.* **111**, 150404 (2013).

[22] M. Arrayás, D. Bouwmeester, and J. Trueba, "Knots in electromagnetism", *Phys. Rep.* **667**, 1–61 (2017).

[23] M. R. Dennis, K. O'Holleran, and M. J. Padgett, "Chapter 5 singular optics: Optical vortices and polarization singularities", (Elsevier, 2009), pp. 293–363.

[24] H. Wolter, "Zur frage des lichtweges bei totalreflexion", *Z. Naturforsch. A* **5**, 276–283 (1950).

[25] F. Goos and H. Hänchen, "Ein neuer und fundamentaler versuch zur totalreflexion", *Ann. Phys.* **436**, 333–346 (1947).

[26] A. Boivin, J. Dow, and E. Wolf, "Energy flow in the neighborhood of the focus of a coherent beam", *J. Opt. Soc. Am.* **57**, 1171–1175 (1967).

[27] W. Braunbek, "Zur darstellung von wellenfeldern", *Zeitschrift Naturforschung A* **6**, 12–15 (1951).

[28] W. Braunbek and G. Laukien, "Einzelheiten zur Halbebenen-Beugung", *Optik* **9**, 174–179 (1952).

[29] A. Sommerfeld, "Optics", (Academic Press, 1964).

[30] M. Born and E. Wolf, *Principles of Optics* (Cambridge University Press, 1999), 7th ed.

[31] J. F. Nye and M. V. Berry, "Dislocations in wave trains", *Proc. R. Soc. A* **336**, 165–190 (1974).

[32] M. V. Berry, M. R. Dennis, and R. L. Lee Jr, "Polarization singularities in the clear sky", *New J. Phys.* **6**, 162 (2004).

[33] Y. Aharonov, F. Colombo, I. Sabadini, D. C. Struppa, and J. Tollaksen, "Some mathematical properties of superoscillations", *J. Phys. A* **44**, 365304 (2011).

[34] M. V. Berry and S. Popescu, "Evolution of quantum superoscillations and optical superresolution without evanescent waves", *J. Phys. A* **39**, 6965–6977 (2006).

[35] M. R. Dennis, "Topological singularities in wave fields", PhD dissertation, University of Bristol (2001).

[36] E. Bartholinus, "Experimenta crystalli islandici disdiaclastici quibus mira et insolita refractio detegitur", *Hafniae* (1669).

[37] C. Brosseau, *Fundamentals of Polarized Light: A Statistical Optics Approach* (John Wiley & Sons, 1998).

[38] E. L. Malus, "Sur une propriété de la lumière réfléchie", *Mem. Soc. Arcueil* **1**, 143–158 (1809).

[39] D. Brewster, "On the polarization of the atmosphere", *Philos. Mag.* **31**, 444–454 (1847).

[40] D. Brewster, "Observations of the polarisation of the atmosphere, made at St. Andrews in 1841, 1842, 1843, 1844, and 1845", *Trans. R. Soc. Edin.* **23**, 211–239 (1863).

[41] J. F. Nye, "Polarization effects in the diffraction of electromagnetic waves: the role of disclinations", *Proc. R. Soc. A* **387**, 105–132 (1983).

[42] J. F. Nye, "Lines of circular polarization in electromagnetic wave fields", *Proc. R. Soc. A* **389**, 279–290 (1983).

[43] M. V. Berry, "The electric and magnetic polarization singularities of paraxial waves", *J. Opt. A: Pure Appl. Opt.* **6**, 475 (2004).

[44] M. Dennis, "Polarization singularities in paraxial vector fields: morphology and statistics", *Opt. Commun.* **213**, 201–221 (2002).

[45] C. Tamm and C. O. Weiss, "Bistability and optical switching of spatial patterns in a laser", *J. Opt. Soc. Am. B* **7**, 1034–1038 (1990).

[46] A. A. Ishaaya, N. Davidson, G. Machavariani, E. Hasman, and A. A. Friesem, "Efficient selection of high-order Laguerre-Gaussian modes in a q-switched Nd:YAG laser", *IEEE Journal of Quantum Electronics* **39**, 74–82 (2003).

[47] M. Okida, T. Omatsu, M. Itoh, and T. Yatagai, "Direct generation of high power Laguerre-Gaussian output from a diode-pumped Nd:$YVO_4$ 1.3-$\mu$m bounce laser", *Opt. Express* **15**, 7616–7622 (2007).

[48] V. Y. Bazenhov, M. V. Vasnetsov, and M. S. Soskin, "Laser beams with screw dislocations in their wavefronts", *JETP Lett.* **52**, 429–431 (1990).

[49] N. R. Heckenberg, R. McDuff, C. P. Smith, H. Rubinsztein-Dunlop, and M. J. Wegener, "Laser beams with phase singularities", *Opt. Quant. Electron* **24**, S951–S962 (1992).

[50] E. Abramochkin and V. Volostnikov, "Beam transformations and nontransformed beams", *Opt. Commun.* **83**, 123–135 (1991).

[51] L. Allen, M. W. Beijersbergen, R. J. C. Spreeuw, and J. P. Woerdman, "Orbital angular momentum of light and the transformation of Laguerre-Gaussian laser modes", *Phys. Rev. A* **45**, 8185–8189 (1992).

[52] M. W. Beijersbergen, L. Allen, H. E. L. O. van der Veen, and J. P. Woerdman, "Astigmatic laser mode converters and transfer of orbital angular momentum", *Opt. Commun.* **96**, 123–132 (1993).

[53] M. W. Beijersbergen, R. P. C. Coerwinkel, M. Kristensen, and J. P. Woerdman, "Helical-wavefront laser beams produced with a spiral phaseplate", *Opt. Commun.* **112**, 321–327 (1994).

[54] `https://www.meadowlark.com`, accessed 31-10-2018.

[55] J. Durnin, "Exact solutions for nondiffracting beams. I. The scalar theory", *J. Opt. Soc. Am. A* **4**, 651–654 (1987).

[56] J. Durnin, J. J. Miceli Jr., and J. H. Eberly, "Diffraction-free beams", *Phys. Rev. Lett.* **58**, 1499–1501 (1987).

[57] J. F. Nye, "Unfolding of higher-order wave dislocations", *J. Opt. Soc. Am. A* **15**, 1132–1138 (1998).

[58] R. P. King, "Knotting of optical vortices", PhD dissertation, University of Southampton (2010).

[59] K. O'Holleran, "Fractality and topology of optical singularities", PhD dissertation, University of Glasgow (2008).

[60] H. Urbantke, "The hopf fibration—seven times in physics", *J. Geom. Phys.* **46**, 125–150 (2003).

[61] M. Nakahara, *Geometry, Topology and Physics* (Institute of Physics Publishing, 1990).

[62] G. E. Martin, *Transformation Geometry* (Springer-Verlag, 1982).

[63] R. Mosseri and R. Dandoloff, "Geometry of entangled states, Bloch spheres and Hopf fibrations", *J. Phys. A* **34**, 10243–10252 (2001).

[64] A. M. Kamchatnov, "Topological soliton in magnetohydrodynamics", *Zh. Eksp. Teor. Fiz.* **55**, 117–124 (1982).

[65] A. Thompson, A. Wickes, J. Swearngin, and D. Bouwmeester, "Classification of electromagnetic and gravitational hopfions by algebraic type", *J. Phys. A* **48**, 205202 (2015).

[66] A. F. Rañada, "A topological theory of the electromagnetic field", *Lett. Math. Phys.* **18**, 97–106 (1989).

[67] T. H. R. Skyrme, "A unified field theory of mesons and baryons", *Nucl. Phys.* **31**, 556–569 (1962).

[68] L. Ferreira, N. Sawado, and K. Toda, "Static Hopfions in the extended Skyrme-Faddeev model", *J. High Energy Phys.* **2009**, 124 (2009).

[69] D. Foster, "Static Hopfions in the extended Skyrme-Faddeev model", *J. High Energy Phys.* **2012**, 81 (2012).

[70] P. Sutcliffe, "Skyrmion knots in frustrated magnets", *Phys. Rev. Lett.* **118**, 247203 (2017).

[71] B. G.-g. Chen, P. J. Ackerman, G. P. Alexander, R. D. Kamien, and I. I. Smalyukh, "Generating the Hopf Fibration Experimentally in Nematic Liquid Crystals", *Phys. Rev. Lett.* **110**, 237801 (2013).

[72] P. J. Ackerman and I. I. Smalyukh, "Diversity of Knot Solitons in Liquid Crystals Manifested by Linking of Preimages in Torons and Hopfions", *Phys. Rev. X* **7**, 011006 (2017).

[73] Y. Kawaguchi, M. Nitta, and M. Ueda, "Knots in a spinor Bose-Einstein condensate", *Phys. Rev. Lett.* **100**, 180403 (2008).

[74] D. S. Hall, M. W. Ray, K. Tiurev, E. Ruokokoski, A. H. Gheorghe, and M. Möttönen, "Tying quantum knots", *Nat. Phys.* **12**, 478–483 (2016).

[75] T. Ollikainen, S. Masuda, M. Möttönen, and M. Nakahara, "Quantum knots in Bose-Einstein condensates created by counterdiabatic control", *Phys. Rev. A* **96**, 063609 (2017).

[76] X.-X. Yuan, L. He, S.-T. Wang, D.-L. Deng, F. Wang, W.-Q. Lian, X. Wang, C.-H. Zhang, H.-L. Zhang, X.-Y. Chang, and L.-M. Duan, "Observation of Topological Links Associated with Hopf Insulators in a Solid-State Quantum Simulator", *Chin. Phys. Lett.* **34**, 060302 (2017).

[77] J. D. Jackson, *Classical Electrodynamics* (John Wiley & Sons, 1975), 2nd ed.

[78] L. Mandel and E. Wolf, *Optical Coherence and Quantum Optics* (Cambridge University Press, 1995).

[79] J. W. Goodman, *Introduction to Fourier Optics* (Roberts & Company Publishers, 2005).

[80] B. R. A. Nijboer, "The diffraction theory of aberrations", PhD dissertation, University of Groningen (1942).

[81] L. Novotny and B. Hecht, *Principles of Nano-Optics* (Cambridge University Press, 2012), 2nd ed.

[82] M. R. Dennis, "Geometric interpretation of the three-dimensional coherence matrix for nonparaxial polarization", *J. Opt. A: Pure Appl. Opt.* **6**, S26–S31 (2004).

[83] M. V. Berry, "Wave dislocation reactions in non-paraxial gaussian beams", *J. Mod. Opt.* **45**, 1845–1858 (1998).

[84] M. R. Dennis, J. B. Götte, R. P. King, M. A. Morgan, and M. A. Alonso, "Paraxial and nonparaxial polynomial beams and the analytic approach to propagation", *Opt. Lett.* **36**, 4452–4454 (2011).

[85] A. Torre, "The appell transformation for the paraxial wave equation", *J. Opt.* **13**, 015701 (2011).

[86] R. Borghi, F. Gori, G. Guattari, and M. Santarsiero, "Decoding divergent series in nonparaxial optics", *Opt. Lett.* **36**, 963–965 (2011).

[87] D. V. Widder, *The heat equation* (Academic Press, 1976).

[88] E. Grosswald, *Bessel Polynomials* (Springer, 1979).

[89] A. J. E. M. Janssen, "Extended Nijboer–Zernike approach for the computation of optical point-spread functions", *J. Opt. Soc. Am. A* **19**, 849–857 (2002).

[90] P. Debye, "Das Verhalten von Lichtwellen in der Nähe eines Brennpunktes oder einer Brennlinie", *Ann. Phys.* **335**, 755–776 (1909).

[91] E. Wolf and Y. Li, "Conditions for the validity of the Debye integral representation of focused fields", *Opt. Commun.* **39**, 205–210 (1981).

[92] C. J. R. Sheppard, "Validity of the Debye approximation", *Opt. Lett.* **25**, 1660–1662 (2000).

[93] A. J. E. M. Janssen, J. J. M. Braat, and P. Dirksen, "On the computation of the Nijboer-Zernike aberration integrals at arbitrary defocus", *J. Mod. Opt.* **51**, 687–703 (2004).

[94] V. S. Ignatovsky, "The relationship between geometric and wave optics and diffraction of an azimuthally symmetric beam", *Trans. Opt. Inst. Petrograd* **1**, paper 3 (1920).

[95] V. S. Ignatovsky, "Diffraction by a lens with arbitrary aperture", *Trans. Opt. Inst. Petrograd* **1**, paper 4 (1920).

[96] E. Wolf, "Electromagnetic diffraction in optical systems. I. An integral representation of the image field", *Proc. R. Soc. A* **253**, 349–357 (1959).

[97] B. Richards and E. Wolf, "Electromagnetic diffraction in optical systems. II. Structure of the image field in an aplanatic system", *Proc. R. Soc. A* **253**, 358–379 (1959).

[98] A. Boivin and E. Wolf, "Electromagnetic field in the neighborhood of the focus of a coherent beam", *Phys. Rev.* **138**, B1561–B1565 (1965).

[99] M. Leutenegger, R. Rao, R. A. Leitgeb, and T. Lasser, "Fast focus field calculations", *Opt. Express* **14**, 11277–11291 (2006).

[100] K. O'Holleran, M. R. Dennis, and M. J. Padgett, "Topology of light's darkness", *Phys. Rev. Lett.* **102**, 143902 (2009).

[101] K. O'Holleran, M. R. Dennis, F. Flossmann, and M. J. Padgett, "Fractality of light's darkness", *Phys. Rev. Lett.* **100**, 053902 (2008).

[102] M. V. Berry and M. R. Dennis, "Topological events on wave dislocation lines: birth and death of loops, and reconnection", *J. Phys. A* **40**, 65–74 (2006).

[103] J. F. Nye and J. V. Hajnal, "The wave structure of monochromatic electromagnetic radiation", *Proc. R. Soc. A* **409**, 21–36 (1987).

[104] G. Burde and H. Zieschang, *Knots*, vol. 5 of *de Gruyter Studies in Mathematics* (Walter de Gruyter, 2003), 2nd ed.

[105] V. Manturov, *Knot Theory* (CRC Press, 2004).

[106] C. M. Gordon and J. Luecke, "Knots are determined by their complements", *Bull. Amer. Math. Soc. (N.S.)* **20**, 83–87 (1989).

[107] K. Alexander, A. J. Taylor, and M. R. Dennis, "Proteins analysed as virtual knots", *Sci. Rep.* **7**, 42300 (2017).

[108] L. H. Kauffman, "Topological quantum information, virtual Jones polynomials and Khovanov homology", *New J. Phys.* **13**, 125007 (2011).

[109] C. N. Little, "On knots, with a census of order ten", *Trans. Connecticut Acad. Sci.* **18**, 374–378 (1885).

[110] P. G. Tait, *On knots I, II, III*, vol. 1 of *Scientific Papers* (Cambridge University Press, 1900).

[111] J. W. Alexander and G. B. Briggs, "On types of knotted curves", *Ann. Math.* **28**, 562–586 (1926).

[112] J. H. Conway, "An enumeration of knots and links, and some of their algebraic properties", in *Computational Problems in Abstract Algebra,* (Pergamon Press, 1967), pp. 329–358.

[113] D. Rolfsen, *Knots and Links* (AMS Chelsea Publishing, 2003).

[114] K. A. Perko, "On the classification of knots", *Proc. Amer. Math. Soc.* **45**, 262–266 (1974).

[115] A. J. Taylor, *Analysis of Quantised Vortex Tangle* (Springer, 2017).

[116] D. Bar-Natan and S. Morrison *et al.*, "The knot atlas", `http://katlas.org`, accessed 31-10-2018.

[117] M. R. Dennis and B. Bode, "Constructing a polynomial whose nodal set is the three-twist knot $5_2$", *J. Phys. A* **50**, 265204 (2017).

[118] J. W. Alexander, "A lemma on systems of knotted curves", *Proc. Natl. Acad. Sci. U.S.A.* **9**, 93–95 (1923).

[119] D. Auroux, J. E. Grigsby, and S. M. Wehrli, "Sutured Khovanov homology, Hochschild homology, and the Ozsváth-Szabó spectral sequence", *Trans. Amer. Math. Soc.* **367**, 7103–7131 (2015).

[120] H. Hopf, "Über die Abbildungen der dreidimensionalen Sphäre auf die Kugelfläche", *Math. Ann.* **104**, 637–665 (1931).

[121] H. Hopf, "Über die Abbildungen von Sphären auf Sphäre niedrigerer Dimension", *Fundam. Math.* **25**, 427–440 (1935).

[122] D. W. Lyons, "An Elementary Introduction to the Hopf Fibration", *Mathe. Mag.* **76**, 87–98 (2003).

[123] R. Bott and L. W. Tu, *Differential Forms in Algebraic Topology* (Springer-Verlag, 1982).

[124] J. Dieudonné, *Treatise in Analysis*, vol. 3 (Academic Press, 1972).

[125] J. H. C. Whitehead, "An Expression of Hopf's Invariant as an Integral", *Proc. Natl. Acad. Sci. U.S.A.* **33**, 117–123 (1947).

[126] H. Kedia, D. Foster, M. R. Dennis, and W. T. M. Irvine, "Weaving knotted vector fields with tunable helicity", *Phys. Rev. Lett.* **117**, 274501 (2016).

[127] J. Bochnak, M. Coste, and M.-F. Roy, *Real algebraic geometry* (Springer, 1998).

[128] K. Brauner, "Das Verhalten der Funktionen in der Umgebung ihrer Verzweigungsstellen", *Abh. Math. Semin. Univ. Hambg.* **6**, 1–55 (1928).

[129] B. Perron, "Le noeud «huit» est algebrique réel", *Invent. Math.* **65**, 441–451 (1982).

[130] J. D. Lawrence, *A catalog of special plane curves* (Dover Publications, 1972).

[131] L. Rudolph, "Isolated critical points of mappings from $R^4$ to $R^2$ and a natural splitting of the Milnor number of a classical fibered link. Part I: Basic theory; examples", *Comment. Math. Helv.* **62**, 630–645 (1987).

[132] B. Bode, M. R. Dennis, D. Foster, and R. P. King, "Knotted fields and explicit fibrations for lemniscate knots", *Proc. R. Soc. A* **473**, 20160829 (2017).

[133] B. Bode and M. R. Dennis, "Constructing a polynomial whose nodal set is any prescribed knot or link", arXiv:1612.06328v2 (2016).

[134] K. O'Holleran, F. Flossmann, M. R. Dennis, and M. J. Padgett, "Methodology for imaging the 3D structure of singularities in scalar and vector optical fields", *J. Opt. A: Pure Appl. Opt.* **11**, 094020 (2009).

[135] A. J. Taylor and M. R. Dennis, "Geometry and scaling of tangled vortex lines in three-dimensional random wave fields", *J. Phys. A* **47**, 465101 (2014).

[136] E. Orlandini and S. G. Whittington, "Statistical topology of closed curves: Some applications in polymer physics", *Rev. Mod. Phys.* **79**, 611–642 (2007).

[137] H. Larocque, D. Sugic, D. Mortimer, A. J. Taylor, R. Fickler, R. W. Boyd, M. R. Dennis, and E. Karimi, "Reconstructing the topology of optical polarization knots", *Nat. Phys.* **14**, 1079–1082 (2018).

[138] A. J. Taylor and other SPOCK contributors, "pyknotid knot identification toolkit v0.5.3", `http://github.com/SPOCKnots/pyknotid`, accessed 09-05-2018.

[139] W. E. Lorensen and H. E. Cline, "Marching cubes: A high resolution 3D surface construction algorithm", *SIGGRAPH Comput. Graph.* **21**, 163–169 (1987).

[140] I. Chavel, *Riemannian geometry: a modern introduction* (Cambridge University Press, 2006), 2nd ed.

[141] J. F. Nye, "Phase saddles in light beams", *J. Opt.* **13**, 075709 (2011).

[142] H. Rubinsztein-Dunlop, A. Forbes, M. V. Berry, M. R. Dennis, D. L. Andrews, M. Mansuripur, C. Denz, C. Alpmann, P. Banzer, T. Bauer, E. Karimi, L. Marrucci, M. Padgett, M. Ritsch-Marte, N. M. Litchinitser, N. P. Bigelow, C. Rosales-Guzmán, A. Belmonte, J. P. Torres, T. W. Neely, M. Baker, R. Gordon, A. B. Stilgoe, J. Romero, A. G. White, R. Fickler, A. E. Willner, G. Xie, B. McMorran, and A. M. Weiner, "Roadmap on structured light", *J. Opt.* **19**, 013001 (2017).

[143] M. V. Berry *et al.*, "Roadmap on superoscillations", *J. Opt.*, to be published.

[144] R. Askey and D. T. Haimo, "Similarities Between Fourier and Power Series", *Am. Math. Mon.* **103**, 297–304 (1996).

[145] W. Qiao, "A simple model of Aharonov-Berry's superoscillations", *J. Phys. A* **29**, 2257–2258 (1996).

[146] J. Romero, J. Leach, B. Jack, M. R. Dennis, S. Franke-Arnold, S. M. Barnett, and M. J. Padgett, "Entangled optical vortex links", *Phys. Rev. Lett.* **106**, 100407 (2011).

[147] R. Fickler, R. Lapkiewicz, W. N. Plick, M. Krenn, C. Schaeff, S. Ramelow, and A. Zeilinger, "Quantum entanglement of high angular momenta", *Science* **338**, 640–643 (2012).

[148] E. Bolduc, N. Bent, E. Santamato, E. Karimi, and R. W. Boyd, "Exact solution to simultaneous intensity and phase encryption with a single phase-only hologram", *Opt. Lett.* **38**, 3546–3549 (2013).

[149] D. Rozas, C. T. Law, and G. A. Swartzlander, "Propagation dynamics of optical vortices", *J. Opt. Soc. Am. B* **14**, 3054–3065 (1997).

[150] R. Fickler, R. Lapkiewicz, S. Ramelow, and A. Zeilinger, "Quantum entanglement of complex photon polarization patterns in vector beams", *Phys. Rev. A* **89**, 060301 (2014).

[151] E. Karimi, J. Leach, S. Slussarenko, B. Piccirillo, L. Marrucci, L. Chen, W. She, S. Franke-Arnold, M. J. Padgett, and E. Santamato, "Spin-orbit hybrid entanglement of photons and quantum contextuality", *Phys. Rev. A* **82**, 022115 (2010).

[152] A. Bhowmik, P. K. Mondal, S. Majumder, and B. Deb, "Interaction of atom with nonparaxial Laguerre-Gaussian beam: Forming superposition of vortex states in Bose-Einstein condensates", *Phys. Rev. A* **93**, 063852 (2016).

[153] L. Marrucci, C. Manzo, and D. Paparo, "Optical spin-to-orbital angular momentum conversion in inhomogeneous anisotropic media", *Phys. Rev. Lett.* **96**, 163905 (2006).

[154] A. Ambrosio, L. Marrucci, F. Borbone, A. Roviello, and P. Maddalena, "Light-induced spiral mass transport in azo-polymer films under vortex-beam illumination", *Nat. Commun.* **3**, 989 (2012).

[155] J. Ni, C. Wang, C. Zhang, Y. Hu, L. Yang, Z. Lao, B. Xu, J. Li, D. Wu, and J. Chu, "Three-dimensional chiral microstructures fabricated by structured optical vortices in isotropic material", *Light: Sci. & Appl.* **6**, e17011 (2017).

[156] D. Sugic and M. R. Dennis, "Singular knot bundle in light", *J. Opt. Soc. Am. A* **35**, 1987–1999 (2018).

[157] R. P. Cameron, "Monochromatic knots and other unusual electromagnetic disturbances: light localised in 3D", *J. Phys. Commun.* **2**, 015024 (2018).

[158] K. Y. Bliokh, F. J. Rodríguez-Fortuño, F. Nori, and A. V. Zayats, "Spin-orbit interactions of light", *Nat. Photonics* **9**, 796–808 (2015).

[159] A. I. Akhiezer and V. B. Berestetsky, *Quantum Electrodynamics* (Interscience Publishers, 1965).

[160] K. Y. Bliokh, E. A. Ostrovskaya, M. A. Alonso, O. G. Rodríguez-Herrera, D. Lara, and C. Dainty, "Spin-to-orbital angular momentum conversion in focusing, scattering, and imaging systems", *Opt. Express* **19**, 26132–26149 (2011).

[161] T. G. Jabbour and S. M. Kuebler, "Vectorial beam shaping", *Opt. Express* **16**, 7203–7213 (2008).

[162] J. J. M. Braat, P. Dirksen, A. J. E. M. Janssen, and A. S. van de Nes, "Extended Nijboer-Zernike representation of the vector field in the focal region of an aberrated high-aperture optical system", *J. Opt. Soc. Am. A* **20**, 2281–2292 (2003).

[163] M. R. Foreman, S. S. Sherif, P. R. T. Munro, and P. Török, "Inversion of the Debye-Wolf diffraction integral using an eigenfunction representation of the electric fields in the focal region", *Opt. Express* **16**, 4901–4917 (2008).

[164] M. Lax, W. H. Louisell, and W. B. McKnight, "From Maxwell to paraxial wave optics", *Phys. Rev. A* **11**, 1365–1370 (1975).

[165] M. V. Berry and M. R. Dennis, "Reconnections of wave vortex lines", *Eur. J. Phys.* **33**, 723–731 (2012).

[166] T. Bauer, S. Orlov, U. Peschel, P. Banzer, and G. Leuchs, "Nanointerferometric amplitude and phase reconstruction of tightly focused vector beams", *Nat. Photonics* **8**, 23–27 (2013).

[167] B. T. Miles, X. Hong, and H. Gersen, "On the complex point spread function in interferometric cross-polarisation microscopy", *Opt. Express* **23**, 1232–1239 (2015).

[168] R. Dorn, S. Quabis, and G. Leuchs, "The focus of light-linear polarization breaks the rotational symmetry of the focal spot", *J. Mod. Opt.* **50**, 1917–1926 (2003).

[169] Y. Zhao, J. S. Edgar, G. D. M. Jeffries, D. McGloin, and D. T. Chiu, "Spin-to-orbital angular momentum conversion in a strongly focused optical beam", *Phys. Rev. Lett.* **99**, 073901 (2007).

[170] F. Maucher, S. Skupin, S. A. Gardiner, and I. G. Hughes, "Creating complex optical longitudinal polarization structures", *Phys. Rev. Lett.* **120**, 163903 (2018).

[171] T. Bauer, P. Banzer, E. Karimi, S. Orlov, A. Rubano, L. Marrucci, E. Santamato, R. W. Boyd, and G. Leuchs, "Observation of optical polarization Möbius strips", *Science* **347**, 964–966 (2015).

[172] S. J. Tempone-Wiltshire, S. P. Johnstone, and K. Helmerson, "Optical vortex knots–one photon at a time", *Sci. Rep.* **6**, 24463 (2016).

[173] S. M. Kelly, T. J. Jess, and N. C. Price, "How to study proteins by circular dichroism", *Biochim. Biophys. Acta* **1751**, 119–139 (2005).

[174] M. Decker, M. W. Klein, M. Wegener, and S. Linden, "Circular dichroism of planar chiral magnetic metamaterials", *Opt. Lett.* **32**, 856–858 (2007).

[175] X. Zambrana-Puyalto, X. Vidal, and G. Molina-Terriza, "Angular momentum-induced circular dichroism in non-chiral nanostructures", *Nat. Commun.* **5**, 4922 (2014).

[176] Y. Gorodetski, N. Shitrit, I. Bretner, V. Kleiner, and E. Hasman, "Observation of optical spin symmetry breaking in nanoapertures", *Nano Lett.* **9**, 3016–3019 (2009).

[177] T. J. White, S. V. Serak, N. V. Tabiryan, R. A. Vaia, and T. J. Bunning, "Polarization-controlled, photodriven bending in monodomain liquid crystal elastomer cantilevers", *J. Mater. Chem.* **19**, 1080–1085 (2009).

[178] H. Wang, K. M. Lee, T. J. White, and W. S. Oates, "*trans-cis* and *trans-cis-trans* microstructure evolution of azobenzene liquid-crystal polymer networks", *Macromol. Theory and Simul.* **21**, 285–301.

[179] J. Bin and W. S. Oates, "A unified material description for light induced deformation in azobenzene polymers", *Sci. Rep.* **5**, 14654 (2015).

[180] R. Pugatch, M. Shuker, O. Firstenberg, A. Ron, and N. Davidson, "Topological stability of stored optical vortices", *Phys. Rev. Lett.* **98**, 203601 (2007).

[181] M. Fleischhauer and M. D. Lukin, "Quantum memory for photons: Dark-state polaritons", *Phys. Rev. A* **65**, 022314 (2002).

[182] A. M. Beckley, T. G. Brown, and M. A. Alonso, "Full Poincaré beams", *Opt. Express* **18**, 10777–10785 (2010).

[183] A. M. Beckley, T. G. Brown, and M. A. Alonso, "Full Poincaré beams II: partial polarization", *Opt. Express* **20**, 9357–9362 (2012).

[184] S. Donati, L. Dominici, G. Dagvadorj, D. Ballarini, M. De Giorgi, A. Bramati, G. Gigli, Y. G. Rubo, M. H. Szymańska, and D. Sanvitto, "Twist of generalized skyrmions and spin vortices in a polariton superfluid", *Proc. Natl. Acad. Sci. U.S.A.* **113**, 14926–14931 (2016).

[185] G. B. Airy, "On the Diffraction of an Object-glass with Circular Aperture", *Trans. Camb. Phil. Soc.* **5**, 283–291 (1835).

[186] W. Lommel, *Abh. Bayer. Akad. Wissensch.* **15**, 229 and 529 (1886).

[187] M. G. B. Gray, A. and T. M. MacRobert, *A Treatise on Bessel Functions* (Macmillan, 1931), 2nd ed.

[188] H. H. Hopkins, "The disturbance near the focus of waves of radially non-uniform amplitude", *Proc. Phys. Soc. B* **62**, 22–32 (1949).

[189] N. Bokor and N. Davidson, "A three dimensional dark focal spot uniformly surrounded by light", *Opt. Commun.* **279**, 229–234 (2007).

[190] J. Lekner, "Tight focusing of light beams: a set of exact solutions", *Proc. R. Soc. A* **472**, 20160538 (2016).

[191] P. Andrejic and J. Lekner, "Topology of phase and polarisation singularities in focal regions", *J. Opt.* **19**, 105609 (2017).

[192] S. van Haver, "The extended Nijboer-Zernike diffraction theory and its applications", PhD dissertation, Delft University of Technology (2010).

[193] C. J. R. Sheppard and P. Török, "Efficient calculation of electromagnetic diffraction in optical systems using a multipole expansion", *J. Mod. Opt.* **44**, 803–818 (1997).

[194] T. X. Hoang, X. Chen, and C. J. R. Sheppard, "Multipole theory for tight focusing of polarized light, including radially polarized and other special cases", *J. Opt. Soc. Am. A* **29**, 32–43 (2012).

[195] S. Orlov, U. Peschel, T. Bauer, and P. Banzer, "Analytical expansion of highly focused vector beams into vector spherical harmonics and its application to mie scattering", *Phys. Rev. A* **85**, 063825 (2012).

[196] L. C. Biedenharn, J. D. Louck, and P. A. Carruthers, *Angular Momentum in Quantum Physics: Theory and Application*, Encyclopedia of Mathematics and its Applications (Cambridge University Press, 1984).

[197] A. J. Devaney and E. Wolf, "Multipole expansions and plane wave representations of the electromagnetic field", *J. Math. Phys.* **15**, 234–244 (1974).

[198] M. R. Dennis, "Canonical representation of spherical functions: Sylvester's theorem, Maxwell's multipoles and Majorana's sphere", *J. Phys. A* **37**, 9487–9500 (2004).

[199] D. M. Brink and G. R. Satchler, *Angular Momentum* (Clarendon Press, 1994).

[200] D. A. Varshalovich, A. N. Moskalev, and V. K. Khersonskii, *Quantum Theory of Angular Momentum* (World Scientific, 1988).

[201] A. Lewis, A. Challinor, and N. Turok, "Analysis of CMB polarization on an incomplete sky", *Phys. Rev. D* **65**, 023505 (2001).

[202] A. Challinor, P. Fosalba, D. Mortlock, M. Ashdown, B. Wandelt, and K. Górski, "All-sky convolution for polarimetry experiments", *Phys. Rev. D* **62**, 123002 (2000).

[203] K. Jahn and N. Bokor, "Revisiting the concentration problem of vector fields within a spherical cap: A commuting differential operator solution", *J. Fourier Anal. Appl.* **20**, 421–451 (2014).

[204] S. Chandrasekhar and P. C. Kendall, "On force-free magnetic fields." *Astrophys. J.* **126**, 457–460 (1957).

[205] X.-l. Xia, H. Qin, and Q. Wang, "Approach to Chandrasekhar-Kendall-Woltjer state in a chiral plasma", *Phys. Rev. D* **94**, 054042 (2016).

[206] H. Moses, "Eigenfunctions of the Curl Operator, Rotationally Invariant Helmholtz Theorem, and Applications to Electromagnetic Theory and Fluid Mechanics", *SIAM J. Appl. Math.* **21**, 114–144 (1971).

[207] P. Sutcliffe, "Knots in the Skyrme-Faddeev model", *Proc. R. Soc. A* **463**, 3001–3020 (2007).

[208] F. Oberhettinger, *Handbook of Mathematical Functions: with Formulas, Graphs, and Mathematical Tables* (Dover, 1972), chap. 15.

[209] M. N. M. Kobayashi, "Toroidal domain walls as hopfions", arXiv:1304.4737v1 (2013).

[210] M. Kobayashi and M. Nitta, "Torus knots as hopfions", *Physics Letters B* **728**, 314–318 (2014).

[211] Y. Liu, R. K. Lake, and J. Zang, "Binding a hopfion in a chiral magnet nanodisk", *Phys. Rev. B* **98**, 174437 (2018).

[212] N. Manton and P. Sutcliffe, *Topological Solitons* (Cambridge University Press, 2004).

[213] L. Isenhower, W. Williams, A. Dally, and M. Saffman, "Atom trapping in an interferometrically generated bottle beam trap", *Opt. Lett.* **34**, 1159–1161 (2009).

[214] Z. Xie, S. He, C. Chen, Y. Feng, H. Yi, A. Liang, L. Zhao, D. Mou, J. He, Y. Peng, X. Liu, Y. Liu, G. Liu, X. Dong, L. Yu, J. Zhang, S. Zhang, Z. Wang, F. Zhang, F. Yang, Q. Peng, X. Wang, C. Chen, Z. Xu, and X. J. Zhou, "Orbital-selective

spin texture and its manipulation in a topological insulator", *Nat. Commun.* **5**, 3382 (2014).

[215] C. Jozwiak, C.-H. Park, K. Gotlieb, C. Hwang, D.-H. Lee, S. G. Louie, J. D. Denlinger, C. R. Rotundu, R. J. Birgeneau, Z. Hussain, and A. Lanzara, "Photoelectron spin-flipping and texture manipulation in a topological insulator", *Nat. Phys.* **9**, 293–298 (2013).

[216] W. Lee, A. H. Gheorghe, K. Tiurev, T. Ollikainen, M. Möttönen, and D. S. Hall, "Synthetic electromagnetic knot in a three-dimensional skyrmion", *Sci. Adv.* **4**, eaao3820 (2018).

[217] A. Fernández-Pacheco, R. Streubel, O. Fruchart, R. Hertel, P. Fischer, and R. P. Cowburn, "Three-dimensional nanomagnetism", *Nat. Commun.* **8**, 15756 (2017).

[218] A. Marzo, S. A. Seah, B. W. Drinkwater, D. R. Sahoo, B. Long, and S. Subramanian, "Holographic acoustic elements for manipulation of levitated objects", *Nat. Commun.* **6**, 8661 (2015).